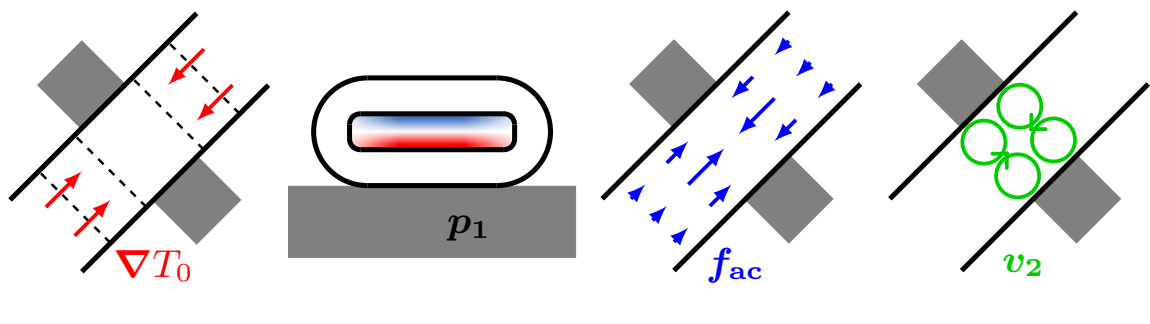


Ph.D. Thesis

# Theory and modeling of thermoviscous acoustofluidics

Jonas Helboe Jørgensen



Supervisor: Henrik Bruus

Department of Physics  
Technical University of Denmark

30 January 2022

**Cover illustration** – Sketch of the thermoacoustic streaming in a glass capillary tube, adapted from Fig. 4.2.

*Theory and modeling of thermoviscous acoustofluidics*

Copyright ©2022 Jonas Helboe Jørgensen All Rights Reserved  
Typeset using L<sup>A</sup>T<sub>E</sub>X

<http://www.fysik.dtu.dk/microfluidics>

# Abstract

The field of acoustofluidics is the interdisciplinary field between microfluidics and acoustics, where ultrasound is used in microfluidic devices to act on particles and cells in a fluid. In the thesis a theoretical and numerical model is developed to study the impact of temperature fields in acoustofluidic devices. The numerical model has three important characteristics compared to previous models, first it includes temperature fields and the temperature dependency of the fluid parameters. Secondly, it is an effective model where the thin thermal and viscous boundary layers are solved analytically and imposed as effective boundary conditions, this enables the possibility of 3D simulations of acoustofluidic devices. Thirdly, a non-perturbative model is developed that includes nonlinear effects due to high acoustic energy density or high streaming velocities.

The numerical model is used to study the thermoacoustic streaming generated in acoustofluidic devices due to temperature gradients in the fluid. The model was used to simulate an acoustofluidic system integrating light absorption from a light emitting diode and to explain well-known but previously unexplainable streaming patterns. The non-perturbative part of the numerical model was utilized to study the change in the streaming pattern due to heating in the viscous boundary layers at high acoustic energy density. Furthermore, the streaming flow in an acoustic tweezer was studied, which at high frequency can be a limiting parameter for the axial trapping force. Lastly the possibility of changing the resonance frequency of a system by changing the temperature was explored and led to the proposal of an acoustic trap controlled by the temperature field. This could result in a movable trap controlled by a light emitting diode.

Hopefully, the thesis provides physical insight and understanding of the importance of the temperature fields in acoustofluidic devices along with the validated numerical model.



# Resumé

Forskningsfeltet akustofluidik beskæftiger sig med det tværfaglige felt om mikrofluidik og akustik, her bruges ultralyd i mikrofluide systemer til at påvirke partikler og celler i væsken. I afhandlingen udledes en teoretisk og numerisk model for at studere betydningen af temperaturfelter i akustofluide systemer. Den numeriske model har tre vigtige egenskaber i forhold til tidligere modeller, den inkluderer temperaturfelter og væskeparametrenes temperaturafhængighed. For det andet er det en effektiv model, hvor de tynde termiske og viskøse randlag løses analytisk og bruges som effektive randbetingelser, dette giver mulighed for at lave 3D-simuleringer af akustofluide systemer. For det tredje udvikles en ikke perturbativ model, der inkluderer ikke lineære effekter på grund af høj akustisk energi densitet eller høje væskestrømningshastigheder.

Den numeriske model bruges til at studere den termoakustiske væskestrømning, der genereres i akustofluide systemer på grund af temperaturgradienter i væsken. Modellen er blevet brugt til at simulere et akustofluidisk system, der integrerer lysabsorption fra en lysdiode. Modellen forklarer også tidligere kendte, men førhen uforklarlige væskestrømningsmønstre. Den iterative del af den numeriske model er blevet brugt til at studere ændringen i strømningsmønsteret på grund af opvarmning i de viskøse randlag ved høj akustisk energitæthed. Derudover studeres væskestrømningen i en akustisk pincet, som ved høje frekvenser kan være en begrænsende parameter for den aksiale kraft. Til sidst er muligheden for at ændre resonansfrekvensen af et system ved at ændre temperaturen blevet undersøgt og ført til forslaget om en akustisk fælde styret af temperaturefeltet. Dette kan resultere i en bevægelig fælde styret af en lysdiode.

Forhåbentlig giver afhandlingen udover en valideret numerisk model en fysisk indsigt og forståelse af temperaturfeltets betydning i akustofluidik.



# Preface

The thesis is submitted in candidacy for the degree of Doctor of Philosophy (PhD) from the Technical University of Denmark (DTU). The work was performed in the Department of Physics, Section of Biophysics and Fluids, in the Theoretical Microfluidics Group in the period from 1 October 2018 to 30 January 2022, with Professor Henrik Bruus as the main supervisor and Professor Per Augustsson, Lund University, as co-supervisor. The PhD project was funded by the Independent Research Fund Denmark, FNU Grant no 8021-00310B. The project included an external stay of three months in the group of Senior research scientist (Directeur de recherche) Jean-Louis Thomas at Institut des NanoSciences de Paris (INSP) at Sorbonne University, Paris.

Kongens Lyngby, 30. January 2022



Jonas Helboe Jørgensen





# Acknowledgements

I have enjoyed my time as a PhD student at the Technical University of Denmark (DTU) which has given me the opportunity to work in the interesting field of acoustofluidics. Even though a concussion and the corona pandemic has made life and work challenging for periods of time. I would like to thank my supervisor Professor Henrik Bruus for the opportunity to work in his group at DTU Physics, even though I did not have a background in either acoustic or microfluidics. It has been a joy to work with an inspiring and passionate supervisor who has thought me a lot about physics and research.

At my time at DTU I have had the pleasure to be part of a wonderful group in the Theoretical Microfluidics Group and the former and current PhD students, Nils, Jacob, André, William, Fabian and Bjørn have created an inspiring work environment in the group together with Associate Professor Massimiliano Rossi and former Postdoc Wei Qiu. The various moose meetings, street food Fridays, and coffee breaks has been a pleasant part of the working day the last three years.

Secondly, I would like to give my big appreciation to our collaborators in the group of Per Augustsson at Lund University. A huge thanks to Wei Qiu for spending countless hours in the laboratory observing streaming flows, to Enrico Corato for numerous discussions over Zoom, and to Professor Per Augustsson for not only being my co-supervisor but also for him and his group driving the research field of thermoviscous acoustofluidics.

Thirdly, a big thanks to Senior Research Scientist Jean-Louis Thomas for welcoming me to his group at Sorbonne University during my external stay in Paris. It was a pleasure to work with Jean-Louis Thomas and Sarah Vincent and get an insight into their inspiring work on acoustic tweezers. And a special thanks to Sarah Vincent and the rest of the PhD group at Sorbonne University for showing my that even during a global pandemic there is more to Paris than work.

And finally a big thanks to my family and friends for supporting me during the three years and especially during the concussion period. I am grateful to my parents for inspiring me to be curious and supporting me throughout my education.



# Contents

|  |              |
|--|--------------|
| <b>List of Publications</b>  | <b>xv</b>    |
| <b>List of figures</b>   | <b>xviii</b> |
| <b>List of tables</b>  | <b>xix</b>   |
| <b>1 Introduction</b>  | <b>1</b>     |
| 1.1 Microfluidics . . . . .  | 1            |
| 1.2 Acoustofluidics . . . . .  | 2            |
| 1.3 Main research focus . . . . .                                      | 3            |
| 1.4 Thesis outline . . . . .   | 5            |
| <b>2 Theory</b>  | <b>7</b>     |
| 2.1 Governing equations . . . . .                                      | 7            |
| 2.1.1 Fluid equations and parameters . . . . .                         | 8            |
| 2.1.2 Solid equations . . . . .  | 10           |
| 2.2 Perturbation theory . . . . .                                      | 11           |
| 2.3 Separation of length scales . . . . .                              | 12           |
| 2.4 Boundary conditions . . . . .                                      | 13           |
| 2.5 Zeroth order – Temperature field . . . . .                         | 14           |
| 2.6 First order – Acoustic fields . . . . .                            | 15           |
| 2.6.1 Equations in the fluid . . . . .                                 | 15           |
| 2.6.2 Equations in the solid . . . . .                                 | 17           |
| 2.6.3 Analytical solutions to the boundary layer fields . . . . .      | 17           |
| 2.6.4 Effective boundary conditions . . . . .                          | 18           |
| 2.6.5 Resonances and time-averaged products . . . . .                  | 18           |
| 2.6.6 Example: Pressure field in a square fluid channel . . . . .      | 19           |
| 2.7 Second order – Streaming field . . . . .                           | 21           |
| 2.7.1 Boundary layer field and effective boundary conditions . . . . . | 22           |
| 2.7.2 Bulk streaming . . . . .   | 23           |
| 2.7.3 Examples: Streaming in a square capillary . . . . .              | 24           |
| 2.8 Second order – Temperature field . . . . .                         | 25           |
| 2.8.1 Bulk temperature field . . . . .                                 | 27           |
| 2.8.2 Example: Heating in viscous boundary layers . . . . .            | 28           |

|          |   |           |
|----------|---|-----------|
| 2.9      | Forces on particles . . . . .                                     | 29        |
| 2.9.1    | Acoustic radiation force in acoustofluidic devices . . . . .      | 30        |
| 2.10     | Non-perturbative acoustofluidics . . . . .                        | 31        |
| 2.10.1   | Range of validity for the perturbation theory . . . . .           | 31        |
| 2.10.2   | Separation of time-scales . . . . .                               | 32        |
| 2.10.3   | Acoustic and stationary equations . . . . .                       | 33        |
| 2.10.4   | Main non-linear effects . . . . .                                 | 35        |
| <b>3</b> | <b>Numerical Methods</b>  | <b>37</b> |
| 3.1      | The finite element method . . . . .                               | 37        |
| 3.1.1    | Boundary conditions . . . . .                                     | 39        |
| 3.1.2    | Formulation in cylindrical coordinates . . . . .                  | 39        |
| 3.1.3    | Symmetry planes and perfectly matched layers . . . . .            | 41        |
| 3.2      | Validation of numerical simulations . . . . .                     | 41        |
| <b>4</b> | <b>Streaming due to temperature gradients</b>                     | <b>45</b> |
| 4.1      | The inhomogeneous acoustic body force . . . . .                   | 46        |
| 4.2      | Trapping glass capillary . . . . .                                | 47        |
| 4.3      | Light absorption from an LED . . . . .                            | 49        |
| 4.4      | Streaming due to heating in the viscous boundary layers . . . . . | 53        |
| 4.5      | Heating in a small volume . . . . .                               | 56        |
| 4.5.1    | Heating from a laser beam . . . . .                               | 58        |
| 4.6      | Concluding remarks . . . . .                                      | 60        |
| <b>5</b> | <b>Streaming in acoustic tweezers</b>                             | <b>61</b> |
| 5.1      | A short introduction to acoustic tweezers . . . . .               | 61        |
| 5.2      | Analytical streaming flow . . . . .                               | 64        |
| 5.2.1    | Stokeslet: Low Reynolds number in free space . . . . .            | 64        |
| 5.3      | Simulations of streaming in acoustic tweezers . . . . .           | 66        |
| 5.3.1    | Matching the Stokeslet solution . . . . .                         | 67        |
| 5.3.2    | High Reynolds number streaming . . . . .                          | 67        |
| 5.3.3    | Impact of nearby boundaries . . . . .                             | 69        |
| 5.3.4    | Drag forces from streaming . . . . .                              | 70        |
| 5.4      | Concluding remarks . . . . .                                      | 70        |
| <b>6</b> | <b>Spatial localization of acoustic fields</b>                    | <b>71</b> |
| 6.1      | Temperature controlled localization . . . . .                     | 71        |
| 6.1.1    | Analytical considerations . . . . .                               | 72        |
| 6.1.2    | Thermal cavity in oil . . . . .                                   | 73        |
| 6.1.3    | Thermal cavity in water . . . . .                                 | 75        |
| 6.2      | Geometry controlled localization . . . . .                        | 78        |
| 6.3      | Trapping strength . . . . .                                       | 80        |
| 6.4      | Concluding remarks . . . . .                                      | 80        |

|          |  |            |
|----------|--|------------|
| <b>7</b> | <b>Papers</b>  | <b>83</b>  |
| 7.1      | Paper I in JASA . . . . .                                    | 83         |
| 7.2      | Paper II in Physical Review Letters . . . . .                | 96         |
| 7.3      | Paper III in Physical Review E (under review) . . . . .      | 109        |
| 7.4      | Paper IV in Physical Review Letters (under review) . . . . . | 127        |
| <b>8</b> | <b>Conclusions and outlook</b>                               | <b>135</b> |
| 8.1      | Conclusions . . . . .  | 135        |
| 8.2      | Outlook . . . . .  | 136        |
| 8.3      | Extending the numerical model . . . . .                      | 137        |
|          | <b>Bibliography</b>  | <b>139</b> |



# List of publications

## Peer-reviewed journal papers – enclosed in Chapter 7

- I. J. H. Joergensen and H. Bruus, *Theory of pressure acoustics with thermoviscous boundary layers and streaming in elastic cavities*, J. Acoust. Soc. Amer. **149**, 3599-3610 (2021).  
Enclosed in Section 7.1, Ref. [1].
- II. W. Qiu, J. H. Joergensen, E. Corato, H. Bruus, and Per Augustsson, *Fast Microscale Acoustic Streaming Driven by a Temperature-Gradient-Induced Nondissipative Acoustic Body Force*, Phys. Rev. Lett. **127**, 064501 1-6 (2021).  
Enclosed in Section 7.2, Ref. [2].
- III. J. H. Joergensen and H. Bruus, *Theory and modeling of nonperturbative effects at high acoustic energy densities in thermoviscous acoustofluidics*, Submitted to Phys. Rev. E.  
Enclosed in Section 7.3, Ref. [3].
- IV. J. H. Joergensen W. Qiu, and H. Bruus, *A transition from boundary- to bulk-driven acoustic streaming due to nonlinear thermoviscous effects at high acoustic energy densities*, Submitted to Phys. Rev. Lett.  
Enclosed in Section 7.4, Ref. [4].

## Conference contributions – not included in the thesis

1. J. H. Joergensen and H. Bruus, *Thermal fields in acoustofluidic devices*, 9th Sommer School Complex Motion in Fluids, 18-24 Aug 2019, Gilleleje, Denmark, **oral presentation**.
2. J. H. Joergensen and H. Bruus, *Modeling of thermoacoustic heating in acoustofluidic devices*, Acoustofluidics Conference, 26-28 Aug 2019, Enschede, Netherlands, **oral presentation**.
3. J. H. Joergensen and H. Bruus, *Thermal fields acoustofluidics*, The Swedish Center for Acoustofluidics and Cell Separation (SWECACS), 2 Dec 2019, Lund, Sweden, **oral presentation**.

4. W. Qiu, J. H. Joergensen, E. Corato, H. Bruus, and Per Augustsson, *Thermal-gradient-induced fast convection in acoustofluidics devices*, Acoustofluidics Conference, 26-27 Aug 2020, Virtual Conference, **oral presentation** by W. Qiu.
5. J. H. Joergensen and H. Bruus, *Theory of temperature-dependent effects in acoustofluidics including thermoviscous boundary layers*, Acoustofluidics Conference, 26-27 Aug 2020, Virtual Conference, **oral presentation**.
6. J. H. Joergensen and H. Bruus, *Theory of thermoviscous effects in acoustics traps*, Trappist II, 20 Jul 2021, Bordeaux, **oral presentation**.
7. J. H. Joergensen, W. Qiu, and H. Bruus, *Qualitative changes in the streaming pattern at high acoustic energy due to friction-induced heating in the viscous boundary layers*, Acoustofluidics Conference, 26-27 Aug 2021, Virtual Conference, **oral presentation**.
8. J. H. Joergensen and H. Bruus, *Novel methods of spatially localizing acoustic fields in straight capillaries*, The Swedish Center for Acoustofluidics and Cell Separation (SWECACS), 7 Dec 2021, Lund, Sweden, **oral presentation**.



# List of Figures

|     |  |    |
|-----|--|----|
| 1.1 | Complex microfluidic system . . . . .  | 2  |
| 1.2 | Classical acoustofluidic system . . . . .                                      | 3  |
| 1.3 | Inhomogeneous acoustic body force sustaining concentration gradients . . . . . | 4  |
| 2.1 | Sketch of boundary layers . . . . .  | 13 |
| 2.2 | Resonance in square capillary . . . . .  | 20 |
| 2.3 | Streaming in square capillary . . . . .  | 25 |
| 2.4 | Heating in boundary layers . . . . .   | 28 |
| 2.5 | Iterative loop . . . . .   | 34 |
| 3.1 | Basis functions . . . . .  | 38 |
| 3.2 | Convergence test . . . . .   | 42 |
| 4.1 | Horizontal streaming rolls in trapping glass capillary. . . . .                | 47 |
| 4.2 | Sketch of streaming in capillary. . . . .                                      | 48 |
| 4.3 | Experimental and numerical model. . . . .                                      | 50 |
| 4.4 | 3D streaming pattern of thermoacoustic streaming. . . . .                      | 51 |
| 4.5 | Transition from boundary to bulk-driven streaming. . . . .                     | 52 |
| 4.6 | 2D model of rectangular channel . . . . .                                      | 54 |
| 4.7 | Nonlinear transition from boundary- to bulk-driven streaming . . . . .         | 55 |
| 4.8 | Sketch of streaming due to local heating . . . . .                             | 57 |
| 4.9 | Simulation of streaming due to a laser spot . . . . .                          | 59 |
| 5.1 | Acoustic tweezers . . . . .  | 62 |
| 5.2 | Pressure and radiation force from acoustic tweezer . . . . .                   | 63 |
| 5.3 | Analytical stokeslet streaming in acoustic tweezer . . . . .                   | 65 |
| 5.4 | Importance of the volume of the force field . . . . .                          | 66 |
| 5.5 | Validation of numerical solution for low Reynolds numbers . . . . .            | 67 |
| 5.6 | Streaming at high Reynolds numbers . . . . .                                   | 68 |
| 5.7 | Impact of nearby boundaries . . . . .  | 69 |
| 6.1 | Sketch of thermal cavity . . . . .   | 72 |
| 6.2 | Thermal cavity in oil . . . . .  | 74 |
| 6.3 | Thermal cavity in water . . . . .  | 76 |

|     |  |    |
|-----|--|----|
| 6.4 | Thermal cavity in cylindrical water domain . . . . . | 77 |
| 6.5 | Sketch of a geometrical cavity . . . . .             | 78 |
| 6.6 | Glass capillary with geometrical cavities . . . . .  | 79 |

# List of Tables

|     |                            |    |
|-----|----------------------------|----|
| 2.1 | Water parameters . . . . . | 10 |
|-----|----------------------------|----|



# Chapter 1

## Introduction

The introduction of the thesis gives a short presentation of microfluidics and acoustofluidics. The research of the thesis is in the field acoustofluidics and the main aspects of the field will be introduced and the research focus of the thesis is motivated and the structure and content of the thesis are presented.

### 1.1 Microfluidics

The field of microfluidics concerns the behaviour of fluid flows and its content (particles, cells etc.) in channels of tenth to hundreds of micrometers [5]. Microfluidics is especially useful for biochemistry analysis, since it gives a cheap platform for analysing small fluid volumes. So-called *Lab-on-a-chip* systems gives the possibility to analyse few drops of biological fluid in cheap devices which do not require the expenses of traditional laboratories [6]. The microfluidic systems take advantage of its small size to analyse small fluid volumes and the laminar fluid flow to have a predictable behaviour of particles and cells in the fluid. The *Lab-on-a-chip* systems are a miniaturized laboratory which consists of different components, as for example mixers, valves, pumps, drop generators, detectors, and biochemistry assays that can be combined to achieve a certain functionality of a device, see an example of a complex microfluidic bioreactor in Fig. 1.1. Microfluidics has promising perspectives in the fields of point-of-care devices for fast diagnostics [7, 8], microfluidic bioreactors [9, 10] (see Fig. 1.1), and organ-on-a-chip devices used for drug testing on artificial organs [11, 12].

To construct these complex microfluidic devices different individual components are combined (mixers, valves, pumps, etc.), to achieve the functionalities of the individual components a wide set of physical principles are used. The variety of physical forces used include inertial [13], gravitational [14], electromagnetic [15–17], optical [18] and acoustic forces [19, 20]. By the use of these forces suspended particles in the fluid might be trapped, up-concentrated or separated based on their physical properties. This thesis focuses on the field of acoustofluidics which is the field of combining microfluidics with acoustic fields and using the acoustic fields to act on the fluid and the particles and cells suspended in the fluid.

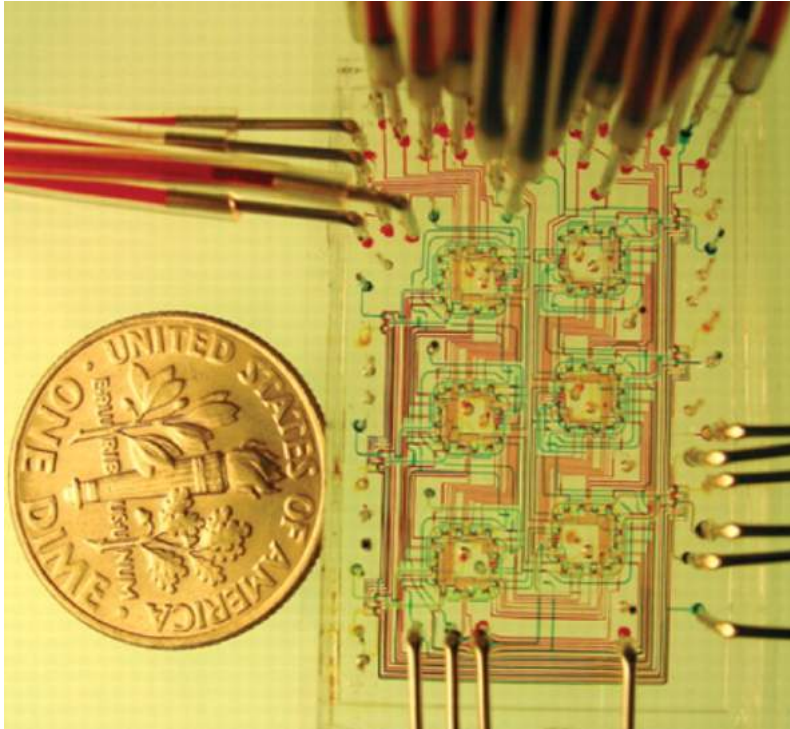


Figure 1.1: Complex microfluidic bioreactor used to observe the dynamics of the bacteria *Escherichia coli*. Figure adapted from Ref. [9].

## 1.2 Acoustofluidics

One of the tools for manipulating the fluid and its content in a microfluidic system is acoustic waves, the research field of acoustic waves in microfluidic systems is called acoustofluidics [8]. In microfluidic devices acoustics are mainly used for mixing fluids, up-concentrating, washing, trapping, and separating particles.

An acoustic field in a fluid can impact particles and cells through two mechanisms, the acoustic radiation force and the drag force from the acoustic streaming flow it induces. The acoustic radiation force arises due to the acoustic wave scattering of a particle transferring momentum to the particle [21, 22] this force typically dominates for larger cells and particles. The acoustic streaming is a steady fluid flow generated due to attenuation of the acoustic waves in the fluid which generate a streaming flow [23, 24] which drags the particles, the drag force is typically dominant for small particles.

Most acoustofluidic devices use the acoustic radiation force as the main force to act on particles. In microfluidic chips designed to up-concentrate, separate or wash particles the acoustic radiation force is used to focus particles in the pressure node or anti-node depending on their physical properties. By focusing the particles in different nodes they can be separated in different outlet channels [25], see Fig. 1.2. A more recent application of acoustic fields are the acoustic tweezer [20, 26–28] where a focalized acoustic vortex beam

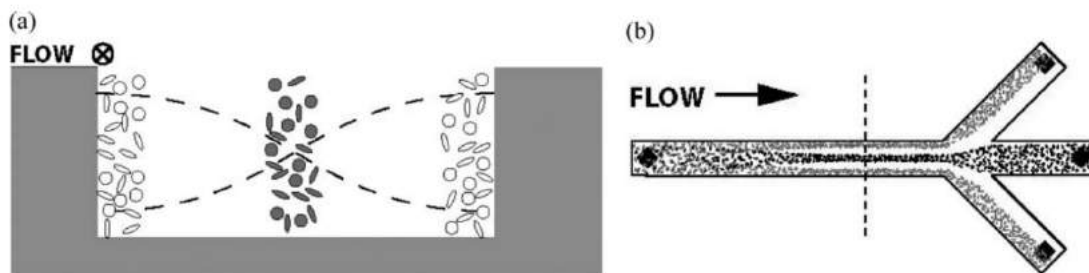


Figure 1.2: Acoustofluidic chip for separating particles from Ref. [25]. (a) Cross-sectional view of the half-wave resonance with cells focusing either at the pressure node or pressure anti-node. (b) Top view of the focusing of particles for a flow through the channel, with one inlet and three outlets separating the cells. Figure from Ref. [25].

is used to trap a particle in a similar manner to an optical tweezer. The acoustic tweezer is promising due to its versatility (wide range of frequencies), selectivity (trap individual particles), and the large forces that it is able to apply to microscale particles and cells.

In most of these devices the acoustic streaming is an annoyance that makes it impossible to focus or trap small particles. The phenomenon of acoustic streaming have been known since Lord Rayleigh in 1884 [23] but has recently seen a development with improved numerical models enabling simulations of actual acoustofluidic devices [29–31] and theories including the effects of gradients in the fluid compressibility and density [32–34]. The improved numerical models has inspired research on how to reduce the acoustic streaming either by electrophoresis [35], shape optimization of the microfluidic channel [36], or inhomogeneous fluids [37, 38].

### 1.3 Main research focus

The main research focus of the thesis is the effects of gradients in the fluid parameters and especially gradients created by temperature fields. Gradients in the fluid parameters are interesting because they induce an inhomogeneous acoustic body force [32] which can induce fast thermoacoustic streaming. The inhomogeneous acoustic body force was theoretically described by J. Karlsen, P. Augustsson, and H. Bruus [32], the force arises when there is an acoustic field in combination with gradients in either the fluid density or compressibility. The groups at Technical University of Denmark (DTU) and Lund University (LU) investigated the impact of the force and its applications, sustaining a concentration gradient [32, 39] (see Fig. 1.3), patterning and reconfiguration of inhomogeneous fluids [40], and streaming suppression [37, 38]. All these studies was with density and compressibility gradients created by gradients of a solute concentration.

Motivated by the research done on the inhomogeneous body force [32, 37–40], the thesis further investigates the force and its impact in acoustofluidic devices. The main focus is on the impact of temperature fields since they create gradients in compressibility, density, and sound speed [29]. Acoustic streaming due to temperature gradients has previously

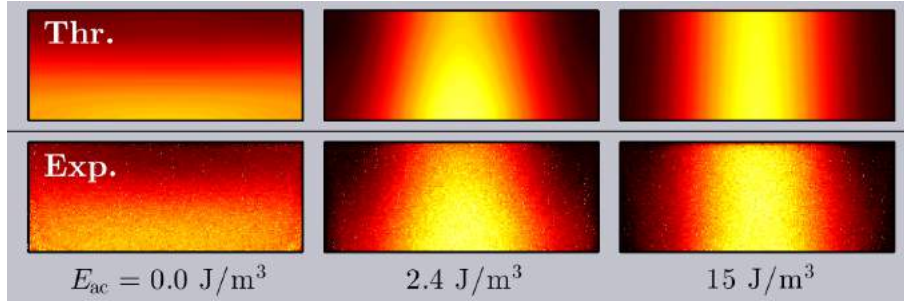


Figure 1.3: Simulation (top) and experimental (bottom) results of a sustained concentration gradient in an acoustofluidic channel with a half-wave acoustic resonance for three different acoustic energies  $E_{ac} = 0, 2.4, \text{ and } 15 \text{ J/m}^3$ . Figure from [32].

been studied in gas, named 'baroclinic' streaming [33, 34, 41, 42].

The main research areas have been the development of an effective thermoviscous model for acoustofluidics and the studies of thermoacoustic bulk streaming. The developed effective thermoviscous model can be implemented either as a perturbation model [1] or an iterative model [3]. The key benefits of the model are:

- I: Being an **effective** model where the thin boundary layers at fluid-solid interfaces are solved analytically and imposed as **effective** boundary conditions. Solving the short-length-scale dynamics in the boundary layers analytically means that it is not necessary to numerically resolve the thin boundary layers, which in return reduces the computational cost and allows simulations of 3D devices on a regular workstation.
- II: It is a **thermoviscous** model that includes both thermal and viscous effects, this is necessary to study the inhomogeneous acoustic body force induced by temperature gradients. Both **thermoviscous** models [29] and effective models [30] has previously been used, but this is to my knowledge the first effective thermoviscous model developed for acoustofluidic devices.
- III: The model can be implemented as either a **perturbation** or an **iterative** model. All previous models in the Theoretical Microfluidics Group at DTU [29, 30, 43] has been **perturbative** models. In a perturbative model the higher order fields cannot influence the lower order fields. In an **iterative** model these non-perturbative effects are included and the iterative solver iterates between the slow and fast-time scale equations until they are both converged. This allows modeling of non-perturbative effects due to internal heating and advective heat transport.

The model has allowed us to study the thermoacoustic bulk streaming in various settings, with temperature gradients induced by a heating piezo-electric transducer [1], light absorption [2], and internal friction in the fluid [4]. To model all these different examples the model needs to be **effective** to model 3D devices, **thermoviscous** to include the temperature fields and **iterative** to include non-linear effects as internal heating and convective heat transport. The obtained agreement between simulations and experiments in [2, 4]



shows that the model describes and captures the effects of temperature gradients on the acoustic streaming pattern.

The investigation of the thermoacoustic streaming has been performed in a great collaboration with Wei Qiu, Enrico Corato and Per Augustsson from Lund University, who have done all the experimental work in the articles [2, 4].

## 1.4 Thesis outline

The main part of the work and research done in the thesis is collected in the published papers in Chapter 7 but the thesis also contains unpublished work on streaming in acoustic tweezers and spatial localization of acoustic fields. The research has been presented at the eight conference presentations listed in the List of Publications together with four scientific papers [1–4]. The thesis contains a main theory chapter introducing the developed thermoviscous model, a numerical chapter surrounding the finite element method (FEM), and then three chapters that focuses on three different aspects of the research performed.

**Chapter 1 – Introduction:** Introduction to microfluidics and acoustofluidics together with a motivation for the research presented in the PhD thesis.

**Chapter 2 – Theory:** Presentation of the thermoviscous model formulated in the enclosed papers in Section 7.1 and Section 7.3. It presents the theory and underlines the importance of having an effective, thermoviscous, and non-perturbative model.

**Chapter 3 – Numerical methods** Presents the finite element method (FEM). The FEM modelling has been used to all the numerical simulations in the thesis.

**Chapter 4 – Streaming due to temperature gradients:** Contains the research done on thermoacoustic streaming caused by the inhomogeneous acoustic body force. It summarizes the research from the papers enclosed in Sections 7.2 and 7.4 together with other examples of thermoacoustic streaming.

**Chapter 5 – Streaming in acoustic tweezers:** Unpublished work done in collaboration with Senior research scientist (Directeur de recherche) Jean-Louis Thomas and Sarah Vincent during my external research stay at Institute of NanoScience de Paris (INSP) at Sorbonne University. The work investigates streaming in acoustic tweezers and its impact on the axial trapping strength.

**Chapter 6 – Spatial localization of acoustic fields:** Unpublished work on methods to spatially localize acoustic fields in acoustofluidic devices. The chapter presents ideas of localizing an acoustic field by either using a temperature field or by changing the chips geometry. The proposal of controlling an acoustic trap by absorption from a light-emitting-diode (LED) is presented and numerically investigated.

**Chapter 7 – Papers:** The four research papers are included, containing the two published papers [1, 2] and the two submitted papers [3, 4] currently under review. The research papers are:

- I. J. H. Joergensen and H. Bruus, *Theory of pressure acoustics with thermoviscous boundary layers and streaming in elastic cavities*, J. Acoust. Soc. Amer. **149**, 3599-3610 (2021).  
Enclosed in Section 7.1, Ref. [1].
- II. W. Qiu, J. H. Joergensen, E. Corato, H. Bruus, and Per Augustsson, *Fast Microscale Acoustic Streaming Driven by a Temperature-Gradient-Induced Nondissipative Acoustic Body Force*, Phys. Rev. Lett. **127**, 064501 1-6 (2021).  
Enclosed in Section 7.2, Ref. [2].
- III. J. H. Joergensen and H. Bruus, *Theory and modeling of nonperturbative effects at high acoustic energy densities in thermoviscous acoustofluidics*, Submitted to Phys. Rev. E.  
Enclosed in Section 7.3, Ref. [3].
- IV. J. H. Joergensen W. Qiu, and H. Bruus, *A transition from boundary- to bulk-driven acoustic streaming due to nonlinear thermoviscous effects at high acoustic energy densities*, Submitted to Phys. Rev. Lett.  
Enclosed in Section 7.4, Ref. [4].

**Chapter 8 – Conclusion:** Conclusions on the work performed during the PhD and an outlook on the perspectives of using controlled temperature fields in acoustofluidics.

# Chapter 2

## Theory

The chapter presents the theoretical model developed during the thesis and shows the strength and limitations of the model. The development of an effective thermoviscous pressure acoustic model was a big part of the PhD thesis, and can be seen as an extension to the purely viscous effective pressure acoustic model of Bach and Bruus (2018)[30] by including temperature fields and the temperature dependency of the material parameters.

The aim is to develop a model for a microfluidic system that contains a fluid domain surrounded by an elastic solid and is actuated with ultrasound, typically frequencies of  $f = 1 - 20$  MHz. The model contains both the fluid and the solid, but the overwhelming focus of the thesis is to understand the physics of the fluid domain while the modelling for the solid follows earlier work [30, 31, 44]. The developed numerical model is an effective model including temperature fields and the model can be implemented either as a perturbative model or as a non-perturbative iterative model.

The chapter builds on known physics [21, 29, 30, 32, 45] and the research work published in the theoretical papers enclosed in Sections 7.1 and 7.3.

### 2.1 Governing equations

The behaviour of the fluid and solid is described by a set of fields, in the fluid the temperature  $T$ , the pressure  $p$  and velocity field  $\mathbf{v}$  and in the elastic solid the temperature  $T$  and the displacement field  $\mathbf{u}$ . These fields are governed by a set of fundamental physical principles, the conservation of mass, the conservation of momentum, and the conservation of energy.

There are two main pictures of describing fields in fluids and solids either the Eulerian or Lagrangian picture. In the Lagrangian picture we identify a fluid particle located at  $x_0$  at time  $t_0$  and then we follow the movement of the fluid particle. In the Eulerian picture the fields are described in fixed positions and the fluid passes through the different points. As in Refs. [30, 31] the Eulerian picture is used in the fluid and the Lagrangian picture is used in the solid. That the fluid and solid domains are described in two different pictures is important to remember when specifying the boundary conditions on the interface between the fluid and solid domains.

All the governing equations in both the fluid and solid stems from conservation of a quantity (mass, momentum, or energy) and are described as transport equations. Analysing a fluid/solid particle with volume  $V$  and surface  $\Omega$  then the change of a quantity  $Q = \int_V q dV$  with density  $q$  in the volume  $V$  has to be equal to the flux  $\mathbf{J}_q$  through the boundary  $\Omega$  and the generation/loss of the quantity  $P_q$  inside the volume  $V$ , thus the equation is,

$$\int_V \partial_t q dV = - \int_{\Omega} \mathbf{n} \cdot \mathbf{J}_q d\Omega + \int_V P_q dV. \quad (2.1)$$

Here  $\mathbf{n}$  is pointing out of the fluid volume such that  $\mathbf{n} \cdot \mathbf{J}_q$  is the flux leaving the volume  $V$  through the surface  $\Omega$ , hence the minus sign. The surface integral over  $\Omega$  can be rewritten as a volume integral using Gauss theorem,

$$\int_{\Omega} \mathbf{n} \cdot \mathbf{J} d\Omega = \int_V \nabla \cdot \mathbf{J} dV. \quad (2.2)$$

By rewriting the surface integral to a volume integral all three terms are volume integrals and the differential form of the transport equation can be written as,

$$\partial_t q = -\nabla \cdot \mathbf{J}_q + P_q. \quad (2.3)$$

The transport equation conserves the quantity  $q$ . For the conservation of energy the flux  $\mathbf{J}_q$  could be heat diffusion or convection and the term  $P_q$  heat generation from the absorption of light.

### 2.1.1 Fluid equations and parameters

The fluid is described in the Eulerian picture and we are modelling a thermoviscous fluid described by the following material parameters: the density  $\rho$ , the dynamic and bulk viscosity  $\eta$  and  $\eta^b$ , the thermal conductivity  $k^{\text{th}}$ , the specific heat capacity at constant pressure  $c_p$  and constant volume  $c_v$ , the thermal expansion coefficient  $\alpha_p$ , the ratio of specific heats  $\gamma = c_p/c_v$ , the isentropic and isothermal compressibilities  $\kappa_s$  and  $\kappa_T = \gamma\kappa_s$ , and the sound speed  $c = 1/\sqrt{\rho\kappa_T}$ .

In the model we describe the fluid by the independent fields of pressure  $p$ , temperature  $T$ , and velocity  $\mathbf{v}$ , thus the dependent fields are the internal energy density  $\epsilon$  and the mass density  $\rho$  which are given from the first law of thermodynamics and the equation of state as, [29, 46, 47]

$$\rho d\epsilon = (\rho c_p - \alpha_p p) dT + (\kappa_T p - \alpha_p T) dp \quad (2.4a)$$

$$d\rho = \rho \kappa_T dp - \rho \alpha_p dT \quad (2.4b)$$

The fields are governed by the conservation of mass  $\rho$ , momentum  $\rho\mathbf{v}$ , and energy  $\rho\epsilon + \frac{1}{2}\rho|\mathbf{v}|^2$ . The equation for conservation of mass is often referred to as the continuity equation. Mass cannot be created or lost so  $P_\rho = 0$  and the only transport of mass is due to convection  $\mathbf{J}_\rho = \rho\mathbf{v}$  resulting in the continuity equation,

$$\partial_t \rho = -\nabla \cdot (\rho\mathbf{v}), \quad (2.5)$$

where the equation of state (2.4b) can be used to substitute the time-derivative of the density  $\rho$  with the time-derivative of the pressure  $p$  and temperature  $T$ .

The conservation of momentum  $\rho\mathbf{v}$  is described by the Navier-Stokes equation, momentum can be transported both by convection or by forces/stresses in the fluid,

$$\partial_t(\rho\mathbf{v}) = \nabla \cdot (\boldsymbol{\sigma} - \rho\mathbf{v}\mathbf{v}) + \mathbf{f}, \quad (2.6)$$

where  $\boldsymbol{\sigma}$  is the stress tensor which together with the advection term  $\rho\mathbf{v}\mathbf{v}$  is responsible for the momentum flux  $\mathbf{J}_{\rho\mathbf{v}}$  and the force  $\mathbf{f}$  can generate momentum. In our study we neglect gravity and therefore the external force is zero  $\mathbf{f} = 0$ . The stress tensor  $\boldsymbol{\sigma}$  is given as,

$$\boldsymbol{\sigma} = -p\mathbf{I} + \boldsymbol{\tau}, \quad (2.7a)$$

$$\boldsymbol{\tau} = \eta \left[ \nabla\mathbf{v} + (\nabla\mathbf{v})^\dagger \right] + \left( \eta^b - \frac{2}{3}\eta \right) (\nabla \cdot \mathbf{v})\mathbf{I}. \quad (2.7b)$$

Here the stress is divided into a gradient of the pressure field and a viscous stress tensor  $\boldsymbol{\tau}$ . The superscript "†" denotes the transposed matrix.

The total energy density is the sum of the internal energy  $\rho\epsilon$  in Eq. (2.4a) and the kinetic energy density  $\frac{1}{2}\rho|\mathbf{v}|^2$ . The energy can be transferred across a boundary by different mechanisms: Mechanical energy can be transferred by work done by a force given as  $\mathbf{v} \cdot \boldsymbol{\sigma}$ , thermal energy can be transferred by heat diffusion  $k^{\text{th}}\nabla T$ , and both kinetic and internal energy can be transferred by advection  $\mathbf{v}\rho \left( \epsilon + \frac{1}{2}|\mathbf{v}|^2 \right)$ . So the transport equation for the conservation of energy is,

$$\partial_t \left( \rho\epsilon + \rho\frac{v^2}{2} \right) = \nabla \cdot \left[ k^{\text{th}}\nabla T + \mathbf{v} \cdot \boldsymbol{\sigma} - \rho\mathbf{v} \left( \epsilon + \frac{v^2}{2} \right) \right] + P, \quad (2.8)$$

where  $P$  is the external power density. The power density  $P$  could be due to absorption of light from an external light source or Joule heating from an electrical wire.

The fluid parameters depends on the temperature and pressure of the fluid, for the density  $\rho$  the dependencies are given by the compressibility  $\kappa_T$  and thermal expansion coefficient  $\alpha_p$  in the equation of state (2.4b). Like the density, any material parameter  $q$  has a pressure and temperature dependency,

$$\frac{1}{q_0}dq = a_q^T \alpha_p dT + a_q^p \kappa_T dp, \quad (2.9a)$$

$$a_q^T = \frac{1}{\alpha_p q_0} \left( \frac{\partial q}{\partial T} \right)_p, \quad a_q^p = \frac{1}{\kappa_T q_0} \left( \frac{\partial q}{\partial p} \right)_T. \quad (2.9b)$$

Here the independent variables are  $T$  and  $p$  following the convention from Ref. [3] enclosed in Section 7.3 (Note the convention in Section 7.1 is  $T$  and  $\rho$  as independent variables). The parameters  $a_q^T$  and  $a_q^p$  are defined as dimensionless and describes the parameters dependency on temperature and pressure. For an acoustic pressure field with an adiabatic temperature field the change in a material parameter is given as,

$$\frac{1}{q_0}dq = a_q^{p,ad} \kappa_s dp, \quad a_q^{p,ad} = \gamma(\gamma - 1)a_q^T + \gamma a_q^p. \quad (2.10)$$

Table 2.1: Parameters for water at  $T = 25C$ . The table shows the parameters value  $q$  and the relevant temperature  $a_q^T$  and adiabatic  $a_q^{p,ad}$  dependencies. Data from Ref. [29].

| Parameter              | symbol          | $q$                                      | $a_q^T$ | $a_q^{p,ad}$ |
|------------------------|-----------------|--|---------|--------------|
| Density                | $\rho$          | 997 kg/m <sup>3</sup>                    | -1      | 1            |
| Compressibility        | $\kappa_T$      | $4.525 \times 10^{-10}$ Pa <sup>-1</sup> | -9.6    | -            |
| Sound speed            | $c$             | 1497 m/s                                 | 6.9     | -            |
| Dynamic viscosity      | $\eta$          | $0.890 \times 10^{-3}$ Pa s              | -88     | -1.3         |
| Bulk viscosity         | $\eta^b$        | $2.485 \times 10^{-3}$ Pa s              | -100    | -1.1         |
| Thermal conductivity   | $k^{\text{th}}$ | 0.606 W m <sup>-1</sup> K <sup>-1</sup>  | 8.4     | 2.3          |
| Thermal expansion      | $\alpha_p$      | $2.573 \times 10^{-4}$ K <sup>-1</sup>   | -       | -            |
| Specific heat capacity | $c_p$           | 4181 Jkg <sup>-1</sup> K <sup>-1</sup>   | -       | -            |
| Heat capacity ratio    | $\gamma$        | 1.011                                    | -       | -            |

The  $a_q$  parameters are determined using the functions from Muller and Bruus (2014) [29]. In acoustofluidic systems there are mainly three forms of gradients in the material parameters due to temperature and pressure fields: (i) Gradients in the stationary temperature field, (ii) time-dependent gradients due to acoustic pressure and adiabatic temperature, and (iii) time-dependent gradients due to the thermal boundary layers of the acoustic temperature field. Cause (i) and (iii) is controlled by the temperature dependency of the material parameters  $a_q^T$  and the (ii) is controlled by the adiabatic dependency  $a_q^{p,ad}$ . A list of the important material parameters and the relevant temperature and adiabatic dependencies are given in Table 2.1.

### 2.1.2 Solid equations

The solid is described in the Lagrangian picture and the elastic solid is characterized by the following material parameters: the density  $\rho$ , the longitudinal and transverse sound speeds  $c_{\text{lo}}$  and  $c_{\text{tr}}$ , the thermal conductivity  $k^{\text{th}}$ , the specific heat at constant pressure  $c_p$  and constant volume  $c_v$ , the ratio of specific heats  $\gamma = c_p/c_v$ , the thermal expansion coefficient  $\alpha_p$ , and the isentropic and isothermal compressibilities  $\kappa_s$  and  $\kappa_T$ . The solid is described by the displacement field  $\mathbf{u}$  which describes the solid particles displacement from the initial position and the temperature  $T$ . The velocity field is given as the time derivative of the displacement field  $\mathbf{v}^{\text{sl}} = \partial_t \mathbf{u}$ , and the governing equations are the transport equations of the momentum density  $\rho \partial_t \mathbf{u}$  and temperature  $T$  [47, 48],

$$\rho \partial_t^2 \mathbf{u} = \nabla \cdot \boldsymbol{\sigma}, \quad (2.11a)$$

$$\rho c_p \partial_t T + \rho c_p \frac{(\gamma - 1)}{\alpha_p} \partial_t (\nabla \cdot \mathbf{u}) = \gamma \nabla \cdot (k^{\text{th}} \nabla T) + P, \quad (2.11b)$$

where  $\boldsymbol{\sigma}$  is the stress tensor, which for an isotropic solids is,

$$\boldsymbol{\sigma} = -\frac{\alpha_p}{\kappa_T} (T - T_0) \mathbf{I} + \boldsymbol{\tau}, \quad (2.12a)$$

$$\boldsymbol{\tau} = \rho c_{\text{tr}}^2 \left[ \nabla \mathbf{u} + (\nabla \mathbf{u})^\dagger \right] + \rho (c_{\text{lo}}^2 - 2c_{\text{tr}}^2) (\nabla \cdot \mathbf{u}) \mathbf{I}, \quad (2.12b)$$

where the superscript "†" indicates the transposed matrix. In this work all solids are assumed to be isotropic.

## 2.2 Perturbation theory

The transport equations for mass, momentum and energy describes the mechanical and temperature fields in the fluid and solid. The governing equations are the fundamental equations for modeling the response of a microfluidic system to an acoustic actuation. The system will be actuated with a frequency  $f$  often in the range  $f = 1 - 20$  MHz. To model the response we use perturbation theory, it is a method to find an approximative solution to the governing equations. It works by finding an exact solution to a similar but simpler problem and then the deviation is modelled by corrections in a small parameter  $\epsilon$ , so that the true solution  $A$  is approximated by a series in  $\epsilon$ ,

$$A \approx A_0 + A_1\epsilon + A_2\epsilon^2 + A_3\epsilon^3 \dots \quad (2.13)$$

The solution is then truncated at a certain term, typically at  $\epsilon$  or  $\epsilon^2$ . The method works for  $\epsilon \ll 1$  so that the higher order terms can be neglected. In our case we have a system at rest which is our zero order solution  $A_0$  and then it is perturbed by an periodic actuation on the boundary with the angular frequency  $\omega = 2\pi f$  given as  $\mathbf{s}_1(\mathbf{r}, t) = \mathbf{s}_1(\mathbf{r}) \exp(-i\omega t)$ , which gives a response with time dependency  $\exp(-i\omega t)$ . The second order terms in the perturbation expansion consists of products of two first order fields, so it will either result in a steady field or a field with time dependency  $\exp(\pm i2\omega t)$ . We are only interested in the time averaged field which will be denoted as  $\int \frac{1}{2} \text{Re} \{A_1 B_1^*\} dt = \langle A_1 B_1 \rangle$  and the notation  $Q_2$  of any field will refer to the steady second order field. So all fields  $Q(\mathbf{r}, t)$  will be described by a steady zeroth order field  $Q_0(\mathbf{r})$ , an oscillating first order field  $\text{Re} \{Q_1(\mathbf{r}) \exp(-i\omega t)\}$ , and a steady second order field  $Q_2(\mathbf{r})$ ,

$$Q(\mathbf{r}, t) = Q_0(\mathbf{r}) + \text{Re} \{Q_1(\mathbf{r}) e^{-i\omega t}\} + Q_2(\mathbf{r}). \quad (2.14)$$

The small parameter that the fields are expanded in is the Mach number  $\epsilon = \frac{v_1}{c} \ll 1$  which is the speed of the fluid/solid particle compared to the sound speed in the fluid/solid so that  $|Q_2| \sim |Q_1| \frac{|v_1|}{c}$ . So the independent fields will all be described by a zeroth, first and second order term,

$$p(\mathbf{r}, t) = p_0(\mathbf{r}) + \text{Re} \{p_1(\mathbf{r}) e^{-i\omega t}\} + p_2(\mathbf{r}) \quad (2.15a)$$

$$\mathbf{v}(\mathbf{r}, t) = \mathbf{v}_0(\mathbf{r}) + \text{Re} \{\mathbf{v}_1(\mathbf{r}) e^{-i\omega t}\} + \mathbf{v}_2(\mathbf{r}) \quad (2.15b)$$

$$T(\mathbf{r}, t) = T_0(\mathbf{r}) + \text{Re} \{T_1(\mathbf{r}) e^{-i\omega t}\} + T_2(\mathbf{r}) \quad (2.15c)$$

$$\mathbf{u}(\mathbf{r}, t) = \mathbf{u}_0(\mathbf{r}) + \text{Re} \{\mathbf{u}_1(\mathbf{r}) e^{-i\omega t}\} + \mathbf{u}_2(\mathbf{r}) \quad (2.15d)$$

Where the pressure and velocity fields are defined in the fluid, the displacement in the solid and the temperature field in both domains. In our model gravity is neglected so for the zeroth-order fields we have  $\nabla p_0 = 0$ ,  $\mathbf{u}_0 = 0$ , and  $\mathbf{v}_0 = 0$ , while the temperature field can have a spatial dependency. The temperature field  $T_0$  is allowed to have a spatial

dependency, but the model does assume  $\nabla(q_0 \mathbf{v}_1) \approx q_0 \nabla \mathbf{v}_1$  where  $q_0$  is a fluid parameter. By using the thermal dependencies in Table 2.1, the validity of the model is limited to temperature gradients below,

$$|\nabla T_0| \ll \left| \frac{k_0}{a_\eta^T \alpha_{p0}} \right| \approx 500 \text{ K/mm}. \quad (2.16)$$

In acoustofluidic devices this assumption is valid.

Due to the temperature and pressure dependencies of the material parameters Eq. (2.9), the material parameters will also be perturbed. For the viscosity the perturbation is given as,

$$\eta(\mathbf{r}, t) = \eta_0(T_0) + \text{Re} \{ \eta_1(T_1, p_1) e^{-i\omega t} \} + \eta_2(T_2, p_2), \quad (2.17a)$$

$$\eta_1(T_1, p_1) = \left( \frac{\partial \eta}{\partial T} \right)_p T_1(\mathbf{r}) + \left( \frac{\partial \eta}{\partial p} \right)_T p_1(\mathbf{r}), \quad (2.17b)$$

$$\eta_2(T_2, p_2) = \left( \frac{\partial \eta}{\partial T} \right)_p T_2(\mathbf{r}) + \left( \frac{\partial \eta}{\partial p} \right)_T p_2(\mathbf{r}), \quad (2.17c)$$

and like-wise for the other material parameters.

With the perturbation theory the governing equations can be split up in a set of equations for the zeroth order fields, a set for the time varying first order fields, and a set for the steady second order fields.

## 2.3 Separation of length scales

Acoustofluidic systems have dynamics on two length scales, one determined by the wavelength of the acoustic waves  $d \sim k_0^{-1}$  with the wavenumber  $k_0 = \frac{\omega}{c}$  and another set by the thermoviscous boundary layers at the fluid-solid interface. The width of the thermal boundary layer (in solid and fluid) is denoted by  $\delta_t$  and the width of the viscous boundary layer  $\delta_s$  (fluid only) are localized near the solid-fluid interface. The length scale of the two boundary layers are jointly referred to as  $\delta$  and are small compared to the long length scale  $d \sim k_0^{-1}$ , so  $\delta k_0 \ll 1$ . The width of the viscous and thermal boundary layers are given as,

$$\delta_s = \sqrt{\frac{2\nu_0}{\omega}}, \quad \delta_t = \sqrt{\frac{2D_0^{\text{th}}}{(1-X)\omega}} \approx \sqrt{\frac{2D_0^{\text{th}}}{\omega}}, \quad (2.18)$$

where  $X = 0$  for fluids and  $X \ll 1$  for solids. Typically (for water),  $\delta_t < \delta_s < 500 \text{ nm}$  which is more than two orders of magnitude smaller than the typical long length scale  $d \sim 100 \text{ }\mu\text{m}$ . The difference in length scales of the boundary and bulk fields are used to separate a field  $Q$  into a boundary layer field and a bulk field  $Q = Q^\delta + Q^d$ , where the boundary layer field  $Q^\delta$  goes to zero away from fluid-solid interface and the bulk field  $Q^d$  only varies on the long length scale  $d$ . In Fig. 2.1 a sketch of the thermal boundary layers are shown; the complete temperature field  $T_1$  (black) consists of a bulk field in the fluid and solid  $T_1^d$  (blue), and two boundary layers  $T_1^\delta$  (red) which ensures that the temperature field fulfils the boundary conditions at the fluid-solid interface.



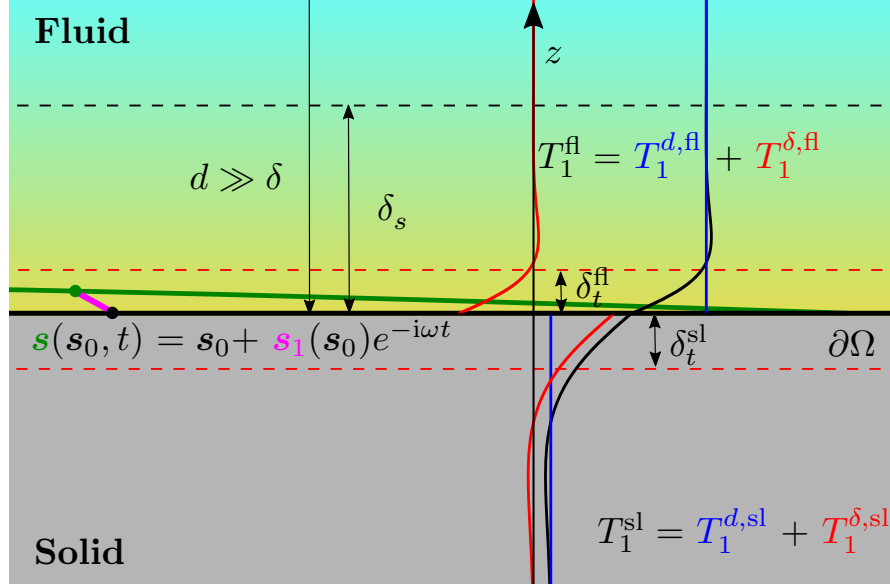


Figure 2.1: Sketch of the thermal boundary layer fields at a fluid-solid interface  $\partial\Omega$ . The position of the interface  $\mathbf{s}$  is given by the steady position  $\mathbf{s}_0$  and the oscillating term  $\mathbf{s}_1$ . The viscous  $\delta_s$  and thermal  $\delta_t$  boundary layer thickness is shown with black/red dashed lines. The temperature field  $T_1$  is divided into a bulk (blue) and boundary layer (red) field in both the fluid and solid. Figure from Ref. [1].

Note that  $\delta \propto \omega^{-1/2}$  while  $d \propto \omega^{-1}$  so at high frequencies (GHz) the difference between the two length scales becomes smaller. When developing the effective boundary conditions only the terms of lowest order in  $\delta k_0$  is kept. So the error on the effective boundary conditions becomes larger at higher frequencies.

## 2.4 Boundary conditions

At the interface between the solid and fluid domain there is a set of boundary conditions on the velocity, stress, temperature, and heat flux. The position of the interface  $\mathbf{s}$  is dependent on the initial position of the interface  $\mathbf{s}_0$  and the time  $t$  as  $\mathbf{s}(\mathbf{s}_0, t) = \mathbf{s}_0 + \mathbf{s}_1(\mathbf{s}_0)e^{-i\omega t}$ , see Fig. 2.1. The boundary conditions on the velocity, stress, temperature, and heat flux are,

$$\mathbf{v}^{\text{fl}}(\mathbf{s}, t) = \mathbf{v}^{\text{sl}}(\mathbf{s}_0, t) \quad (2.19a)$$

$$\mathbf{n} \cdot \boldsymbol{\sigma}^{\text{fl}}(\mathbf{s}, t) = \mathbf{n} \cdot \boldsymbol{\sigma}^{\text{sl}}(\mathbf{s}_0, t) \quad (2.19b)$$

$$T^{\text{fl}}(\mathbf{s}, t) = T^{\text{sl}}(\mathbf{s}_0, t) \quad (2.19c)$$

$$k_0^{\text{th,fl}} \mathbf{n} \cdot \nabla T^{\text{fl}}(\mathbf{s}, t) = k_0^{\text{th,sl}} \mathbf{n} \cdot \nabla T^{\text{sl}}(\mathbf{s}_0, t) \quad (2.19d)$$

Note that because the solid is in the Lagrangian picture it depends on  $\mathbf{s}_0$  while the fluid in the Eulerian picture depends on  $\mathbf{s}$ . The eight boundary conditions is the amount

needed to govern the four independent fields in each domain. On the boundary we define  $V_1^0 = \partial_t \mathbf{u}_1(\mathbf{s}_0)$  to be the velocity of the fluid-solid interface. The model includes gradients in  $T_0$  and therefore gradients in the zeroth order material parameters  $q_0$ .

For the perturbation theory we need to specify the boundary condition for each order. For the zeroth order fields only the temperature field is non trivial and the boundary conditions are at  $\mathbf{s} = \mathbf{s}_0$ ,

$$T_0^{\text{fl}}(\mathbf{s}_0) = T_0^{\text{sl}}(\mathbf{s}_0) \quad (2.20a)$$

$$k_0^{\text{th,fl}} \mathbf{n} \cdot \nabla T_0^{\text{fl}}(\mathbf{s}_0) = k_0^{\text{th,sl}} \mathbf{n} \cdot \nabla T_0^{\text{sl}}(\mathbf{s}_0) \quad (2.20b)$$

For the first order fields the boundary conditions are at the position  $\mathbf{s} = \mathbf{s}_0 + \mathbf{s}_1 \exp(-i\omega t)$ ,

$$\mathbf{v}_1(\mathbf{s}_0) = \partial_t \mathbf{u}_1(\mathbf{s}_0) \quad (2.21a)$$

$$\mathbf{n} \cdot \boldsymbol{\sigma}_1^{\text{sl}}(\mathbf{s}_0) = \mathbf{n} \cdot \boldsymbol{\sigma}_1^{\text{fl}}(\mathbf{s}_0) \quad (2.21b)$$

$$T_1^{\text{fl}}(\mathbf{s}_0) + \mathbf{s}_1 \cdot \nabla T_0^{\text{fl}}(\mathbf{s}_0) = T_1^{\text{sl}}(\mathbf{s}_0) \quad (2.21c)$$

$$k_0^{\text{th,fl}} \mathbf{n} \cdot [\nabla T_1^{\text{fl}}(\mathbf{s}_0) + \nabla(\mathbf{s}_1 \cdot \nabla T_0^{\text{fl}}(\mathbf{s}_0))] = k_0^{\text{th,sl}} \mathbf{n} \cdot \nabla T_1^{\text{sl}}(\mathbf{s}_0) \quad (2.21d)$$

The terms containing  $\mathbf{s}_1$  are negligible when operating at an acoustic resonance frequency. The second order boundary conditions are [1],

$$\mathbf{v}_2(\mathbf{s}_0) = -\langle (\mathbf{s}_1 \cdot \nabla) \mathbf{v}_1 \rangle|_{\mathbf{s}_0} \quad (2.22a)$$

$$\mathbf{n} \cdot \boldsymbol{\sigma}_2^{\text{sl}}(\mathbf{s}_0) = \mathbf{n} \cdot \boldsymbol{\sigma}_2^{\text{fl}}(\mathbf{s}_0) + \langle (\mathbf{s}_1 \cdot \nabla) \boldsymbol{\sigma}_1^{\text{fl}}(\mathbf{s}_0) \cdot \mathbf{n} \rangle|_{\mathbf{s}_0} \quad (2.22b)$$

$$T_2^{\text{sl}}(\mathbf{s}_0) = T_2^{\text{fl}}(\mathbf{s}_0) + \langle \mathbf{s}_1 \cdot \nabla T_1^{\text{fl}} \rangle|_{\mathbf{s}_0} \quad (2.22c)$$

$$\begin{aligned} k_0^{\text{th,sl}} \mathbf{n} \cdot \nabla T_2^{\text{sl}} + k_2^{\text{th,sl}} \mathbf{n} \cdot \nabla T_0^{\text{sl}} + \langle k_1^{\text{th,sl}} \mathbf{n} \cdot \nabla T_1^{\text{sl}} \rangle \\ = k_0^{\text{th,fl}} \mathbf{n} \cdot \nabla T_2^{\text{fl}}(\mathbf{s}_0) + \langle k_1^{\text{th,fl}} \mathbf{n} \cdot \nabla T_1^{\text{fl}}(\mathbf{s}_0) \rangle \\ + k_2^{\text{th,fl}} \mathbf{n} \cdot \nabla T_0^{\text{fl}}(\mathbf{s}_0) + \langle \mathbf{s}_1 \cdot \nabla [k_0^{\text{th,fl}} \nabla T_1^{\text{fl}}(\mathbf{s}_0)] \cdot \mathbf{n} \rangle \\ + \langle \mathbf{s}_1 \cdot \nabla [k_1^{\text{th,fl}} \nabla T_0^{\text{fl}}(\mathbf{s}_0)] \cdot \mathbf{n} \rangle. \end{aligned} \quad (2.22d)$$

The three sets of boundary conditions will be used in the following sections to develop the effective thermoviscous model.

## 2.5 Zeroth order – Temperature field

For the unperturbed zeroth-order fields we have  $\nabla p_0 = 0$ ,  $\mathbf{u}_0 = 0$ ,  $\mathbf{v}_0 = 0$  and all the time derivatives are zero, so the transport equations for mass and momentum are satisfied by the null solution and only the transport equation for energy is non-trivial. The governing equation for the temperature field in the fluid and solid is given as,

$$0 = \nabla \cdot [k_0^{\text{th}} \nabla T_0] + P \quad (2.23)$$

Temperature gradients can be created either by outer boundary conditions or a energy source  $P$ . The energy source could be Joule heating from a current or light absorption.

In Section 7.2 we study the effect of gradients in  $T_0$  created by absorption from a light-emitting diode (LED). When there are temperature gradients there should be a convection flow  $\mathbf{v}_0$ , but in the model we neglect gravity and therefore there is no driving force for the convection flow. Gravity can be included and it was included in the model shown in Ref. [2] enclosed in Section 7.2 where the convective flow is modelled and compared to experimental measurements in the supplemental material.

## 2.6 First order – Acoustic fields

The acoustic fields or first order fields all has the time-dependency  $a(\mathbf{r}, t) = a(\mathbf{r})e^{-i\omega t}$  both in the fluid and in the solid, where  $a$  is a complex valued field and the physical field is given as the real part  $a_{\text{phys}}(\mathbf{r}, t) = \text{Re}\{a(\mathbf{r}, t)\}$ . The section will introduce the acoustic equations in the fluid and solid domains and describe time-averaged fields and resonances.

### 2.6.1 Equations in the fluid

The first order governing equations are derived from Eqs. (2.5), (2.6), and (2.8) using the time dependency  $\partial_t = -i\omega t$  and  $\nabla \cdot (q_0 \mathbf{v}_1) \approx q_0 \nabla \cdot \mathbf{v}_1$  as previously assumed,

$$-i\omega(\alpha_{p0}T_1 - \kappa_{T0}p_1) = \nabla \cdot \mathbf{v}_1, \quad (2.24a)$$

$$-i\omega\rho_0\mathbf{v}_1 = -\nabla p_1 + \beta\eta_0\nabla(\nabla \cdot \mathbf{v}_1) + \eta_0\nabla^2\mathbf{v}_1, \quad (2.24b)$$

$$-i\omega\left(T_1 - (\gamma - 1)\frac{\kappa_{s0}}{\alpha_{p0}}p_1\right) = \gamma D_0^{\text{th}}\nabla^2 T_1. \quad (2.24c)$$

where  $\beta = \eta_0^b/\eta_0 + 1/3$  and  $D_0^{\text{th}} = k_0^{\text{th}}/(\rho_0 c_{p0})$ . Following the procedure in Ref. [47] the equations are solved using potential theory where the velocity is decomposed using the Helmholtz decomposition,

$$\mathbf{v}_1 = \nabla(\phi_c + \phi_t) + \nabla \times \mathbf{\Psi}, \quad (2.25)$$

where  $\phi_c$  is the compressional potential,  $\phi_t$  is the thermal potential, and  $\mathbf{\Psi}$  is the shear vector potential. The Helmholtz decomposition separates the velocity field into a curl-free part  $\nabla(\phi_c + \phi_t)$  and a divergence free part  $\nabla \times \mathbf{\Psi}$ . Ref. [47] shows that the three potentials are governed by the wavenumbers  $k_c$ ,  $k_t$ , and  $k_s$ ,

$$\nabla^2\phi_c + k_c^2\phi_c = 0, \quad k_c = \frac{\omega}{c}(1 + i\Gamma_{0c}) \quad (2.26a)$$

$$\nabla^2\phi_t + k_t^2\phi_t = 0, \quad k_t = \frac{1 + i}{\delta_t}(1 + i\Gamma_{0t}) \quad (2.26b)$$

$$\nabla^2\mathbf{\Psi} + k_s^2\mathbf{\Psi} = 0, \quad k_s = \frac{1 + i}{\delta_s}. \quad (2.26c)$$

Here,  $\Gamma_{0c} = [\Gamma_s + (\gamma - 1)\Gamma_t]/2$  and  $\Gamma_{0t} = (\gamma - 1)[\Gamma_s - \Gamma_t]/2$  are the resulting damping coefficients expressed by  $\Gamma_s = (1 + \beta)(k_0\delta_s)^2/2$  and  $\Gamma_t = (k_0\delta_t)^2/2$ . The wavenumbers  $k_t$  and  $k_s$  has a complex component of similar size to the real component resulting in  $\phi_t$  and

$\Psi$  being damped over one wavelength. This mean that they are boundary layer fields that do not propagate in the bulk of the fluid.

The independent physical fields  $p_1$ ,  $T_1$  and  $\mathbf{v}_1$  are given by the potentials. The velocity field  $\mathbf{v}_1$  is given as,

$$\mathbf{v}_1 = \nabla(\phi_c + \phi_t) + \nabla \times \Psi = \mathbf{v}_1^{d,p} + \mathbf{v}_1^{d,T} + \mathbf{v}_1^\delta \quad (2.27a)$$

$$\mathbf{v}_1^{d,p} = \nabla\phi_c, \quad \mathbf{v}_1^{d,T} = \nabla\phi_t, \quad \mathbf{v}_1^\delta = \nabla \times \Psi. \quad (2.27b)$$

It consists of a bulk field  $\mathbf{v}_1^{d,p}$  and two boundary layer fields  $\mathbf{v}_1^{d,T}$  and  $\mathbf{v}_1^\delta$ . Note that  $\mathbf{v}_1^{d,T}$  is a boundary layer field even though it is noted with a  $d$ , this is because  $d$  in this specific case refers to a Helmholtz decomposition and that the field is curl-free [1]. The pressure field  $p_1$  is given by the  $\phi_c$  and  $\phi_t$  as,

$$p_1 = i\omega\rho_0(\phi_c + \phi_t) + (1 + \beta_0)\eta_0(k_c^2\phi_c + k_t^2\phi_t). \quad (2.28)$$

The acoustic temperature field  $T_1$  consists of a boundary layer field  $T_1^\delta$  and bulk field  $T_1^d$ ,

$$T_1 = b_c\phi_c + b_t\phi_t = T_1^d + T_1^\delta, \quad T_1^d = b_c\phi_c, \quad T_1^\delta = b_t\phi_t, \quad (2.29a)$$

$$b_c = \frac{i\omega(\gamma - 1)}{\alpha_{p0}c_0^2}, \quad b_t = \frac{1}{\alpha_{p,0}D^{\text{th}}}. \quad (2.29b)$$

In our acoustofluidic system the temperature field  $T_1$  is driven by the adiabatic temperature rise  $T_1^d = b_c\phi_c$  in the bulk of the fluid and the thermal boundary layer  $T_1^\delta = b_t\phi_t$  is therefore of the same magnitude as  $T_1^d$ . So  $|\phi_c| \approx \frac{b_t}{b_c}|\phi_t| \gg |\phi_t|$ . Therefore we can describe the system by the fields  $p_1$ ,  $T_1^\delta$ , and  $\mathbf{v}_1^\delta$  governed by [1],

$$\nabla^2 p_1 + k_c^2 p_1 = 0, \quad k_c = \frac{\omega}{c} (1 + i\Gamma_{0c}), \quad (2.30a)$$

$$\nabla^2 T_1^\delta + k_t^2 T_1^\delta = 0, \quad k_t = \frac{1 + i}{\delta_t} (1 + i\Gamma_{0t}), \quad (2.30b)$$

$$\nabla^2 \mathbf{v}_1^\delta + k_s^2 \mathbf{v}_1^\delta = 0, \quad k_s = \frac{1 + i}{\delta_s}. \quad (2.30c)$$

Here the pressure field  $p_1$  is the only bulk field and  $T_1^\delta$  and  $\mathbf{v}_1^\delta$  are boundary layer fields. The bulk velocity  $\mathbf{v}_1^{d,p}$ , thermal boundary layer velocity  $\mathbf{v}_1^{d,T}$ , and bulk temperature  $T_1^d$  is given by  $p_1$  and  $T_1^\delta$  as,

$$\mathbf{v}_1^{d,p} = \nabla \left[ -i \frac{1 - i\Gamma_s}{\omega\rho_0} p_1 \right], \quad \mathbf{v}_1^{d,T} = \nabla [\alpha_{p0} D_0^{\text{th}} T_1^\delta], \quad (2.31a)$$

$$T_1^d = (\gamma - 1) \frac{k_{s0}}{\alpha_{p0}} p_1. \quad (2.31b)$$

Thus, the acoustic behaviour of the fluid can be described by a bulk acoustic pressure  $p_1$ , thermal boundary layer field  $T_1^\delta$  and a shear boundary layer velocity field  $\mathbf{v}_1^\delta$ .

### 2.6.2 Equations in the solid

The solid equations are derived from Eq. (2.11) governing momentum and energy conservation. The linearised equations for the displacement field  $\mathbf{u}_1$  and temperature field  $T_1$  are,

$$-\omega^2 \rho_0 \mathbf{u}_1 = -\frac{\alpha_{p,0}}{\kappa_{T0}} \nabla T_1 + (c_{10}^2 - c_{tr}^2) \nabla (\nabla \cdot \mathbf{u}_1) + c_{tr}^2 \nabla^2 \mathbf{u}_1 \quad (2.32a)$$

$$-i\omega T_1 - i\omega \frac{\gamma - 1}{\alpha_{p,0}} \nabla \cdot \mathbf{u}_1 = \gamma D^{\text{th}} \nabla^2 T_1 \quad (2.32b)$$

These two equations are used in our numerical models to simulate the acoustic behaviour of the solid, but it is beneficial for the analytical work on the effective boundary conditions to describe the solid fields by potentials similarly as for the fluid fields.

The derivation is similar to the derivation for the fluid fields, the displacement is decomposed into a curl-free and gradient-free component  $-i\omega \mathbf{u}_1 = \nabla(\phi_c + \phi_t) + \nabla \times \Psi = -i\omega(\mathbf{u}_1^{\text{lo}} + \mathbf{u}_1^{\text{tr}})$  and one obtain the following three Helmholtz equations and wavenumbers,

$$\nabla^2 \phi_c + k_c^2 \phi_c = 0, \quad k_c = \frac{\omega}{c} \left( 1 + i\Gamma_{0c}^{\text{sl}} \right), \quad (2.33a)$$

$$\nabla^2 T_1^\delta + k_t^2 T_1^\delta = 0, \quad k_t = \frac{1 + i}{\delta_t} \left( 1 + i\Gamma_{0t}^{\text{sl}} \right), \quad (2.33b)$$

$$\nabla^2 \mathbf{u}_1^{\text{tr}} + k_s^2 \mathbf{u}_1^{\text{tr}} = 0, \quad k_s = \frac{\omega}{c_{tr}}. \quad (2.33c)$$

Here,  $c_0^2 = c_{10}^2 + \frac{\gamma-1}{\rho_0 \kappa_{T0}}$  and  $\Gamma_{0c}^{\text{sl}}$  and  $\Gamma_{0t}^{\text{sl}}$  are damping coefficients given in Ref. [1]. Note that in the solid only the thermal compression field  $\phi_t$  is a boundary layer field while the transverse displacement field can travel in the bulk of the solid unlike the velocity field  $\mathbf{v}_1^\delta$  in the fluid.

### 2.6.3 Analytical solutions to the boundary layer fields

The boundary layer fields  $T_1^\delta$  and  $\mathbf{v}_1^\delta$  are thin compared to the bulk wavelength and dimensions of the acoustofluidic system. Therefore they are numerically extremely expensive to resolve in simulations. We therefore solve them analytically and use the analytical solutions to impose effective boundary conditions on the bulk field  $p_1$  in the fluid and  $\mathbf{u}_1$  in the solid. The derivations of the boundary layer fields use the governing equations (2.30)(2.33), the boundary conditions (2.21), and that  $\nabla^2 \approx \partial_z^2$  for the boundary layer fields. The viscous boundary layer field is only present in the fluid and is given as [1, 30],

$$\mathbf{v}_1^\delta(x, y, z) = \mathbf{v}_1^{\delta 0}(x, y) e^{ik_s z}, \quad \mathbf{v}_1^{\delta 0}(x, y) = -i\omega \mathbf{u}_1^0(x, y) - \mathbf{v}_1^{d0}(x, y), \quad (2.34)$$

where superscript '0' denotes the field on the fluid-solid interface. The exponential  $z$  dependency ensures that the field goes to zero far away from the boundary.

The temperature field is both the fluid and solid domain, therefore there is a boundary layer field in each domain. The analytical solutions to the thermal boundary layers are derived in Ref. [1] enclosed in Section 7.2 and are,

$$T_1^{\delta,\text{fl}}(x, y, z) = T_1^{\delta 0,\text{fl}}(x, y)e^{ik_t^{\text{fl}}z}, \quad T_1^{\delta 0,\text{fl}}(x, y) = -\frac{\tilde{Z}}{1 + \tilde{Z}}\Delta T_1^d \quad (2.35a)$$

$$T_1^{\delta,\text{sl}}(x, y, z) = T_1^{\delta 0,\text{sl}}(x, y)e^{-ik_t^{\text{sl}}z}, \quad T_1^{\delta 0,\text{sl}}(x, y) = \frac{1}{1 + \tilde{Z}}\Delta T_1^d \quad (2.35b)$$

$$\tilde{Z} = \frac{k_0^{\text{th,sl}}k_t^{\text{sl}}}{k_0^{\text{th,fl}}k_t^{\text{fl}}} \quad (2.35c)$$

where  $\Delta T_1^d = T_1^{d 0,\text{sl}} - T_1^{d 0,\text{fl}}$ . Notice the difference in sign in the exponential which indicates that the fluid field goes to zero when  $z$  goes to  $\infty$  and the solid field when  $z$  goes to  $-\infty$ .

#### 2.6.4 Effective boundary conditions

The no-slip boundary condition on the acoustic velocity field  $\mathbf{v}_1$  can be reformulated as an effective boundary condition on the pressure field  $p_1$  including the effects of the thermal and viscous boundary layers. The derivation uses the incompressibility of the viscous boundary layer field  $\mathbf{v}_1^\delta$ . The effective boundary condition on the pressure  $p_1$  and displacement  $\mathbf{u}_1$  are given as [1]

$$\partial_z p_1 = i\frac{\omega\rho_0}{1 - i\Gamma_s}(V_{1z}^0 - \frac{i}{k_s}\nabla \cdot \mathbf{V}_1^0) - \frac{i}{k_s}(k_c^2 + \partial_z^2)p_1 + \frac{i}{k_t}\frac{\alpha p_0}{\kappa T_0}k_0^2 T_1^{\delta 0}, \quad (2.36a)$$

$$\boldsymbol{\sigma}_1^{\text{sl}} \cdot \mathbf{e}_z = -p_1 \mathbf{e}_z + ik_s \eta_0 \left[ \mathbf{v}_1^{d 0,\text{sl}} + \frac{i}{\omega\rho_0} \nabla p_1 \right]_{s_0}. \quad (2.36b)$$

The last term in Eq. (2.36a) including  $k_t$  is the correction from the thermal boundary layer  $T_1^\delta$  while the terms including  $k_s$  are the corrections from the viscous boundary layer  $\mathbf{v}_1^\delta$  as given in Ref. [30]. The two boundary conditions are the no-slip boundary condition and the continuity of the normal stress across the fluid-solid interface given in Section 2.4.

#### 2.6.5 Resonances and time-averaged products

The time-varying acoustic field can be described by a set of time-averaged quantities. First we can describe the energy stored in the acoustic field, the local acoustic energy density  $E_{\text{ac}}$  is given as a sum of the kinetic and potential energy density,

$$\begin{aligned} E_{\text{ac}}(\mathbf{r}) &= E_{\text{pot}}(\mathbf{r}) + E_{\text{kin}}(\mathbf{r}) \\ &= \frac{1}{2}\kappa_s \langle p_1 p_1 \rangle + \frac{1}{2}\rho_0 \langle \mathbf{v}_1 \cdot \mathbf{v}_1 \rangle \\ &= \frac{1}{4}\kappa_s |p_1|^2 + \frac{1}{4}\rho_0 |\mathbf{v}_1|^2. \end{aligned} \quad (2.37)$$

Here the well-known entity  $\langle a_1 a_1 \rangle = \frac{1}{2} \text{Re} \{ a_1 a_1^* \} = \frac{1}{2} |a_1|^2$  is used, where superscript "\*" denotes the complex conjugate. In an acoustofluidic device the acoustic energy density  $E_{\text{ac}}$

is often taken as an average over a volume  $V$ , thus the time-and-spatial averaged acoustic energy density  $\hat{E}_{ac}$  is given as,

$$\hat{E}_{ac} = \frac{1}{V} \int_V E_{ac}(\mathbf{r}) dV. \quad (2.38)$$

Another time-averaged parameter is the acoustic energy flux density  $\mathbf{S}_{ac}$ ,

$$\mathbf{S}_{ac}(\mathbf{r}) = \langle p_1 \mathbf{v}_1 \rangle. \quad (2.39)$$

It is a vector and describes the flow of the acoustic energy density, it is especially important for travelling waves and rotating acoustic waves. Lastly, we have the Lagrangian density  $\mathcal{L}_{ac}$  given as the difference in potential and kinetic energy,

$$\mathcal{L}_{ac}(\mathbf{r}) = E_{pot}(\mathbf{r}) - E_{kin}(\mathbf{r}) = \frac{1}{4} \kappa_s |p_1|^2 - \frac{1}{4} \rho_0 |\mathbf{v}_1|^2. \quad (2.40)$$

For a standing wave the Lagrangian density will be positive at positions with high potential energy (pressure anti-nodes) and negative at high kinetic energy (pressure nodes).

Acoustofluidic devices are run at a resonant frequency to achieve a high acoustic energy density. An acoustic resonance can be described by a Lorentzian with a resonance frequency  $f_{res}$  and the dampening coefficient  $\Gamma$ ,

$$E_{ac} = \frac{\left(\frac{1}{2}\Gamma\right)^2 E_{ac}^{max}}{\left(\frac{f}{f_{res}} - 1\right)^2 + \left(\frac{1}{2}\Gamma\right)^2} \quad (2.41)$$

Where  $E_{ac}^{max}$  is the acoustic energy density at the resonance frequency  $f = f_{res}$ . The full width at half maximum (FWHM) of the resonance peak is given as  $\Gamma f_{res}$ . The dampening  $\Gamma$  is used to describe the  $Q$ -factor of a device  $Q = \Gamma^{-1}$  which is the ratio between energy lost in an acoustic cycle  $t = f^{-1}$  and the total acoustic energy in the system  $\hat{E}_{ac}$ . Acoustofluidic devices typically have a  $Q$ -factor in the range  $Q = 100 - 1000$ . So a resonance peak is characterized by the resonance frequency  $f_0$  and the  $Q$ -factor.

### 2.6.6 Example: Pressure field in a square fluid channel

To demonstrate the benefits of the effective boundary conditions an example of a long fluid channel with a square cross-section  $230 \times 230 \mu\text{m}$  will be investigated. For simplicity only the fluid domain are modeled, with an actuation on the top and bottom by  $\mathbf{u}_1 = d_0 e^{-i\omega t} \mathbf{e}_z$  and on the side walls at  $y = -115$  and  $y = 115 \mu\text{m}$  with  $\mathbf{u}_1 = id_0 e^{-i\omega t} \mathbf{e}_y$ . The actuation will create a half-wave acoustic resonance in both the width and height direction which are out phase, thereby creating a rotating acoustic wave [49], see Fig. 2.2(a).

Fig. 2.2(a) also demonstrates the mesh needed to converge for a full simulation to the right and an effective simulation to the left, showing the large computational gain of using the pressure acoustics with effective boundary conditions [1]. Fig. 2.2(b) shows the acoustic resonance as a function of the frequency, the resonance peak is shown for

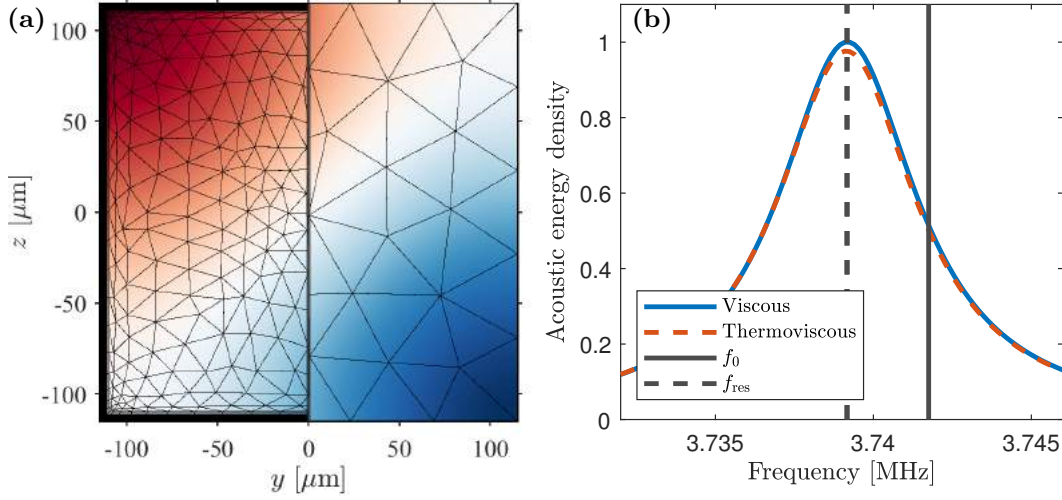


Figure 2.2: (a) Color plot of the acoustic field at a time  $t$  for a rotating acoustic field in a long acoustofluidic channel with a square cross-section. In the right half the mesh required to converge for the effective model and to the left the mesh required for the full model to fulfil the same convergence criteria. (b) Resonance plot for the square fluid channel with and without thermal effects, shown together with  $f_0 = c/(2W)$  and the resonance frequency  $f_{\text{res}}$ . Figure (a) is adapted from Ref. [1].

both a viscous theory and thermoviscous theory, the thermal corrections are minor for the pressure field in a fluid.

The shift of resonance frequency from  $f_0 = c/(2W)$ , where  $W = 230 \mu\text{m}$  is the width of the channel, to  $f_{\text{res}}$  can be understood by closer examining the effective boundary conditions. The resonance frequency can be found analytically for a half-wave resonance in the width direction, the governing equations (2.30) and effective boundary conditions (2.36) are to leading order in  $\epsilon$  at resonance given as [30],

$$0 = \nabla^2 p_1 + k_0^2 p_1, \quad (2.42a)$$

$$\partial_y p_1 = i\omega V_{1y}^0 w(z), \quad y = \pm \frac{1}{2}W, \quad (2.42b)$$

$$\mp \partial_z p_1 = -\frac{i}{k_s} k_0^2 p_1 + \frac{i}{k_t} \frac{\alpha_p}{\kappa_T} k_0^2 T_1^{\delta 0}, \quad z = \pm \frac{1}{2}H \quad (2.42c)$$

The problem is solved by separation of variables following the derivation of Ref. [30], thus introducing the wavenumbers  $k_y$  and  $k_z$  with  $k_y^2 + k_z^2 = k_0^2$ . The function  $w(z)$  is an envelope function chosen to be  $w(z) = \cos(k_z z)$ , and the solution will be on the form  $p_1 = A \sin(k_y y) \cos(k_z z)$ . First we need to rewrite  $T_1^{\delta 0}$  as a function of  $p_1$ . We assume a surrounding solid with high thermal conductivity so  $\tilde{Z} \gg 1$ , such that  $T_1^{\delta 0} =$



$-(\gamma - 1)\frac{\kappa_s}{\alpha_p}p_1$ , using  $\kappa_T = \gamma\kappa_s$  the boundary condition Eq. (2.42c) becomes,

$$\mp \partial_z p_1 = -i\left[\frac{1}{k_s} + \frac{\gamma - 1}{\gamma k_t}\right]k_0^2 p_1. \quad (2.43)$$

Assuming the solution to be on the form  $p_1 = A \sin(k_y y) \cos(k_z z)$ , then requires  $k_z$  to satisfy,

$$k_z \tan\left(k_z \frac{H}{2}\right) = -i\left[\frac{1}{k_s} + \frac{\gamma - 1}{\gamma k_t}\right]k_0^2, \quad (2.44)$$

using  $\tan\left(k_z \frac{H}{2}\right) \approx k_z \frac{H}{2}$  for  $k_z H \ll 1$ , we obtain for  $k_z$  and  $k_y$ ,

$$k_z^2 = -(1 + i)\left[\frac{\delta_s}{H} + \frac{\gamma - 1}{\gamma} \frac{\delta_t}{H}\right]k_0^2, \quad k_y^2 = \left(1 + (1 + i)\left[\frac{\delta_s}{H} + \frac{\gamma - 1}{\gamma} \frac{\delta_t}{H}\right]\right)k_0^2. \quad (2.45)$$

The amplitude  $A$  of the pressure field  $p_1$  can be found using the boundary condition (2.42b) to be,

$$A = \frac{i\omega\rho_0 V_{1y}^0}{k_y \cos(k_y W/2)}. \quad (2.46)$$

The amplitude  $A$  is maximum for a resonance frequency  $f_{\text{res}}$  given as,

$$f_{\text{res}} = \left(1 - \frac{1}{2}\Gamma_{\text{bl}}\right)f_0, \quad \text{with } \Gamma_{\text{bl}} = \left[\frac{\delta_s}{H} + \frac{\gamma - 1}{\gamma} \frac{\delta_t}{H}\right]. \quad (2.47)$$

Thereby lowering the resonance frequency slightly as seen in Fig. 2.2(b) and resulting in a  $Q$ -factor of  $Q = \Gamma_{\text{bl}}^{-1}$ . This also demonstrates why the thermal corrections are minor, since for a fluid  $\gamma - 1 = 0.01 \ll 1$  and therefore negligible compared to the viscous term. There will be larger effects for gasses, where for example dry air has  $\gamma \approx 1.4$ .

## 2.7 Second order – Streaming field

Acoustic streaming is a phenomenon where an acoustic wave in a fluid gives rise to a steady fluid flow. The streaming flow is created due to attenuation of the acoustic field, the attenuation can either be in the thin viscous and thermal boundary layers or in the bulk of the fluid. To evaluate the time-averaged streaming flow we study the second-order time-averaged continuity and Navier-Stokes equations,

$$0 = -\nabla \cdot (\rho_0 \mathbf{v}_2) + \dot{\rho}_{\text{ac}} \quad (2.48a)$$

$$0 = -\nabla p_2 + \nabla \cdot \boldsymbol{\tau}_2 + \hat{\mathbf{f}}_{\text{ac}} \quad (2.48b)$$

$$\boldsymbol{\tau}_2 = \eta_0 [\nabla \mathbf{v}_2 + (\nabla \mathbf{v}_2)^\dagger] + \left[\eta_0^b - \frac{2}{3}\eta_0\right] (\nabla \cdot \mathbf{v}_2) \mathbf{I} \quad (2.48c)$$

Where, the excess-density rate  $\dot{\rho}_{\text{ac}}$  and the acoustic body force  $\hat{\mathbf{f}}_{\text{ac}}$  are time-averaged products of the acoustic first order fields,

$$\dot{\rho}_{\text{ac}} = -\nabla \cdot \langle \rho_1 \mathbf{v}_1 \rangle, \quad (2.49a)$$

$$\hat{\mathbf{f}}_{\text{ac}} = \nabla \cdot (\boldsymbol{\tau}_{11} - \rho_0 \langle \mathbf{v}_1 \mathbf{v}_1 \rangle), \quad (2.49b)$$

$$\boldsymbol{\tau}_{11} = \langle \eta_1 [\nabla \mathbf{v}_1 + (\nabla \mathbf{v}_1)^\dagger] + \left[\eta_1^b - \frac{2}{3}\eta_1\right] (\nabla \cdot \mathbf{v}_1) \mathbf{I} \rangle. \quad (2.49c)$$

The excess-density rate and acoustic body force are the driving terms of the time-averaged fluid flow  $\mathbf{v}_2$ . The first order fields consists of a boundary layer and a bulk fields and we can therefore split up the excess-density rate and acoustic body force into a boundary layer term (superscript " $\delta$ ") that consists of all terms with at least one boundary layer field and a bulk term (superscript " $d$ ") that consist of only bulk fields  $\hat{\mathbf{f}}_{\text{ac}} = \hat{\mathbf{f}}_{\text{ac}}^{\delta} + \hat{\mathbf{f}}_{\text{ac}}^d$ . We similarly split up all the second order fields into a boundary layer field (superscript " $\delta$ ") which is a response to  $\hat{\mathbf{f}}_{\text{ac}}^{\delta}$  and  $\dot{\rho}_{\text{ac}}^{\delta}$  and a bulk field that is the response to  $\hat{\mathbf{f}}_{\text{ac}}^d$  and  $\dot{\rho}_{\text{ac}}^d$ ,

$$p_2 = p_2^{\delta} + p_2^d, \quad \mathbf{v}_2 = \mathbf{v}_2^{\delta} + \mathbf{v}_2^d, \quad T_2 = T_2^{\delta} + T_2^d, \quad \boldsymbol{\tau}_2 = \boldsymbol{\tau}_2^{\delta} + \boldsymbol{\tau}_2^d \quad (2.50)$$

The Navier-Stokes and continuity equation can be split up in one set of equations governing the bulk fields and another set governing the boundary layer fields. It is possible to separate the boundary and bulk fields because there are no mixing terms, since mixing terms will be at least fourth order terms. The  $d$  and  $\delta$  fields are governed by two different set of equations in the bulk, but are connected by the common no-slip boundary condition at the solid-fluid interface. For the velocity the no-slip boundary condition requires

$$\mathbf{v}_2^{d0} + \mathbf{v}_2^{\delta 0} = -\langle \mathbf{s}_1 \cdot \nabla \mathbf{v}_1 \rangle|_{\mathbf{s}_0} \quad (2.51)$$

In the next section we solve the boundary layer field  $\mathbf{v}_2^{\delta}$  analytically and impose it as an effective boundary condition (slip velocity) on the bulk streaming field  $\mathbf{v}_2^d$ .

### 2.7.1 Boundary layer field and effective boundary conditions

As for the first order fields the boundary layer fields are solved analytically and then imposed as an effective boundary condition for the bulk fields. This requires the analytical solutions to the first order boundary layer fields in Section 2.6.3 and a longer derivation starting from the Navier-Stokes equation to find the velocity at the fluid-solid interface  $\mathbf{v}_2^{\delta 0}$ . The full derivation of the effective boundary condition is found in Ref. [1] enclosed in Section 7.1, the derivation has the following steps: (i) write the Navier-Stokes equation for the boundary layer field driven by  $\hat{\mathbf{f}}_{\text{ac}}^{\delta}$ , (ii) take advantage of  $\nabla^2 \approx \partial_z^2$  to write an differential equation of the parallel part of the boundary layer velocity field  $\mathbf{v}_{2,\parallel}^{\delta}$ , (iii) integrate the equation twice from  $z = \infty$  to  $z = 0$  to get an expression for  $\mathbf{v}_{2,\parallel}^{\delta 0}$ , (iv) use the continuity equation to find the perpendicular component  $v_{2,z}^{\delta 0}$ . The parallel and perpendicular components of the boundary layer velocity at the interface are given as [1],

$$\begin{aligned} \mathbf{v}_{2,\parallel}^{\delta 0} &= \frac{1}{2\omega} \text{Re} \left[ \frac{1}{2} \nabla \cdot (\mathbf{v}_1^{\delta 0} \mathbf{v}_1^{\delta 0*}) + i \nabla \cdot (\mathbf{v}_1^{\delta 0} \mathbf{V}_1^{0*}) - i \nabla \cdot (\mathbf{V}_1^0 \mathbf{v}_1^{\delta 0*}) \right. \\ &\quad \left. + \frac{1}{\delta} \mathbf{v}_1^{\delta 0} v_{1z}^{\delta 0*} - i \mathbf{v}_1^{\delta 0} \partial_z v_{1z}^{d*} - \frac{1-i}{\delta} \mathbf{V}_1^0 v_{1z}^{\delta 0*} - \frac{1+i}{\delta} \mathbf{v}_1^{\delta 0} V_{1z}^{0*} \right]_{\parallel} \\ &\quad - \frac{1}{2\rho_0} \frac{\delta_t^2}{\delta_s^2} \text{Re} \left[ \frac{\delta_s}{\delta_s - i\delta_t} \mathbf{v}_1^{\delta 0} \rho_1^{\delta 0*} + \mathbf{v}_1^{d0,p} \rho_1^{\delta 0*} \right]_{\parallel} \\ &\quad - \frac{1}{2\eta_0} \text{Re} \left[ \frac{\delta_t}{\delta_t - i\delta_s} \eta_1^{\delta 0} \mathbf{v}_1^{\delta 0*} + \eta_1^{d0} \mathbf{v}_1^{\delta 0*} \right]_{\parallel}, \end{aligned} \quad (2.52a)$$

$$v_{2,z}^{\delta 0} = -\frac{1}{2\omega} \text{Re} \left[ \nabla_{\parallel} \cdot (i \mathbf{v}_1^{\delta 0} V_{1z}^{0*}) \right] - \frac{1}{2\rho_0} \text{Re} \left[ \rho_1^{\delta 0*} v_{1z}^{d0,p} \right] \quad (2.52b)$$

The viscous terms are the same as found by Bach and Bruus [30] and the corrections caused by the temperature fields are the terms including  $\rho_1$  or  $\eta_1$ . We do not analytically describe the full flow field of the boundary layer field  $\mathbf{v}_2^\delta$ , since we only need the velocity on the fluid-solid interface, where it shares boundary condition with the bulk streaming field  $\mathbf{v}_2^d$ . The analytical solution of  $\mathbf{v}_2^{\delta 0}$  given purely by known first order fields together with the boundary condition Eq. (2.51) enables us to make an effective boundary condition on the bulk streaming field  $\mathbf{v}_2^d$ . Evaluating the term  $-\langle \mathbf{s}_1 \cdot \nabla \mathbf{v}_1 \rangle|_{s_0}$  and using Eq. (2.52) the effective slip velocity on  $\mathbf{v}_2^d$  is given as [1],

$$\mathbf{v}_2^{d0} = (\mathbf{A} \cdot \mathbf{e}_x) \mathbf{e}_x + (\mathbf{A} \cdot \mathbf{e}_y) \mathbf{e}_y + (\mathbf{B} \cdot \mathbf{e}_z) \mathbf{e}_z, \quad (2.53a)$$

$$\begin{aligned} \mathbf{A} = & -\frac{1}{2\omega} \operatorname{Re} \left[ \mathbf{v}_1^{\delta 0*} \cdot \nabla \left( \frac{1}{2} \mathbf{v}_1^{\delta 0} - i \mathbf{V}_1^0 \right) - i \mathbf{V}_1^{0*} \cdot \nabla \mathbf{v}_1^{d,p} \right. \\ & \left. + \left\{ \frac{2-i}{2} \nabla \cdot \mathbf{v}_1^{\delta 0*} + i (\nabla \cdot \mathbf{V}_1^{0*} - \partial_z v_{1z}^{d,p*}) \right\} \mathbf{v}_1^{\delta 0} \right], \\ & + \frac{1}{2\rho_0} \frac{\delta_t^2}{\delta_s^2} \operatorname{Re} \left[ \frac{\delta_s}{\delta_s - i\delta_t} \mathbf{v}_1^{\delta 0} \rho_1^{\delta 0*} + \mathbf{v}_1^{d0,p} \rho_1^{\delta 0*} \right] \\ & + \frac{1}{2\eta_0} \operatorname{Re} \left[ \frac{\delta_t}{\delta_t - i\delta_s} \eta_1^{\delta 0} \mathbf{v}_1^{\delta 0*} + \eta_1^{d0} \mathbf{v}_1^{\delta 0*} \right] \end{aligned} \quad (2.53b)$$

$$\begin{aligned} \mathbf{B} = & \frac{1}{2\omega} \operatorname{Re} \left[ i \mathbf{v}_1^{d0,p*} \cdot \nabla \mathbf{v}_1^{d,p} \right] \\ & + \frac{1}{2\rho_0} \operatorname{Re} \left[ (\mathbf{v}_1^{d0,p} - \mathbf{V}_1^0) \rho_1^{\delta 0*} \right]. \end{aligned} \quad (2.53c)$$

Here the slip velocity  $\mathbf{v}_2^{d0}$  is given by the two tensors  $\mathbf{A}$  and  $\mathbf{B}$  relating to the parallel and perpendicular velocity component, respectively. The vectors  $\mathbf{e}_x$  and  $\mathbf{e}_y$  are unity vectors in the plane of the interface and  $\mathbf{e}_z$  is perpendicular to the interface.

## 2.7.2 Bulk streaming

With the solution to the boundary layer field we can return to the governing equations for the bulk fields. In the bulk acoustic body force  $\hat{\mathbf{f}}_{ac}^d$  the term  $-\nabla \cdot (\rho_0 \langle \mathbf{v}_1^{d,p} \mathbf{v}_1^{d,p} \rangle)$  can be rewritten and the force  $\hat{\mathbf{f}}_{ac}^d$  given as [1],

$$\begin{aligned} \hat{\mathbf{f}}_{ac}^d &= \nabla \cdot (\boldsymbol{\tau}_{11} - \rho_0 \langle \mathbf{v}_1^{d,p} \mathbf{v}_1^{d,p} \rangle) \\ &= \nabla \mathcal{L}_{ac} - \frac{1}{4} |\mathbf{v}_1^{d,p}|^2 \nabla \rho_0 - \frac{1}{4} |p_1|^2 \nabla \kappa_{s0} \\ &\quad + \frac{\Gamma\omega}{c_0^2} \langle \mathbf{v}_1^d, p_1 \rangle + \nabla \cdot \boldsymbol{\tau}_{11} \end{aligned} \quad (2.54)$$

The gradient of the Lagrangian  $\mathcal{L}_{ac} = \frac{1}{4} \kappa_{s0} |p_1|^2 - \frac{1}{4} \rho_0 |\mathbf{v}_1^d|^2$  does not induce streaming. This is general for all gradient forces, but they do induce a second order pressure field  $p_2^d$  [50]. The next two terms are the inhomogeneous acoustic body force described by Karlsen, Augustsson, and Bruus [32]. The gradients in density  $\rho_0$  and compressibility  $\kappa_{s0}$  can be induced either by solvents [39, 40] or temperature fields [2, 4]. The third term is

the source of traditional Eckart streaming due to attenuation of the the acoustic wave in the bulk and the last term  $\nabla \cdot \boldsymbol{\tau}_{11}$  is a force due to the temperature dependency of the viscosity.

The streaming flow  $\mathbf{v}_2^d$  can be assumed to be incompressible because  $\nabla \cdot (\rho_0 \mathbf{v}_2^d) \approx \rho_0 \nabla \cdot \mathbf{v}_2$  and because each component of  $\nabla \mathbf{v}_2$  is and order of  $\Gamma^{-1}$  larger than  $\dot{\rho}_{ac}/\rho_0$ . Thus, with an incompressible fluid, the acoustic body force, and effective boundary conditions the governing equations of the second order pressure field  $p_2^d$  and streaming field  $\mathbf{v}_2^d$  is given as [1],

$$0 = \nabla \cdot \mathbf{v}_2^d, \quad (2.55a)$$

$$0 = -\nabla [p_2^d - \langle \mathcal{L}_{ac}^d \rangle] + \eta_0 \nabla^2 \mathbf{v}_2^d + \mathbf{f}_{ac}^d, \quad (2.55b)$$

$$\mathbf{f}_{ac}^d = -\frac{1}{4} |\mathbf{v}_1^{d,p}|^2 \nabla \rho_0 - \frac{1}{4} |p_1|^2 \nabla \kappa_{s0} + \frac{\Gamma \omega}{c_0^2} \langle \mathbf{v}_1^{d,p} p_1 \rangle + \nabla \cdot \boldsymbol{\tau}_{11}, \quad (2.55c)$$

$$\mathbf{v}_2^{d0} = (\mathbf{A} \cdot \mathbf{e}_x) \mathbf{e}_x + (\mathbf{A} \cdot \mathbf{e}_y) \mathbf{e}_y + (\mathbf{B} \cdot \mathbf{e}_z) \mathbf{e}_z. \quad (2.55d)$$

Here, the Lagrangian density  $\mathcal{L}_{ac}$  is merged with  $p_2^d$  as an excess pressure and the remaining acoustic body force is renamed  $\mathbf{f}_{ac}^d$ . The removal of  $\nabla \mathcal{L}_{ac}$  from the force term makes the numerical simulations more accurate. This is because the components of  $\nabla \mathcal{L}_{ac}$  is orders of magnitude larger than the other terms of  $\mathbf{f}_{ac}^d$ , so even though it does not induce streaming it requires a high numerical accuracy to reduce the noise from the term. So its removal from the acoustic body force and merging with  $p_2$  makes the numerical simulations more accurate [50], and makes it possible to use a coarser mesh in the bulk of the fluid domain [30]. The bulk streaming field  $\mathbf{v}_2^d$  can be driven either by the bulk acoustic body force  $\mathbf{f}_{ac}^d$  or the effective boundary conditions  $\mathbf{v}_2^{d0}$ , the two different mechanisms gives rise to the distinction between bulk-driven streaming and boundary-driven streaming.

The streaming due to the inhomogeneous acoustic body force has been a mayor focus of the PhD thesis and a longer explanation of the force and examples are shown in Chapter 4 while the bulk driven streaming due to the attenuation  $\frac{\Gamma \omega}{c_0^2} \langle \mathbf{v}_1^{d,p} p_1 \rangle + \nabla \cdot \boldsymbol{\tau}_{11}$  is examined in the following example of a rotating acoustic wave and in Chapter 5 on bulk-driven streaming in acoustic tweezers.

### 2.7.3 Examples: Streaming in a square capillary

To show the importance of including the thermoviscous terms in the bulk acoustic body force Eq. (2.55c) and the effective boundary condition Eq. (2.53) the streaming field induced by a rotating acoustic field in a square capillary is investigated. The example is a continuation of the example in Section 2.6.6 concerning a long fluid channel with a square cross-section  $230 \times 230 \mu\text{m}$  and a rotating acoustic wave actuated in the channel, see Fig. 2.2.

Because the acoustic wave is rotating both the boundary-driven streaming and bulk-driven streaming are important [51]. The bulk driven streaming is important because the acoustic velocity  $\mathbf{v}_1$  and acoustic pressure  $p_1$  in the bulk is not out of phase in a rotating acoustic wave. In Fig. 2.3 the streaming field simulated using an effective viscous model (Ref. [30]), an effective thermoviscous model (Ref. [1]), and a full thermoviscous model

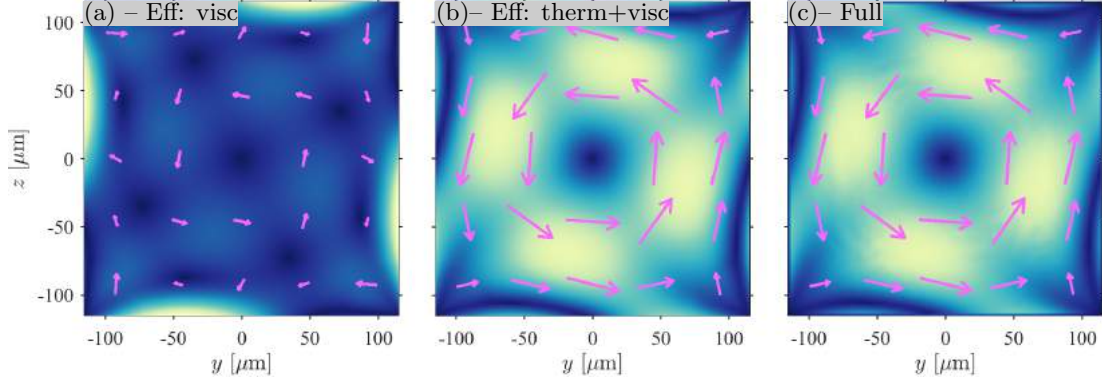


Figure 2.3: Vector plots of the streaming field  $\mathbf{v}_2^d$  with the velocity amplitude as a color plot from blue 0 to yellow 20  $\mu\text{m/s}$  in square capillary. The acoustic energy density is  $E_{ac} = 19 \text{ J/m}^3$ . (a) Simulated based on an effective viscous model without thermal effects in Ref. [30]. (b) Simulated based on the effective thermoviscous model from Ref. [1]. (c) Simulated with the full thermoviscous model in Ref. [29]. Figure adapted from Ref. [1].

(Ref. [29]) are shown. First there is a clear difference between the viscous model and the two thermoviscous models showing the importance of both the thermal corrections to the effective boundary conditions Eq. (2.53) and the term  $\nabla \cdot \boldsymbol{\tau}_{11}$  in the bulk acoustic body force  $\mathbf{f}_{ac}^d$  in Eq. (2.55c). The bulk acoustic body force clearly enhances the streaming velocity in the bulk of the fluid. Secondly, the agreement between the full and effective thermoviscous model validates the effective boundary conditions (2.53) developed in Ref. [1]. The difference in mesh required to converge with the effective and full model is shown in Fig. 2.2(a). Further details on the numerical setup can be found in Ref. [1] enclosed in Section 7.1.

## 2.8 Second order – Temperature field

The dissipation of energy from the acoustic field transform either into momentum in the acoustic streaming field or into heat that causes a second order stationary temperature field  $T_2$ . The second order temperature field is a response to the heat generation of power  $P_{ac}$  and is controlled by the heat diffusion in the chip and the boundary conditions (heat sink, isolator, etc.). The temperature field is in both the solid  $T_2^{sl}$  and the fluid domain  $T_2^{fl}$ . In the fluid the second order equation for energy conservation is given as,

$$0 = \nabla \cdot \left[ k_0^{th} \nabla T_2^{fl} + k_2^{th} \nabla T_0^{fl} \right] - c_p \rho_0 \mathbf{v}_2 \cdot \nabla T_0^{fl} + P_{ac}, \quad (2.56a)$$

$$P_{ac} = \nabla \cdot \left[ \langle k_1^{th} \nabla T_1^{fl} \rangle - \langle p_1 \mathbf{v}_1 \rangle + \langle \mathbf{v}_1 \cdot \boldsymbol{\tau}_1 \rangle \right] - c_p \langle \rho_1 \mathbf{v}_1 \rangle \cdot \nabla T_0^{fl}, \quad (2.56b)$$

and in the solid the second order equation is given as,

$$0 = \nabla \cdot \left[ k_0^{\text{th,sl}} \nabla T_2^{\text{sl}} + k_2^{\text{th,sl}} \nabla T_0^{\text{sl}} \right] + P_{\text{ac}} \quad (2.57a)$$

$$P_{\text{ac}} = \nabla \cdot \langle k_1^{\text{th,sl}} \nabla T_1^{\text{sl}} \rangle \quad (2.57b)$$

The temperature fields are induced due to an acoustic power density  $P_{\text{ac}}$  or convection of the zeroth order field  $T_0^{\text{fl}}$  and governed by heat diffusion. As for the streaming field we separate the acoustic power density  $P_{\text{ac}}$  into a term consisting solely of first-order bulk fields  $P_{\text{ac}}^d$  and a field including first-order boundary layer fields  $P_{\text{ac}}^\delta$ , so  $P_{\text{ac}} = P_{\text{ac}}^d + P_{\text{ac}}^\delta$ . The fields are split up in a boundary and a bulk component Eq. (2.50) and specifically for the temperature fields  $T_2^{\text{xl}} = T_2^{\text{xl},d} + T_2^{\text{xl},\delta}$  where 'xl' either denotes the fluid 'fl' or the solid 'sl' field. The bulk and boundary layer fields are connected at the fluid-solid interface where all four fields are connected by two boundary conditions, the first requiring constant temperature and the second requiring constant heat flux, Eq. (2.22).

As for the streaming field, we solve the boundary layer fields analytically and impose them as effective boundary conditions on the bulk fields. The same procedure as for the streaming field is used (i) separate the governing equation in a bulk  $d$  and boundary layer  $\delta$  part, (ii) take advantage of  $\nabla^2 \approx \partial_z^2$  to write an differential equation for the boundary layer temperature field  $T_2^\delta$ , (iii) integrate the equation once from  $z = \infty$  to  $z = 0$  to get an expression for the heat flux  $\mathbf{n} \cdot \nabla T_2^{\delta 0}$  at the interface, (iv) and integrate twice to get an expression for the temperature  $T_2^{\delta 0}$  at the interface. The derivations are shown in Ref. [3] enclosed in Section 7.3. The normal derivative of the boundary layer temperature field  $\partial_z T_2^{\text{fl},\delta 0}$  at the interface is given as,

$$\begin{aligned} \partial_z T_2^{\text{fl},\delta 0} = \text{Re} \left[ \frac{1+i}{4D_0^{\text{th}}} \left\{ \frac{1-i}{2} \frac{\delta_s \omega}{c_p} \mathbf{v}_1^{\delta 0} \cdot \mathbf{v}_1^{\delta 0*} - \frac{\delta_t \omega \alpha_{p0}}{c_p \rho_0} p_1^0 T_1^{\delta 0*} \right. \right. \\ - \frac{\delta_s}{\delta_s + i\delta_t} \left[ \delta_t \nabla_{\parallel} T_1^{\delta 0} \cdot \mathbf{v}_{1,\parallel}^{\delta 0*} - (1-i) T_1^{\delta 0} v_{1,z}^{\delta 0*} \right] \\ - iT_1^{\delta 0} \left[ v_{1,z}^{d,T0*} + (1+i) v_{1,z}^{d,p0*} - \delta_t \omega \kappa_s p_1^0 \right] \\ \left. \left. - \delta_t \nabla_{\parallel} T_1^{\delta 0} \cdot \mathbf{v}_{1,\parallel}^{d,p0*} + \delta_t \omega \frac{k_1^{\text{th},\delta 0} + 2k_1^{\text{th},d0}}{k_0^{\text{th}}} T_1^{\delta 0*} \right\} \right]. \quad (2.58) \end{aligned}$$

And the boundary layer temperature field  $T_2^{\text{fl},\delta 0}$  at the interface is given as,

$$\begin{aligned} T_2^{\text{fl},\delta 0} = \frac{\delta_t}{4D_0^{\text{th}}} \text{Re} \left\{ - \frac{\delta_s^2 \omega}{2\delta_t c_p} \mathbf{v}_1^{\delta 0} \cdot \mathbf{v}_1^{\delta 0*} + \frac{\delta_t \omega \alpha_{p0}}{c_p \rho_0} p_1^0 T_1^{\delta 0*} \right. \\ + i \frac{\delta_s^2}{(\delta_s + i\delta_t)^2} \left[ \delta_t \nabla_{\parallel} T_1^{\delta 0} \cdot \mathbf{v}_{1,\parallel}^{\delta 0*} - (1-i) T_1^{\delta 0} v_{1,z}^{\delta 0*} \right] \\ - T_1^{\delta 0} \left[ \frac{1-i}{2} v_{1,z}^{d,T0*} + (1+i) v_{1,z}^{d,p0*} - \delta_t \omega \kappa_s p_1^0 \right] \\ \left. + i\delta_t \nabla_{\parallel} T_1^{\delta 0} \cdot \mathbf{v}_{1,\parallel}^{d,p0*} - \delta_t \omega \frac{(1+i)k_1^{\text{th},\delta 0} + 2k_1^{\text{th},d0}}{2k_0^{\text{th}}} T_1^{\delta 0*} \right\}. \quad (2.59) \end{aligned}$$

The induced heating in the solid boundary layer is negligible compared to the heating in the fluid boundary layer and therefore we set  $\partial_z T_2^{\text{fl},\delta 0} = 0$  and  $T_2^{\text{sl},\delta 0} = 0$  in the simulations.

### 2.8.1 Bulk temperature field

With an analytical solution to the boundary layer fields at the interface, it is possible to setup a set of governing equations for the bulk temperature fields with a set of effective boundary conditions. The governing equation in the fluid is Eq. (2.56),

$$0 = \nabla \cdot \left[ k_0^{\text{th}} \nabla T_2^{\text{fl},d} + k_2^{\text{th}} \nabla T_0^{\text{fl}} \right] - c_p \rho_0 \mathbf{v}_2^d \cdot \nabla T_0^{\text{fl},d} + P_{\text{ac}}^d, \quad (2.60a)$$

$$P_{\text{ac}}^d = \nabla \cdot \left[ \langle k_1^{\text{th},d} \nabla T_1^{\text{fl},d} \rangle - \langle p_1 \mathbf{v}_1^{d,p} \rangle + \langle \mathbf{v}_1^{d,p} \cdot \boldsymbol{\tau}_1^d \rangle \right] - c_p \langle \rho_1^d \mathbf{v}_1^{d,p} \rangle \cdot \nabla T_0^{\text{fl},d} \quad (2.60b)$$

and the solid equation is the bulk part of Eq. (2.57),

$$0 = \nabla \cdot \left[ k_0^{\text{th}} \nabla T_2^{\text{sl},d} + k_2^{\text{th,sl}} \nabla T_0^{\text{sl}} \right] + P_{\text{ac}}^d \quad (2.61a)$$

$$P_{\text{ac}}^d = \nabla \cdot \langle k_1^{\text{th,sl}} \nabla T_1^{\text{sl},d} \rangle. \quad (2.61b)$$

There is a sign error in the submitted articles enclosed in Sections 7.3 and 7.4 for both the bulk fields in the solid and fluid, this error will be fixed before publishing. The terms  $k_2^{\text{th}} \nabla T_0$  are negligible in most cases, unless there is a high gradient in the zeroth-order temperature field  $T_0$ . The constant temperature boundary condition is imposed on the temperature field in the fluid [3],

$$T_2^{\text{fl},d} = T_2^{\text{sl},d} - T_2^{\text{fl},\delta 0} - \frac{1}{2} \text{Re} \left\{ \mathbf{s}_1 \cdot \nabla T_1^{\text{fl},d*} - k_t^{\text{fl}} (\mathbf{s}_1 \cdot \mathbf{n}) T_1^{\text{fl},\delta 0*} \right\}. \quad (2.62)$$

The constant temperature boundary condition is applied on the fluid domain because the fluid domain in most cases is only in contact with the solid domain. Therefore it would be numerically unstable to only have a flux boundary condition on the fluid domain. The flux boundary condition is applied on the solid domain, the effective boundary condition is given as [3],

$$-k_0^{\text{th,sl}} \mathbf{n} \cdot \nabla T_2^{\text{sl},d} = -k_0^{\text{th,fl}} \mathbf{n} \cdot \nabla T_2^{\text{fl},d} - k_0^{\text{th,fl}} \partial_z T_2^{\text{fl},\delta} - \frac{1}{2} \text{Re} \left\{ k_t^{\text{fl}} k_1^{\text{th,fl}} T_1^{\text{fl},\delta*} - \frac{2i}{\delta_t^2} k_0^{\text{th,fl}} (\mathbf{s}_1 \cdot \mathbf{n}) T_1^{\text{fl},\delta*} \right\} \quad (2.63)$$

With the governing equations and the effective boundary conditions for the bulk temperature fields the perturbative model is complete including the zeroth order temperature field, the first order acoustics, the second order streaming and temperature fields. All boundary layers are solved analytically and imposed as effective boundary conditions so that the thermal and viscous boundary layers do not need to be numerically resolved.

### 2.8.2 Example: Heating in viscous boundary layers

To demonstrate the internal heating in an acoustofluidic device due to frictional losses in the viscous boundary layers we study a silicon chip with a rectangular fluid channel and a glass lid, see Fig. 2.4(a). The acoustofluidic chip is actuated at resonance frequency to generate a horizontal half-wave resonance in the fluid channel. The model is actuated on the bottom of the silicon where the temperature is also held constant mimicking an external heat sink. The resulting temperature increase is shown in Fig. 2.4(b), heating up 8.7 mK at an acoustic energy density of  $E_{ac} = 28 \text{ J/m}^3$  [3].

The heating occurs in the two boundary layers at the top and bottom of the chip, at the bottom the heat is generated very close to the silicon chip  $\delta_s < 500 \text{ nm}$  which has a high heat conductivity and therefore effectively transports the heat away. While at the top the heat is generated close to the glass lid which compared to silicon has a low heat conductivity, hence a thermal gradient through the fluid is created in order to transport the heat to the heat sink. The temperature field in Fig. 2.4(b) shows the importance of the solids thermal parameters in modeling the second order temperature field. In Fig. 2.4 the effective model is validated against a full model showing a line plot at  $y = W/4$  for both the full and effective model.

The last important learning from this example is the magnitude of the second order temperature  $T_2$ . When the magnitude becomes comparable to the magnitude of first order temperature field  $\max(|T_1|) \approx (\gamma - 1) \frac{\kappa_T}{\alpha_p} \max(|p_1|)$  then the perturbation theory is no longer valid. At an acoustic energy density  $E_{ac} = 28 \text{ J/m}^3$  the maximum first order

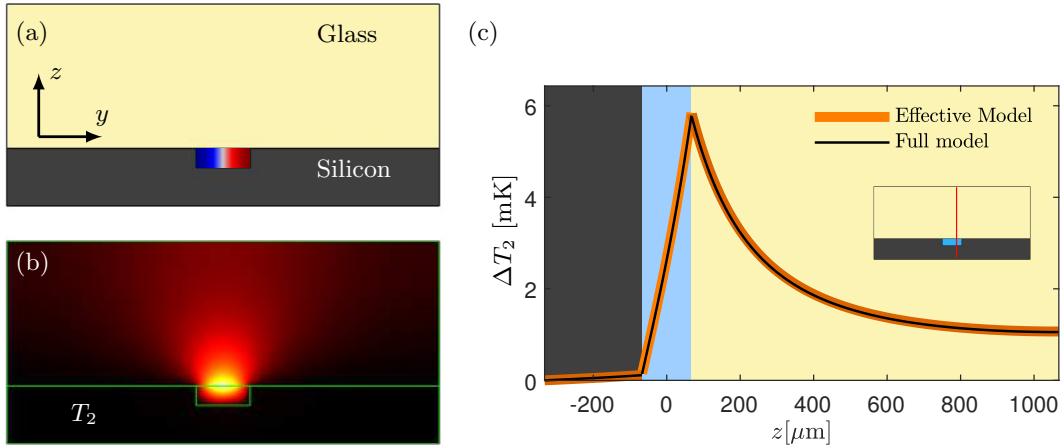


Figure 2.4: (a) Model of an acoustofluidic system with silicon (grey), glass (beige), and the acoustic field (red to blue) shown in the fluid domain. (b) Color plot of the temperature field  $T_2$  from black 0 to yellow 8.7 mK. (c) Line plot of the temperature field  $T_2$  from an effective (orange) and full (black) model along a line at  $y = W/4$  visualized with a red line on the inset. Figure is adapted from [3].



temperature is given as

$$\begin{aligned}\max(|T_1|) &= (\gamma - 1) \frac{\kappa T}{\alpha_p} \max(|p_1|) \\ &= (\gamma - 1) \frac{\kappa T}{\alpha_p} \sqrt{4E_{ac}/\kappa T} \approx 10 \text{ mK},\end{aligned}\tag{2.64}$$

which is comparable to the second temperature field  $T_2 = 8.7 \text{ mK}$ . To address this problem with the perturbative model a non-perturbative model was developed in Ref. [3], which will be presented in Section 2.10.

## 2.9 Forces on particles

The previous sections have presented a model to simulate the solid and fluid behaviour, but it is beneficial to remember that the purpose of the acoustofluidic devices are to affect particles and cells in the fluid. This section describes the forces that act on particles located in an acoustic field. There are two main forces on the particles, the acoustic radiation force  $\mathbf{F}^{\text{rad}}$  from the acoustic wave scattering of the particles, and the drag force  $\mathbf{F}^{\text{drag}}$  from the acoustic streaming field  $\mathbf{v}_2$ .

The acoustic radiation force  $\mathbf{F}^{\text{rad}}$  is due to the acoustic wave scattering of the suspended particles. Generally scattering phenomenons are complex problems, acoustofluidics are often in the regime where the particle radius  $a$  is a lot smaller than the acoustic wavelength  $\lambda$  and bigger than the thermal and viscous boundary layers, so  $\delta \ll a \ll \lambda$ . In this regime the acoustic radiation force  $\mathbf{F}^{\text{rad}}$  can be expressed as [22],

$$\mathbf{F}^{\text{rad}} = -\pi a^3 \left( \frac{2\kappa_0}{3} \text{Re} [f_1^* p_1^* \nabla p_1] - \rho_0 \text{Re} [f_2^* \mathbf{v}_1^* \cdot \nabla \mathbf{v}_1] \right),\tag{2.65a}$$

$$f_1 = 1 - \tilde{\kappa}, \quad f_2 = \frac{2(\tilde{\rho} - 1)}{2\tilde{\rho} + 1},\tag{2.65b}$$

where  $p_1$  and  $\mathbf{v}_1$  are evaluated at the center of the particle and  $\tilde{\kappa} = \kappa_p/\kappa_0$  and  $\tilde{\rho} = \rho_p/\rho_0$ . Note that there are two terms a monopole term coupling to the acoustic pressure field  $p_1$  depending on the compressibility  $\kappa_p$  of the particle through  $f_1$  and a dipole term related to the acoustic velocity field  $\mathbf{v}_1$  depending on the density  $\rho_p$  of the particle through  $f_2$ . For a standing wave the acoustic radiation force can be described as a potential force by the Gorkov potential  $U$  [21, 22],

$$\mathbf{F}^{\text{rad}} = -\nabla U,\tag{2.66a}$$

$$U = \frac{4\pi a^3}{3} \left[ f_1 \frac{\kappa_0}{2} \langle p_1^2 \rangle - f_2 \frac{3\rho_0}{4} \langle \mathbf{v}_1^2 \rangle \right].\tag{2.66b}$$

In acoustofluidics most particles and devices are in the regime  $\delta \ll a \ll \lambda$  where the Gorkov potential is valid, but for small particles  $\delta \sim a$  effects from the boundary layers are important to include, in this regime Doinikov [52–54] has included many of the extra corrections including effects due to microstreaming.

The second force on the particle is the drag force from a velocity difference between the particle and the surrounding fluid. The drag force on a spherical particle moving with velocity  $\mathbf{v}_{\text{par}}$  in a fluid moving at velocity  $\mathbf{v}_2$  is given as

$$\mathbf{F}^{\text{drag}} = -6\pi\eta a(\mathbf{v}_{\text{par}} - \mathbf{v}_2). \quad (2.67)$$

A particle is under the influence of both the acoustic radiation force and the drag force, the momentum of the particle is negligible for the trajectory, therefore the resulting particle velocity  $\mathbf{v}_{\text{par}}$  is given by balancing the two forces,

$$\mathbf{v}_{\text{par}} = \mathbf{v}_2 - \frac{2a^2}{3\eta_0} \left( f_1 \nabla E_{\text{pot}} - \frac{3}{2} f_2 \nabla E_{\text{kin}} \right) \quad (2.68)$$

Because  $\mathbf{F}^{\text{drag}}$  scales as  $a$  and  $\mathbf{F}^{\text{rad}}$  scales as  $a^3$  small particles will be dominated by the drag force and big particles by the acoustic radiation force.

### 2.9.1 Acoustic radiation force in acoustofluidic devices

In most acoustofluidic devices the acoustic radiation force is the primary force on the particles and used to up-concentrate, separate and trap particles. In many bulk acoustofluidic systems the acoustic wave is primarily a standing one-dimensional acoustic wave with the form  $p_1 = p_a \cos(ky)$  with a wave number  $k = \frac{n\pi}{W}$  where  $W$  is the width between two coplanar walls. Then the acoustic radiation force Eq. (2.66) reduces to the expression given by Yosioka and Kawasima [55],

$$F^{\text{rad}} = 4\pi\Phi(\tilde{\kappa}, \tilde{\rho})a^3kE_{\text{ac}} \sin(2kz). \quad (2.69)$$

Where the acoustic energy density is  $E_{\text{ac}} = \frac{1}{4}\kappa_s p_a^2$  and  $\Phi(\tilde{\kappa}, \tilde{\rho})$  is the acoustic contrast factor between the particle and fluid,

$$\Phi(\tilde{\kappa}, \tilde{\rho}) = \frac{1}{3}f_1(\tilde{\kappa}) + \frac{1}{2}f_2(\tilde{\rho}). \quad (2.70)$$

If the contrast factor is positive (negative) the force pushes the particles to the pressure nodes (anti-nodes). Thus, the acoustic radiation force can be used to separate particles with different contrast factors. If there is a gradient in the fluid parameters such that there is a gradient in the contrast factor, a particle will focus at the position in the fluid where the contrast factor is zero. This effect is named iso-acoustic focusing and was demonstrated by Augustsson et al. 2016 [39].

With the acoustic radiation force in Eq. (2.69) and the drag force Eq. (2.67) it is possible to calculate the time it takes to focus a particle  $t_{\text{foc}}$  or cell in an acoustofluidic device. The characteristic focusing time are proportional to the  $E_{\text{ac}}$  and  $(W/a)^2$ , and given as [56],

$$t_{\text{foc}} \approx \frac{3}{4\Phi} \frac{W^2}{\pi^2 a^2} \frac{\eta}{E_{\text{ac}}}. \quad (2.71)$$

For a polystyrene particle with  $a = 5 \mu\text{m}$  and  $\Phi = 0.17$ , in a channel with  $W = 400 \mu\text{m}$  and  $E_{\text{ac}} = 100 \text{ J/m}^3$  the focusing time will be  $t_{\text{foc}} \approx 26 \text{ ms}$ . In microfluidic systems

it is difficult to measure the strength of the acoustic field directly, so often the acoustic energy density is measured by the focusing time of a well known particle solution. This is the method used to measure the acoustic energy density in the two enclosed papers in Sections 7.2 and 7.4. The critical radius  $a_{\text{crit}}$  for when the radiation force dominates are for a polystyrene particle with  $\Phi = 0.17$  at frequency  $f = 2$  MHz approximately  $a_{\text{crit}} \approx 1 \mu\text{m}$ . The critical radius depends on the angular frequency  $\omega$ , contrast factor  $\Phi$ , and dynamic viscosity  $\nu_0$ , as  $a_{\text{crit}} \propto \left(\frac{\nu_0}{\omega\Phi}\right)^{1/2}$ .

In an acoustic trap it is not sufficient to focus the particle in the pressure node it is also necessary to localize the particle within the plane (line) of the pressure node. The pressure node is either a 2D plane (in a trapping capillary tube) or a 1D line (in an acoustic tweezer). When the particles are in the pressure node the pressure field is zero so the force component in the nodal plane is solely due to the  $f_2$  term related to the acoustic velocity field,

$$\mathbf{F}_{\text{node}}^{\text{rad}} = -4\pi a^3 f_2 \nabla E_{\text{ac}}. \quad (2.72)$$

So a heavy particle  $f_2 > 0$  is attracted to a region with high acoustic energy density while a light particle  $f_2 < 0$  is pushed away from an acoustic hotspot. So in an acoustic trapping capillary or an acoustic tweezer the ability to trap particles against the flow is determined by the contrast factor  $f_2$ , size of the particle  $a$ , and the gradient in the acoustic energy density  $\nabla E_{\text{ac}}$ . Thus, a good acoustic trap has a large gradient in the acoustic energy density and the easiest particles to trap are large particles with high density.

## 2.10 Non-perturbative acoustofluidics

This section presents the theoretical work on non-perturbative acoustofluidic published in Ref. [3] enclosed in Section 7.3. Non-perturbative refers to the domain where the acoustic fields are so large that the perturbation theory is no longer valid. High acoustic energies are often desirable in acoustofluidics because it leads to faster focusing times, and stronger acoustic traps which both are important to achieve a high flow through in a device. Because of the small scale of acoustofluidic systems the flow through is often a limiting parameter for acoustofluidics devices for practical usage. First, we discuss when the perturbation theory breaks down, then the model developed in Ref. [3] is presented, and lastly a discussion of the main non-perturbative effects in acoustofluidic devices.

### 2.10.1 Range of validity for the perturbation theory

The main non-perturbative effect is due to heating in the device which can create temperature gradients. In a device where there are no zeroth order temperature gradients, the gradients in the second order temperature field can lead to a non-negligible inhomogeneous acoustic body force. This force will in perturbation theory be a fourth order term and therefore not included in the second order equations. When this effects become important the perturbation theory is no longer valid.

A limit for when the non-perturbative effect is no longer negligible can be estimated based on the temperature difference across the fluid domain. It is estimated by comparing

the inhomogeneous acoustic body force with the acoustic body force driving the classical Eckart streaming. When the inhomogeneous acoustic body force is larger than the classical acoustic body force, the non-linear effects should be included,

$$\begin{aligned} \left| \frac{1}{4} |p_1|^2 \nabla \kappa_{s,2} \right| &> \left| \frac{\Gamma \omega}{c_0^2} \langle \mathbf{v}_1^{d,p} p_1 \rangle \right|, \\ \frac{1}{4} |p_1|^2 \kappa_{s0} a_{\kappa_s} \alpha_p d^{-1} \Delta T_2 &> \Gamma \kappa_{s0} d^{-1} |p_1|^2, \\ &\rightarrow \Delta T_2 > \frac{4\Gamma}{\alpha_p a_{\kappa_s}} \sim 30 \text{ mK}. \end{aligned} \quad (2.73)$$

Here it is assumed that the characteristic length scale of the thermal field and acoustic field ' $d$ ' are comparable and  $\Delta T_2$  is the temperature difference across the fluid channel or a wavelength. So when there is a temperature difference of  $\Delta T_2 \sim 30$  mK the perturbation theory is no longer valid. The temperature gradient created across a fluid channel is difficult to directly link to an acoustic energy density because the heating depends heavily on the thermal parameters of the surrounding solid, as seen in Section 2.8.2. Hence, the acoustic energy density corresponding to  $\Delta T_2 \sim 30$  mK depends on the acoustofluidic device used. For the chip investigated in Section 2.8.2 an acoustic energy density of  $E_{ac} \sim 100 \text{ J/m}^3$  is needed to get a temperature difference of  $\Delta T_2 \sim 30$  mK. The temperature increase of 30 mK is comparable to when the non-perturbative model in Ref. [4] enclosed in Section 7.4 starts to deviate from the perturbative model.

The other important non-perturbative effect is convective heat transport due to high acoustic streaming. The convective heat transport is important when the Péclet number  $Pe = \frac{|\mathbf{v}|d}{D^{th}}$  is similar or larger than one. So the perturbation theory is not valid for streaming velocities higher than  $|\mathbf{v}| \sim \frac{D^{th}}{d}$ , where  $d$  is the characteristic length scale of the system. For  $d = 500 \text{ } \mu\text{m}$  the maximum streaming velocity for a Péclet number of one is  $|\mathbf{v}| = 300 \text{ } \mu\text{m/s}$ .

### 2.10.2 Separation of time-scales

To avoid the assumptions of the perturbation theory the steady and acoustic fields are separated based on time-scales. The separation of time-scales does not assume that the acoustic fields are small compared to the stationary fields. The fast acoustic time-scale is set by the frequency of the acoustic field. Most acoustofluidic devices are driven in the frequency range  $f = 1 - 20 \text{ MHz}$ , resulting in a fast acoustic time scale  $t$ ,

$$t = \frac{1}{\omega} = \frac{1}{2\pi f} = 8 - 160 \text{ ns}. \quad (2.74)$$

The steady or slow time scale  $\tau$  is given by the hydrodynamic and thermal flows. Following Karlsen and Bruus [32], for a typical aqueous suspension in a channel of height  $H = 0.5 \text{ mm}$  with density  $\rho$ , relative density difference  $\hat{\rho} = 0.1$  induced by gradients in either concentration or temperature, and kinematic viscosity  $\nu = \eta/\rho$ , the characteristic

time scales for thermal relaxation  $t_{\text{therm}} = H^2/D^{\text{th}}$ , viscous relaxation  $t_{\text{visc}} = H^2/\nu_0$ , inertial motion  $t_{\text{inert}} \approx \sqrt{H/(g\hat{\rho})}$ , and steady shear motion  $t_{\text{shear}} \approx \nu_0/(Hg\hat{\rho})$  are estimated to all be in the order of 10 ms. Thus the slow time scale  $\tau$  is given as,

$$\tau \approx t_{\text{therm}} \approx t_{\text{visc}} \approx t_{\text{inert}} \approx t_{\text{shear}} \approx 10 \text{ ms.} \quad (2.75)$$

Thus the slow thermo-hydrodynamic and fast acoustic time scales are separated by 4-5 orders of magnitude. Therefore the fast and slow dynamics are solved separately. The slow time scale is assumed to be stationary and all physical fields  $Q_{\text{phys}}$  are decomposed in a stationary field  $Q_0$  and an acoustic field  $Q_1 e^{-i\omega t}$

$$Q_{\text{phys}}(t) = Q_0 + \text{Re} \{ Q_1 e^{-i\omega t} \}. \quad (2.76)$$

Both time scales will depend on each other, the stationary fields sets the density and compressibility of the fluid, which governs the acoustic fields. And the fast acoustic time scale induces a time-averaged acoustic body force  $\mathbf{f}_{\text{ac}}$  and acoustic heating-power density  $P_{\text{ac}}$  that enters the governing equations for the stationary fields. The fields are described by a stationary field and an acoustic field with angular frequency  $\omega$ , thus we have neglected the double harmonic terms with time-dependence  $e^{-2i\omega t}$ . So the theory is only valid in the limit where the double harmonics can be neglected. If it is desired to include higher order harmonics it is to my knowledge necessary to solve the full time-dependent equations.

### 2.10.3 Acoustic and stationary equations

The governing equations for the stationary and acoustic fields are derived in Ref. [4] enclosed in Section 7.3. Most of the equations are very similar to the governing equations in the perturbation theory as they are governed by the same conservation laws. The governing equations for the acoustic fields are exactly the same as the first order equations (Section 2.6) of the perturbation theory, and the effective boundary conditions on both the acoustic and stationary fields are also the same as the perturbation theory. The only differences are for the stationary fields. The governing equations for the stationary fields are slightly different from the second order equations because some terms that previous was higher order terms are included, for example the advective term  $\nabla \cdot (\rho_0 \mathbf{v}_0^d \mathbf{v}_0^d)$ . Therefore we only present the altered bulk equations for the stationary fields while the equations for the acoustic fields can be found in Section 2.6. The steady streaming field is governed by stationary part of the continuity and Navier-Stokes equation Eqs. (2.5) and (2.6) together with the effective boundary conditions,

$$0 = \nabla \cdot \mathbf{v}_0 \quad (2.77a)$$

$$0 = \nabla \cdot (p_0^d - \mathcal{L}_{\text{ac}}^d) + \eta_0 \nabla^2 \mathbf{v}_0^d - \nabla \cdot (\rho_0 \mathbf{v}_0^d \mathbf{v}_0^d) + \mathbf{f}_{\text{ac}}^d \quad (2.77b)$$

$$\mathbf{f}_{\text{ac}}^d = -\frac{1}{4} |\mathbf{v}_1^{d,p}|^2 \nabla \rho_0 - \frac{1}{4} |p_1|^2 \nabla \kappa_{s0} + \frac{\Gamma \omega}{2 c_0} \langle \mathbf{v}_1^{d,p} p_1 \rangle + \nabla \cdot \boldsymbol{\tau}_{11}^d, \quad (2.77c)$$

$$\mathbf{v}_0^{d0} = (\mathbf{A} \cdot \mathbf{e}_x) \mathbf{e}_x + (\mathbf{A} \cdot \mathbf{e}_y) \mathbf{e}_y + (\mathbf{B} \cdot \mathbf{e}_z) \mathbf{e}_z. \quad (2.77d)$$

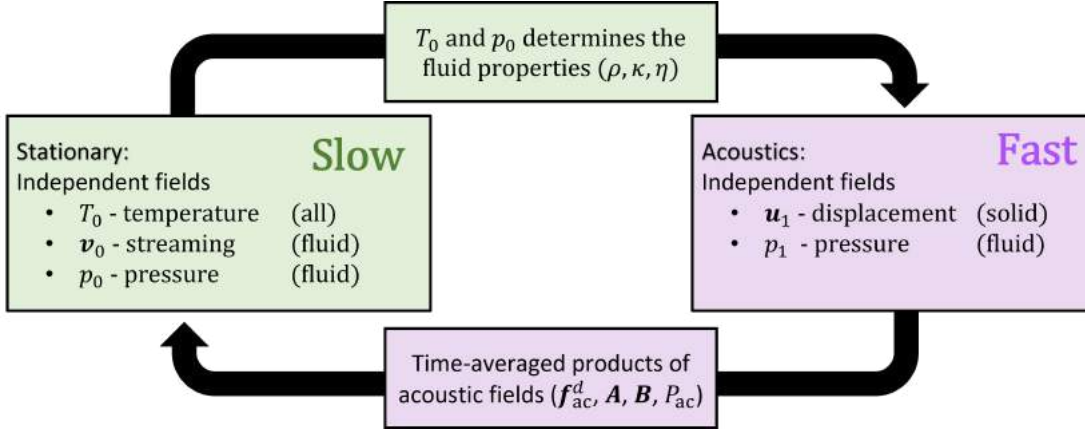


Figure 2.5: Sketch of the iterative solver iterating between the stationary equations and acoustic equations. The stationary fields determine the material properties for the acoustic equations, and time-averaged products of the acoustic fields act as forces and heating in the stationary equations.

The tensors  $\mathbf{A}$  and  $\mathbf{B}$  are defined in Eq. (2.53) and are the same as in the perturbation model. The only difference from the second-order equations in Eq. (2.55) is the inclusion of the advection term  $\nabla \cdot (\rho_0 \mathbf{v}_0^d \mathbf{v}_0^d)$ . The acoustic field drives the streaming through the bulk acoustic body force  $\mathbf{f}_{ac}^d$  and the no-slip velocity  $\mathbf{v}_2^{d0}$  given by  $\mathbf{A}$  and  $\mathbf{B}$ .

The steady temperature field in the bulk of the fluid  $T_0^{\text{fl},d}$  is governed by the stationary part of the equation of energy conservation (2.8),

$$0 = \nabla \cdot \left[ k_0^{\text{th}} \nabla T_0^{\text{fl},d} \right] - c_p \rho_0 \mathbf{v}_0 \cdot \nabla T_0^{\text{fl},d} + P_{ac}^d + P, \quad (2.78a)$$

$$P_{ac}^d = \nabla \cdot \left[ \langle k_1^{\text{th},d} \nabla T_1^d \rangle - \langle p_1 \mathbf{v}_1^{d,p} \rangle + \langle \mathbf{v}_1^{d,p} \cdot \boldsymbol{\tau}_1^d \rangle \right] - c_p \langle \rho_1^d \mathbf{v}_1^{d,p} \rangle \cdot \nabla T_0^d \quad (2.78b)$$

It is similar to the second order temperature field in the perturbation theory, but with the external power  $P$  included (in perturbation theory this field was a zeroth order term). And likewise for the solid where the heating can either be due to the external heating  $P$  or heating caused by the acoustic field  $P_{ac}^d$

$$0 = \nabla \cdot \left[ k_0^{\text{th}} \nabla T_0^{\text{sl},d} \right] + P_{ac}^d + P \quad (2.79a)$$

$$P_{ac}^d = \nabla \cdot \langle k_1^{\text{th},sl} \nabla T_1^{\text{sl},d} \rangle, \quad (2.79b)$$

with the effective boundary conditions derived in Section 2.8. In this model both the acoustic and stationary fields depend on each other thus, it is necessary to use an iterative solver to solve the equations. The iterative solver, sketched in Fig. 2.5, iterates between the stationary equations governing the independent fields  $T_0$ ,  $\mathbf{v}_0$ , and  $p_0$  and the acoustic equations governing the independent fields  $\mathbf{u}_1$  and  $p_1$  until all fields are converged.

There is one important notion regarding the derivation of the effective boundary conditions for the non-perturbative model. A key assumption in deriving the effective boundary conditions is that there are no mixing terms of the boundary layer field  $\mathbf{v}_0^\delta$  and bulk field  $\mathbf{v}_0^d$ , this means that the advective term  $\nabla \cdot (\rho_0 \mathbf{v}_0^d \mathbf{v}_0^\delta)$  has to be negligible. That requires the Reynolds number in the boundary layer to be small  $\text{Re}^\delta = \frac{\delta_s |\mathbf{v}_0|}{\nu_0} \ll 1$ , but still allows the Reynolds number in the bulk  $\text{Re}^d = \frac{d |\mathbf{v}_0|}{\nu_0}$  to be large.

#### 2.10.4 Main non-linear effects

There are two main non-perturbative effects in thermoviscous acoustofluidics which first becomes important. The two effects are the inhomogeneous acoustic body force due to internal heating from friction in the viscous boundary layers and convective heat transport due to fast streaming velocities.

The non-linear effect due to heating in the viscous boundary layers and the inhomogeneous acoustic body force is important in systems where there is no steady temperature gradient  $\nabla T_0$  without the acoustics. The traditional boundary streaming and Eckart streaming depends linearly on the acoustic energy density  $E_{ac}$ , while the inhomogeneous acoustic body force  $\mathbf{f}_{ac}^{\text{in}} = \frac{1}{4} |p_1|^2 \nabla \kappa_{T0} + \frac{1}{4} |\mathbf{v}_1|^2 \nabla \rho_0$  depends on the acoustic energy density squared  $\mathbf{f}_{ac}^{\text{in}} \propto E_{ac}^2$ , if the gradients in compressibility and density are due to frictional heating from the acoustic wave. Therefore at low acoustic energy density the boundary-driven and Eckart streaming will be dominant, but at some acoustic energy density the inhomogeneous acoustic body force  $\mathbf{f}_{ac}^{\text{in}}$  will become dominant. This transition was thoroughly studied in the paper enclosed in Section 7.4 and is summarized in Section 4.4. In the studied system the transition occurs at an acoustic energy of  $E_{ac} \sim 400 \text{ J/m}^3$ .

The second non-linear effect is convective heat transport, this is mainly important in systems with an initial temperature gradient  $\nabla T_0$ . The initial temperature gradient can lead to fast thermoacoustic streaming due to the inhomogeneous acoustic body force [2]. In a system with temperature gradients the convective heat transport becomes important when it is comparable to the diffusive heat transport. This is when the Péclet number  $\text{Pe} \approx 1$ , which correspond to a streaming velocity of

$$v_{\text{Pe}} \sim \frac{D^{\text{th}}}{d} \quad (2.80)$$

where  $D^{\text{th}}$  is the thermal diffusivity and  $d$  is the characteristic length scale in the microfluidic device. In a microfluidic channel  $d \sim 100 \text{ } \mu\text{m}$  with water  $D^{\text{th}} \sim 1.5 \times 10^{-7} \text{ m}^2/\text{s}$  the velocity where convection becomes important are  $v_{\text{Pe}} \approx 1.5 \text{ mm/s}$ . In the paper enclosed Section 7.2 the characteristic length-scale is  $h = 360 \text{ } \mu\text{m}$  and the streaming velocity reaches  $|\mathbf{v}| \sim 850 \text{ } \mu\text{m/s}$ , resulting in a Péclet number higher than 1 and therefore the used perturbation model is on the limit of its validity. Both these effects are thermal effects and therefore require a thermoviscous model.

Other non-linear effects include the importance of the term  $\nabla \cdot (\rho_0 \mathbf{v}_0^d \mathbf{v}_0^d)$  at high streaming velocities, this effect is investigated in relation to streaming in acoustic tweezers in Chapter 5. This effect is a purely mechanical effect and is therefore also present in purely viscous acoustofluidics.





## Chapter 3

# Numerical Methods

The thesis is build on theoretical, numerical and some (external) experimental work. The theoretical work is able to give fundamental insights into for example the streaming and heating mechanisms in an acoustofluidic system, but an acoustofluidic device quickly becomes very complex and require numerical simulations to be able to compare with experiments. In this section the numerical framework of the thesis is presented. All modelling is done using the COMSOL Multiphysics software [57] using a Finite Element Method (FEM). Using a commercial software like COMSOL has allowed me to focus on the physics (the governing equations and boundary condition) instead of settings for the numerical solvers and meshing. The numerical model developed in Chapter 2 is implemented in COMSOL using the "Weak Form Module".

The chapter introduces the general finite element method (FEM) with the weak formulation, boundary conditions, formulation in cylindrical coordinates, and the usage of symmetry planes and perfectly matched layers (PML).

### 3.1 The finite element method

With the FEM model we seek to solve partial differential equations (PDE) that can be written by a general source term  $F$  and a general flux  $\mathbf{J}$ ,

$$0 = \nabla \cdot \mathbf{J}(u(\mathbf{r})) - F(\mathbf{r}) \quad (3.1)$$

Where the  $u(\mathbf{r}, t)$  is the field controlled by the differential equation. The form is the same as the differential transport equation Eq. (2.3) and thereby the form of all the governing equations derived in Chapter 2. This formulation is called the strong formulation and can in some cases be solved analytically. But often it is needed to numerically solve the equation by computing an approximate solution to the differential equation. This is the case for the finite element method (FEM) the solution  $u(\mathbf{r}, t)$  is discretized onto a set of test-functions  $\phi_n$  to give an approximate solution  $\hat{u}$ ,

$$u(\mathbf{r}) \approx \hat{u}(\mathbf{r}) = \sum_{n=1}^N c_n \phi_n(\mathbf{r}) \quad (3.2)$$

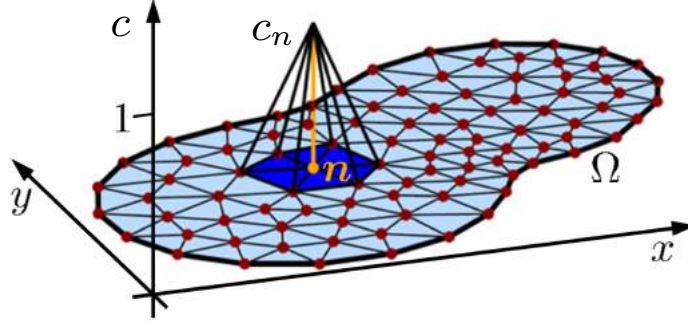


Figure 3.1: Illustration of a mesh on the domain  $\Omega$  with a basis function  $\phi_n$  which are non-zero at node  $n$  and the corresponding constant  $c_n$ . Figure adapted from [58].

Here  $N$  is the number of nodes (mesh points),  $\phi_n(\mathbf{r})$  are the set of basis functions and has the property  $\phi_i(\mathbf{r}_j) = \delta_{ij}$  where  $\delta_{ij}$  is the Kronecker's delta, and  $c_n$  are the constants that are fitted and they have the property  $c_n \approx u(\mathbf{r}_n)$ . The basis functions are sketched in Fig. 3.1 where its property of being non-zero at one node and zero at all other nodes is sketched. The approximate solution  $\hat{u}$  has a non-zero error  $\delta$  compared to the true solution to the differential equation,

$$\delta(\mathbf{r}) = \nabla \cdot \mathbf{J}(\hat{u}(\mathbf{r})) - F(\mathbf{r}). \quad (3.3)$$

By demanding that the projection of the error  $\delta$  on all test functions  $\phi_m$  vanishes we get the weak-formulation of the partial differential equation (PDE),

$$0 = \int_V \phi_m \left[ \nabla \cdot \mathbf{J}(\hat{u}(\mathbf{r})) - F(\mathbf{r}) \right] dV, \quad \text{for all } m. \quad (3.4)$$

The weak form formulation of the PDE is the form that are solved in the FEM models. For a flux  $\mathbf{J}$  that depends linearly on  $u$  we can write  $\mathbf{J}(\hat{u}(\mathbf{r})) = \sum_n c_n \mathbf{J}(\phi_n(\mathbf{r}))$ , thus we can introduce the stiffness matrix  $K_{mn}$  and the force vector  $F_m$ ,

$$K_{mn} = \int_V \phi_m(\mathbf{r}) \nabla \cdot \mathbf{J}(\phi_n(\mathbf{r})) dV, \quad (3.5a)$$

$$F_m = \int_V \phi_m(\mathbf{r}) F(\mathbf{r}) dV \quad (3.5b)$$

The matrix  $K_{mn}$  will be a sparse matrix and only be non-zero on the diagonal and at entrances where  $m$  and  $n$  are nodes in the same element. The weak formulation from Eq. (3.4) can be written as a matrix problem,

$$K_{mn} c_n = F_m. \quad (3.6)$$

Thus, the unknown constants  $c_n$  can be determined by matrix inversion to find the approximate solution  $\hat{u} = \sum_n c_n \phi_n(\mathbf{r})$ .

### 3.1.1 Boundary conditions

The physical system consists of both the governing equations and a set of boundary conditions, which needs to be implemented in the matrix system. The two simplest boundary conditions are the Dirichlet and Neumann boundary conditions,

$$\text{Dirichlet :} \quad u(\mathbf{r}) = f(\mathbf{r}), \quad \mathbf{r} \in \partial\Omega, \quad (3.7a)$$

$$\text{Neumann :} \quad \mathbf{n} \cdot \mathbf{J}(u(\mathbf{r})) = q(\mathbf{r}), \quad \mathbf{r} \in \partial\Omega. \quad (3.7b)$$

The Dirichlet boundary condition specifies the value of the field  $\mathbf{u}$  on the surface  $\partial\Omega$  to  $f(\mathbf{r})$ , and the Neumann boundary condition specifies the normal component of the generalised flux  $\mathbf{J}$  to  $q(\mathbf{r})$ . It should be noted that a problem cannot only have Neumann boundary conditions since it will not have a unique solution, because if  $u(\mathbf{r})$  is a solution so is  $u(\mathbf{r}) + C$ . If a system only have Neumann boundary conditions the average value of the field can be set by a global constraint imposing  $\int_V u(\mathbf{r})dV = C$ .

The Dirichlet boundary condition sets a value for the field  $u(\mathbf{r}) = f(\mathbf{r})$  for  $\mathbf{r}$  located on the boundary  $\partial\Omega$ . Thus, it determines the constants  $c_i = f(\mathbf{r}_i)$  for  $i \in \partial\Omega$  located on the boundary. Taking the matrix system  $K_{mn}c_n = F_m$  we can then define for  $i \in \partial\Omega$  the vector  $K_{mi}c_i = b_m$  since  $c_i$  is known, then the matrix system for the remaining nodes  $n \notin \partial\Omega$  is given as,

$$K_{mn}c_n = F_m - b_m, \quad n \notin \partial\Omega \quad (3.8)$$

So the Dirichlet boundary conditions reduces the order of the matrix by the number of elements on the boundary  $\partial\Omega$ .

To implement the Neumann boundary condition it is needed to revisit the weak formulation of the PDE (3.4). Using  $\nabla \cdot (\phi_m \mathbf{J}) = (\nabla \phi_m) \cdot \mathbf{J} + \phi_m \nabla \cdot \mathbf{J}$  and Gauss's theorem to rewrite Eq. (3.4) into,

$$0 = \int_V -\nabla \phi_m \cdot \mathbf{J}(\hat{u}(\mathbf{r})) - \phi_m F(\mathbf{r})dV + \int_{\partial\Omega} \phi_m \mathbf{n} \cdot \mathbf{J}(\hat{u}(\mathbf{r}))dA, \quad \text{for all } m. \quad (3.9)$$

The boundary integral is only non-zero if the mesh node  $m$  is located on the boundary. The Neumann boundary condition is now straight forward to implement by setting  $\mathbf{n} \cdot \mathbf{J}(\hat{u}(\mathbf{r})) = q(\mathbf{r})$ . This modifies the matrix system by changing the force vector to  $F_m = \int_V \phi_m(\mathbf{r})F(\mathbf{r})dV - \int_{\partial\Omega} \phi_m q(\mathbf{r})dA$ , where  $\partial\Omega$  is the part of the boundary having a Neumann boundary condition.

### 3.1.2 Formulation in cylindrical coordinates

The weak formulation is generally given in Eq. (3.4) with the boundary conditions set in Section 3.1.1. In this section a 2D axis-symmetric formulation of the weak form PDE is presented. In an axis-symmetrical system in cylindrical coordinates  $dV = 2\pi r dr dz$ . And the derivatives in cylindrical coordinates are given as,

$$\nabla = \left[ \mathbf{e}_r \partial_r + \frac{1}{r} \mathbf{e}_\phi \partial_\phi + \mathbf{e}_z \partial_z \right] \quad (3.10)$$

In the axis-symmetric case the  $\phi$  derivatives of the fields  $\mathbf{u}$ ,  $\mathbf{J}$  and  $\mathbf{F}$  are zero. But it is important to note that the derivatives of the unit vectors are not all zero, there is two non-vanishing derivatives,

$$\partial_\phi \mathbf{e}_r = \mathbf{e}_\phi, \quad \partial_\phi \mathbf{e}_\phi = -\mathbf{e}_r, \quad (3.11)$$

these terms coming from the  $\partial_\phi$  is essential to include in the axis-symmetric formulation to achieve the correct radial behaviour of the fields. The weak form formulation of the PDE is given as,

$$0 = \int_A \phi_m \cdot \left[ \nabla \cdot \mathbf{J}(\mathbf{u}(\mathbf{r})) - \mathbf{F}(\mathbf{r}) \right] 2\pi r dr dz, \quad (3.12)$$

Where the integral is over the  $r$ - $z$  surface, we would like to manipulate the equations such that it gets the form of a generalized flux  $\mathbf{J}_{rz}$  and generalized force term  $\mathbf{F}_{rz}$ . We use that the divergence of a symmetric tensor  $\mathbf{T}$  is given as,

$$\begin{aligned} \nabla \cdot \mathbf{T} = & \left( \left[ \partial_r T_{rr} + \partial_z T_{rz} + \frac{1}{r} T_{rr} - \frac{1}{r} T_{\phi\phi} \right] \mathbf{e}_r \right. \\ & \left[ \partial_r T_{\phi r} + \partial_z T_{\phi z} + \frac{1}{r} T_{\phi r} + \frac{1}{r} T_{r\phi} \right] \mathbf{e}_\phi \\ & \left. \left[ \partial_r T_{zr} + \partial_z T_{zz} + \frac{1}{r} T_{zr} \right] \mathbf{e}_\phi \right) \end{aligned} \quad (3.13)$$

Notice the five terms arising from  $\partial_\phi$  even though  $\mathbf{T}$  is axis-symmetric (all the terms including  $1/r$ ). Finally we use partial derivatives to move the factor  $2\pi r$  originating from  $dV$  inside the divergence. This causes three extra terms that cancels with three of the  $\frac{1}{r}$  terms,

$$\begin{aligned} 2\pi r \nabla \cdot \mathbf{T} = & \left[ \partial_r 2\pi r T_{rr} + \partial_z 2\pi r T_{rz} - 2\pi T_{\phi\phi} \right] \mathbf{e}_r \\ & \left[ \partial_r 2\pi r T_{\phi r} + \partial_z 2\pi r T_{\phi z} + 2\pi T_{r\phi} \right] \mathbf{e}_\phi \\ & \left[ \partial_r 2\pi r T_{zr} + \partial_z 2\pi r T_{zz} \right] \mathbf{e}_z \\ = & \nabla_{rz} \cdot (2\pi r \mathbf{T}) - 2\pi T_{\phi\phi} \mathbf{e}_r + 2\pi T_{r\phi} \mathbf{e}_\phi \end{aligned} \quad (3.14)$$

We get a divergence in the  $rz$ -plane and two extra source terms in the  $r$  and  $\phi$  component. So the weak formulation for an axis-symmetric system in cylindrical coordinates can be set up as,

$$0 = \int_A \phi_m \cdot \left[ \nabla_{rz} \cdot \left( \mathbf{J}_{rz}(\mathbf{u}(\mathbf{r})) \right) - \mathbf{F}_{rz}(\mathbf{r}) \right] dr dz, \quad (3.15a)$$

$$\mathbf{F}_{rz} = 2\pi r \mathbf{F} + 2\pi J_{\phi\phi} \mathbf{e}_r - 2\pi J_{r\phi} \mathbf{e}_\phi \quad (3.15b)$$

$$\mathbf{J}_{rz} = 2\pi r \mathbf{J} \quad (3.15c)$$

$$\nabla_{rz} = \mathbf{e}_r \partial_r + \mathbf{e}_z \partial_z \quad (3.15d)$$

This is a 2D axis-symmetric formulation which enables simulations of 3D systems axial symmetry. The two extra terms in the force  $\mathbf{F}_{rz}$  is important to get the correct

$r$ -dependency of the solutions. Note that the field  $\mathbf{u}$  are allowed to have a  $\phi$  component so  $\mathbf{F}_{rz}$  and  $\mathbf{J}_{rz}$  have three components, but the fields cannot depend on  $\phi$ .

An axis-symmetric system has a special boundary condition at  $r = 0$  where fields needs to be symmetric since  $\mathbf{u}(\phi = 0) = \mathbf{u}(\phi = \pi)$ . For a vector field  $\mathbf{u}$  that implies that the  $\phi$  and  $r$  component has to be zero  $u_\phi = u_r = 0$  and the radial derivative of the  $z$ -component is zero  $\partial_r u_z = 0$  at  $r = 0$ .

### 3.1.3 Symmetry planes and perfectly matched layers

When modelling 3D devices the numerical model can quickly become numerically large therefore we use symmetry planes and the technique perfectly matched layers (PML) to avoid simulating the entire chip:

- I: **Symmetry planes** – If a device has symmetry planes they can be exploited to reduce the size of the numerical model. Instead of simulating the entire device only one half of the device is simulated and a set of symmetry conditions is applied as boundary conditions at the symmetry plane. For the numerical in Section 7.2 two symmetry planes are used to only model a quarter system.
- II: **Perfectly matched layers** – PML is a technique to mimic a wave travelling out of the system [59, 60]. In this thesis PML is used for long channels with an actuation at the center. Then to avoid modelling the acoustic wave travelling away from the actuation region a perfectly matched layer is applied. A perfectly matched layer models a long channel as an infinite long channel, and are useful when there is no reflections from the end of the channel. The PML technique is only used for the acoustic fields.

The symmetry planes are identified based on the chip design and the acoustic resonance in the system. The symmetry planes are implemented by a boundary condition either setting the field to zero (antisymmetric) or the flux to zero (symmetric). A perfectly matched layer is implemented as a region where artificial dampening is added to dampen the acoustic fields [59, 60]. Both symmetry planes and a PML region is used in the numerical model in Ref. [2] showed in Fig. 3.2(a) to reduce the size of the numerical model.

## 3.2 Validation of numerical simulations

Numerical simulations are a great tool but they need to be validated here we discuss mesh convergence, numerical validation of the effective boundary layer theory, and comparisons with experiments.

When making FEM simulations the objective is to estimate the real field  $u$ , to do that test functions and mesh elements are used as a mathematical tool. Thus, ideally the numerical solution should be independent of the chosen mesh and order of test functions. The finer the used mesh is the greater is the accuracy but also the computational requirements. Therefore a mesh convergence test is made, to ensure convergence and to estimate

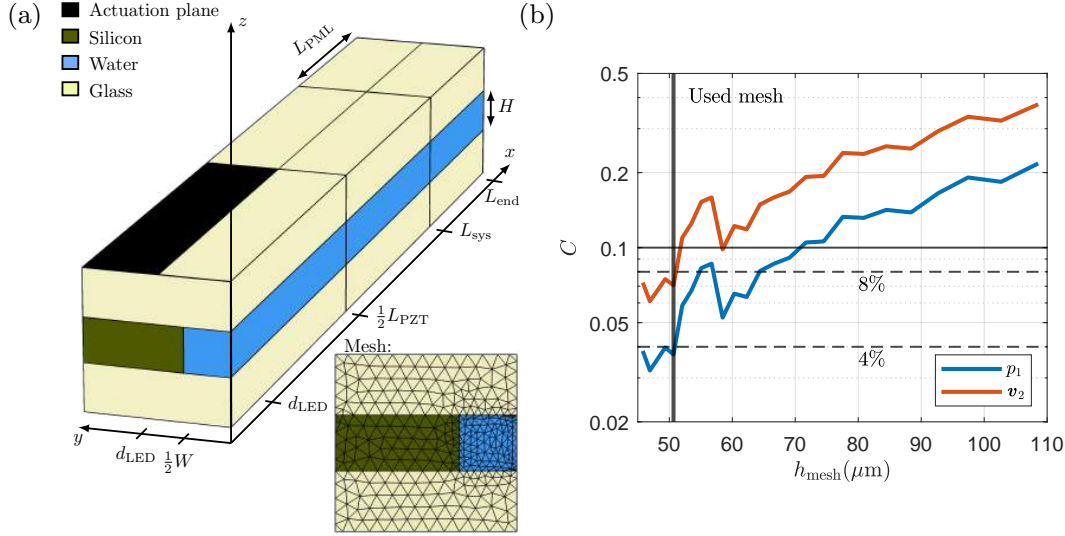


Figure 3.2: (a) Numerical 3D model used in Ref. [2], symmetry planes used at  $x = 0$  and  $y = 0$  and a PML region of length  $L_{PML}$ . (b) Line plots of the convergence analysis, the  $L_2$  error  $C$  for the pressure field  $p_1$  blue and streaming field  $v_2$  red. The used mesh is marked by a thick black line obtaining a convergence of 4% and 8% for  $p_1$  and  $v_2$ , respectively. Figure adapted from the supplemental material for Ref. [2].

the error of the numerical solution. A mesh is characterized by the mesh length element  $h_{mesh}$  and the error estimate is the relative  $L_2$ -norm referring to the finest mesh (smallest  $h_{mesh}$ ) as the true value,

$$\|x\|_{L_2} = \sqrt{\frac{\sum_{i=1}^N |x_i - x_i^{fine}|^2}{\sum_{i=1}^N |x_i^{fine}|^2}}. \quad (3.16)$$

For a model using  $n$ -order test functions the error should be proportional to  $h_{mesh}$  as  $\|x\|_{L_2} \propto (h_{mesh})^n$ . The convergence test for the acoustic pressure  $p_1$  and the streaming velocity  $v_2$  of the model used in Ref. [2] enclosed in Section 7.2 is shown in Fig. 3.2. Because the second order field inherits the error of the first order equations, the error on the second order equations are expected to be twice the error of the first order fields.

In Chapter 2 a model with effective boundary conditions was developed. To check that the effective boundary conditions are correct they are compared to a full simulation with the boundary layers numerically resolved. The comparison is done for a 2D-model so a full simulation is doable and the physical fields in the bulk of the fluid are compared. In Fig. 2.4(c) a line plot of temperature field  $T_2$  for both a full and effective is shown to validate the effective boundary conditions on the steady temperature field  $T_2$ , and in Fig. 2.3 a colour plot of the streaming field of an effective and full simulation are compared to validate the effective boundary conditions on the streaming field  $v_2$ .

Lastly the objective of the simulations are to model reality and therefore comparisons

to experiments are important to demonstrate the validity and relevance of a numerical model. When comparing to experimental results it is often beneficial to simplify and ensure control over the experimental setup. If the experiment is complex by nature it would be preferable to validate the numerical model against a simplified experimental setup. In this work I have been fortunate to work with a group of great experimentalists at Lund University that has made it possible to achieve great match between experiments and numerical simulations. These comparisons are shown in Sections 4.3 and 4.4 and published in Refs. [2, 4] enclosed in Sections 7.2 and 7.4.





## Chapter 4

# Streaming due to temperature gradients

A large part of the research during my thesis has focused on studying the effects of temperature fields in an acoustofluidic system, especially the streaming due to the inhomogeneous acoustic body force  $\mathbf{f}_{ac}^d$  in a fluid with temperature gradients. The acoustic body force is generally given as Eq. (2.55c),

$$\mathbf{f}_{ac}^d = -\frac{1}{4}|\mathbf{v}_1^{d,p}|^2 \nabla \rho_0 - \frac{1}{4}|p_1|^2 \nabla \kappa_{s0} + \frac{\Gamma \omega}{c_0^2} \langle \mathbf{v}_1^{d,p} p_1 \rangle + \nabla \cdot \boldsymbol{\tau}_{11}. \quad (4.1)$$

The inhomogeneous acoustic body force consists of the first two terms which depend on the gradient in density and compressibility. This section will present the research done on the acoustic body force when the gradients in the material parameters are caused by gradients in the temperature field.

The inhomogeneous acoustic body force was described and studied by J.T Karlsen, P. Augustsson, and H. Bruus in 2016 [32] where the gradients were created by a solute in the fluid. Gradients due to solutions has been used to stabilize a heavy fluid in the center of a channel [39], suppressing streaming [37, 38], and relocation of fluid [40]. The main drawback with gradients caused by solution gradients is that they diffuse over time. The work in this PhD has only been on gradients in density  $\rho_0$  and compressibility  $\kappa_{s0}$  caused by temperature gradients. Temperature gradients in a device can either be by design or they can be unintentional, in both cases they can be important for understanding the streaming pattern. Temperature gradients can unintentionally appear in a device by for example heating due the piezo-electric actuation, in these cases it is important to understand the heating to model the device correctly. The more interesting case is the possibility to use temperature fields actively in the design of a microfluidic device. This gives the possibility to have an extra parameter to control the streaming pattern in the device. Controlling a temperature field can be done by Peltier elements, Joule heating, or light absorption.

The chapter gives an overview over the published and unpublished research done in regards to streaming driven by the inhomogeneous acoustic body force. Section 4.1 will

present general characteristics of the body force when it is induced by temperature gradients. In Section 4.2 the streaming in a typical acoustofluidic trapping glass capillary tube is investigated and explained [1]. Section 4.3 goes through the streaming due to light absorption from an LED studied in Ref. [2] with our collaborators W. Qiu, E. Corato, and P. Augustsson from Lund University. In Section 4.4 we discuss how the inhomogeneous acoustic body force together with heating from the viscous boundary layers induces non-linear effects at high acoustic energy, and in Section 4.5 the streaming from localized light absorption is studied. Lastly concluding remarks on the acoustic force and the 0examples in Section 4.6.

## 4.1 The inhomogeneous acoustic body force

The inhomogeneous acoustic body force created by temperature gradients is given as,

$$\begin{aligned} \mathbf{f}_{\text{ac}}^d &= -\frac{1}{4}|\mathbf{v}_1^{d,p}|^2 \nabla \rho_0(T_0) - \frac{1}{4}|p_1|^2 \nabla \kappa_{s0}(T_0) \\ &= -\frac{1}{4} \left[ a_\rho^T \rho_0 |\mathbf{v}_1^{d,p}|^2 + a_{\kappa_s}^T \kappa_{s,0} |p_1|^2 \right] \alpha_{p,0} \nabla T_0 \\ &= - \left[ a_\rho^T E_{\text{kin}} + a_{\kappa_s}^T E_{\text{pot}} \right] \alpha_{p,0} \nabla T_0 \end{aligned} \quad (4.2)$$

Here  $a_\rho^T$  and  $a_{\kappa_s}^T$  are dimensionless parameters which describes the temperature dependency of  $\rho$  and  $\kappa_s$ , respectively, they are defined in Eq. (2.9) and given in Table 2.1. The following guidelines are valid for the force in water:

- I: Both density and compressibility decreases with temperature ( $a_\rho^T, a_{\kappa_s}^T < 0$ ) so the force points towards regions with high temperature. The direction of the force is determined only by the temperature gradient.
- II: Since  $a_\rho^T = -1$  and  $a_{\kappa_s}^T = -10$  and the spatial average of  $E_{\text{pot}}$  and  $E_{\text{kin}}$  are the same, then the inhomogeneous body-force is typically dominated by the  $|p_1|^2$ -term ( $E_{\text{pot}}$ -term) and therefore largest in the pressure anti-nodes.
- III: If the temperature gradient is created by an external heat source (absorption of light or Peltier element) then the inhomogeneous acoustic body force and the absolute streaming velocity scales as the acoustic energy density  $\mathbf{f}_{\text{ac}} \propto E_{\text{ac}}$ . This is the same scaling as the boundary driven streaming.
- IV If the gradients in the temperature field  $\nabla T_0$  is due to the acoustic field (friction losses in viscous boundary layers or heating in the piezo-electric material) then it will depend on the acoustic energy density squared  $\mathbf{f}_{\text{ac}} \propto E_{\text{ac}}^2$ , this will create a transition from boundary- to bulk-driven streaming at a certain acoustic energy density. For this it is necessary to use the iterative solver in Section 2.10.

The inhomogeneous acoustic body force has a fundamentally different origin than the boundary driven streaming and traditional bulk-driven Eckart streaming. Both the

boundary-driven and Eckart streaming are driven from viscous losses in the acoustic wave either in the boundary layer or in the bulk, during this process energy is transformed into both a mechanical streaming flow and into heat energy. The inhomogeneous acoustic body force is created due to the acoustic wave scattering, not on a surface but on a gradient, therefore heat is not created and it is non-dissipative. Because it arises due to scattering of the acoustic wave it has similarities to the acoustic radiation force, they both have a compressibility term linked to the potential energy density  $E_{\text{pot}}$  and a density term linked to the kinetic energy density  $E_{\text{kin}}$ .

## 4.2 Trapping glass capillary

This section is based on the modeling of example II in Ref. [1] enclosed in Section 7.1. A glass capillary tube is a widely used acoustofluidic device which consist of a fluid channel ( $2 \times 0.2$  mm) in a thin glass capillary (wall thickness of  $140 \mu\text{m}$ ). It is used to create an acoustic trap by gluing a thin piezoelectric transducer on the glass capillary that creates a localized acoustic field in the fluid in the region just above the piezoelectric transducer. The device has been studied experimentally [61] and numerically [44], and used commercially by AcouSort AB [62]. These acoustic trapping glass capillaries exhibits a very characteristic streaming pattern with four streaming rolls in the horizontal plane of the capillary, this was observed experimentally by B. Hammarström, T. Laurell and J. Nilsson (2012) [61], see Fig. 4.1.

In a glass capillary the acoustic trap is located just above the piezo-electric transducer

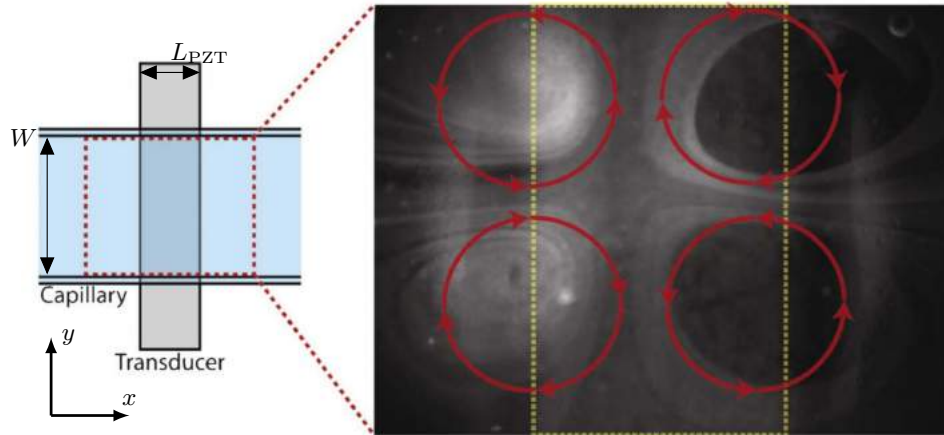


Figure 4.1: To the left a sketch of the acoustofluidic device with a glass capillary tube with width  $W = 2$  mm, height  $H = 0.2$  mm, and a piezo-electric transducer glued underneath with a width of  $L_{\text{PZT}} \sim 1$  mm. To the right the streaming field  $\mathbf{v}_2$  in the fluid domain above the PZT (indicated by dashed yellow lines). The streaming pattern is visualized using  $490$  nm particles and the red arrows indicate the rotation of the four streaming rolls. Figure from Ref. [61].

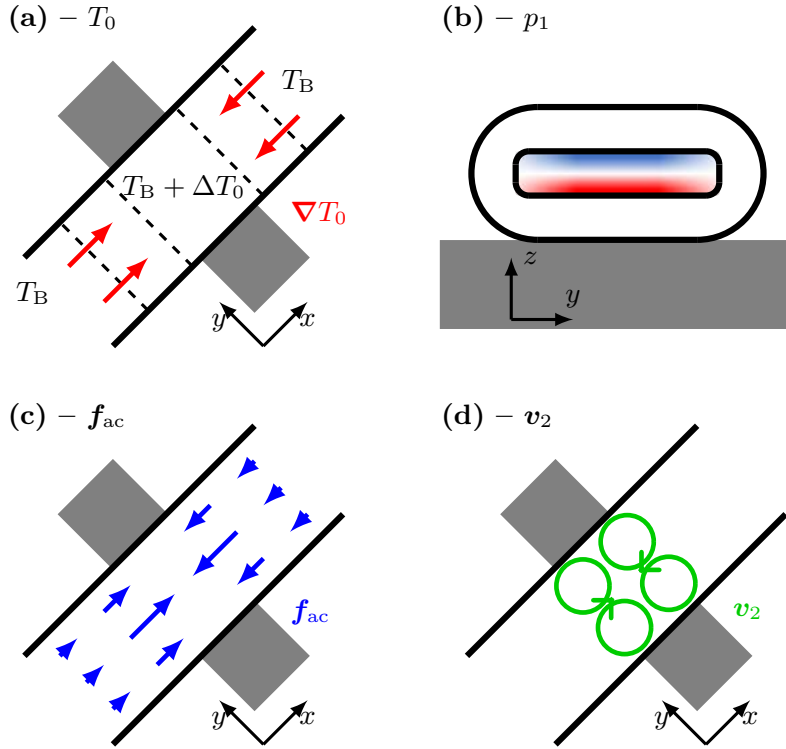


Figure 4.2: Sketch of streaming field in a glass capillary tube. (a) Contour field of the temperature field  $T_0$  and the temperature gradient  $\nabla T_0$  (red) in the  $xy$ -plane. (b) Pressure field  $p_1$  (blue to red) in  $yz$ -plane. (c) Acoustic body force  $f_{ac}$  (blue) in  $xy$ -plane. (d) Streaming pattern  $v_2$  (green) in the  $xy$ -plane.

in the center of the channel, where the acoustic wave is localized. Large particles will be trapped by the acoustic radiation force while small particles below the critical limit are dragged by the streaming in the four characteristic streaming rolls. In Ref. [61] the large particles in the trap are used as seed particles, so the streaming rolls guide the small particles into the vicinity of the big seed particles where they are trapped due to secondary acoustic radiation forces. The seed particles enables trapping of particles below the critical limit and the streaming are used to ensure that the small particles comes into the vicinity of the acoustic trap.

The characteristic streaming pattern cannot be explained by a purely mechanical model but is quite simply understood using the guideline I and II of the inhomogeneous acoustic body force from the previous section, to see the full modeling and simulations see Section 7.1. To understand the streaming pattern it is necessary to know the general shape of the temperature field and the acoustic field. The temperature field is created by heat generation in the piezo-electric transducer and therefore heats up the glass capillary above, see Fig. 4.2(a). Thus, there is a temperature gradient in the  $x$ -direction pointing towards the center at  $x = 0$ . The capillary is actuated at a frequency  $f_0$  just below 4 MHz and

actuates a standing half-wave resonance mode in the vertical direction, see Fig. 4.2(b). The acoustic pressure field will be strongest above the piezo-electric transducer, and it is stronger in the center of the channel than at the sides. With the steady temperature field  $T_0$  and the acoustic pressure field  $p_1$  we can from principle I and II in the previous section find the form of acoustic body force  $\mathbf{f}_{ac}$ : (1) from principle I it will point in the x-direction towards  $x = 0$  and (2) from principle II it will be strongest where the acoustic energy is highest at the center of the chip close to the PZT, the resulting  $\mathbf{f}_{ac}$  is sketched in Fig. 4.2(c). The acoustic body force pushes the fluid towards  $x = 0$  in the center of the chip and the fluid has to recirculate along the sides of the capillary, this creates the four streaming rolls sketched in Fig. 4.2(d).

In the modeling example II in Section 7.1 the same pattern is observed with a slight skewness in the streaming rolls because there is a small temperature gradient in the  $z$ -direction. The model in Section 7.1 is a perturbative model where the temperature field and acoustic field is modeled as generated by two different mechanism, but in reality they are coupled and both generated by the piezo-electric transducer. If the PZT was included in the model and the only actuation was the voltage on the PZT then a perturbative model would not be valid and a non-perturbative iterative solver presented in Section 2.10 is required.

### 4.3 Light absorption from an LED

This section will introduce and discuss the numerical and experimental results of Ref. [2] enclosed in Section 7.2, the paper is written in collaboration with W. Qiu, E. Corato, and P. Augustsson from Lund University and my supervisor Henrik Bruus. The experimental work was performed by the group at Lund University while the numerical modeling was performed at DTU. The work studies the effect of inhomogeneities induced by temperature gradients, and has the big advantage that the temperature field and acoustic field is controlled separately. The experimental setup is a long straight rectangular acoustofluidic glass-silicon-glass channel with a standing half wave resonance around 1 MHz, see Fig. 4.3. A LED is focused to a spot size of  $\sim 1$  mm and is absorbed in the fluid, where a dye concentration controls the absorption coefficient. The decision to use a sandwich glass-silicon-glass chip has several benefits,

- I: Experimentally it enables optical access from both above and below the chip. Therefore the heating LED and microscope can be positioned on opposite sides of the chip, see Fig. 4.3(a).
- II: The silicon wafer creates a short distance between the heat source (light absorption) and heat sink (silicon wafer) this is important because it creates a temperature gradient over the fluid channel width instead of the chip width. This enables high temperature gradients even though the temperature difference is quite small.
- III: The heating from the piezoelectric transducer is transported away by the silicon wafers so that it does not affect the temperature field in the fluid channel. As seen

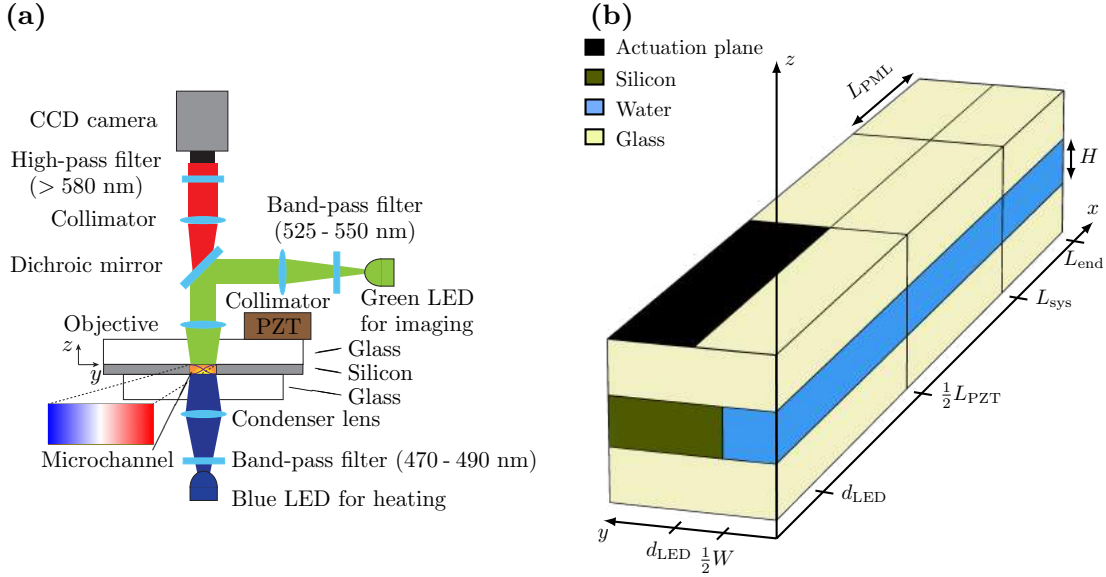


Figure 4.3: (a) Experimental setup for the measurements of streaming flow. The glass-silicon-glass chip gives the possibility to have the heat source and microscope on opposite sites of the chip. For more details of the experiment see Ref. [2]. (b) The numerical model with symmetry planes at  $x = 0$  and  $y = 0$ . The model contains a fluid domain (blue) of width  $\frac{1}{2}W$  and height  $H$ , glass (beige), silicon (dark green) and an actuation region (black). A PML region  $L_{\text{sys}} < x < L_{\text{end}}$  is used to dampen the wave to mimic an infinite long channel and a Gaussian light beam is modeled with center at  $x = y = 0$  and characteristic width  $d_{\text{LED}} = 650 \mu\text{m}$ . Figures adapted from Ref. [2].

in Fig. 4.3(a) the piezo-electric transducer (PZT) is located asymmetrically off center to enable optical access from both the top and the bottom. For more details on the experimental setup see the paper enclosed in Section 7.2.

The simulation uses the effective thermoviscous perturbative model introduced in Chapter 2 and in the paper enclosed in Section 7.1. The numerical model can be seen in Fig. 4.3(b), the model consists of a fluid domain (blue) of width  $\frac{1}{2}W$  and height  $H$ , a glass domain (beige), a silicon domain (dark green) and an actuation surface (black), symmetry planes to enable only modelling a quarter of the channel, and a perfectly matched layer (PML) to mimic an infinite long channel, see Fig. 4.3(b). For further details on the implementation of the numerical model see the supplementary material for Ref. [2] enclosed in Section 7.2

The LED spot is modeled as a Gaussian light beam [63] with the intensity given as,

$$I_{\text{LED}}(x, y, z) = \frac{2P_{\text{LED}}}{\pi w^2(z)} \exp \left[ -\frac{2(x^2 + y^2)}{w^2(z)} - \alpha z \right]. \quad (4.3)$$

Where the  $P_{\text{LED}}$  is the total LED power,  $\alpha$  is the absorption coefficient in the fluid and

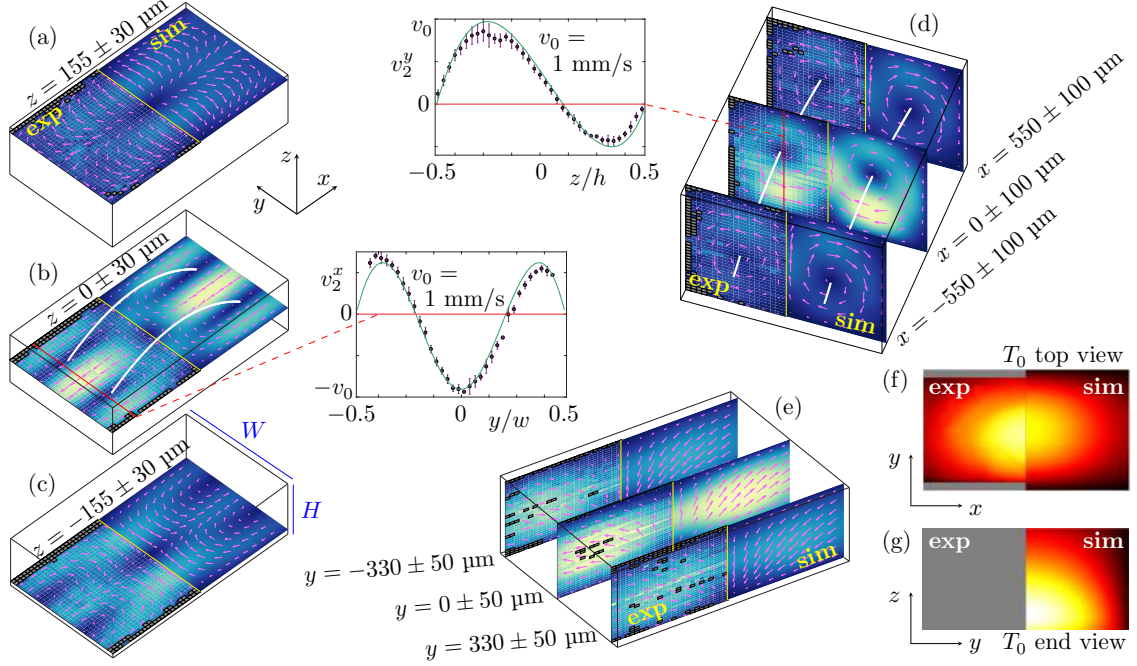


Figure 4.4: (a)-(e) The measured (left half) and simulated (right half) streaming patterns for  $\Delta T_0 = 3.71$  K across the channel width  $W$ , observed in different planes  $x$ - $y$  horizontally,  $x$ - $z$  vertically, and  $y$ - $z$  vertically. The vector plot (magenta) in a plane is the in-plane velocity and the color plot is the magnitude from 0 (dark blue) to  $1042 \mu\text{m s}^{-1}$  (yellow). The simulation is with  $E_{ac} = 23 \text{ J/m}^3$ . The curved white lines in (b) and (d) represent the centerlines of the two counter-rotating 3D cylindrical streaming flow rolls. The two line-plots show the measured (purple) and the simulated (green)  $x$  (or  $y$ ) component  $v_2^x$  (or  $v_2^y$ ) of the velocity along the red lines. (f) Color plot from  $25.0 \text{ }^\circ\text{C}$  (black) to  $30.1 \text{ }^\circ\text{C}$  (white) of the measured and simulated temperature  $T_0$  in the horizontal  $x$ - $y$  plane at  $z = 0$ . (g)  $T_0$  as in panel (f) but for the vertical  $y$ - $z$  plane at  $x = 0$ , and only the simulation results are shown. Figure from Ref. [2].

$w(z)$  is the width of the Gaussian beam at height  $z$  for a focalized beam given as,

$$w(z) = w_0 \sqrt{1 + \left( \frac{\lambda z}{\pi w_0^2} \right)^2}, \quad (4.4)$$

where  $w_0$  is the width at the focal plane  $z = 0$  and  $\lambda$  is the wavelength of the light. The local heat absorption at a position  $(x, y, z)$  is given as  $P(x, y, z) = \alpha I_{\text{LED}}(x, y, z)$ . For the LED spot in the experiment  $w_0^2 \gg \lambda H$  so the width of the beam is approximately constant through the entire chip  $w(z) \approx w_0$ .

The resulting temperature field is shown in Fig. 4.4(f-g), with the simulated temperature field to the right and the experimental measured temperature field to the left. The pressure field  $p_1$  is a half-wave standing wave resonance in the width direction with a

pressure node in the center at  $y = 0$  and pressure anti-nodes at  $y = \pm \frac{1}{2}W$ . The resulting force field will be strongest at the pressure anti-nodes at the bottom of the channel at the position of the LED spot (largest temperature gradient) and point towards the center of the channel  $y = 0$ . This creates a 3D-streaming flow shown in Fig. 4.4 with experimental data on the left and simulations on the right. The resulting 3D-streaming rolls from the top ( $xy$ -plane) appear as four horizontal streaming rolls Fig. 4.4(a-c) and in the cross-sectional  $yz$ -plane as two big streaming rolls Fig. 4.4(d). As a 3D streaming pattern it is two streaming rolls in each side of the channel that rotates around a curved centerline (white). This appears as four streaming rolls in  $xy$ -plane because the white centerline crosses the  $xy$ -plane.

In the investigated channel at  $\Delta T_0 = 5.1$  K the streaming is completely dominated by the acoustic body force and it is well known that for  $\Delta T_0 = 0$  K it is dominated by boundary-driven streaming, in Fig. 4.5 the shift from boundary- to bulk-driven streaming is investigated. Fig. 4.5(a) shows the streaming pattern in the  $yz$ -plane at  $x = 0$  for six different LED powers and thereby six different  $\Delta T_0$ , with both experimental (left) and simulation data (right). There is a good agreement both for the boundary driven streaming and during the transition to bulk-driven streaming. The transition is quantified by two parameters the maximum velocity in the  $z$ - direction  $\max(v_2^z)$  and the geometrical parameter  $\Delta$  which denotes the distance from the top of the channel to the center of the top streaming rolls, see Fig. 4.5(b). Maybe a bit surprisingly the bulk-driven streaming is dominant down to temperature increases of 170 mK. This demonstrates how powerful the inhomogeneous acoustic body force can be, in this system the acoustic energy density is kept constant, and the inhomogeneous acoustic body force is able to drive a streaming flow with an amplitude almost two magnitudes larger than the boundary-driven streaming.

In the modeling of the streaming flow we had two free parameters 1) the width of the

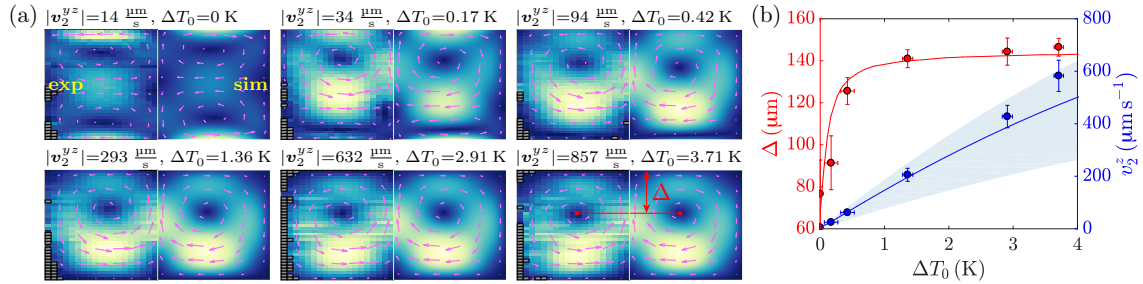


Figure 4.5: (a) Measured (left half) and simulated (right half) in-plane streaming velocity  $v_2^{yz}$  (magenta vectors) and its magnitude  $|v_2^{yz}|$  from 0 (dark blue) to its maximum (yellow) in the vertical  $y$ - $z$  plane for six temperature differences  $\Delta T_0$  across the channel. Simulations are performed with the energy density  $E_{ac}$  for which  $|v_2^{yz}|$  matches the experimental one under each  $\Delta T_0$ . (b) Dependence of the vortex size  $\Delta$  (red) and the velocity in the  $z$ -direction  $|v_2^z|$  (blue) on  $\Delta T_0$ . Simulated  $\Delta$  is indicated by a red solid line. Light blue region shows the simulated  $|v_2^z|$  under  $E_{ac}$  from 9.24 Pa (lower bound) to 23 Pa (upper bound) with a reference (solid blue line) obtained at  $E_{ac} = 18$  Pa. Figure from Ref. [2].



LED spot this is determined by the temperature field in Fig. 4.4(f) and 2) the acoustic energy density which is determined by the absolute streaming velocity. Since this is a perturbative model the acoustic energy density does not alter the streaming pattern but only the absolute streaming velocity. The change in streaming pattern is solely controlled by the temperature field. The great match between the experimental and simulation results can be attributed the following factors:

- I: The ability of our collaborators at Lund University to create a very clean experiment. This is necessary when the simulations are based on symmetry planes assuming clean symmetries in the experimental setup.
- II: Because the temperature gradients are very localized the only requirement for the acoustic field is that it is well behaved at the LED spot and not globally in the entire chip. This means that the streaming is less sensitive to the formation of hot-spots and other irregularities in the acoustic field.
- III: The fact that the temperature field and acoustic field is decoupled allows to examine the effect of each. This enables control experiments and simulations of the streaming flow with only acoustics or temperature fields. This ensures a good calibration and reduces the amount of free parameters in the experiment.

The research done in Ref. [2] was a great demonstration of the importance of temperature gradients for streaming in acoustofluidics and an experimental validation of the thermoviscous model developed in Section 7.1. It also indicated the need for a non-perturbative model since the high streaming velocities pushes the Péclet number above 1, such that convection due to the streaming field  $\mathbf{v}_2$  cannot be neglected.

## 4.4 Streaming due to heating in the viscous boundary layers

This section discusses the research presented in Section 7.4, the research is done in collaboration with Wei Qiu from Lund University who has done the experimental work. This section differs from the previous two because it investigates the effect of internal heating due to friction in the viscous boundary layers instead of external heating from light absorption or a heating piezo-electric transducer. To study the effect of internal heating the perturbative model cannot be used and it is necessary to use the non-perturbative model based on separation of time-scales presented in Section 2.10.

To study the effect of frictional heating we select a chip design based on two principles, first the distance from the heat generation to heat sink should be as short as possible (gives large gradients even for low temperature differences) and secondly the chip design should be asymmetric. The asymmetry ensures that there is a rotation in the inhomogeneous acoustic body-force field which is necessary to induce streaming. Therefore a rectangular channel in a silicon chip with a glass lid is used. The silicon works as a heat sink and the glass lid induces an up/down asymmetry in the system. It is a long channel with a long piezo-electric transducer therefore the resulting acoustic and streaming fields will be weakly dependent on the  $x$ -coordinate, we therefore model it as a 2D system showed in

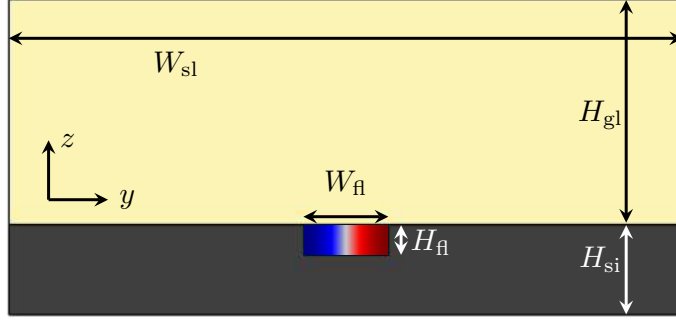


Figure 4.6: Silicon chip with a glass lid with a fluid channel of width  $W_{fl} = 375 \mu\text{m}$  and height  $H_{fl} = 135 \mu\text{m}$ . The silicon chip has height  $H_{si} = 0.4 \text{ mm}$  and width  $W_{sl} = 3 \text{ mm}$  with a glass lid of thickness  $H_{gl} = 1 \text{ mm}$ . The a half-wave resonance in the simulation is located at  $f = 1.91 \text{ MHz}$ . Figure from Ref. [4].

Fig. 4.6. The chip has a fluid channel of width  $W_{fl} = 375 \mu\text{m}$  and height  $H_{fl} = 135 \mu\text{m}$  in a silicon chip with height  $H_{si}$  and width  $W_{sl}$  and a glass lid of thickness  $H_{gl}$ . The chip has a half-wave resonance at  $f = 1.91 \text{ MHz}$  in the simulations. It is a standard chip design that is used by various groups to separate or up-concentrate particles [64–66], and has four boundary driven Rayleigh streaming rolls in the perturbative regime at low acoustic energy density.

The motivation for this study is to investigate nonlinear effects due to the inhomogeneous acoustic body force. The nonlinear effects arises because the boundary driven streaming and bulk driven streaming depends differently on the acoustic energy density  $E_{ac}$  in the system. The boundary driven streaming is linear with the acoustic energy density  $E_{ac}$  while the bulk driven streaming depends on the acoustic energy density squared  $E_{ac}^2$ . This is clear since the temperature gradient  $\nabla T_0$  is linear with  $E_{ac}$  and the body force is given as Eq. (4.2)

$$\mathbf{f}_{ac}^d = - \left[ a_{\rho}^T E_{kin} + a_{\kappa_s}^T E_{pot} \right] \alpha_{p,0} \nabla T_0 \quad (4.5)$$

Therefore, at some acoustic energy density there will be a transition from boundary to bulk driven streaming. The transition is showed in Fig. 4.7(a-d) which shows the streaming field at four different  $E_{ac}$  with simulation results to left and experimental results to the right. There is no experimental results for the highest acoustic energy density this is due to the streaming velocity being too high for the experimental setup. The transition from boundary- to bulk driven streaming occurs at  $E_{ac} \approx 500 \text{ J/m}^3$ . The transition is quantified in Fig. 4.7(e) by the maximum streaming velocity  $v_0^{\max}$  and the geometrical quantity  $\Delta_v$  which denotes the distance from the bottom of the channel to the height with the highest velocity in the  $y$ -direction (see white bar in Fig. 4.7(a-d)). Fig. 4.7(e) shows good agreement between the simulation (lines) and experimental data throughout the transition, this demonstrates that the non-perturbative iterative theory of Section 7.3 captures the nonlinear transition from boundary to bulk-driven streaming.

The temperature field  $T_0$  generated by the friction in the viscous boundary layers are

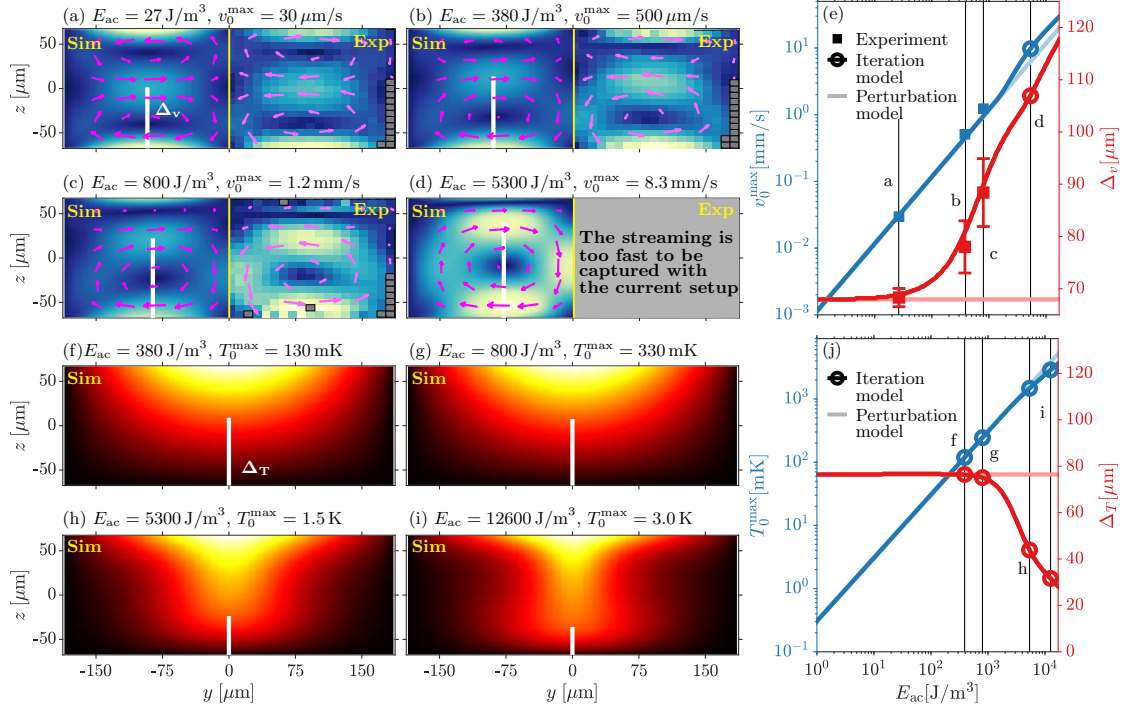


Figure 4.7: (a)-(d) Vector plot (magenta) of the streaming velocity with its magnitude as a color plot from 0 (blue) to  $v_0^{\max}$  (yellow) at four different acoustic energy densities  $E_{ac}$ . Simulations results are to the left and experimental measurements to the right. The quantity  $\Delta_v$  is shown as a white bar and denotes the distance from the bottom to the maximum horizontal velocity toward the center of the channel. (e) Line plots of the maximum streaming velocity  $v_0^{\max}$  (blue) and  $\Delta_v$  (red) as a function of the  $E_{ac}$ , with experimental data as square markers. The experimental error on the acoustic energy density and maximum streaming velocity is within the square markers. The light blue and light red lines denotes the simulation results using a perturbative model. (f)-(i) color plot of the simulated temperature field at four acoustic energy densities from 0 (black) to  $T_0^{\max}$  (white). The quantity  $\Delta_T$  is the height where the temperature is  $T_0^{\max}/2$ . (j) Line plots of  $T_0^{\max}$  and  $\Delta_T$  as function of  $E_{ac}$ . Figure from Ref. [4].

shown in Fig. 4.7(f). The temperature field is created due to the heat generation in the boundary layers at the top and bottom of the channel. At the bottom of the channel the silicon wafer transports the heat away while at the top of the channel the low heat conductivity of the glass lid results in a temperature gradient across the fluid channel. Hence the acoustic body is strongest in the top of the channel (largest temperature gradient) and at the sides (pressure anti-node) and thus creating two large streaming rolls. The temperature field looks similar to the 2D-thermal field in Section 4.3, but with the high temperature at the top of the channel instead of the bottom of the channel. Therefore the

two big streaming rolls has opposite rotation of the streaming rolls in Fig. 4.5. After the transition occurs it could be expected that the streaming velocity will continue to increase with the acoustic energy squared  $E_{ac}^2$ , but quickly the streaming reaches a velocity where convection are important for the heat transport. The influence of convection can be seen in Fig. 4.7(f-i) and is quantified by the maximum temperature increase  $T_0^{\max}$  and geometrical quantity  $\Delta_T$  which is the distance from the bottom to the position where  $T_0 = T_0^{\max}/2$  indicated by the white bars in Fig. 4.7(f-i). Due to convection the temperature field rises slower and therefore the bulk-driven streaming due not increase as  $E_{ac}^2$ .

The fact that the nonlinear effects plays an important role at an high but obtainable acoustic energy density demonstrates the importance of having a non-perturbative model and an understanding of which nonlinear effects are important in a given device. The two most important nonlinear effects to take into account are the inhomogeneous acoustic body force due to internal heating and convection due to fast streaming velocities.

## 4.5 Heating in a small volume

In this section we discuss the impact of a temperature field induced locally in a region a lot smaller than the device length-scales (acoustic wavelength  $\lambda$ , channel height  $H$  and width  $W$ ). While the earlier sections went through published work this section is unpublished work and tries to show the possibilities of working with localized heating in acoustofluidics. Before discussing a specific device or method of heating we will generally discuss the streaming occurring from a local heat source in the bulk of a fluid, where the heat source is far from solid interfaces and is a lot smaller than the acoustic wavelength. So that the pressure field at  $\mathbf{r} = (x, y, z)$  in the vicinity of the heat source  $\mathbf{r}_0 = (x_0, y_0, z_0)$  can be described as,

$$p_1(\mathbf{r}) = p_1(\mathbf{r}_0) + (\mathbf{r} - \mathbf{r}_0) \cdot \nabla p_1(\mathbf{r}_0). \quad (4.6)$$

Locating the heat source in  $\mathbf{r}_0 = \mathbf{0}$  and arranging the coordinate system so that the gradient only has an component in the  $\mathbf{e}_x$  direction the pressure is given as,

$$p_1(x) = p_1^0 + x \left( \frac{\partial p_1}{\partial x} \right)_{x=0}, \quad (4.7)$$

with  $p_1^0 = p_1(\mathbf{r} = \mathbf{0})$ . The temperature field surrounding a local heat source will be a solution to the Laplace equation,

$$0 = \nabla^2 T_0. \quad (4.8)$$

So for heating in a point or a sphere the temperature field will decay as  $1/r$  and the temperature gradient as  $1/r^2$ . That the temperature gradient decays as  $1/r^2$  and the fluid volume  $dV$  increases as  $r^2$  means that the acoustic body force integrated over volume induced by the local heating is not a local body force, but will extend into the bulk of the fluid. In Fig. 4.8 a sketch of the force and the streaming induced by it is shown, but because it is a non-local effect it is necessary to simulate a specific acoustofluidic device.

The temperature gradient  $\nabla T_0$  will be in the radial direction towards the heated area and the pressure field will be estimated as a constant gradient in the x-direction Eq. (4.7),

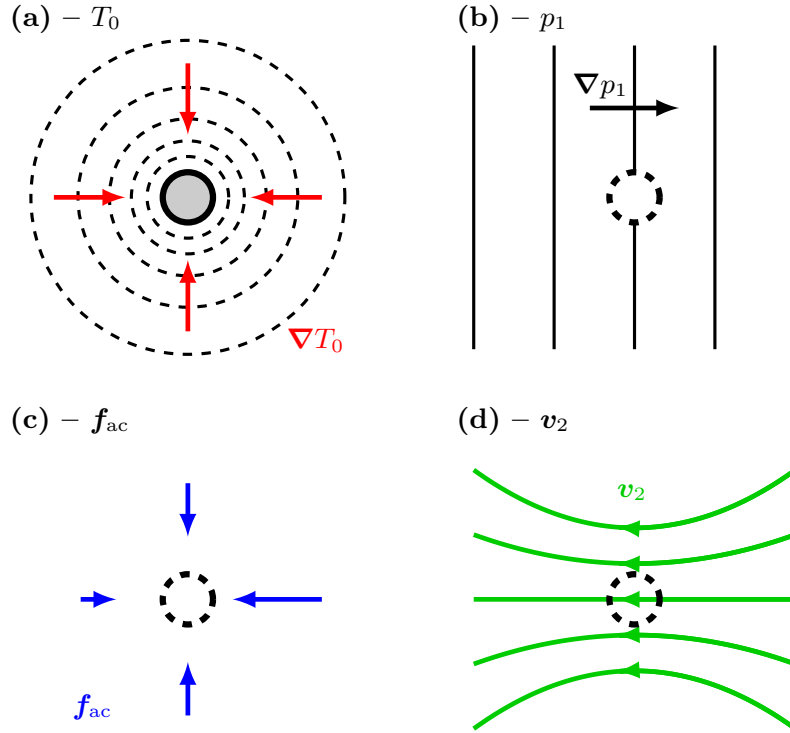


Figure 4.8: Sketch of the acoustic body force  $f_{ac}$  around a locally heated area. (a) Contour plot of the temperature field around the heated area (grey) with red arrows indicating the temperature gradient  $\nabla T_0$ . (b) Contour plot of the pressure field around the heated area (dashed circle), the pressure node  $p_1 = 0$  is to the left and anti-node to the right. (c) Vector plot of the acoustic body force  $f_{ac}$  (blue), pointing in the direction of  $\nabla T_0$  and amplitude depending on  $|p_1|^2$ . (d) The streaming field  $v_2$  (green) at the heated area, the exact streaming field depends on the geometry of the acoustofluidic device. The sketched forces and streaming flow are valid for either heating in a sphere or in a cylindrical volume with a symmetry axis out of the plane.

depicted in Fig. 4.8(a–b). The inhomogeneous acoustic body force using the principles from Section 4.1 points towards the heated area and the absolute force will be proportional to the potential energy density  $E_{pot} \propto |p_1|^2$ , thus the acoustic body force is largest on the right side of the heated area in Fig. 4.8(c). The acoustic body force depicted in Fig. 4.8(c) will create a streaming flow from right to left Fig. 4.8(d). So the streaming at the heated area will be towards the pressure node and the recirculation flow will depend on the device geometry.

If the spherical heat source is a particle absorbing light the particle would move with the streaming until reaching the pressure node. This is assuming that the drag force is dominating the particle trajectory, so either a small particle or a particle with contrast factor  $\Phi = 0$ . As a thought experiment consider a suspension of particles in a fluid with  $\Phi = 0$ , the particles has similar properties but different colors. When flowing through a

region with a blue LED the particles that absorb the blue light will heat up and create streaming, hence it could be possible to separate particles based on their color. The effect of heating particles with an LED has been studied experimentally by Dumy, Hoyos, and Aider in two articles [67, 68]. These publications study particles in an acoustic trap and what happens when they shine an LED light on them. The experiment shows that the particles when heated leaves the acoustic trap while still being in the pressure nodal plane. In Ref. [68] it is suggested that the phenomenon is due to streaming caused by the inhomogeneous acoustic body force  $\mathbf{f}_{ac}$ . This experiment and phenomenon of heated particles could be interesting to model and investigate further.

The next section will show simulations of a heated volume due to a laser beam it will heat up a cylindrical volume but demonstrates the creation of a streaming flow towards the pressure node and gives an idea of the temperature differences needed. The sketch in Fig. 4.8 is also valid for a heated cylindrical volume with the correct orientation i regards to the pressure gradient  $\nabla p_1$ .

#### 4.5.1 Heating from a laser beam

This section will study the streaming due to heating from a laser spot. The heating will be in a cylinder through the fluid channel. The acoustic body force and streaming due to heating in a thin cylinder with radius  $r$  a lot smaller than the acoustic wavelength  $\lambda$  follows the same analysis as for a sphere in Fig. 4.8. In Section 4.3 the light absorption from an LED was studied, here a focalized laser is focused to spot of radius  $d_{laser} = 10 \mu\text{m}$  is investigated. There are two main differences from the LED, first the spot size is a lot smaller than the LED spotsize of  $d_{LED} = 650 \mu\text{m}$  and secondly a lower absorption coefficient is used meaning the light beam has approximately the same light intensity throughout the fluid channel.

As a case study we investigate a rectangular fluid channel with width  $W = 375 \mu\text{m}$  and  $H = 180 \mu\text{m}$  which has a half-wave standing wave resonance at  $f = 1.90 \text{ MHz}$ , see Fig. 4.9. The 3D model has length  $L = 1 \text{ mm}$  and symmetry boundary conditions at  $x = 0$  and  $x = L$ . The laser spot is focused at  $y_0 = \frac{1}{4}W$  and  $x_0 = z_0 = 0$ . Due to the symmetry planes in the model the modeled system is an infinite long channel with infinite laser spots spaced  $2L$  from each other.  $L$  has been chosen such that the temperature and streaming field due to the laser is independent of the other laser spots. The laser spot is modeled as a focused Gaussian beam similarly to the LED spot in Section 4.3,

$$I_{laser}(x, y, z) = \frac{2P_{laser}}{\pi w^2(z)} \exp \left[ -\frac{2((x - x_0)^2 + (y - y_0)^2)}{w^2(z)} - \alpha z \right]. \quad (4.9)$$

Where the  $P_{laser}$  is the total laser power,  $\alpha$  is absorption coefficient in the fluid and  $w(z)$  is the width of the Gaussian beam at height  $z$  for a focalized beam given as,

$$w(z) = w_0 \sqrt{1 + \left( \frac{\lambda(z - z_0)}{\pi w_0^2} \right)^2}, \quad (4.10)$$

where  $x_0$ ,  $y_0$ , and  $z_0$  is the spatial focus of the laser. A red laser with wavelength  $\lambda = 670 \text{ nm}$ , power  $P_{laser} = 10 \text{ mW}$ , and a focus width of  $w_0 = 10 \mu\text{m}$  is used. The mesh shown

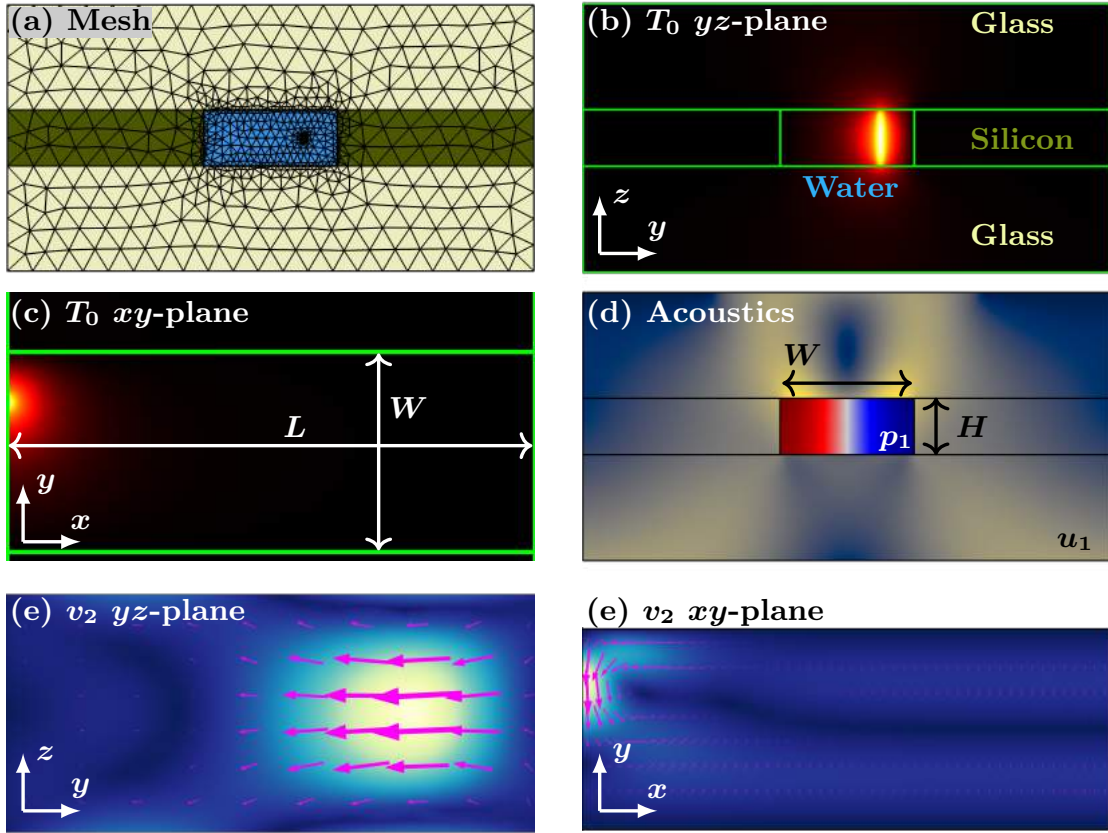


Figure 4.9: 3D model of streaming induced by heating from a laser beam. (a) 2D cross-section of the model containing fluid (blue), glass (beige), and silicon (dark green) with the mesh in the  $yz$ -plane of the model. (b) Color plot of the  $\Delta T_0 = T_0 - T_B$  in the  $yz$ -plane at  $x = 0$  from black 0 to white 1.1 K. (c) Color plot of the  $\Delta T_0$  in the  $xy$ -plane at  $z = 0$  from black 0 to white 1.1 K. (d) Color plot of the absolute displacement field  $|\mathbf{u}_1|$  in the solid and the pressure field  $p_1$  in the fluid. (e) Vector plot of the streaming field  $\mathbf{v}_2$  and its absolute value as a color plot from blue 0 to yellow 105  $\mu\text{m/s}$  in the  $yz$ -plane at an acoustic energy density of  $E_{\text{ac}} = 23.2 \text{ J/m}^3$ . (f) Same as (e) but in the  $xy$ -plane and with the same color scale.

in Fig. 4.9(a) is fine at the focal point of the laser to be able to handle the small length scale of the laser beam. The resulting temperature field  $T_0$  is shown in Fig. 4.9(b-c) for the  $yz$  and  $xy$ -planes is a cylinder of hot fluid along the path of the laser beam. It creates a temperature gradient localized close to the laser spot and restricted to one side of the fluid channel. The chip is actuated anti-symmetric at a resonance frequency of  $f_0 = 1.90 \text{ MHz}$  which results in the acoustic displacement  $\mathbf{u}_1$  and pressure field  $p_1$  shown in Fig. 4.9(d). As discussed in the previous section the average acoustic body force around a heated spot will tend to push the fluid towards the pressure node, this results in the streaming pattern shown in Fig. 4.9(e-f). The streaming pattern at the heated fluid is towards the pressure

node while the recirculation flow happens in the  $xy$ -plane. The simulations shows that a temperature increase of 1.1 K can induce a fast localized streaming flow towards the pressure node. In Fig. 4.9(f) it is shown that far away from the laser spot the streaming is the classical boundary driven Rayleigh streaming, this validates that the chosen length  $L$  is enough to ensure that the individual laser spots are independent.

## 4.6 Concluding remarks

The inhomogeneous acoustic body force induced by temperature gradients can be the cause of fast thermoacoustic streaming in acoustofluidic devices. Thermoacoustic streaming can occur in a system due to internal heating either in the piezo-electric transducer Section 4.2 or in the viscous boundary layers in the fluid Section 4.4 in these cases it is necessary to include the temperature fields to model the systems behaviour and understand the underlying physics. With the understanding of the phenomenon it opens up the possibility to use thermoacoustic streaming actively in the design of acoustofluidic devices by including heat sources as LED's or lasers. The knowledge can also be used to remove unwanted streaming for example by adding a conducting layer of silicon or metal between the piezo-electric transducer and glass capillary tube in Section 4.2.

In this work only stationary temperature fields from an LED or laser was studied, but an LED gives an excellent temporal and spatial control which could allow for use-cases where the streaming field can be turned on/off or moved in a device. This gives a design parameter such that both the acoustic and temperature field can be designed to manipulate particles in the desired manner. To model transient problems modifications has to be made to the numerical model.



## Chapter 5

# Streaming in acoustic tweezers

The chapter introduces the concept of acoustic tweezers and the unpublished work on streaming in acoustic tweezers done in collaboration with Sarah Vincent and Senior research scientist (Directeur de recherche) Jean-Louis Thomas during my three months external stay at Institut des NanoSciences de Paris (INSP) at Sorbonne University in the summer of 2021.

The research area of acoustic tweezers is new and exciting, the concept was proposed in 2013 by D. Baresch, J.L. Thomas and R. Marchiano [69] and later realised in 2016 [20]. One of the difficulties with acoustic tweezers is that most particles focus at the pressure node, so in contrast to an optical tweezer a pressure node is needed on the symmetry axis. D. Baresch, J.L. Thomas and R. Marchiano [69] proposed to use a focalised vortex beam, which has a nodal line in the center of the beam. A focalized vortex beam traps particles in the pressure node on the centerline and because it is a focalized beam it traps particles at the focal plane due to gradients in the acoustic energy density. The focalised vortex beam are able to trap particles in a fluid against gravity as demonstrated experimentally at 1 MHz in Ref. [20] with the tweezer shown in Fig. 5.1(a).

The potential of acoustic tweezers was further demonstrated by M. Baudoin et al. [27] which integrated an acoustic tweezer in a microscope setup and demonstrated the use of controlling and moving individual particles. In their setup the acoustic vortex beam is generated by an electrode pattern on a piezo-electric substrate, see Fig. 5.1(b) which is designed to ensure the correct phase of the acoustic displacement. The electrode design has enabled to go to higher frequencies demonstrated up to 47 MHz in Ref. [28].

The chapter will introduce the basic principles of an acoustic tweezer and the work of modelling the streaming which can be a limiting factor in trapping particles in an acoustic tweezer.

### 5.1 A short introduction to acoustic tweezers

First the form of the acoustic beam is presented and then from the expression of the acoustic radiation force in Eq. (2.65) it is explained why a particle can be trapped in a focalized acoustic vortex beam (FAVB). A FAVB can be decomposed with spherical Bessel

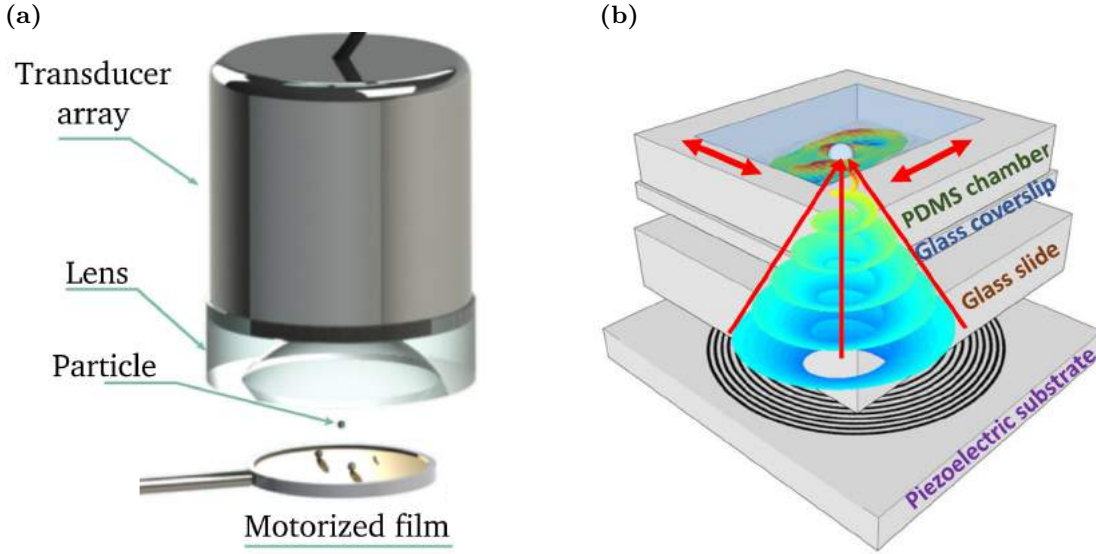


Figure 5.1: Two different designs of acoustic tweezers that both generate a focalized acoustic vortex beam. (a) Design by D. Baresch, JL. Thomas, and R. Marchiano [20] for an acoustic tweezer at 1 MHz. The acoustic wave is generated by an array of transducers where the phase can be controlled to ensure the formation of an acoustic vortex beam. (b) Design by M. Baudoin et al [27] used for a 47 Mhz acoustic tweezer. Here the electrode pattern on the piezoelectric substrate ensures the correct phase. This tweezer is designed to be integrated in a microscope setup.

functions and described by their beam shape coefficients (BSC)  $A_n^m$  [69, 70],

$$p_1(r, 0, \phi, t) = p_a \sum_{n=0}^{\infty} \sum_{m=-n}^n A_n^m j_n(kr) Y_n^m(0, \phi) e^{-i\omega t}. \quad (5.1)$$

Where  $j_n(kr)$  are the spherical Bessel functions,  $Y_n^m$  are the spherical harmonics, and  $p_a$  is the characteristic amplitude of the acoustic field. For a focalized acoustic vortex beam the beam shape coefficients are given as [70],

$$A_n^m = N_n^m (kr_0)^2 h_n^{(1)}(kr_0) (-1)^{n+m} \int_{\cos\alpha_0}^1 P_n^m(x) dx \quad (5.2)$$

Where  $r_0$  is the distance from the transducer to the vortex,  $h_n^{(1)}(kr_0)$  is the spherical Hankel function of the first kind,  $\alpha_0$  is the aperture angle of the transducer,  $P_n^m(x)$  is the associated Legendre polynomial and  $N_n^m$  is given as,

$$N_n^m = \sqrt{\frac{(2n+1)(n-m)!}{4\pi(n+m)!}} \quad (5.3)$$

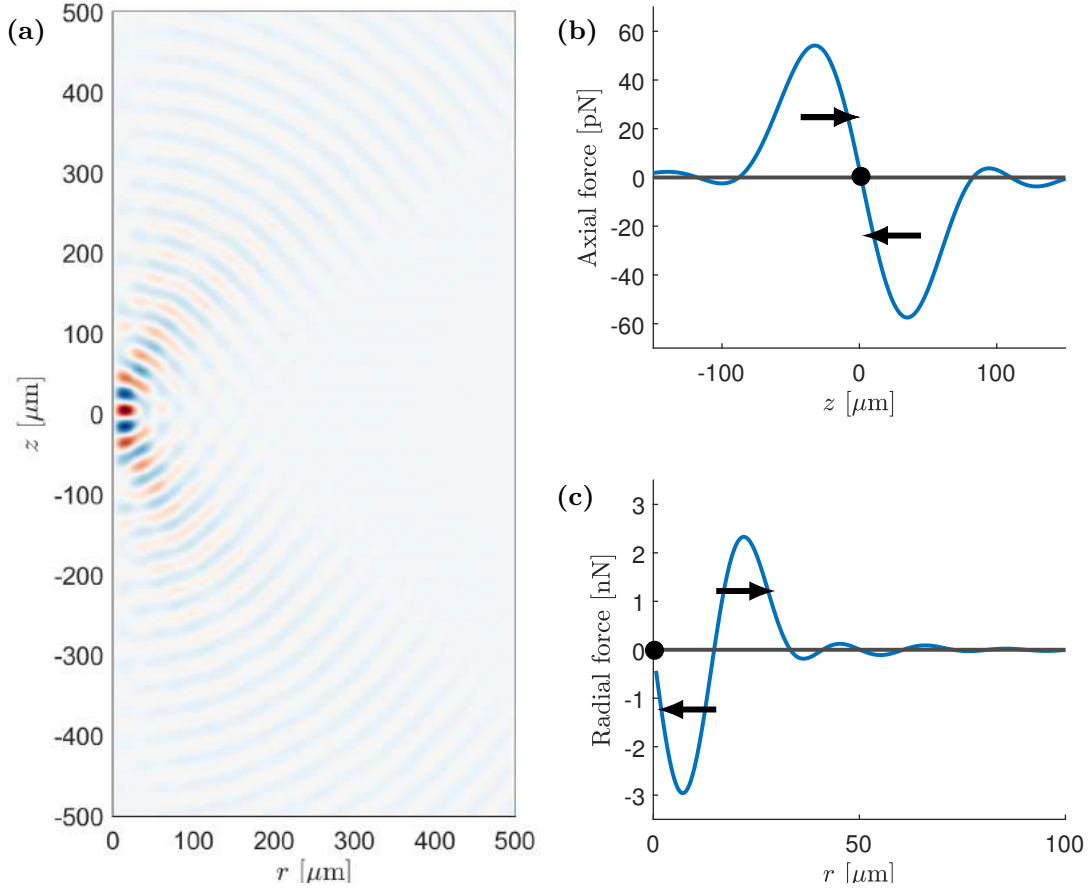


Figure 5.2: (a) Colorplot of the real part of the acoustic pressure field  $p_1$  at a time  $t$  in the  $rz$ -plane from blue  $-1.0$  to red  $1.0$  MPa of a focalized acoustic vortex beam with  $f_0 = 47$  MHz,  $r_0 = 2.4$  mm, and  $\alpha_0 = 54.8$ . (b) The axial force  $F_z^{\text{rad}}$  along the  $z$ -axis at  $r = 0$  on a polystyrene sphere with radius  $a = 5$   $\mu\text{m}$ . (c) The radial force  $F_r^{\text{rad}}$  at  $z = 0$  on a polystyrene sphere with radius  $a = 5$   $\mu\text{m}$ .

For a vortex beam with the parameters  $r_0 = 2.4$  mm,  $\alpha_0 = 54.8$  and  $f_0 = 47$  MHz the real part of the pressure field is shown in Fig. 5.2(a) in the  $rz$ -plane, the focus of the tweezer are in  $r = z = 0$ .

To have a trap in three directions a trapping force is needed in the radial direction  $r$  and axial direction  $z$ . In Fig. 5.2(b-c) the axial and radial radiation forces are shown for a polystyrene particle with radius  $a = 5$   $\mu\text{m}$ . In the radial direction, Fig. 5.2(c), there is a strong trapping force towards the pressure node at  $r = 0$ . The force in the  $z$ -direction is notably weaker, see Fig. 5.2(b), the axial force in the pressure node stems from the dipole term in the radiation force (Eq. (2.72)) which for a particle with a higher density than the fluid points towards the region with the highest acoustic kinetic energy density at  $z = 0$ . The streaming from an acoustic tweezer will flow away from the actuation region along the  $z$ -axis, if the streaming is too fast the drag force can be stronger than the axial trapping

strength of the acoustic tweezer. An acoustic tweezer is a travelling wave, but it has some similarities with a standing acoustic wave. It has a constant pressure node in  $r = 0$  and it has a clear patterning of the time averaged acoustic potential and kinetic energy density. Therefore the radiation force calculated with the Gorkov potential Eq. (2.66) gives the same radiation force as the more general Eq. (2.65) even though the Gorkov potential is not valid for travelling acoustic waves.

It should be noted that a particle with radius of  $a = 5 \mu\text{m}$  and an acoustic field with wavelength  $\lambda \approx 30 \mu\text{m}$  does not satisfy the condition of the small particle limit under which the expression for the acoustic radiation in Section 2.9 is valid. But it is not in the scope of this work to investigate the acoustic radiation force on large particles. Thus, the forces in Fig. 5.2(b–c) are only to get an estimate of the magnitude and shape of the acoustic trap, and an understanding of how a focused acoustic vortex beam can create a trap both in the radial and axial direction.

## 5.2 Analytical streaming flow

The acoustic vortex beam creates an acoustic body force  $\mathbf{f}_{\text{ac}}$  in the fluid that generates bulk-driven Eckart streaming,

$$\mathbf{f}_{\text{ac}} = \frac{\Gamma\omega}{c_0^2} \langle \mathbf{v}_1 p_1 \rangle \quad (5.4)$$

where  $\mathbf{v}_1 = -i \frac{1-i\Gamma}{\omega\rho_0} \nabla p_1$ , in this section we neglect thermoviscous effects. The acoustic body force is axis-symmetric even though the acoustic pressure field has a angular dependency.

We will consider an incompressible fluid, where the flow  $\mathbf{v}$  is driven by an acoustic body force  $\mathbf{f}$ . The incompressibility is ensured by the continuity equation,

$$0 = \nabla \cdot \mathbf{v}, \quad (5.5)$$

and the Navier-Stokes equation governs the steady streaming flow driven by the force  $\mathbf{f}$ ,

$$0 = \nabla \cdot (-p\mathbf{I} + \eta\nabla^2\mathbf{v} - \rho\mathbf{v}\mathbf{v}) + \mathbf{f}. \quad (5.6)$$

The equation contains the stress tensor  $\boldsymbol{\sigma} = -p\mathbf{I} + \eta\nabla^2\mathbf{v}$  and the convective term  $\rho\mathbf{v}\mathbf{v}$ . The Navier–Stokes equation has two main regimes one where the viscous term  $\eta\nabla^2\mathbf{v}$  dominates and one where the convective term  $\rho\mathbf{v}\mathbf{v}$  dominates, described by the Reynolds number,

$$\text{Re} = \frac{\rho|\mathbf{v}|d}{\eta} \quad (5.7)$$

where  $|\mathbf{v}|$  is the characteristic velocity in the system and  $d$  the characteristic length scale. When  $\text{Re} \gg 1$  the inertial term is dominant and for  $\text{Re} \ll 1$  the viscous term dominates.

### 5.2.1 Stokeslet: Low Reynolds number in free space

In free space and at low Reynolds number  $\text{Re} \ll 1$  the fluid flow from a point force can be found analytically by using the so-called Stokeslet solutions [71]. In the viscous regime

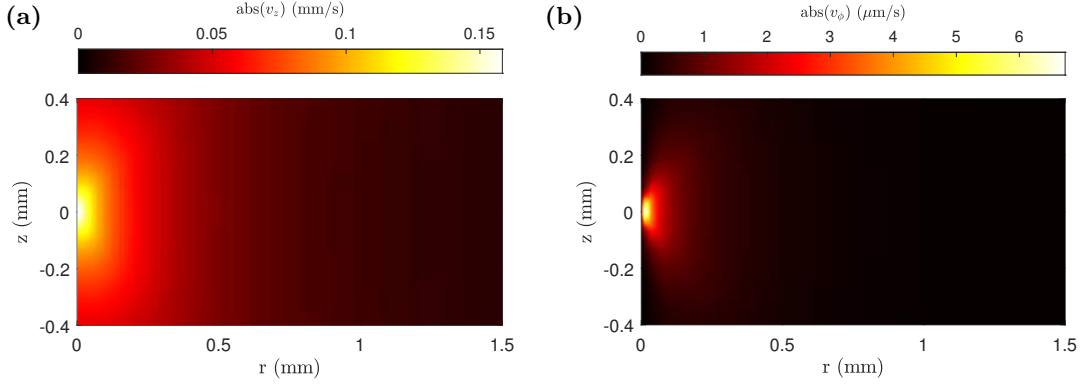


Figure 5.3: Streaming flow calculated with Stokeslet functions for an acoustic vortex beam with  $\max(p_1) = 1$  MPa. (a) Color plot of the magnitude of  $v_z$  the direction is  $-\mathbf{e}_z$  since the tweezer is located at  $z = r_0$ . (b) Color plot of the magnitude of  $v_\phi$

at low Reynolds number  $\text{Re} \ll 1$  the inertial term can be neglected in the Navier–Stokes equation and the streaming caused by a point force at  $\mathbf{r} = \mathbf{0}$  is governed by the equations,

$$0 = \nabla \cdot \mathbf{v} \quad (5.8a)$$

$$0 = -\nabla \cdot (p\mathbf{I} + \eta\nabla^2\mathbf{v}) + \mathbf{f}\delta(\mathbf{r}). \quad (5.8b)$$

$$|\mathbf{v}|, p \rightarrow 0 \quad \text{as} \quad |\mathbf{r}| \rightarrow \infty \quad (5.8c)$$

Where  $\delta(\mathbf{r})$  is the Dirac delta function which is one at  $\mathbf{r} = \mathbf{0}$  and zero everywhere else and the streaming and pressure field goes to zero as  $\mathbf{r}$  goes to infinity.

The Green functions solving this set of equation is a Stokeslet [71] and for the velocity field is given as,

$$\mathbf{v} = \frac{\mathbf{f}}{8\pi\eta} \cdot \left( \frac{\mathbf{I}}{|\mathbf{r}|} + \frac{\mathbf{r}\mathbf{r}}{|\mathbf{r}|^3} \right), \quad (5.9)$$

and the solution to the pressure field  $p$  as,

$$p = \frac{\mathbf{f} \cdot \mathbf{r}}{4\pi|\mathbf{r}|^3}. \quad (5.10)$$

It can be noted that the pressure field decreases as  $r^{-2}$  while the streaming field is decaying as  $r^{-1}$ . The Stokeslet is the solution to a linear equation (only valid at  $\text{Re} \ll 1$ ) therefore the streaming field from  $n$  point forces can be found by summing up the individual streaming fields,

$$\mathbf{v} = \sum_{i=1}^n \frac{\mathbf{f}_i}{8\pi\eta} \cdot \left( \frac{\mathbf{I}}{|\mathbf{r}|} + \frac{\mathbf{r}\mathbf{r}}{|\mathbf{r}|^3} \right) \quad (5.11)$$

The bulk-driven streaming from an acoustic tweezer in free-space can be solved semi-analytically by the Stokeslet functions when the Reynolds number is low  $\text{Re} \ll 1$ . This

is done by discretizing the acoustic body force  $\mathbf{f}_{ac}$  (5.4) on a grid with a point force  $\mathbf{F} = \mathbf{f}_{ac}dV$  in each grid point. Then the streaming can be calculated by summing up over all grid points, see Eq. (5.11). To remain in the low Reynolds number limit we have a maximum acoustic pressure of  $\max(p_1) = 0.1$  MPa in the acoustic tweezer. The resulting  $z$ -velocity field is shown in Fig. 5.3(a) and  $\phi$ -component in Fig. 5.3(b). The  $z$  component is 30 times larger than the  $\phi$ -component, so the velocity is mainly in the  $z$ -direction away from the actuation region. Secondly we can see that the  $z$ -component decreases with  $r^{-1}$  as suggested by the Stokeslet. While the  $\phi$  velocity decreases as  $r^{-2}$  because the acoustic body force  $\mathbf{f}_{ac}$  points in opposite direction for  $\phi = 0$  and  $\phi = \pi$ , hereby creating a dipole term that decreases faster.

### 5.3 Simulations of streaming in acoustic tweezers

An axis-symmetric FEM solver has been setup in COMSOL to numerically calculate the streaming field. The acoustic body force will be calculated analytically from Eq. (5.4) and Eq. (5.1) and only the stationary streaming and pressure field are simulated governed by Eqs. (5.5) and (5.6). Because the force field is axis-symmetric the simulations will be using the axis-symmetric weak formulation derived in Section 3.1.2.

In the simulations we import the acoustic body force  $\mathbf{f}_{ac}$  derived from the analytical pressure field Eqs. (5.1) and (5.4), the first consideration surrounds the volume size where the acoustic body force  $\mathbf{f}_{ac}$  is important. Intuitively one could imagine that the force is only important in the vicinity of the focal point because of the nature of the pressure field, see Fig. 5.2(a). But as the pressure field decreases away from the focal point the volume increases. How big a volume that is important is studied numerically by the model presented in Fig. 5.4(a) which contains a large fluid domain (blue) and a cylindrical volume

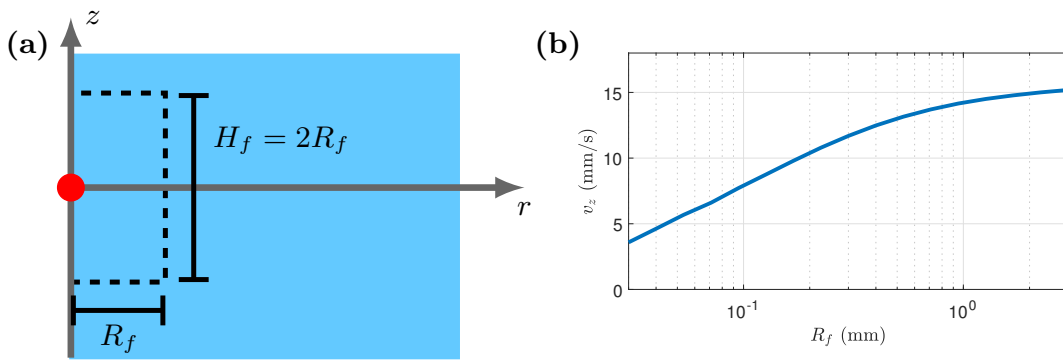


Figure 5.4: (a) Sketch of the numerical model containing a large fluid volume (blue) with the acoustic body force active in the dashed cylinder with radius  $R_f$  and height  $H_f = 2R_f$  and an acoustic tweezer focused at  $r = z = 0$  at the red dot. (b) Line plot of the maximum streaming velocity in the  $z$ -direction from an acoustic tweezer with  $\max(p_1) = 1$  MPa as a function of the radius  $R_f$ .

of radius  $R_f$  and height  $H_f = 2R_f$  where the acoustic body force is active.  $R_f$  is varied from  $30 \mu\text{m}$  (the wavelength of the tweezer) to  $3 \text{ mm}$ . The maximum streaming velocity does not become constant in this interval for  $p_1 = 1 \text{ MPa}$ , so it is important to use a large volume for the acoustic body force. The working distance of the tweezer is  $2.4 \text{ mm}$  so above the tweezer the box should not be bigger than  $2.4 \text{ mm}$ . In the rest of this section the volume included is  $R_f = 2 \text{ mm}$  and  $H_f = 2R_f = 4 \text{ mm}$ .

### 5.3.1 Matching the Stokeslet solution

To validate the axis-symmetrical numerical model the streaming in free-space and at low Reynolds number is modelled and compared to the analytical streaming field obtained in Section 5.2.1. To mimic a field in free space with no boundaries a big cylinder with radius  $R = 40 \text{ mm}$  and height  $H = 40 \text{ mm}$  with the acoustic tweezer in the center is simulated. The solution is compared to the Stokeslet solution by line plots. In Fig. 5.5(a) the  $v_z$  is showed along  $r$  at  $z = 0$ , Fig. 5.5(b) shows  $v_z$  along  $z$  at  $r = 0$ , and Fig. 5.5(c) shows  $v_\phi$  along  $r$  at  $z = 0$ , all plots shows agreement between the analytical and numerical solution.

In Fig. 5.5 close to the vortex the  $v_\phi$  decreases as  $1/r$  because the vortex appears as an infinite long cylinder, further away it appears as a point source and the velocity decreases as  $1/r^2$ . Similar for the  $v_z$  component that decreases as  $1/r$  far away from the vortex. Because it is at low Reynolds number the streaming is symmetric and the maximum streaming velocity is located at the focal point  $z = 0$ .

### 5.3.2 High Reynolds number streaming

At high Reynolds numbers (not a lot smaller than 1) the inertial term  $\rho\mathbf{v}\mathbf{v}$  in Eq. (5.6) is important and cannot be neglected. The inclusion of the term creates non-linear effects so that the streaming can no longer be seen as a summation of streaming flows from different point sources. The Reynolds number in the fluid is given by the characteristic length scale

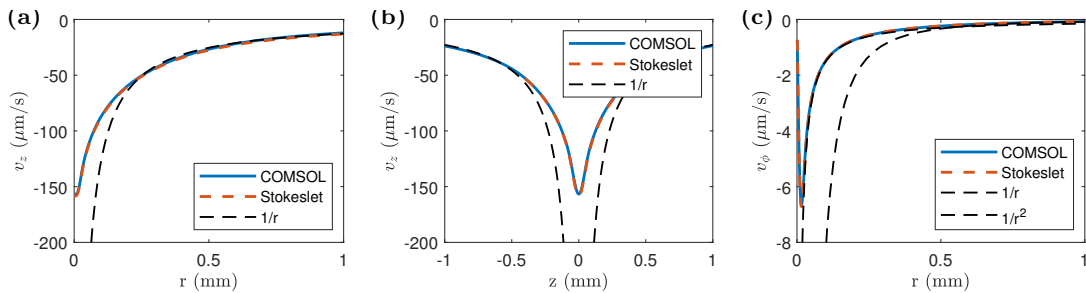


Figure 5.5: Comparison of the analytical and numerical streaming field at low Reynolds number. (a) Line plot of  $v_z$  as a function of  $r$  at  $z = 0$ . The function  $1/r$  is plotted to show the decrease far away from the vortex matches the theoretical prediction. (b) Line plot of  $v_z$  as a function of  $z$  at  $r = 0$ . (c) Line plot of  $v_\phi$  as a function of  $r$  at  $z = 0$ . The function  $1/r$  and  $1/r^2$  are plotted to show the decrease away from the vortex matches the theoretical prediction.

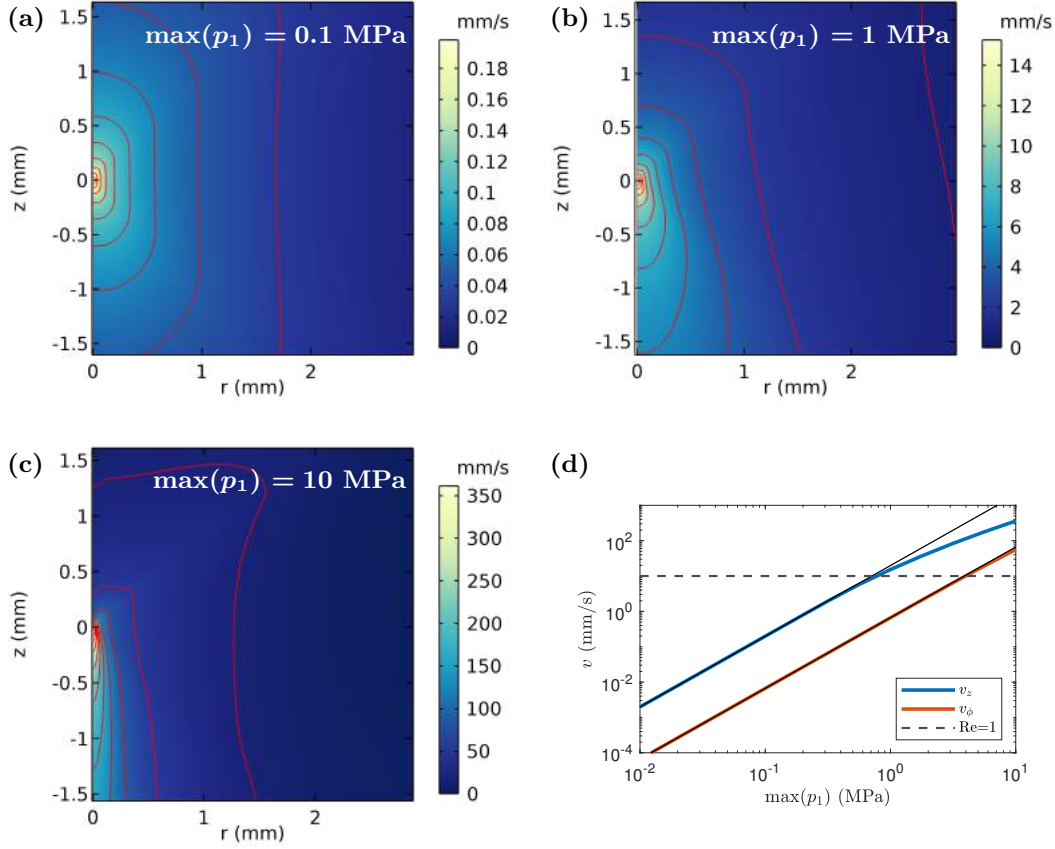


Figure 5.6: Streaming for an acoustic tweezer in free field (no nearby boundaries,  $R = 40$  mm) at high Reynolds number. (a – c) Color plot of the absolute streaming velocity  $|\mathbf{v}|$  at three different pressure amplitudes  $\max(p_1) = 0.1, 1,$  and  $10$  MPa. (d) The maximum absolute streaming velocity  $\max(|\mathbf{v}|)$  as a function of  $\max(p_1)$ .

in the system, the length of the acoustic vortex  $d \sim 100$   $\mu\text{m}$ . So the Reynolds number is 1 when the streaming velocity is,

$$|\mathbf{v}| = \frac{\eta}{\rho d} \approx 10 \text{ mm/s} \quad (5.12)$$

In Fig. 5.6(a–c) the streaming field for the maximum acoustic pressures  $\max(p_1) = 0.1, 1,$  and  $10$  MPa are shown. And in Fig. 5.6(d) the maximum streaming velocity in the  $z$ - and  $\phi$ -component are shown as a function of the maximum acoustic pressure in the acoustic tweezer  $\max(p_1)$ . In the regime where the inertial term is negligible  $\text{Re} \ll 1$  the streaming are proportional to  $|p_1|^2$  while at higher Reynolds numbers the streaming velocity increases slower as  $\propto |p_1|$ .

There are two important things to notice about the streaming at high Reynolds number (1) the pattern changes and the position of the maximum streaming is moved below



the acoustic vortex and (2) the maximum streaming does not increase proportional to  $\max(p_1)^2$ . The last point means that the streaming increases slower than the acoustic radiation force which are beneficial in an acoustic vortex beam trying to use the radiation force to trap particles.

### 5.3.3 Impact of nearby boundaries

In many applications there will be boundaries close to the acoustic tweezer. If used in a microscope setup [27, 28] the fluid domain would be thin but wide so the nearby boundaries would be in the  $z$ -direction. To investigate the dependency of the streaming velocity on the height  $H$  of the fluid chamber, the numerical model in Fig. 5.7(a) with 2D-axis-symmetric fluid domain of radius  $R = 10$  mm and a variable height  $H$  is used. For an acoustic tweezer focused at  $(0,0)$  (the red dot) with a maximum acoustic pressure  $\max(p_1) = 1$  MPa, the maximum streaming velocity in the  $z$ -direction is shown as a function of the height  $H$  in Fig. 5.7(b). At  $H > 10$  mm the streaming velocity is constant, but for thinner fluid domains the velocity is proportional to  $\log(H)$ .

When reducing the height of the fluid domain there is two mechanisms lowering the streaming velocity, (1) the nearby boundaries reduces the streaming because it forces a smaller fluid flow roll and thereby increases the viscous losses, and (2) the volume of the force field is reduced which was shown in Fig. 5.4 to reduce the streaming velocity. Since the first reason is related with the viscous term in the Navier-Stokes equation the height dependency of the streaming velocity is different for high Reynolds number streaming. For applications in thin fluid domains as Refs. [27, 28] the streaming velocity is reduced significantly, and thus extends the frequency range where the streaming is not a concern for the trapping strength of the acoustic tweezers.

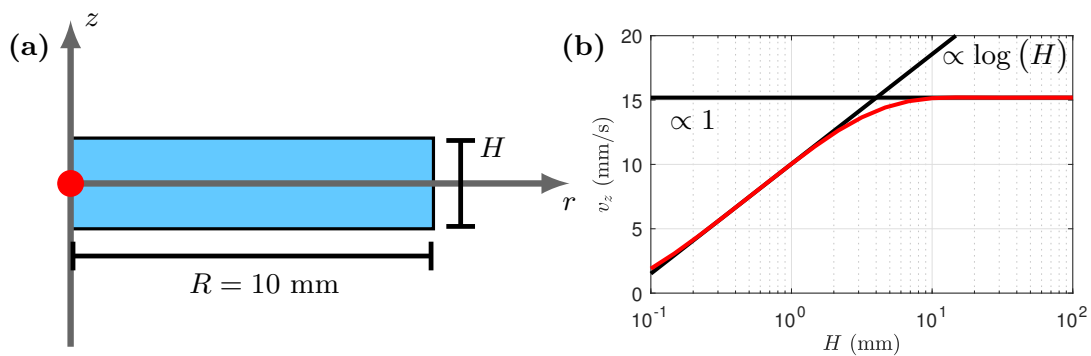


Figure 5.7: (a) Sketch of the numerical model of an 2D-axisymmetric fluid domain (blue) of height  $H$  and radius  $R = 10$  mm with an acoustic tweezer focused at the red dot at  $(0,0)$ . (b) Line plot of the maximum streaming velocity for  $\max(p_1) = 1$  MPa as a function of the height  $H$  of the fluid domain. At  $H > 10$  mm the velocity is constant but at smaller  $H$  the velocity is proportional to  $\log(H)$ .

### 5.3.4 Drag forces from streaming

The main reason for studying the streaming in an acoustic tweezer is the drag force on the particles that can destroy the acoustic trap in the axial direction. The drag force on a stationary particle is given as Eq. (2.67),

$$\mathbf{F}^{\text{drag}} = 6\pi\eta a\mathbf{v}. \quad (5.13)$$

For a particle with radius  $a = 5 \mu\text{m}$  in water and a streaming velocity of  $|\mathbf{v}| = 16 \text{ mm/s}$ , the force is  $F^{\text{drag}} \approx 130 \text{ pN}$  which is comparable to the axial trapping strength of  $60 \text{ pN}$  in Fig. 5.2(b). It should be noted that the forces shown in Fig. 5.2 are using the small particle assumption and therefore not accurate for large particles. But the size of the drag force shows that the streaming is important to consider when designing tweezers at high frequencies. The axial trapping strength could be improved by having a larger mass density difference of the fluid and particle. As an example a glass particle has a  $f_2$  that is approximately ten times larger than a polystyrene particle and thus result in a ten times stronger axial acoustic radiation force.

## 5.4 Concluding remarks

As the driving frequency of acoustic tweezers increases to enable capturing smaller particles the attenuation in the bulk increases and therefore creates faster streaming flows. A fast streaming flow sets a requirement to the axial trapping force of the tweezers that need to be able to hold the particle against the drag force from the streaming flow. For systems integrated in microscope setup [27, 28] where the tweezer is primarily trapping in 2D the streaming does not impose a problem since the radial trap is significantly stronger than the axial trap and secondly the nearby boundaries would significantly reduce the acoustic streaming.

A natural next step in the investigation of streaming in acoustic tweezers would be to vary the frequency and determine at which frequencies it would be possible to axially trap a particle against streaming and gravity with no nearby boundaries. To make a proper assessment of the axial trap it is necessary to model the radiation force accurately for a large particle.

## Chapter 6

# Spatial localization of acoustic fields

A major application in acoustofluidics is acoustic traps that can localize and trap particles in a microfluidic device. This can either be a single trapping side in a glass capillary tube (see Section 4.2) [44, 61] or a grid of multiple trapping sides [72, 73]. An acoustic trap is an efficient way to trap particles using the acoustic radiation force and are efficient for large particles that are not affected by streaming. Most particles ( $\rho_p > \rho_{\text{water}}$  and  $\kappa_p > \kappa_{\text{water}}$ ) suspended in a fluid will be focused at the pressure node and trapped at the location with the highest acoustic energy density  $E_{\text{ac}}$ . In most single node or multi-node traps there are a resonance in the height of the channel with either one [61, 73] or multiple pressure nodes [74]. The particles will be trapped vertically in the pressure node and then horizontally trapped at the position with highest acoustic energy density  $E_{\text{ac}}$ . Importantly the trapping strength in the plane is given by the gradient of  $E_{\text{ac}}$ , see Eq. (2.72). In the glass capillary traps the spacial localization in the plane is determined by the thin piezo-electric transducer, so that the acoustic field is localized above the transducer. In this section we will investigate two other techniques to localize an acoustic field in a microfluidic system.

We investigate systems that are actuated with a half-wave resonance in the height of the fluid chamber and which in-plane length scales are a lot larger than the height, which is the case for either a wide rectangular glass capillary [44] or two microscope slides separated by spacers [73]. In the next sections two methods to locally change the resonance will be investigated: first by changing the sound speed of the fluid by heating up local regions of the chip and secondly by making the chip thicker in local regions and thereby changing the resonance frequency at the specific spots.

### 6.1 Temperature controlled localization

This section takes advantage of the temperature dependency of the fluid parameters to create two domains with different sound speeds. In the studies on streaming due to temperature gradients in Chapter 4 the temperature dependency of the density and the

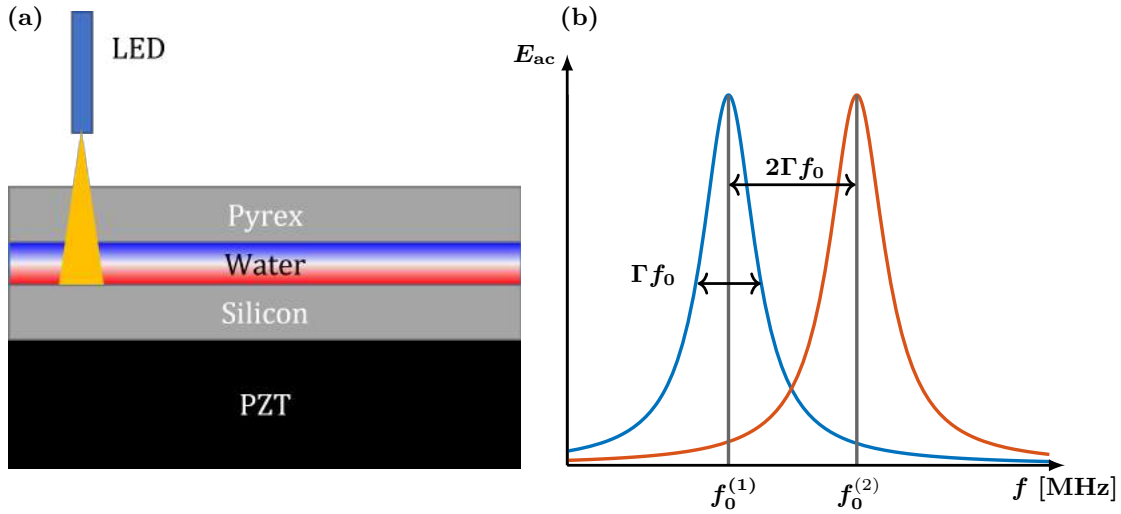


Figure 6.1: Idea of temperature induced cavity. (a) Sketch of temperature induced cavity consisting of a piezo-electric transducer (PZT), fluid domain, and a solid chip (Pyrex/silicon) and an LED spot that is absorbed in the fluid. (b) Line plot of two resonance curves with resonance frequencies  $f_0^{(1)}$  and  $f_0^{(2)}$  and full width half maximum of  $\Gamma f_0$ .

compressibility were important, for the resonance frequency it is the temperature dependency of the sound speed  $c^2 = (\rho\kappa)^{-1}$  that is important. The temperature gradients will be created by light absorption as in Section 4.3. A simplified sketch of the model is shown in Fig. 6.1(a) with a half-wave acoustic resonance in the height and an LED spot. The heating of the fluid needs to change the sound speed enough to separate the resonance peak in the cold and hot part of the fluid, see Fig. 6.1(b). For the design in Fig. 6.1 to work it is important to have sharp temperature gradients and therefore it is important that there is a short distance between the location of the heat absorption and the heat sink. This can either be done by using a silicon chip or a thin glass capillary with a heat sink attached.

The next section will analytically investigate when an acoustic wave can be localized and study temperature induced localization of acoustic waves in oil and water. Oil and water are fundamentally different in this regard because the sound speed in water increases with temperature and for oil the sound speed decreases with temperature.

### 6.1.1 Analytical considerations

We will analytically consider how an acoustic wave will behave in a system with two fluid domains with two different sound speeds  $c_0$  and thereby wave-number  $k_0 = \omega/c_0$ . Let's consider an axis-symmetrical system ( $\mathbf{r} = r\mathbf{e}_r + \phi\mathbf{e}_\phi + z\mathbf{e}_z$ ) with two domains: domain A with  $|\mathbf{r}| < r_0$  has wave-number  $k_A$  and domain B with  $|\mathbf{r}| > r_0$  has wave-number  $k_B$ . Assuming that separation of variables is valid, and that the system is axis-symmetric, then

$p_1(\mathbf{r}) = R(r)Z(z)\Phi(\phi) = R(r)Z(z)$ . In this case the Helmholtz equation separates into an equation for  $R(r)$  and  $Z(z)$ , as

$$0 = \left( \partial_r^2 + \frac{1}{r} \partial_r \right) R(r) + k_r^2 R(r) \quad (6.1a)$$

$$0 = \partial_z^2 Z(z) + k_z^2 Z(z), \quad \text{with } k_0^2 = k_z^2 + k_r^2 \quad (6.1b)$$

where  $k_0 = k_A$  in domain A and  $k_0 = k_B$  in domain B. At the interface  $r = r_0$  between domain A and B we have the condition  $Z_A(z) = Z_B(z) \rightarrow k_{z,A} = k_{z,B} = k_z$ . For a frequency which in domain A gives a half-wave height resonance, so  $k_z \approx k_A$  and  $k_{r,A} \approx 0$  in domain A. Then in domain B  $k_B^2 = k_{r,B} + k_{z,B}^2$  with  $k_{z,B}^2 = k_{z,A}^2 \approx k_A^2$ , hence we get  $k_{r,B}^2 \approx k_B^2 - k_A^2$ . So we have two cases:

- $k_B^2 > k_A^2$  – then  $k_{r,B}$  is real and the solution to Eq. (6.1) is a combination of cylindrical Bessel functions. This gives a set of planar resonance modes in domain B and the acoustic field is not localized to domain A.
- $k_B^2 < k_A^2$  – then  $k_{r,B}$  is imaginary and the acoustic field is evanescent in domain B. Thus, the acoustic field is localized in domain A.

Hence, it is possible to localize acoustic fields in the domain with the highest wave number  $k_0$  and therefore the lowest sound speed  $c$ . For water the sound speed increases with temperature, thus it is possible to localize an acoustic wave in a cold domain and not in a hot domain. This is slightly inconvenient since it is easier to heat than to cool a fluid. For most other fluids, oil and alcohols, the sound speed decreases with temperature and the acoustic field can be localized in the hot domain.

To understand what temperature difference is needed to separate the resonance peaks in the two domains, see Fig. 6.1(b), we consider the width of the resonance peaks. The two resonance frequencies should be separated by more than the width of the resonance peak. The resonance peaks are described by a Lorentzian,

$$E_{ac}(f) = \frac{A}{\left( \frac{f}{f_0} - 1 \right)^2 + \left( \frac{1}{2Q} \right)^2} \quad (6.2)$$

with the maximum at  $f = f_0$  with  $E_{ac}(f_0) = 4AQ^2$ . The acoustic energy is half the maximum at  $f = f_0(1 \pm \frac{1}{2Q})$ , so the full width half maximum (FWHM) is  $f_0Q^{-1}$ . A typical acoustofluidic device has a quality factor of  $Q = 100 - 500$ , so the resonance frequency needs to shift  $\sim 1\%$  which means that the sound speed needs to shift  $\sim 1\%$ . For water this corresponds to a  $\sim 5$  K temperature difference between the two domains.

### 6.1.2 Thermal cavity in oil

In oil the sound speed decreases with temperature therefore a heated region has a lower sound speed and therefore an acoustic field can be localized at the spot where light is absorbed. Thus, it is possible to create an acoustic trap controlled by an LED spot, which

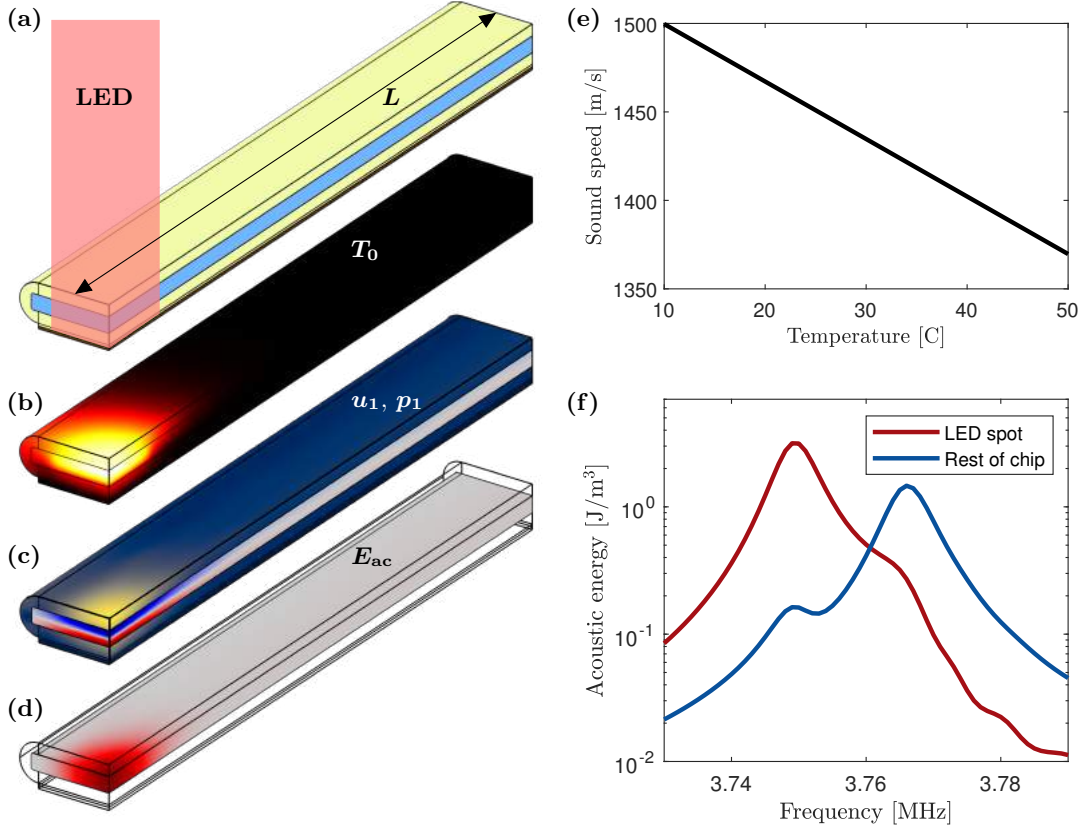


Figure 6.2: Simulation results for a thermal cavity in oil. (a) Model of glass capillary tube with oil (blue) and length  $L = 8$  mm with an LED. (b) Color plot of the steady temperature field  $T_0$  from black 15 to white 20.5 °C. (c) Color plot of the pressure field  $p_1$  in the fluid from blue  $-0.25$  to red 0.25 MPa and the absolute displacement field  $|u_1|$  in the solid from blue 0 to yellow 1.7 nm at the resonance frequency  $f = 3.75$  MHz. (d) Color plot of the acoustic energy density  $E_{ac}$  from 0 to 9.5 J/m<sup>3</sup> at  $f = 3.75$  MHz. (e) Line plot of the sound speed in oil as a function of temperature [75]. (f) Line plot of the acoustic resonance peaks at the LED spot (red) and in the rest of the chip (blue).

can be turned on/off and moved by the LED. To demonstrate this we model a device with a rapeseed oil with the following temperature dependent density  $\rho_0$  and sound speed  $c_0$  at  $T_B = 20$  °C [75],

$$\begin{aligned} \rho_0(T_0) &= \rho_0(T_B) + \left. \frac{\partial \rho}{\partial T} \right|_{T_B} (T_0 - T_B), & \rho_0(T_B) &= 927 \text{ kg/m}^3, & \left. \frac{\partial \rho}{\partial T} \right|_{T_B} &= -0.65 \text{ kg/m}^3 \text{ K}^{-1} \\ c_0(T_0) &= c_0(T_B) + \left. \frac{\partial c}{\partial T} \right|_{T_B} (T_0 - T_B), & c_0(T_B) &= 1467 \text{ m/s}, & \left. \frac{\partial c}{\partial T} \right|_{T_B} &= -3.25 \text{ m/s K}^{-1}. \end{aligned} \quad (6.3)$$

We model a glass capillary actuated by a large piezo-electric transducer and an LED spot, see Fig. 6.2(a). The numerical model is a glass capillary tube of length  $L = 8$  mm with

an LED spot at  $x = 0$ , the model is actuated on the bottom along the entire channel, and has symmetry boundary conditions on the planes  $x = 0$ ,  $x = L$ , and  $y = 0$ . Hence, the model is simulating an infinitely long glass capillary tube with an infinite number of LED spots spaced with a distance  $2L$ . The resulting temperature field  $T_0$  from the light absorption is shown in Fig. 6.2(b) and has a temperature increase of 5.5 K. The temperature field is localized at the LED spot due to the copper foil beneath the glass capillary functioning as a heat sink. In Fig. 6.2(f) the resonance peaks of the heated domain (red) and cold domain (blue) are shown, the two resonance peaks are clearly separated and the resonance has shifted  $\sim 0.5\%$ . The resonance in the heated region is at  $f = 3.75$  MHz and here the acoustic energy density in the heated spot is more than a magnitude larger than the rest of the chip. The acoustic pressure field  $p_1$  and absolute displacement field  $|\mathbf{u}_1|$  for  $f = 3.75$  MHz is shown in Fig. 6.2(c) and the corresponding acoustic energy density in Fig. 6.2(d). Both of these show an acoustic field that is localized at the spot of the LED and are evanescent in the cold fluid domain.

In the simulation the  $Q$ -factor is relatively high which results in thin resonance peaks and therefore a clear separation of the peaks even when the resonance peaks are only separated by a 0.5 % of the resonance frequency. In a real experiment you might have broader resonance peaks requiring a larger resonance shift.

### 6.1.3 Thermal cavity in water

Most acoustofluidic applications are with water or an aqueous solution, thus for research and future practical applications it is of interest to work with water as the fluid. Using water presents one fundamental problem compared to oil, that the sound speed increases with temperature. Therefore a domain with cold fluid is suitable for localizing an acoustic field. It is difficult to cool a fluid in a specific spot, therefore we pursue the idea of localizing an acoustic wave by making a surrounding barrier of hot fluid and localize an acoustic field in the center. This will require a ring formed light profile in this work we do not consider how such a light source is generated but assume that we have a light profile that is constant between for  $R_1 < r < R_2$  and otherwise zero.

First we study a glass capillary with a setup similar to the thermal cavity in oil in the previous section, the capillary is modelled with length  $L$ , a light source centered at  $x = y = 0$ , and symmetry boundary conditions at  $x = 0$ ,  $x = L$ , and  $y = 0$ , see Fig. 6.3(a). The light source will have  $R_1 = 0.75$  mm and  $R_2 = 1.5$  mm and focused at  $x = y = 0$ , the resulting temperature field can be seen in Fig. 6.3(b) with a temperature difference of 11 K. Although the trapping zone in the center of the ring is warmer than the fluid outside and therefore the temperature barrier is less than 11 K. Because the fluid outside the LED spot is colder than the fluid in the center the acoustic field outside the LED spot will not be an evanescent field. Hence patterns in the acoustic field are expected in the entire chip. To ensure that the length  $L$  does not influence the resonance peaks they are shown for  $L = 6, 8, 10, 20$  mm in Fig. 6.3(f) (with the longest length presented in the darkest color). For all lengths a resonance peak for the LED spot (red) and rest of chip (blue) are separated and the resonance peak in the LED spot has the highest frequency. At the resonance in the LED spot at  $f = 3.89$  MHz the acoustic energy in the LED spot is

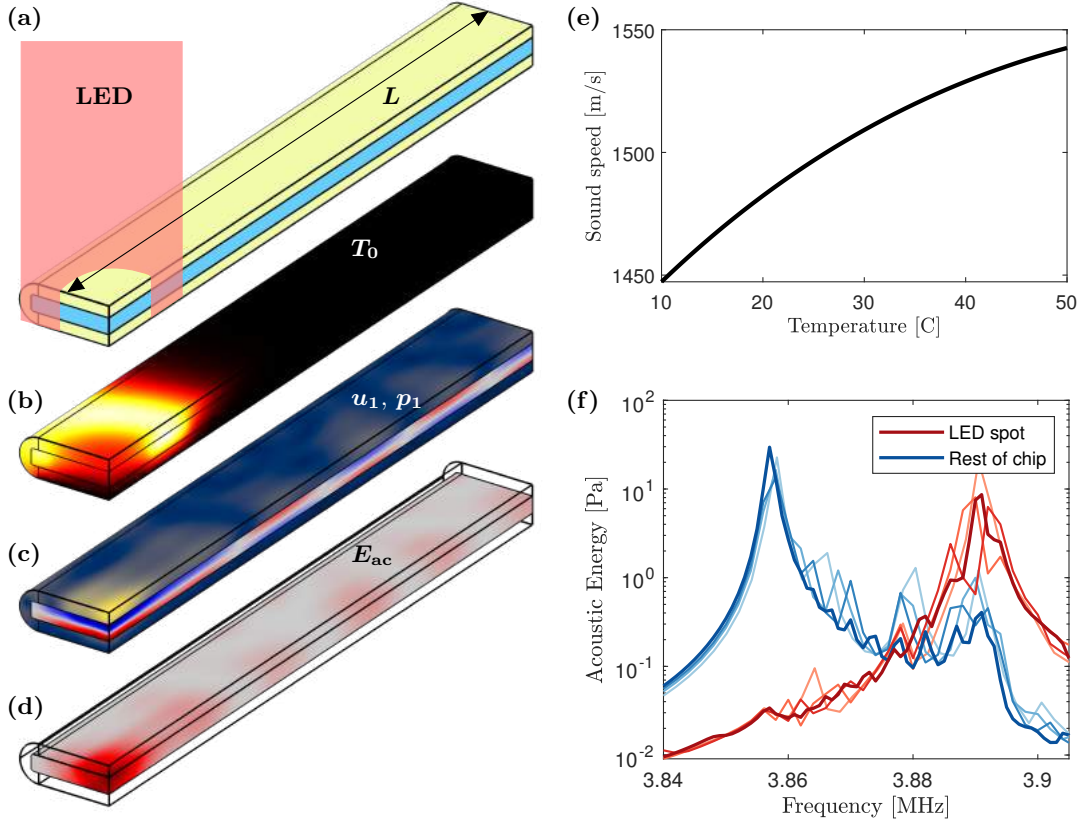


Figure 6.3: Simulation results for a thermal cavity in water. (a) Model of glass capillary with water (blue) of length  $L = 8$  mm. (b) Color plot of the steady temperature field  $T_0$  from black 24 to white 35 °C. (c) Color plot of the pressure field  $p_1$  in the fluid from blue  $-0.4$  to red 0.4 MPa and the absolute displacement field  $|u_1|$  in the solid from blue 0 to yellow 3 nm at the frequency  $f = 3.89$  MHz. (d) Color plot of the acoustic energy density  $E_{ac}$  from 0 to 28 J/m<sup>3</sup> at the frequency  $f = 3.89$  MHz. (e) Line plot of the sound speed in water as a function of temperature, from Ref. [29]. (f) Line plot of the acoustic resonance peaks in at the LED spot (red) and in the rest of the chip (blue) for four different length  $L = 6, 8, 10, 20$  mm, the darkest line corresponds to the longest chip.

a magnitude large than the rest of the chip. The acoustic field for  $f = 3.89$  MHz is shown in Fig. 6.3(c) for  $L = 8$  mm showing the resonant pattern in the cold domain of the fluid, this resonant pattern also appears in the acoustic energy density  $E_{ac}$  in Fig. 6.3(d). With the ring shaped light profile it is possible to localize and acoustic field in the center of the ring, but because the sound speed is lower outside the ring, there is a planar resonant mode in the rest of the chip.

To further study the possibilities of the thermal cavity in water we continue with a cylindrical fluid domain with a large radius  $R$  and shallow height  $H$ , see Fig. 6.4(a). Our system is a fluid domain of radius  $R = 10$  mm and height  $H = 0.4$  mm in a silicon disc



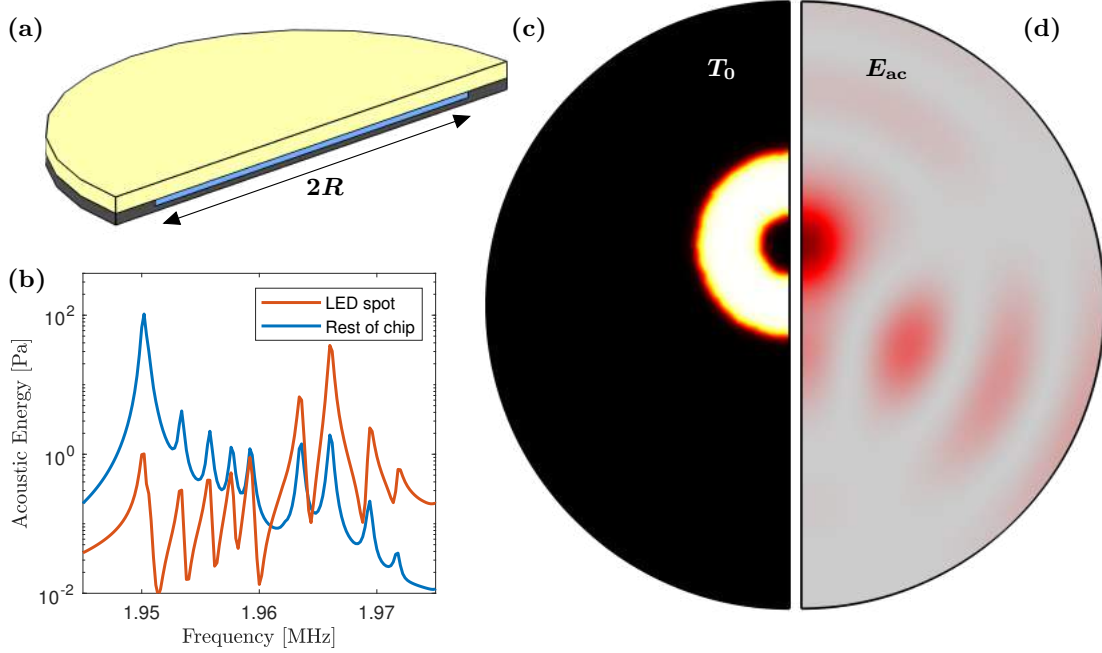


Figure 6.4: Simulation results for a thermal cavity in water. (a) Model of a fluid domain in a silicon disc with a glass lid with radius  $R = 10$  mm and height  $H = 0.4$  mm of the fluid domain. (b) Line plot of the acoustic resonance peaks in at the LED spot (red) and in the rest of the chip (blue) (c) Color plot of the steady temperature field  $T_0$  from black 15 to white 22.5 °C. (d) Color plot of the acoustic energy density  $E_{ac}$  from grey 0 to red 50 J/m<sup>3</sup> at the frequency  $f = 1.966$  MHz.

with a glass lid. The silicon functions as a heat sink due to its large heat conductivity. The system will be actuated at a frequency  $f$  on the bottom and a ring shaped LED spot will be absorbed in the fluid creating a temperature difference  $\Delta T_0$ . The spot is located off center and we take advantage of one symmetry plane to only simulate half the fluid domain. The light intensity is constant in the ring for  $1 \text{ mm} < r < 2 \text{ mm}$  around the center of the ring, the resulting temperature field in the center plane of the fluid is shown in Fig. 6.4(c) with a temperature increase of  $\Delta T_0 = 7.5$  K.

The acoustic energy in the center of the ring (red) and the rest of the chip (blue) is shown as a function of the frequency in Fig. 6.4(b). At the resonance at the LED spot  $f = 1.966$  MHz the acoustic energy density is more than a magnitude larger than the rest of the chip, and the corresponding acoustic energy density in the  $xy$ -plane is plotted in Fig. 6.4(d). There is a good spatial localization of the acoustic field, but as expected there is a resonant pattern outside the LED spot. If this is used as a trap it will therefore result in patterning of particles away from the LED spot.

## 6.2 Geometry controlled localization

In the previous section the resonance frequency was changed by altering the material parameters resulting in two domains with a different resonance frequency. In this section the geometry of our system are changed, the dimensions of the fluid channel is not changed, but the geometry of the glass capillary is changed. The simple idea is to glue a thin slice of glass on top of the glass capillary, see Fig. 6.5(a) and thereby locally change the resonance frequency. We are taking advantage of the fact that the resonance frequency in a glass capillary is not solely dependent on the fluid but also the surrounding solid, similar to the idea of whole-system resonances in soft polymer based systems [76]. As for the temperature induced cavity it is required to shift the resonance frequency enough to separate the two resonance peaks of the domain with a thin glass lid and the one with a thick glass lid, Fig. 6.5(b). The acoustic wave can be localized in the area with the thick glass lid, since it will have a longer wavelength and hence a lower resonance frequency.

To investigate the principle of a spatial localization in an acoustic field by altering the solid geometry we again study the glass capillary tube as an example. In the example we glue three thin glass slits on the glass capillary of thicknesses  $d = 50, 100, \text{ and } 150 \mu\text{m}$  and width of  $0.75 \text{ mm}$  placed with a gap of  $0.75 \text{ mm}$  between them as sketched in Fig. 6.6(a). We simulate a glass capillary of length  $L = 10 \text{ mm}$  with symmetry boundary conditions at  $x = 0$  and  $x = L$  so that we are mimicking a infinite long capillary with and infinite amount of glass slices placed a distance  $L$  apart.

The three different glass thicknesses gives three different resonance frequencies in the three regions marked A, B and C under the glass slits, Fig. 6.6(a), with the thickest glass slit resulting in the lowest resonance frequency. The acoustic energy density  $E_{ac}$  at the

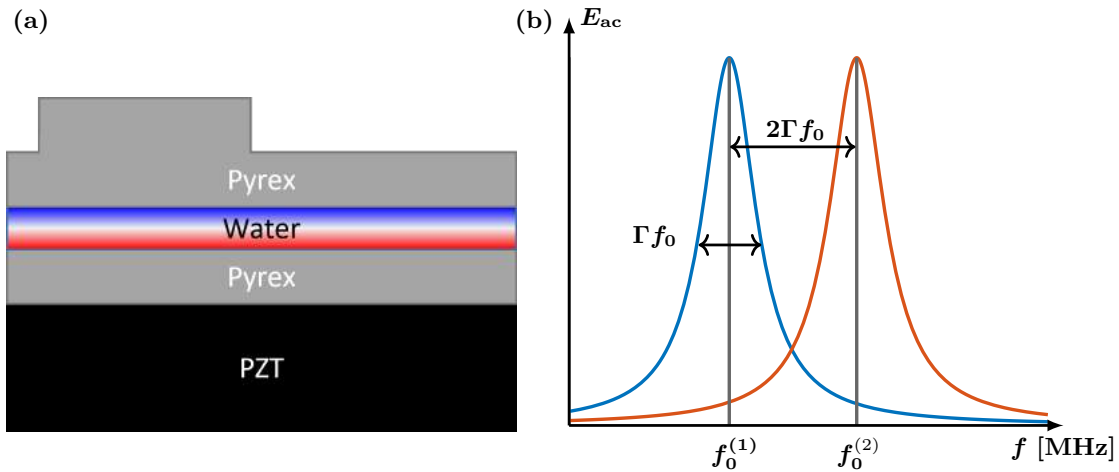


Figure 6.5: Idea of geometrically induced cavity. (a) Sketch of geometrical induced cavity consisting of a piezo-electric transducer (PZT), fluid domain, and a solid with a with a varying height. (b) Line plots of two resonance curves with resonance frequencies  $f_0^{(1)}$  and  $f_0^{(2)}$  and full width half maximum of  $\Gamma f_0$ .

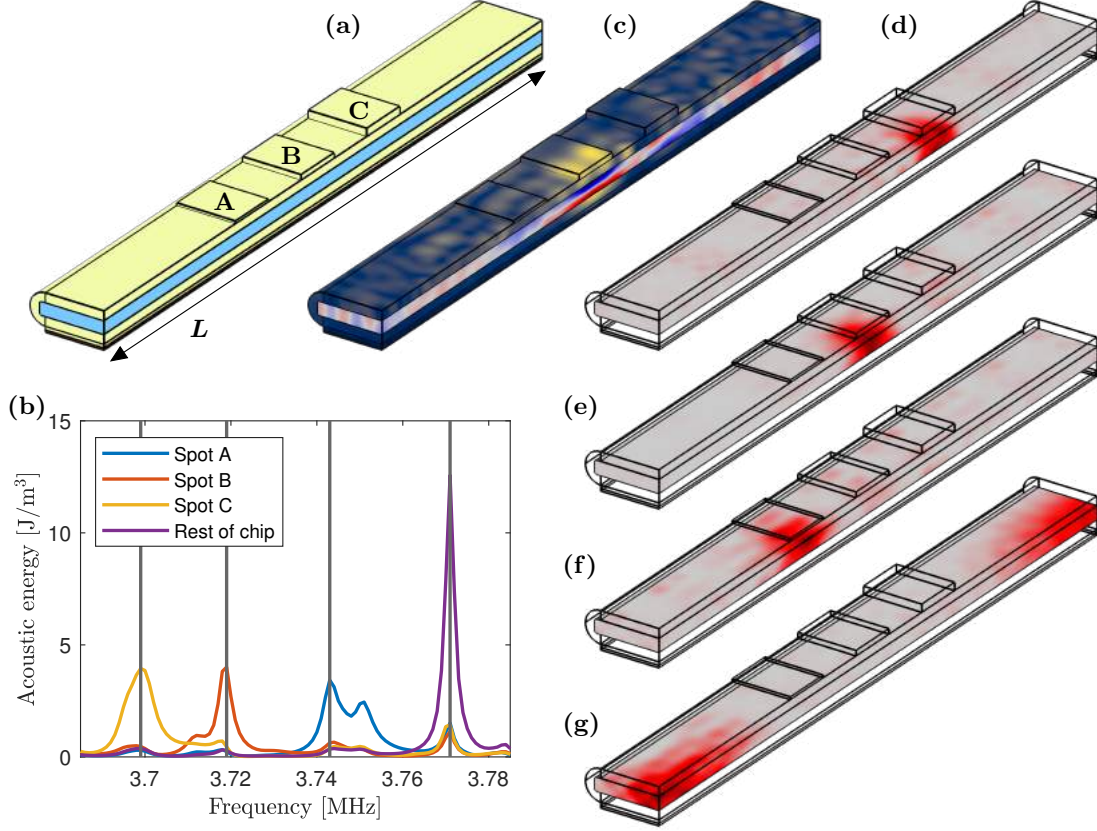


Figure 6.6: Simulation results for a glass capillary tube with three geometrical cavities. (a) Model of the glass capillary with three glass slits of thicknesses  $d = 50, 100,$  and  $150 \mu\text{m}$  at respectively domain A, B, and C. (b) Line plot of the acoustic energy density at the three domains A (blue), B (red), and C (yellow) and the rest of chip (purple) as a function of frequency. (c) Color plot of the pressure  $p_1$  from blue  $-0.3$  to red  $0.3$  MPa and absolute displacement in the solid  $|\mathbf{u}_1|$  from blue  $0$  to yellow  $1.5$  nm at the resonance in domain B at  $f = 1.966$  MHz. (d–g) Color plot of the acoustic energy density  $E_{ac}$  at the four resonance frequencies marked in (b)  $f = 3.699, 3.719, 3.743,$  and  $3.771$  MHz.

three spots A, B, C, and the rest of the chip is shown as a function of the frequency in Fig. 6.6(b). The resonance peaks of the three spots are all separated by approximately 20 kHz and at its resonances has an energy density of approximately a magnitude higher than the rest of the chip. The acoustic pressure  $p_1$  and absolute displacement field  $|\mathbf{u}_1|$  for the resonance frequency at region B  $f = 3.719$  MHz are shown in Fig. 6.6(c). It has a clear height resonance in region B and not in the rest of the chip. Fig. 6.6(d–g) plots the acoustic energy density  $E_{ac}$  in the fluid at the four resonance frequencies  $f = 3.699, 3.719, 3.743,$  and  $3.771$  MHz marked in Fig. 6.6(b). There is a good spatial localization of the acoustic fields under the three glass slits at three different resonant frequencies. This enables a

device where it is possible with one piezo-electric transducer to change the location of the acoustic trap by changing the frequency on the piezo-electric transducer.

As with the simulations of the thermal cavity the  $Q$ -factor in the simulations are high since it does not include the losses in the transducer and the glue layers. Therefore in an experiment it is expected to have significantly broader resonance peaks.

### 6.3 Trapping strength

In the two previous sections we have explored the possibilities of localizing acoustic waves using either light absorption or glueing glass slits on a glass capillary tube, here we investigate their trapping strengths. The trapping strength is important since it determines how fast a fluid flow a trap can resist. The fluid flow can either be a Poiseuille flow through the glass capillary or because of movement of the acoustic trap. The trapping strength is governed by the dipole term of the acoustic radiation force as discussed in Section 2.9 and given as Eq. (2.72),

$$\mathbf{F}_{\text{node}}^{\text{rad}} = 4\pi a^3 f_2 \nabla E_{\text{ac}}, \quad f_2 = \frac{2(\tilde{\rho} - 1)}{2\tilde{\rho} + 1}. \quad (6.4)$$

and the drag force from the fluid flow  $\mathbf{v}_2$  is given as Eq. (2.67),

$$\mathbf{F}^{\text{drag}} = 6\pi\eta a \mathbf{v}_2 \quad (6.5)$$

For the acoustic traps in this section the acoustic field decays over the length scale of 0.5 mm so we estimate  $|\nabla E_{\text{ac}}| \sim 2 \text{ mm}^{-1} E_{\text{ac}}$ . Then for a glass particle  $f_2 \sim 0.5$  with radius  $a = 5 \text{ }\mu\text{m}$  the trap will be able to hold up to a flow velocity  $v_{\text{max}}$ , depending on the acoustic energy density  $E_{\text{ac}}$ ,

$$v_{\text{max}} = \frac{2a^2 f_2}{3\eta} |\nabla E_{\text{ac}}| \sim 20 \text{ }\mu\text{m/s} \frac{E_{\text{ac}}}{1 \text{ J/m}^3} \quad (6.6)$$

The trapping strength depends on the radius and density of the particles. To hold against a flow velocity of 2 mm/s an acoustic energy of  $E_{\text{ac}} \sim 100 \text{ J/m}^3$  is needed, and a polystyrene particle with  $f_2 \sim 0.05$  requires an acoustic energy density of  $E_{\text{ac}} \sim 1000 \text{ J/m}^3$ .

### 6.4 Concluding remarks

The chapter has numerically investigated the possibility of spatially localizing acoustic fields either by controlling the temperature field or changing the geometry in order to create an acoustic trap. Simulations indicate that it is possible to localize acoustic fields by controlling the temperature field in the channel or altering the solid geometry of the chip. Especially the possibility of having a temperature induced trap is interesting and provides the possibility to spatially move a trap by controlling an LED light. In the examples the light was absorbed in the fluid as in Section 4.3. For some applications it might be impractical to add dye to the fluid, instead it might be possible to use a colored glass lid that absorbs the light at frequencies of the LED, while still permitting optical access at a different frequency.

A concern for the temperature induced trap is the streaming in the acoustofluidic device. As demonstrated thoroughly in Chapter 4 a gradient in the temperature will induce an acoustic body force and thereby acoustic streaming. The temperature gradients created in the trap is similar to the ones in Section 4.3 therefore fast acoustic streaming can be expected and should be modeled before designing an experiment. It may be possible to control the streaming field induced by an LED by having an elliptical LED spot. This could potentially be used to strengthen the acoustic trap in the direction of the drag force. For the geometrically induced trap there is no temperature gradients and no significant streaming field is expected.



## Chapter 7

# Papers

### 7.1 Paper I in JASA

*Theory of pressure acoustics with thermoviscous boundary layers and streaming in elastic cavities*

**Authors:** J. H. Joergensen and H. Bruus.

**Journal:** J. Acoust. Soc. Am. **149**, 3599-3610 (2021)

# Theory of pressure acoustics with thermoviscous boundary layers and streaming in elastic cavities<sup>a)</sup>

Jonas Helboe Joergensen and Henrik Bruus<sup>b)</sup>

Department of Physics, Technical University of Denmark, DTU Physics Building 309, DK-2800 Kongens Lyngby, Denmark

## ABSTRACT:

We present an effective thermoviscous theory of acoustofluidics including pressure acoustics, thermoviscous boundary layers, and streaming for fluids embedded in elastic cavities. By including thermal fields, we thus extend the effective viscous theory by Bach and Bruus [J. Acoust. Soc. Am. **144**, 766 (2018)]. The acoustic temperature field and the thermoviscous boundary layers are incorporated analytically as effective boundary conditions and time-averaged body forces on the thermoacoustic bulk fields. Because it avoids resolving the thin boundary layers, the effective model allows for numerical simulation of both thermoviscous acoustic and time-averaged fields in three-dimensional models of acoustofluidic systems. We show how the acoustic streaming depends strongly on steady and oscillating thermal fields through the temperature dependency of the material parameters, in particular the viscosity and the compressibility, affecting both the boundary conditions and spawning additional body forces in the bulk. We also show how even small steady temperature gradients ( $\sim 1$  K/mm) induce gradients in compressibility and density that may result in very high streaming velocities ( $\sim 1$  mm/s) for moderate acoustic energy densities ( $\sim 100$  J/m<sup>3</sup>).

© 2021 Acoustical Society of America. <https://doi.org/10.1121/10.0005005>

(Received 14 December 2020; revised 30 March 2021; accepted 23 April 2021; published online 26 May 2021)

[Editor: Max Denis]

Pages: 3599–3610

## I. INTRODUCTION

Modeling and simulation are important for designing microscale acoustofluidic systems. Traditionally, most models have been purely mechanical, but some include thermal effects, such as in the studies of the acoustic radiation force acting on suspended microparticles<sup>1–3</sup> and of acoustic streaming in rigid cavities.<sup>4,5</sup>

Here, we focus on acoustic streaming, where recent developments in the field point to the necessity of making a full thermoviscous analysis. Karlsen *et al.*<sup>6</sup> introduced the acoustic body force acting on a liquid governed by solute-induced gradients in the compressibility and density of the liquid. This force has explained the iso-acoustic focusing of microparticles,<sup>7</sup> patterning of concentration profiles,<sup>8</sup> and suppression of acoustic streaming.<sup>9,10</sup> Simultaneously, Bach and Bruus<sup>11</sup> developed the effective theory for pressure acoustics and streaming in elastic cavities, in which the viscous boundary layer was solved analytically and imposed as an effective boundary condition to the bulk field. This model has enabled simulations of cm-sized three-dimensional (3D) acoustofluidic systems,<sup>12,13</sup> with hitherto prohibitive computational costs, and it has provided a deeper insight into the physics of boundary- and bulk-induced streaming, but without thermal effects.<sup>14</sup>

In this work, we combine our previous work on thermoviscous streaming in rigid systems,<sup>5</sup> thermoviscous potential

theory,<sup>3</sup> the theory of pressure acoustics with viscous boundary layers and streaming in curved elastic cavities,<sup>11</sup> and the 3D numerical modeling of acoustofluidic systems using the latter theory,<sup>12</sup> and develop an *effective thermoviscous theory* for a fluid-filled cavity embedded in an elastic solid. The theory includes both steady and acoustic temperature fields for pressure acoustics with thermoviscous boundary layers and for streaming with thermoviscous body forces. In Sec. II, we set up the basic theory and model assumptions. In Secs. III–V, the governing equations and boundary conditions are derived from the theory for the zeroth, first, and second order in the acoustic perturbation, respectively. In Sec. VI, the theory is implemented in a numerical model, which is then used in two examples to show the nature and importance of thermal effects in acoustofluidics. Finally, we conclude in Sec. VII.

## II. BASIC THEORY AND MODEL ASSUMPTIONS

We consider an acoustofluidic device consisting of an elastic solid containing a microchannel filled with a thermoviscous Newtonian fluid and actuated by a piezoelectric transducer at a single frequency in the MHz range. This time-harmonic actuation establishes an acoustic field in the system, which in the fluid, by the internal dissipation and hydrodynamic nonlinearities, results in a time-averaged response that leads to acoustic streaming.

### A. Governing equations

In this work, unlike prior work,<sup>12</sup> we leave the piezoelectric transducer out of the analysis and only represent it

<sup>a)</sup>This paper is part of a special issue on Theory and Applications of Acoustofluidics.

<sup>b)</sup>Electronic mail: bruus@fysik.dtu.dk, ORCID: 0000-0001-5827-2939.



by an oscillating displacement condition on part of the surface of the elastic solid. The response of the fluid embedded in the elastic solid to this oscillating-displacement boundary condition is controlled by the hydro-, elasto-, and thermodynamic governing equations of the coupled thermoviscous fluid and elastic solid.

The linear elastic solid is described in the Lagrangian picture by the fields of the density  $\rho$ , the displacement  $\mathbf{u}$ , and the temperature  $T$ , as well as the stress tensor  $\boldsymbol{\sigma}$ . Further, for isotropic solids, there are eight material parameters: the longitudinal and transverse sound speeds  $c_{10}$  and  $c_{tr}$ , the thermal conductivity  $k^{\text{th}}$ , the specific heat  $c_p$ , the ratio of specific heats  $\gamma = c_p/c_v$ , the thermal expansion coefficient  $\alpha_p$ , and the isothermal and isentropic compressibilities  $\kappa_s$  and  $\kappa_T = \gamma\kappa_s$ . The velocity field is given as the time derivative of the displacement field  $\mathbf{v}^{\text{sl}} = \partial_t \mathbf{u}$ , so no advection occurs, and the governing equations are the transport equations of the momentum density  $\rho \partial_t \mathbf{u}$  and temperature  $T$ ,<sup>3,15</sup>

$$\rho \partial_t^2 \mathbf{u} = \nabla \cdot \boldsymbol{\sigma}, \quad (1a)$$

$$\partial_t T + \frac{(\gamma - 1)}{\alpha_p} \partial_t (\nabla \cdot \mathbf{u}) = \frac{\gamma}{\rho c_p} \nabla \cdot (k^{\text{th}} \nabla T), \quad (1b)$$

$$\boldsymbol{\sigma} = -\frac{\alpha_p}{\kappa_T} (T - T_0) \mathbf{I} + \boldsymbol{\tau}, \quad (1c)$$

$$\boldsymbol{\tau} = \rho c_{tr}^2 [\nabla \mathbf{u} + (\nabla \mathbf{u})^T] + \rho (c_{10}^2 - 2c_{tr}^2) (\nabla \cdot \mathbf{u}) \mathbf{I}, \quad (1d)$$

where superscript ‘‘T’’ indicates a transposed matrix.

The fluid is described in the Eulerian picture by the fields of the density  $\rho$ , the pressure  $p$ , the velocity  $\mathbf{v}$ , the temperature  $T$ , and the energy per mass unit  $\epsilon$ , and by the material parameters as before:  $k^{\text{th}}$ ,  $c_p$ ,  $\alpha_p$ ,  $\gamma$ ,  $\kappa_s$ ,  $\kappa_T$ , but with  $c_{tr}$  replaced by the dynamic and bulk viscosity  $\eta$  and  $\eta^b$ . The governing equations are the transport equations for the density of mass  $\rho$ , momentum  $\rho \mathbf{v}$ , and internal energy  $\rho \epsilon$ ,<sup>3,5,16</sup>

$$\partial_t \rho = -\nabla \cdot (\rho \mathbf{v}), \quad (2a)$$

$$\partial_t (\rho \mathbf{v}) = \nabla \cdot (\boldsymbol{\sigma} - \rho \mathbf{v} \mathbf{v}), \quad (2b)$$

$$\partial_t \left( \rho \epsilon + \rho \frac{v^2}{2} \right) = \nabla \cdot \left[ k^{\text{th}} \nabla T + \mathbf{v} \cdot \boldsymbol{\sigma} - \rho \mathbf{v} \left( \epsilon + \frac{v^2}{2} \right) \right] + P, \quad (2c)$$

$$\boldsymbol{\sigma} = -p \mathbf{I} + \boldsymbol{\tau}, \quad (2d)$$

$$\boldsymbol{\tau} = \eta [\nabla \mathbf{v} + (\nabla \mathbf{v})^T] + \left( \eta^b - \frac{2}{3} \eta \right) (\nabla \cdot \mathbf{v}) \mathbf{I}. \quad (2e)$$

Here,  $P$  is the external heat power density.

Pressure and temperature are related to the internal energy density by the first law of thermodynamics and to the density by the equation of state,<sup>3,5,17</sup>

$$\rho d\epsilon = (\rho c_p - \alpha_p p) dT + (\kappa_T p - \alpha_p T) dp, \quad (3a)$$

$$d\rho = \rho \kappa_T dp - \rho \alpha_p dT. \quad (3b)$$

The thermodynamics also shows up in the temperature and density dependency<sup>5</sup> of any material parameter  $q$ ,

$$dq = \left( \frac{\partial q}{\partial T} \right)_\rho dT + \left( \frac{\partial q}{\partial \rho} \right)_T d\rho. \quad (4)$$

The temperature sensitivity of each parameter is quantified by the dimensionless quantity  $a_q = 1/\alpha_p q (\partial q / \partial T)_\rho$ ,

$$\begin{aligned} a_\rho &= -1, & a_\eta &= -89, & a_{\eta^b} &= -100, \\ a_{k^{\text{th}}} &= 11, & a_{\alpha_p} &= 145, & a_{\kappa_s} &= -10, \end{aligned} \quad (5)$$

where the values are for water at  $T = 25^\circ\text{C}$ .<sup>5</sup> The temperature dependency of the parameters implies that thermal gradients may induce gradients in, say, density and compressibility. This leads to the appearance of the inhomogeneous acoustic body force  $\mathbf{f}_{\text{ac}}$  introduced in acoustofluidics for solute-induced gradients by Karlsen *et al.*<sup>6</sup>

## B. Acoustic actuation and perturbation expansion

Following Ref. 11, we actuate time-harmonically with angular frequency  $\omega$  by a displacement of a surface, so an element at equilibrium position  $s_0$ , at time  $t$  will have the position  $\mathbf{s}(s_0, t) = s_0 + s_1(s_0) e^{-i\omega t}$ . For models containing only a fluid, the displacement will be on the fluid boundary, whereas for models containing both a fluid and a solid domain, the actuation is on the solid boundary. For models including the piezoelectric transducer driving the system, the actuation parameter is the applied voltage.<sup>12</sup> However, this is not included in this work.

The acoustic response to the actuation parameter  $s_1$  is linear, and the resulting fields will be complex fields  $Q_1(\mathbf{r}) e^{-i\omega t}$ , the so-called first-order fields with subscript 1. The non-linearity of the governing equation results in higher order responses to the actuation. We are only interested in the time-averaged second-order response and define  $Q_2(\mathbf{r}) = \langle Q_2(\mathbf{r}, t) \rangle = (\omega/2\pi) \int_0^{2\pi/\omega} Q_2(\mathbf{r}, t) dt$ . A time-average of a product of two first-order fields is also a second-order term, written as  $\langle A_1 B_1 \rangle = (1/2) \text{Re}[A_1 B_1^*]$ , where the asterisk denote complex conjugation. Thus, a given field  $Q(\mathbf{r}, t)$  in the model, such as density  $\rho$ , temperature  $T$ , pressure  $p$ , velocity  $\mathbf{v}$ , displacement  $\mathbf{u}$ , and stress  $\boldsymbol{\sigma}$ , is written as the sum of the unperturbed field, the acoustic response, and the time-averaged response,

$$Q(\mathbf{r}, t) = Q_0(\mathbf{r}) + Q_1(\mathbf{r}) e^{-i\omega t} + Q_2(\mathbf{r}). \quad (6)$$

Similarly, through their dependency on temperature and density, all material parameters, such as thermal conductivity  $k^{\text{th}}$ , compressibility  $\kappa$ , and (for liquids) viscosity  $\eta$ , are written as exemplified by the viscosity,

$$\eta(\mathbf{r}, t) = \eta_0(T_0) + \eta_1(T_1, \rho_1) e^{-i\omega t} + \eta_2(T_2, \rho_2), \quad (7a)$$

$$\eta_1(T_1, \rho_1) = \left( \frac{\partial \eta}{\partial T} \right)_{T_0} T_1(\mathbf{r}) + \left( \frac{\partial \eta}{\partial \rho} \right)_{T_0} \rho_1(\mathbf{r}), \quad (7b)$$

$$\eta_2(T_2, \rho_2) = \left(\frac{\partial \eta}{\partial T}\right)_{T_0} T_2(\mathbf{r}) + \left(\frac{\partial \eta}{\partial \rho}\right)_{T_0} \rho_2(\mathbf{r}). \quad (7c)$$

### C. Separation of length scales

Acoustofluidic systems exhibit dynamics on two length-scales, set by the acoustic wavelength and the thermoviscous boundary layer width. The boundary conditions on the temperature, heat flux, velocity, and stress at a fluid-solid interface result in the appearance of a thermal boundary layer (in fluids and solids) of width  $\delta_t$  and in a viscous boundary layer (in fluids only) of width  $\delta_s$ , localized near fluid-solid interfaces. Their dynamically-defined widths, jointly referred to as  $\delta$ , are small compared to a typical device size or wavelength  $d$ , so  $\delta \ll d$ ,<sup>3</sup>

$$\delta_s = \sqrt{\frac{2\nu_0}{\omega}}, \quad \delta_t = \sqrt{\frac{2D_0^{\text{th}}}{(1-X)\omega}} \approx \sqrt{\frac{2D_0^{\text{th}}}{\omega}}, \quad (8)$$

where  $X=0$  for fluids and  $X = (\gamma - 1)(4c_{\text{tr}}^2/3c_{\text{lo}}^2) \leq 0.01$  for solids,  $\nu_0 = (\eta_0/\rho_0)$ , and  $D_0^{\text{th}} = k_0^{\text{th}}/\rho_0 c_{p0}$ . Typically,  $\delta_t \leq \delta_s \leq 500$  nm, which is more than two orders of magnitude smaller than  $d \sim 100$   $\mu\text{m}$ . In this paper, the various fields are decomposed into a bulk field ( $d$ ) and a boundary-layer field ( $\delta$ ) that are connected by the boundary conditions. In Fig. 1, this decomposition is sketched near the fluid-solid boundary for the acoustic temperature field  $T_1$ . Also shown are the boundary-layer widths  $\delta_s$  and  $\delta_t$  together with the instantaneous position  $s(t) = s_0 + s_1(s_0, t)$  of the oscillating boundary.

### D. Boundary conditions

In the usual Lagrangian picture,<sup>11</sup> an element with equilibrium position  $s_0$  in an elastic solid has at time  $t$  the

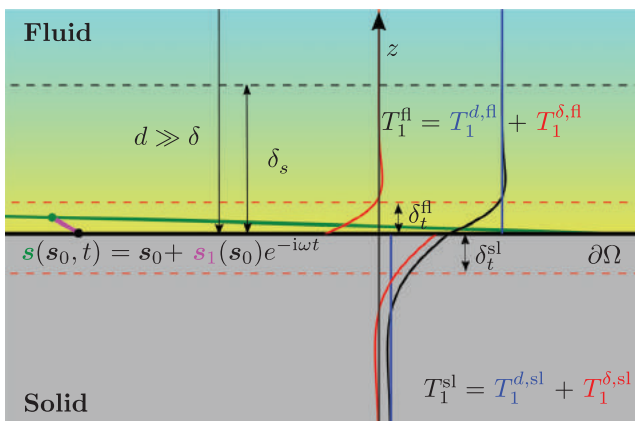


FIG. 1. (Color online) Sketch of the fields at the fluid-solid interface.  $s_0$  is the equilibrium position of the interface  $\partial\Omega$ ,  $s_1$  the time-dependent displacement away from  $\partial\Omega$ , and  $s = s_0 + s_1$  the instantaneous position. The dashed lines represent the viscous and thermal boundary-layer widths  $\delta_s$  (black) and  $\delta_t$  (red) in the solid and fluid.  $\delta$  without a subscript refers to either  $\delta_s$  or  $\delta_t$ , and  $d$  refers to the bulk lengthscale, so  $\delta_t \leq \delta_s \sim \delta \ll d$ . The temperature  $T_1^{\text{sl}}$  (black) is the sum of a bulk field  $T_1^{d,\text{sl}}$  (blue) and a boundary-layer field  $T_1^{\delta,\text{sl}}$  (red).

position  $s(s_0, t) = s_0 + s_1(s_0)e^{-i\omega t}$  and velocity  $\mathbf{V}^0 = \partial_t s = \mathbf{V}_1^0(s_0)e^{-i\omega t}$  with  $\mathbf{V}_1^0(s_0) = -i\omega s_1(s_0)$ . On the solid-fluid interface, the no-slip condition applies, so the velocity of the solid wall at a given time and position must equal the Eulerian-picture fluid velocity  $\mathbf{v}^{\text{fl}}$ ,

$$\mathbf{v}^{\text{fl}}(s_0 + s_1 e^{-i\omega t}, t) = \mathbf{V}_1^0(s_0) e^{-i\omega t}. \quad (9)$$

This boundary condition must be obeyed separately for the first- and second-order fields (subscript 1 and 2, respectively), so a Taylor expansion yields<sup>11</sup>

$$\mathbf{v}_1(s_0) = \mathbf{V}_1^0(s_0), \quad (10a)$$

$$\mathbf{v}_2(s_0) = -\langle (\mathbf{s}_1 \cdot \nabla) \mathbf{v}_1 \rangle|_{s_0} = -\frac{1}{\omega} \langle (i\mathbf{V}_1^0 \cdot \nabla) \mathbf{v}_1 \rangle|_{s_0}. \quad (10b)$$

At position  $s_0$  on the fluid-solid interface with surface normal  $\mathbf{n}$ , also the stress  $\boldsymbol{\sigma} = \boldsymbol{\sigma}_1 + \boldsymbol{\sigma}_2$  must be continuous in the first- and second-order contributions  $\boldsymbol{\sigma}_1$  and  $\boldsymbol{\sigma}_2$  separately,

$$\boldsymbol{\sigma}_1^{\text{sl}}(s_0) \cdot \mathbf{n} = \boldsymbol{\sigma}_1^{\text{fl}}(s_0) \cdot \mathbf{n}, \quad (11a)$$

$$\boldsymbol{\sigma}_2^{\text{sl}}(s_0) \cdot \mathbf{n} = \boldsymbol{\sigma}_2^{\text{fl}}(s_0) \cdot \mathbf{n} + \langle (\mathbf{s}_1 \cdot \nabla) \boldsymbol{\sigma}_1^{\text{fl}}(s_0) \cdot \mathbf{n} \rangle|_{s_0}. \quad (11b)$$

Here, the thermal effects enter through the temperature dependency of the viscosity parameters  $\eta$  and  $\eta^b$ , see Eqs. (2d) and (7).

Similarly, the temperature  $T = T_0 + T_1 + T_2$  must be continuous across the solid-fluid interface in each order separately,

$$T_i^{\text{sl}}(s_0) = T_i^{\text{fl}}(s_0), \quad i = 0, 1, \quad (12a)$$

$$T_2^{\text{sl}}(s_0) = T_2^{\text{fl}}(s_0) + \langle \mathbf{s}_1 \cdot \nabla T_1^{\text{fl}} \rangle|_{s_0}. \quad (12b)$$

Also, the heat flux  $\mathbf{n} \cdot (-k^{\text{th}} \nabla T)$  must be continuous across the interface,

$$k^{\text{th,sl}} \mathbf{n} \cdot \nabla T^{\text{sl}}(s_0, t) = k^{\text{th,fl}} \mathbf{n} \cdot \nabla T^{\text{fl}}(s_0 + s_1 e^{-i\omega t}, t), \quad (13)$$

which order by order becomes

$$k_0^{\text{th,sl}} \mathbf{n} \cdot \nabla T_i^{\text{sl}}(s_0) = k_0^{\text{th,fl}} \mathbf{n} \cdot \nabla T_i^{\text{fl}}(s_0), \quad i = 0, 1, \quad (14a)$$

$$\begin{aligned} k_0^{\text{th,sl}} \mathbf{n} \cdot \nabla T_2^{\text{sl}} + k_2^{\text{th,sl}} \mathbf{n} \cdot \nabla T_0^{\text{sl}} + \langle k_1^{\text{th,sl}} \mathbf{n} \cdot \nabla T_1^{\text{sl}} \rangle \\ = k_0^{\text{th,fl}} \mathbf{n} \cdot \nabla T_2^{\text{fl}}(s_0) + \langle k_1^{\text{th,fl}} \mathbf{n} \cdot \nabla T_1^{\text{fl}}(s_0) \rangle \\ + k_2^{\text{th,fl}} \mathbf{n} \cdot \nabla T_0^{\text{fl}}(s_0) + \langle \mathbf{s}_1 \cdot \nabla [k_0^{\text{th,fl}} \nabla T_1^{\text{fl}}(s_0)] \cdot \mathbf{n} \rangle \\ + \langle \mathbf{s}_1 \cdot \nabla [k_1^{\text{th,fl}} \nabla T_0^{\text{fl}}(s_0)] \cdot \mathbf{n} \rangle. \end{aligned} \quad (14b)$$

### E. Range of validity of the model

We briefly discuss the range of validity imposed by the main assumptions. First, perturbation theory is valid when lower-order terms are much larger than and unaffected by higher-order terms, say,  $\rho_0 \gg |\rho_1|$  and  $|\mathbf{v}_1| \gg |\mathbf{v}_2|$ , and

when the latter can be neglected in the governing equations. For example, zeroth-order heat Eq. (16) is only valid if the timescale for advective heat transport  $t_{adv} = d_t/|v_2|$  is much longer than that of diffusion  $t_{dif} = d_t^2/D_0^{th}$  in a system with characteristic length  $d_t$ . For  $d_t = 1$  mm this requires  $|v_2| \ll (D_0^{th}/d_t) \approx 150 \mu\text{m/s}$ .

Second, due to low oscillatory advection, we assume  $\nabla \cdot (q_0 v_1) \approx q_0 \nabla \cdot v_1$ , where  $q_0$  is a parameter of the fluid. This requires  $|q_0 \nabla \cdot v_1| \gg |\nabla q_0 \cdot v_1|$ . By using the parameter  $a_q$  of Eq. (5), the validity of our theory is limited by

$$|\nabla T_0| \ll \left| \frac{k_c}{a_\eta \alpha_{p0}} \right| \approx 5000 \frac{\text{K}}{\text{mm}}. \quad (15)$$

Here,  $a_\eta$  is used as the viscosity that has the strongest temperature dependency. In conventional acoustofluidic systems,  $|\nabla T_0| \lesssim 50 \text{ K/mm} \ll 5000 \text{ K/mm}$ .

Third, the effective boundary-layer theory requires the boundary-layer width to be much smaller than the bulk wavelength,  $k_0 \delta \ll 1$ , see Sec. IIC, which is true for MHz acoustics in water.

### III. ZEROth ORDER: STEADY BACKGROUND FIELDS

Before turning on the acoustics,  $p_0$  is constant and  $v_0 = \mathbf{0}$  in the acoustofluidic system. The temperature  $T_0$  is determined by boundary conditions set by the surroundings and the heat power density  $P_0$  from given sources and sinks.  $T_0$  is governed by the energy conservation [Eq. (2c)] to zeroth order in the acoustic actuation,

$$0 = \nabla \cdot [k_0^{th} \nabla T_0] + P_0. \quad (16)$$

$T_0$  determines the zeroth-order water parameters, such as  $\rho_0(T_0)$  and  $\eta_0(T_0)$ , and thereby affects the resonance frequency and the Q-factor of the acoustofluidic system.

### IV. FIRST ORDER: ACOUSTICS

For the first-order fields, we solve the viscous and thermal boundary layers analytically and use these solutions to derive a set of effective boundary conditions for the bulk fields. The analysis is based on our previous work: the governing equations derived in Refs. 3 and 5, the potential theory derived in Ref. 3, and the effective boundary method derived for viscous but not thermal boundary layers in Ref. 11. The result is a model where we solve for the displacement field  $u_1$  in the solid and for the pressure  $p_1$  in the fluid, and both these bulk fields are subject to the effective boundary conditions that implicitly contain the boundary layers. The temperature  $T_1$  is incorporated through  $p_1$ ,  $u_1$  in the first-order equations and the effective boundary conditions.

#### A. Acoustic equations and potential theory for fluids

The governing equations for the complex-valued acoustic field amplitudes in a fluid are given in Eq. (11) of Ref. 5: the mass continuity equation, the momentum equation, and

the heat equation, which couple together the pressure  $p_1$ , the velocity  $v_1$ , and the temperature  $T_1$ ,

$$-i\omega \alpha_{p0} T_1 + i\omega \kappa_{T0} p_1 = \nabla \cdot v_1, \quad (17a)$$

$$-i\omega \rho_0 v_1 = -\nabla p_1 + \beta \eta_0 \nabla (\nabla \cdot v_1) + \eta_0 \nabla^2 v_1, \quad (17b)$$

$$-i\omega T_1 + i\omega (\gamma - 1) \frac{\kappa_{s0}}{\alpha_{p0}} p_1 = D_0^{th} \nabla^2 T_1, \quad (17c)$$

where  $\beta = (\eta_0^b/\eta_0) - (2/3)$ . Following Ref. 3, these equations are solved using potential theory based on the standard Helmholtz decomposition of the velocity field,  $v_1 = \nabla(\phi_c + \phi_t) + \nabla \times \Psi = v_1^d + v_1^\delta$ , where  $\phi_c$  is the compressional potential,  $\phi_t$  is the thermal potential, and  $\Psi$  is the shear vector potential. At the fluid-solid interface  $|T_1^\delta| \approx |T_1^d|$ , and combining this with  $T_1 = T_1^d + T_1^\delta = [i(\gamma - 1)\omega/\alpha_{p0}c_0^2]\phi_c + (1/\alpha_{p0}D_0^{th})\phi_t$  with the typical acoustofluidic parameter values inserted, we can deduce  $|\phi_t| \approx (\gamma - 1)(\omega D_0^{th}/c_0^2)|\phi_c| \approx 10^{-8}|\phi_c| \ll |\phi_c|$ . From this follows that  $p_1 \approx i\omega \rho_0(1 + i\Gamma_s)\phi_c$ , and we replace  $\phi_c$ ,  $\phi_t$ , and  $\Psi$  by  $p_1$ ,  $T_1^\delta$ , and  $v_1^\delta$ ,

$$p_1 \approx i\omega \rho_0(1 + i\Gamma_s)\phi_c, \quad T_1^\delta = \frac{\phi_t}{\alpha_{p0}D_0^{th}}, \quad v_1^\delta = \nabla \times \Psi. \quad (18)$$

Finally, using the smallness of the damping coefficients,  $\Gamma_s = (1/2)(1 + \beta)(k_0\delta_s)^2 \ll 1$  and  $\Gamma_t = (1/2)(k_0\delta_t)^2 \ll 1$ , with  $k_0 = \omega/c$ , approximate solutions to Eq. (17) are obtained from the potentials solving three Helmholtz equations,

$$\nabla^2 p_1 = -k_c^2 p_1, \quad k_c = \frac{\omega}{c_0}(1 + i\Gamma_{0c}^n), \quad (19a)$$

$$\nabla^2 T_1^\delta = -k_t^2 T_1^\delta, \quad k_t = \frac{1 + i}{\delta_t}(1 + i\Gamma_{0t}^n), \quad (19b)$$

$$\nabla^2 v_1^\delta = -k_s^2 v_1^\delta, \quad k_s = \frac{1 + i}{\delta_s}. \quad (19c)$$

Here,  $\Gamma_{0c}^n = [\Gamma_s + (\gamma - 1)\Gamma_t]/2$  and  $\Gamma_{0t}^n = (\gamma - 1)[\Gamma_s - \Gamma_t]/2$  are the resulting damping coefficients, whereas the complex-valued wave numbers  $k_s$  and  $k_t$  reveal the existence of the viscous and thermal boundary layers of thickness  $\delta_s$  and  $\delta_t$ , respectively, see Fig. 1. The full velocity  $v_1$  and temperature  $T_1$  are given by  $p_1$ ,  $v_1^\delta$ , and  $T_1^\delta$  as,

$$v_1 = v_1^d + v_1^\delta = v_1^{d,p} + v_1^{d,T} + v_1^\delta, \quad (20a)$$

$$v_1^{d,p} = \nabla \left[ -i \frac{1 - i\Gamma_s}{\omega \rho_0} p_1 \right], \quad v_1^{d,T} = \nabla \left[ \alpha_{p0} D_0^{th} T_1^\delta \right], \quad (20b)$$

$$T_1 = T_1^d + T_1^\delta, \quad T_1^d = (\gamma - 1) \frac{\kappa_{s0}}{\alpha_{p0}} p_1. \quad (20c)$$

Note that both  $v_1^{d,p}$  and  $v_1^{d,T}$  are gradient fields in the Helmholtz decomposition, but that  $v_1^{d,T}$  despite its superscript ‘‘d’’ is a boundary-layer field. Because  $T_1$  is split into a

bulk and a boundary layer field, the material parameters  $q = q_0 + q_1$  are split similarly. For example, the first-order viscosity  $\eta_1$  introduced in Eq. (7) (and similar for other material parameters) becomes

$$\eta_1 = \partial_T \eta_0 (T_1^d + T_1^\delta) + \partial_\rho \eta_0 (\rho_1^d + \rho_1^\delta) = \eta_1^d + \eta_1^\delta. \quad (21)$$

### B. Acoustic equations and potential theory for solids

For a linear elastic isotropic solid with density  $\rho_0$ , longitudinal sound speed  $c_{l0}$ , and transverse sound speed  $c_{tr}$ , the governing equations are the linearized form of the momentum and heat equation [Eq. (1)] for the displacement field  $\mathbf{u}_1$  and the temperature  $T_1$ ,<sup>3</sup>

$$-\omega^2 \rho_0 \mathbf{u}_1 = -\frac{\alpha_{p0}}{\kappa_{T0}} \nabla T_1 + (c_{l0}^2 - c_{tr}^2) \nabla (\nabla \cdot \mathbf{u}_1) + c_{tr}^2 \nabla^2 \mathbf{u}_1, \quad (22a)$$

$$-i\omega T_1 - i\omega \frac{\gamma - 1}{\alpha_{p0}} \nabla \cdot \mathbf{u}_1 = D_0^{\text{th}} \nabla^2 T_1. \quad (22b)$$

In analogy with the fluid, the governing equations for the solid are solved by potential theory, again following Ref. 3. The displacement field is Helmholtz decomposed as  $-i\omega \mathbf{u}_1 = \nabla(\phi_c + \phi_t) + \nabla \times \Psi = -i\omega(\mathbf{u}_1^{\text{lo}} + \mathbf{u}_1^{\text{tr}})$ , where  $\phi_c$  is the compressional potential,  $\phi_t$  is the thermal potential, and  $\Psi$  is the shear vector potential, and where we have used  $\mathbf{v}_1^{\text{sl}} = -i\omega \mathbf{u}_1$ . Using the same approximations as for the fluid, we have  $T_1 = T_1^d + T_1^\delta = [i(\gamma - 1)\omega/\alpha_{p0}c_0^2]\phi_c + (1/\chi\alpha_{p0}D_0^{\text{th}})\phi_t$ . We keep  $\phi_c$ , but use  $T_1^\delta = (1/\chi\alpha_{p0}D_0^{\text{th}})\phi_t$  instead of  $\phi_t$ , and  $\mathbf{u}_1^{\text{tr}} = \nabla \times \Psi$  instead of  $\Psi$ . The solution to Eq. (22) is obtained from the potentials solving the following three Helmholtz equations:

$$\nabla^2 \phi_c = -k_c^2 \phi_c, \quad k_c = \frac{\omega}{c_0} (1 + i\Gamma_{0c}^{\text{sl}}), \quad (23a)$$

$$\nabla^2 T_1^\delta = -k_t^2 T_1^\delta, \quad k_t = \frac{1 + i}{\delta_t} (1 + i\Gamma_{0t}^{\text{sl}}), \quad (23b)$$

$$\nabla^2 \mathbf{u}_1^{\text{tr}} = -k_s^2 \mathbf{u}_1^{\text{tr}}, \quad k_s = \frac{\omega}{c_{tr}}. \quad (23c)$$

Here,  $c_0^2 = c_{l0}^2 + (\gamma - 1)/\rho_0\kappa_{T0}$ ,  $\Gamma_{0c}^{\text{sl}} = (\gamma - 1)\chi\Gamma_t/2$ , and  $\Gamma_{0t}^{\text{sl}} = \gamma^2\Gamma_t/8(1 - X)$  are damping coefficients,  $\delta_t$  and  $\Gamma_t$  are given by Eq. (8),  $\chi = 1 - 4c_{tr}^2/3c^2 \approx 1/2$ , and  $X = (\gamma - 1)4c_{tr}^2/3c^2 \approx (\gamma - 1)/2$ . For a solid, only  $T_1^\delta$  is a dampened field confined to the boundary layer, whereas  $\phi_c$  and  $\mathbf{u}_1^{\text{tr}}$  are bulk fields. The transverse waves in fluids and solids are qualitatively different:  $v_1^\delta$  cannot propagate in a fluid and is restricted to the boundary layer, whereas  $\mathbf{u}_1^{\text{tr}}$  can propagate in a solid and is not associated with a boundary layer. The full displacement  $\mathbf{u}_1$  and temperature  $T_1$  are given by  $\phi_c$ ,  $\mathbf{u}_1^{\text{tr}}$ , and  $T_1^\delta$  as

$$\mathbf{u}_1 = \mathbf{u}_1^{\text{lo}} + \mathbf{u}_1^{\text{tr}}, \quad \mathbf{u}_1^{\text{lo}} = \frac{i}{\omega} \nabla \phi_c, \quad (24a)$$

$$T_1 = T_1^d + T_1^\delta, \quad T_1^d = \frac{i(\gamma - 1)\omega}{\alpha_{p0}c_0^2} \phi_c. \quad (24b)$$

For most solids, the bulk thermal field  $T_1^d$  is negligible and the displacement can be modelled by Eq. (22a).

The explicit expression for the stress tensor  $\sigma_1^{\text{xl}}$  in the fluid (xl = fl) and in the solid (xl = sl) can be formulated jointly in potential theory as<sup>3</sup>

$$\sigma_1^{\text{xl}} = -p_1^{\text{xl}} \mathbf{I} + \eta_0^{\text{xl}} [(2k_c^2 - k_s^2)\phi_c + (2k_t^2 - k_s^2)\phi_t] \mathbf{I} + \eta_0^{\text{xl}} [\nabla \mathbf{v}_1^{\text{sl}} + (\nabla \mathbf{v}_1^{\text{sl}})^\dagger], \quad (25)$$

where in the solid  $p_1^{\text{sl}} = 0$ ,  $\eta_0^{\text{sl}} = (i/\omega) \rho_0 c_{tr}^2$ ,  $\mathbf{v}_1^{\text{sl}} = -i\omega \mathbf{u}_1$ .

### C. The thermal boundary layer

The temperature fields  $T_1^{\delta, \text{xl}}$  in the fluid (xl = fl) and the solid (xl = sl) are given by Eqs. (19b) and (23b). Following Ref. 11 with  $x$  and  $y$  parallel to the interface and  $z$  perpendicular, an analytical solution can be found using the thin-boundary-layer approximation  $\nabla^2 \approx \partial_z^2$  in these equations in combination with the condition that the field decays away from the boundary,

$$T_1^{\delta, \text{fl}}(x, y, z) = T_1^{\delta 0, \text{fl}}(x, y) e^{ik_t^{\text{fl}} z} \quad \text{for } z > 0, \quad (26a)$$

$$T_1^{\delta, \text{sl}}(x, y, z) = T_1^{\delta 0, \text{sl}}(x, y) e^{-ik_t^{\text{sl}} z} \quad \text{for } z < 0. \quad (26b)$$

The amplitude of the boundary fields  $T_1^{\delta 0, \text{fl}}(x, y)$  and  $T_1^{\delta 0, \text{sl}}(x, y)$  is determined by the boundary conditions in Eqs. (12a) and (14a) as follows: The normal vector  $\mathbf{n} = -\mathbf{e}_z$  points away from the fluid, so  $\mathbf{n} \cdot \nabla = -\partial_z$ , and we obtain

$$T_1^{\delta 0, \text{fl}} = T_1^{\delta 0, \text{sl}} - \Delta T_1^{d0}, \quad (27a)$$

$$k_0^{\text{th, fl}} \partial_z T_1^{\delta, \text{fl}} = k_0^{\text{th, sl}} \partial_z T_1^{\delta, \text{sl}} \quad \text{for } z = 0, \quad (27b)$$

where  $\Delta T_1^{d0} = -(T_1^{d0, \text{fl}} - T_1^{d0, \text{sl}})$ . From Eq. (27b), it follows

$$T_1^{\delta 0, \text{fl}} = -\frac{k_0^{\text{th, sl}} k_t^{\text{sl}}}{k_0^{\text{th, fl}} k_t^{\text{fl}}} T_1^{\delta 0, \text{sl}} = -\tilde{Z} T_1^{\delta 0, \text{sl}}, \quad (28)$$

where  $\tilde{Z} = Z^{\text{sl}}/Z^{\text{fl}}$  is the ratio of  $Z = k_0^{\text{th}} k_t = \sqrt{k_0^{\text{th}} c_{p0} \rho_0}$  of the solid and the fluid, respectively. Combining Eqs. (27a) and (28) leads to the final expression for the boundary-layer fields,

$$T_1^{\delta, \text{fl}}(x, y, z) = -\frac{\tilde{Z}}{1 + \tilde{Z}} \Delta T_1^{d0}(x, y) e^{ik_t^{\text{fl}} z}, \quad (29a)$$

$$T_1^{\delta, \text{sl}}(x, y, z) = +\frac{1}{1 + \tilde{Z}} \Delta T_1^{d0}(x, y) e^{-ik_t^{\text{sl}} z}. \quad (29b)$$

### D. The viscous boundary layer

The viscous boundary layer exists only in the fluid since in the solid both  $\mathbf{u}_1^{\text{lo}}$  and  $\mathbf{u}_1^{\text{tr}}$  are bulk fields. The velocity field

in the fluid is given in Eq. (20a) as  $\mathbf{v}_1 = \mathbf{v}_1^d + \mathbf{v}_1^\delta$ , where  $\mathbf{v}_1^d$  depends on the bulk field  $p_1$  and the boundary field  $T_1^\delta$ . The boundary field  $\mathbf{v}_1^\delta$  is given by the Helmholtz Eq. (19c), to which an analytical solution can be found using the thin-boundary-layer approximation  $\nabla^2 \approx \partial_z^2$  in combination with the condition that the field decays away from the boundary,<sup>11</sup>

$$\mathbf{v}_1^\delta = \mathbf{v}_1^{\delta 0}(x, y) e^{ik_s z}. \quad (30)$$

The amplitude  $\mathbf{v}_1^{\delta 0}$  of the boundary field is determined by the no-slip condition [Eq. (10a)],

$$\mathbf{v}_1^{\delta 0} = \mathbf{V}_1^0 - \mathbf{v}_1^{d0} = -i\omega \mathbf{u}_1^0 - \mathbf{v}_1^{d0}. \quad (31)$$

### E. The effective boundary condition for the velocity

Given the analytical solutions of the three boundary-layer fields, we only need to numerically solve the three bulk fields, namely,  $\phi_c$  and  $\Psi$  in the solid and  $\phi_c$  in the fluid, or equivalently, the displacement  $\mathbf{u}_1$  in the solid and the pressure  $p_1$  in the fluid. Therefore, we set two effective boundary conditions on these bulk fields using the analytical solutions for the boundary-layer fields: One effective boundary condition on the displacement  $\mathbf{u}_1$  in the solid derived from the condition on the stress, and another on the pressure in the fluid.

First, from the no-slip condition [Eq. (10a)], we derive the boundary condition for the first-order pressure field  $p_1$ , which takes the viscous and thermal boundary-layer effects into account through terms with  $k_s$ ,  $k_t$ , and  $T_1^{\delta 0}$ . We express the compressional velocity  $v_{1,z}^{d0,fl}$  on the fluid-solid interface through the no-slip condition [Eq. (31)], then use the incompressibility condition on the boundary-layer velocity,  $ik_s v_{1,z}^{\delta 0,fl} + \nabla \cdot \mathbf{v}_1^{\delta 0,fl} = 0$ , to get rid of the  $z$ -component  $v_{1,z}^{\delta 0,fl}$ , and finally introduce the bulk fields in the fluid,

$$\begin{aligned} v_{1,z}^{d0,fl} &= v_{1,z}^{d0,sl} - v_{1,z}^{\delta 0,fl} = v_{1,z}^{d0,sl} - \frac{i}{k_s} \nabla \cdot \mathbf{v}_1^{\delta 0,fl} \\ &= v_{1,z}^{d0,sl} - \frac{i}{k_s} \nabla \cdot [\mathbf{v}_1^{d0,sl} - \mathbf{v}_1^{d0,fl}] \\ &= \left[ v_{1,z}^{d0,sl} - \frac{i}{k_s} \nabla \cdot \mathbf{v}_1^{d0,sl} \right] + \frac{i}{k_s} \left[ \nabla \cdot \mathbf{v}_1^{d,fl} - \partial_z v_{1,z}^{d,fl} \right]_{z=0}. \end{aligned} \quad (32)$$

Combining Eqs. (17a) and (20c), we obtain

$$\nabla \cdot \mathbf{v}_1^d = i \frac{(1 - i\Gamma_s) k_c^2}{\omega \rho_0} p_1 - i\omega \alpha_{p0} T_1^\delta. \quad (33a)$$

Then using Eq. (20a), we write  $v_{1,z}^{d0,fl}$  and  $\partial_z v_{1,z}^{d,fl}$  evaluated at the solid-fluid interface at  $z = 0$ , and arrive at

$$v_{1,z}^{d0,fl} = -\frac{i}{\omega \rho_0} (1 - i\Gamma_s) \partial_z p_1 + \alpha_{p0} D_0^{\text{th}} \partial_z T_1^\delta, \quad (33b)$$

$$\partial_z v_{1,z}^{d,fl} = -\frac{i}{\omega \rho_0} (1 - i\Gamma_s) \partial_z^2 p_1 + \alpha_{p0} D_0^{\text{th}} \partial_z^2 T_1^\delta. \quad (33c)$$

Inserting Eqs. (33) and (10a) into Eq. (32) leads to the final form of the effective boundary condition on  $p_1$ ,

$$\begin{aligned} \partial_z p_1 &= i \frac{\omega \rho_0}{1 - i\Gamma_s} \left( V_{1z}^0 - \frac{i}{k_s} \nabla \cdot \mathbf{V}_1^0 \right) - \frac{i}{k_s} (k_c^2 + \partial_z^2) p_1 \\ &\quad + \frac{i}{k_t} \frac{\alpha_{p0}}{\kappa_{T0}} k_0^2 T_1^{\delta 0} \quad \text{for } z = 0. \end{aligned} \quad (34a)$$

The first two terms on the right-hand were derived by Bach and Bruus,<sup>11</sup> whereas the last term is a new correction due to the thermal boundary layer. For  $T_1^d \approx T_1^\delta$  at  $z = 0$ , this thermal correction is of the order  $[(\gamma - 1)/k_t] k_c^2 p_1$ . We emphasize, that although formulated as an effective boundary condition on the pressure gradient, Eq. (34a) is the no-slip velocity condition.

### F. The effective boundary condition for the stress

Next, using the explicit expressions for  $\sigma_1^{\text{sl}}$  and  $\sigma_1^{\text{fl}}$ , we turn to the stress boundary condition [Eq. (11a)], the continuity of the stress  $\sigma_1$  across the fluid-solid interface,  $\sigma_1^{\text{sl}} \cdot \mathbf{e}_z = \sigma_1^{\text{fl}} \cdot \mathbf{e}_z$ . For the fluid, we use  $k_s \gg k_c$ ,  $|\phi_c| \gg |\phi_t|$ , and  $|\partial_z v_1^\delta| \gg |\nabla v_1^d|$  in Eq. (25), and find

$$\sigma_1^{\text{fl}} \cdot \mathbf{e}_z = -p_1 \mathbf{e}_z + ik_s \eta_0 \left[ v_{1,z}^{d0,sl} + \frac{i}{\omega \rho_0} \nabla p_1 \right]_{s_0}. \quad (34b)$$

For the solid, we neglect in Eq. (25) the derivative  $\partial_{\parallel} \phi_t$  along the surface, as it is a factor  $\Gamma_t = (1/2)(k_0 \delta_t)^2$  smaller than  $\partial_{\parallel} \phi_c$ . The remaining  $\phi_t$ -dependent boundary-layer terms cancel out, leaving only the bulk-term part  $\sigma_1^{d,sl}$  of  $\sigma_1^{\text{sl}}$ . The resulting effective stress boundary condition is

$$\sigma_1^{d,sl} \cdot \mathbf{e}_z = \sigma_1^{\text{fl}} \cdot \mathbf{e}_z. \quad (34c)$$

As the thermal boundary-layer fields do not enter, this expression is identical to the effective boundary condition for the stress derived in Ref. 11.

## V. SECOND ORDER: ACOUSTIC STREAMING

For the second-order fields in the fluid, we follow Eq. (6) and consider only the time averaged fields, namely, the velocity  $\mathbf{v}_2$ , pressure  $p_2$ , and stress  $\sigma_2$ . The temperature field  $T_2$  does not enter the second-order continuity or Navier–Stokes equation, so we drop the heat equation. The first-order temperature field  $T_1$  enters the equations through the material parameters of the fluid,

$$0 = -\nabla \cdot (\rho_0 \mathbf{v}_2) + \dot{\rho}_{\text{ac}}, \quad (35a)$$

$$0 = -\nabla p_2 + \nabla \cdot \tau_2 + \hat{\mathbf{f}}_{\text{ac}}, \quad (35b)$$

$$\tau_2 = \eta_0 \left[ \nabla \mathbf{v}_2 + (\nabla \mathbf{v}_2)^{\dagger} \right] + \left[ \eta_0^b - \frac{2}{3} \eta_0 \right] (\nabla \cdot \mathbf{v}_2) \mathbf{I}, \quad (35c)$$

$$\mathbf{v}_2^0 = -\frac{1}{\omega} \langle (i\mathbf{V}_1^0 \cdot \nabla) \mathbf{v}_1 \rangle |_{r=s_0}. \quad (35d)$$

Here, the excess-density rate-of-change  $\dot{\rho}_{\text{ac}}$  and the acoustic body force  $\hat{\mathbf{f}}_{\text{ac}}$  are defined as time-averaged products of fast

varying first-order fields in the limit  $\rho_0 \mathbf{v}_1 \gg \rho_1 \mathbf{v}_0$ , which holds for typical acoustofluidic devices,

$$\dot{\rho}_{ac} = -\nabla \cdot \langle \rho_1 \mathbf{v}_1 \rangle, \quad (36a)$$

$$\hat{\mathbf{f}}_{ac} = \nabla \cdot [-\rho_0 \langle \mathbf{v}_1 \mathbf{v}_1 \rangle + \boldsymbol{\tau}_{11}], \quad (36b)$$

$$\boldsymbol{\tau}_{11} = \langle \eta_1 [\nabla \mathbf{v}_1 + (\nabla \mathbf{v}_1)^\dagger] \rangle + \left[ \eta_1^b - \frac{2}{3} \eta_1 \right] (\nabla \cdot \mathbf{v}_1) \mathbf{I}. \quad (36c)$$

The slowly varying second-order fields are split up in a bulk field (superscript “ $d$ ”) and a boundary field (superscript “ $\delta$ ”) according to their response to the boundary and bulk part of the acoustic force  $\hat{\mathbf{f}}_{ac} = \hat{\mathbf{f}}_{ac}^d + \hat{\mathbf{f}}_{ac}^\delta$ , and they are coupled by the boundary conditions

$$p_2 = p_2^d + p_2^\delta, \quad \mathbf{v}_2 = \mathbf{v}_2^d + \mathbf{v}_2^\delta, \quad (37a)$$

$$\boldsymbol{\tau}_2 = \boldsymbol{\tau}_2^d + \boldsymbol{\tau}_2^\delta, \quad \boldsymbol{\tau}_{11} = \boldsymbol{\tau}_{11}^d + \boldsymbol{\tau}_{11}^\delta. \quad (37b)$$

Note that in contrast to the first-order fields, this is not a Helmholtz decomposition: by definition, a second-order boundary-layer field “ $\delta$ ” contains at least one first-order boundary-layer field. The computation strategy for second-order streaming is similar to the one for first-order acoustics: (1) find analytical solution to the boundary layers, (2) formulate effective boundary conditions, and (3) solve the bulk fields with the effective boundary conditions. This decomposition enables simulations of the bulk fields without resolving the boundary-layer fields.

## A. Short-range boundary-layer streaming

The short-range part “ $\delta$ ” of Eq. (35) is given by the short-range part of the second-order fields as well as all source terms containing at least one boundary-layer field,

$$0 = \nabla \cdot (\rho_0 \mathbf{v}_2^\delta) + \dot{\rho}_{ac}^\delta, \quad (38a)$$

$$0 = -\nabla p_2^\delta + \nabla \cdot \boldsymbol{\tau}_2^\delta + \hat{\mathbf{f}}_{ac}^\delta, \quad (38b)$$

$$\text{where } \mathbf{v}_2^\delta \rightarrow 0 \text{ as } z \rightarrow \infty. \quad (38c)$$

At the boundary, the advection term can be neglected compared to the viscous term because of the large gradients induced by the small lengthscale  $\delta$ . The thermal boundary layer  $T_1^\delta$  and the associated boundary-layer velocity  $\mathbf{v}_1^{d,T}$  introduce a correction  $\mathbf{v}_2^{\delta,T}$  to the purely viscous boundary-layer term  $\mathbf{v}_2^{\delta,p}$  computed in Ref. 11,

$$\mathbf{v}_2^\delta = \mathbf{v}_2^{\delta,p} + \mathbf{v}_2^{\delta,T}. \quad (39)$$

In the parallel component of  $\mathbf{v}_2^\delta$ , the pressure field can be neglected because  $\partial_{\parallel} p_2^\delta \ll \eta_0 \partial_z^2 \mathbf{v}_{2\parallel}^\delta$ .<sup>11</sup> Thus, combining Eqs. (36b) and (38b), the parallel component of the short-range velocity field  $\mathbf{v}_2^{\delta,T}$  obeys

$$\nu_0 \partial_z^2 \mathbf{v}_{2\parallel}^{\delta,T} = \left[ \nabla \cdot \langle \mathbf{v}_1^\delta \mathbf{v}_1^{d,T} + \mathbf{v}_1^{d,T} \mathbf{v}_1^\delta + \mathbf{v}_1^{d,p} \mathbf{v}_1^{d,T} + \mathbf{v}_1^{d,T} \mathbf{v}_1^{d,p} + \mathbf{v}_1^{d,T} \mathbf{v}_1^{d,T} \rangle - \frac{1}{\rho_0} \nabla \cdot \boldsymbol{\tau}_{11}^\delta \right]_{\parallel}. \quad (40)$$

Here,  $\boldsymbol{\tau}_{11}^\delta$  depends on  $T_1$  through  $\eta_1(T_1)$ , whereas the velocity  $\mathbf{v}_1^{d,T}$ , given in Eq. (20a), depends on the thermal boundary layer  $T_1^\delta$ . From Sec. IV and, in particular, Eqs. (20), (26), and (30), follow the relations  $\nabla \cdot \mathbf{v}_1^\delta = 0$ ,  $|\mathbf{v}_{1,\parallel}^\delta| \approx |\mathbf{v}_{1,\parallel}^d|$ ,  $|v_{1,z}^\delta| \approx (k_c \delta_s) |v_{1,z}^d|$ ,  $|T_1^\delta| \approx |T_1^d|$ ,  $\nabla \cdot \mathbf{v}_1^{d,T} \approx (\gamma - 1) \nabla \cdot \mathbf{v}_1^{d,p}$ ,  $|\mathbf{v}_{1,z}^{d,T}| \approx (\gamma - 1) (k_c \delta_t) |\mathbf{v}_{1,z}^{d,p}|$ ,  $|\mathbf{v}_{1,\parallel}^{d,T}| \approx (\gamma - 1) (k_c \delta_t)^2 |\mathbf{v}_{1,\parallel}^{d,p}|$ , and  $\mathbf{v}_1^{d,T} = \alpha_{p0} D_0^{\text{th}} \nabla T_1^\delta$ . To lowest order in  $k_c \delta \ll 1$  (involving  $\partial_z T_1^\delta$  and  $\partial_z \mathbf{v}_1^\delta$ , respectively), these relations combined with time averaging  $\text{Re}[a_1] \text{Re}[b_1] = (1/2) \text{Re}[a_1 b_1^*]$  change Eq. (40) to

$$\begin{aligned} \nu_0 \partial_z^2 \mathbf{v}_{2\parallel}^{\delta,T} &= \left[ \left\langle (\partial_z \mathbf{v}_1^\delta) v_{1,z}^{d,T} \right\rangle + \left\langle (\mathbf{v}_1^\delta + \mathbf{v}_1^{d,p}) (\partial_z v_{1,z}^{d,T}) \right\rangle \right. \\ &\quad \left. - \frac{1}{\rho_0} \left( \langle (\partial_z \eta_1^\delta) \partial_z \mathbf{v}_1^\delta \rangle + \langle (\eta_1^\delta + \eta_1^d) \nabla^2 \mathbf{v}_1^\delta \rangle \right) \right]_{\parallel} \\ &= \frac{1}{2} \text{Re} \left[ \frac{2\alpha_{p0} D_0^{\text{th}}}{\delta_t^2} \left( \frac{\delta_t + i\delta_s}{\delta_s} \mathbf{v}_1^\delta + i\mathbf{v}_1^{d,p} \right) T_1^{\delta*} \right. \\ &\quad \left. - \frac{2}{\rho_0 \delta_s^2} \left( \frac{\delta_s + i\delta_t}{\delta_t} \eta_1^\delta + i\eta_1^d \right) \mathbf{v}_1^{\delta*} \right]_{\parallel}. \quad (41) \end{aligned}$$

The integration of Eq. (41) after  $z$  twice is facilitated by using the analytical forms [Eqs. (26) and (30)] for  $\mathbf{v}_1^{d,T}$ ,  $T_1^\delta$ , and  $\mathbf{v}_1^\delta$ , and by noting that in the boundary layer  $\eta_1^d \approx \eta_1^{d0} + z \partial_z \eta_1^d \approx (1 + k_c \delta_s) \eta_1^{d0} \approx \eta_1^{d0}$  and similarly  $\mathbf{v}_1^d \approx \mathbf{v}_1^{d0}$ ,

$$\mathbf{v}_1^\delta = \mathbf{v}_1^{\delta 0}(x, y) q(z) \quad \text{with } q(z) = e^{ik_s z}, \quad (42a)$$

$$T_1^\delta = T_1^{\delta 0}(x, y) r(z) \quad \text{with } r(z) = e^{ik_t z}, \quad (42b)$$

$$\eta_1^\delta = \eta_1^{\delta 0}(x, y) r(z), \quad (42c)$$

$$\mathbf{v}_1^d \approx \mathbf{v}_1^{d0} \quad \text{and} \quad \mathbf{v}_1^{d,p} \approx \mathbf{v}_1^{d0,p} \quad \text{for } z \ll d. \quad (42d)$$

Following the procedure of Ref. 11, we introduce the integrals  $I_{ab}^{(n)}$  of the integrand  $a(z) b(z)^*$ , where  $a(z)$  and  $b(z)$  are any of the functions 1,  $q(z)$ , and  $r(z)$ ,

$$\begin{aligned} I_{ab}^{(n)} &= \int dz_n \int dz_{n-1} \cdots \int dz_1 a(z_1) b(z_1)^* \Big|_{z=0}, \\ I_{ab}^{(n)} &\propto \delta^n \quad \text{with } \delta = \delta_s, \delta_t \text{ and } n = 1, 2, 3, \dots \quad (43) \end{aligned}$$

With this notation, Eq. (41) is easily integrated to give

$$\begin{aligned} \mathbf{v}_{2\parallel}^{\delta 0,T} &= \frac{\alpha_{p0} D_0^{\text{th}}}{\nu_0 \delta_t^2} \text{Re} \left[ \frac{\delta_t + i\delta_s}{\delta_s} I_{qr}^{(2)} \mathbf{v}_1^{\delta 0} T_1^{\delta 0*} + i I_{1r}^{(2)} \mathbf{v}_1^{d0,p} T_1^{\delta 0*} \right]_{\parallel} \\ &\quad - \frac{1}{\eta_0 \delta_s^2} \text{Re} \left[ \frac{\delta_s + i\delta_t}{\delta_t} I_{rq}^{(2)} \eta_1^{\delta 0} \mathbf{v}_1^{\delta 0*} + i I_{1q}^{(2)} \eta_1^{d0} \mathbf{v}_1^{\delta 0*} \right]_{\parallel}, \quad (44a) \end{aligned}$$

where the integrals are given by  $I_{ba}^{(n)} = [I_{ab}^{(n)}]^*$  and

$$I_{1r}^{(2)} = -\frac{i}{2}\delta_t^2, \quad I_{1q}^{(2)} = -\frac{i}{2}\delta_s^2, \quad I_{rq}^{(2)} = \frac{i\delta_s^2\delta_t^2}{2(\delta_s + i\delta_t)^2}. \quad (44b)$$

When inserting  $\rho_1^\delta = -\rho_0\alpha_p T_1^\delta$  in the final expression for the thermal correction,  $\mathbf{v}_{2\parallel}^{\delta 0,T}$  becomes

$$\begin{aligned} \mathbf{v}_{2\parallel}^{\delta 0,T} = & -\frac{1}{2\rho_0}\frac{\delta_t^2}{\delta_s^2}\text{Re}\left[\frac{\delta_s}{\delta_s - i\delta_t}\mathbf{v}_1^{\delta 0}\rho_1^{\delta 0*} + \mathbf{v}_1^{d0,p}\rho_1^{\delta 0*}\right]_{\parallel} \\ & -\frac{1}{2\eta_0}\text{Re}\left[\frac{\delta_t}{\delta_t - i\delta_s}\eta_1^{\delta 0}\mathbf{v}_1^{\delta 0*} + \eta_1^{d0}\mathbf{v}_1^{\delta 0*}\right]_{\parallel}, \end{aligned} \quad (45)$$

where two terms are due to the change in density and two to the change in viscosity. The perpendicular part of the short-ranged streaming velocity  $\mathbf{v}_{2z}^{\delta 0,T}$  can be found by integrating the continuity Eq. (35a),  $\partial_z v_{2z}^{\delta 0,T} = -\nabla_{\parallel} \cdot \mathbf{v}_{2\parallel}^{\delta 0,T} - \frac{1}{\rho_0}\nabla \cdot \langle \rho_1 \mathbf{v}_1 \rangle^{\delta 0,T}$ , once with respect to  $z$ ,

$$\mathbf{v}_{2z}^{\delta 0,T} = -\nabla_{\parallel} \cdot \int^z \mathbf{v}_{2\parallel}^{\delta 0,T} dz - \frac{1}{\rho_0} \int^z \nabla \cdot \langle \rho_1 \mathbf{v}_1 \rangle^{\delta 0,T} dz. \quad (46)$$

The term  $\int^z \mathbf{v}_{2\parallel}^{\delta 0,T} dz$  is given by Eq. (44a) by substituting all  $I_{ab}^{(2)}$  by  $I_{ab}^{(3)} \propto I_{ab}^{(2)}\delta$ , so  $|\nabla_{\parallel} \cdot \int^z \mathbf{v}_{2\parallel}^{\delta 0,T} dz| \sim (k_c\delta)|\mathbf{v}_{2\parallel}^{\delta 0,T}|$ , and  $\int^z \nabla \cdot \langle \rho_1 \mathbf{v}_1 \rangle^{\delta 0,T} dz \approx \int^z \partial_z \langle \rho_1 v_{1,z}^{d,p} \rangle dz = \langle \rho_1 v_{1,z}^{d,p} \rangle$ . Including pre-factors, we obtain to leading order in  $k_c\delta$ ,

$$\mathbf{v}_{2,z}^{\delta 0,T} = -\frac{1}{2\rho_0}\text{Re}\left[\rho_1^{\delta 0*}v_{1z}^{d0,p}\right]. \quad (47)$$

## B. Bulk field and effective boundary condition

With the short-range boundary-layer streaming term  $\mathbf{v}_2^{\delta 0} = \mathbf{v}_2^{\delta 0,p} + \mathbf{v}_2^{\delta 0,T}$  in place, it is now possible to set up the governing equations and boundary conditions for the second-order bulk acoustic streaming  $\mathbf{v}_2^d$ ,

$$0 = \nabla \cdot (\rho_0 \mathbf{v}_2^d) - \dot{\rho}_{ac}^d, \quad (48a)$$

$$0 = -\nabla p_2^d + \nabla \cdot \boldsymbol{\tau}_2^d + \hat{\mathbf{f}}_{ac}^d, \quad (48b)$$

$$\boldsymbol{\tau}_2^d = \eta_0 \left[ \nabla \mathbf{v}_2^d + (\nabla \mathbf{v}_2^d)^\dagger \right] + \beta \eta_0 (\nabla \cdot \mathbf{v}_2) \mathbf{I}, \quad (48c)$$

$$\mathbf{v}_2^{d0} = -\mathbf{v}_2^{\delta 0} - \frac{1}{\omega} \langle (i\mathbf{V}_1^0 \cdot \nabla) \mathbf{v}_1 \rangle|_{r=s_0}. \quad (48d)$$

Here,  $\dot{\rho}_{ac}^d$  and  $\hat{\mathbf{f}}_{ac}^d$  are the bulk terms in Eq. (36). In the mass-conservation equation,  $\nabla \cdot \mathbf{v}_2^d$  becomes

$$\nabla \cdot \mathbf{v}_2^d = -\frac{\nabla \cdot \langle \rho_1^d \mathbf{v}_1^{d,p} \rangle}{\rho_0} = \Gamma \frac{k_0 |\mathbf{v}_1^{d,p}|^2}{2c_0}. \quad (49)$$

Each term of  $\nabla \cdot \mathbf{v}_2^d$  scales as  $(k_0/c_0)|\mathbf{v}_1^{d,p}|^2 \gg (1/2)\Gamma(k_0/c_0)|\mathbf{v}_1^{d,p}|^2$ , so  $(1/\rho_0)\nabla \cdot \langle \rho_1^d \mathbf{v}_1^{d,p} \rangle$  is negligible compared to the individual terms in  $\nabla \cdot \mathbf{v}_2^d$ . We thus conclude that

$\nabla \cdot \mathbf{v}_2^d = 0$ , and that the streaming flow is incompressible. The acoustic body force  $\hat{\mathbf{f}}_{ac}^d$  may be expressed as follows, where  $\nabla \rho_0$  and  $\nabla \kappa_{s0}$  unlike in previous work<sup>6,9</sup> can be induced by temperature gradients:

$$\hat{\mathbf{f}}_{ac}^d = -\nabla \cdot \langle \rho_0 \mathbf{v}_1^{d,p} \mathbf{v}_1^{d,p} \rangle + \nabla \cdot \boldsymbol{\tau}_{11}^d \quad (50a)$$

$$\begin{aligned} & = -\nabla \langle \mathcal{L}_{ac}^d \rangle + \frac{1}{4} |\mathbf{v}_1^{d,p}|^2 \nabla \rho_0 + \frac{1}{4} |p_1|^2 \nabla \kappa_{s0} \\ & \quad - \frac{\Gamma \omega}{c_0^2} \langle \mathbf{v}_1^d p_1 \rangle + \nabla \cdot \boldsymbol{\tau}_{11}^d. \end{aligned} \quad (50b)$$

The gradient force  $-\nabla \langle \mathcal{L}_{ac}^d \rangle$  of the Lagrangian  $\langle \mathcal{L}_{ac}^d \rangle = (1/4) \kappa_{s0} |p_1|^2 - (1/4) \rho_0 |\mathbf{v}_1^d|^2$  does not induce streaming.<sup>11,18</sup> The next two terms form the inhomogeneous acoustic body force spawned by gradients in the density  $\rho_0$  and in the compressibility  $\kappa_{s0}$ .<sup>6</sup> The subsequent Eckart-streaming force term is important for either large systems or for rotating acoustic waves where  $\mathbf{v}_1^d$  and  $p_1$  have significant in-phase components.<sup>14</sup> The last contribution  $\nabla \cdot \boldsymbol{\tau}_{11}^d$  is due to the temperature-dependent viscosity,  $\eta_1^d = a_\eta \eta_0 \alpha_{p0} T_1^d = a_\eta (\gamma - 1) \eta_0 \kappa_{s0} p_1$ . Using  $\mathbf{v}_1^{d,p} \approx -i(1/\omega \rho_0) \nabla p_1$  as well as  $\nabla \cdot [\nabla \mathbf{v}_1^{d,p} + (\nabla \mathbf{v}_1^{d,p})^\dagger] = 2\nabla(\nabla \cdot \mathbf{v}_1^{d,p}) = -2k_c^2 \mathbf{v}_1^{d,p}$ ,  $\nabla \eta_1^d = a_\eta \eta_0 (\gamma - 1)(ik_c/c_0) \mathbf{v}_1^{d,p}$ , and  $\langle \eta_1(\nabla \cdot \mathbf{v}_1^{d,p}) \rangle \propto \langle p_1(ip_1) \rangle = 0$ , we reduce  $\nabla \cdot \boldsymbol{\tau}_{11}^d$  to

$$\begin{aligned} \nabla \cdot \boldsymbol{\tau}_{11}^d = & 2(\gamma - 1) a_\eta \eta_0 \frac{\omega^2}{c_0^2} \\ & \times \left[ \left\langle \left( \frac{i}{\omega} \mathbf{v}_1^{d,p} \cdot \nabla \right) \mathbf{v}_1^{d,p} \right\rangle - \kappa_{s0} \langle \mathbf{v}_1^{d,p} p_1 \rangle \right]. \end{aligned} \quad (51)$$

Here, the first and second term involve the Stokes drift and the classical Eckart attenuation [Eq. (50b)], respectively. Now, collecting the results [Eqs. (49)–(51)], the governing equations [Eq. (48a)–(48c)] of the acoustic streaming become

$$0 = \nabla \cdot \mathbf{v}_2^d, \quad (52a)$$

$$0 = -\nabla [p_2^d - \langle \mathcal{L}_{ac}^d \rangle] + \eta_0 \nabla^2 \mathbf{v}_2^d + \mathbf{f}_{ac}^d, \quad (52b)$$

$$\begin{aligned} \mathbf{f}_{ac}^d = & -\frac{1}{4} |\mathbf{v}_1^{d,p}|^2 \nabla \rho_0 - \frac{1}{4} |p_1|^2 \nabla \kappa_{s0} \\ & + \left[ 1 - \frac{2a_\eta(\gamma - 1)}{\beta + 1} \right] \frac{\Gamma \omega}{c_0^2} \langle \mathbf{v}_1^{d,p} p_1 \rangle \\ & + 2a_\eta \eta_0 (\gamma - 1) \frac{\omega}{c_0^2} \langle i \mathbf{v}_1^{d,p} \cdot \nabla \mathbf{v}_1^{d,p} \rangle. \end{aligned} \quad (52c)$$

Here, the Lagrangian density  $\langle \mathcal{L}_{ac}^d \rangle$  is merged with  $p_2^d$  as an excess pressure. Since  $\nabla \langle \mathcal{L}_{ac}^d \rangle$  is orders of magnitude larger than  $\mathbf{f}_{ac}^d$ , its merging with  $\nabla p_2^d$  renders the numerical simulation more accurate,<sup>18</sup> and makes it possible to use a coarser mesh in the bulk of the fluid domain.<sup>11</sup> The term  $-[2a_\eta(\gamma - 1)]/(\beta + 1) \approx 0.44$  leads to an increase in the bulk-driven Eckart streaming by 44% compared to a purely viscous model. The last term is due

to gradients in the viscosity  $\eta_1^d$ , so a fluid particle oscillating  $\mathbf{s}_1 = (i/\omega)\mathbf{v}_1^{d,p}$  experiences a varying viscosity during its oscillation period.

Finally, the thermal corrections to the boundary condition [Eq. (48d)] stem from  $\mathbf{v}_2^{\delta 0,T}$  in the boundary-layer velocity  $\mathbf{v}_2^{\delta 0} = \mathbf{v}_2^{\delta 0,p} + \mathbf{v}_2^{\delta 0,T}$ , see Eqs. (45) and (47), and from  $\mathbf{v}_1^{d,T}$  in  $\mathbf{v}_1 = \mathbf{v}_1^\delta + \mathbf{v}_1^{d,p} + \mathbf{v}_1^{d,T}$  in the Stokes drift term  $-(1/\omega) \langle (i\mathbf{V}_1^0 \cdot \nabla) \mathbf{v}_1 \rangle|_{r=s_0}$ . As  $|\mathbf{v}_{1\parallel}^{d,T}| \ll |v_{1z}^{d,T}|$ , then  $\mathbf{V}_1^0 \cdot \nabla \mathbf{v}_1^{d,T} \approx V_{1,z}^0 \alpha_{p0} D_0^{\text{th}} \partial_z^2 T_1^\delta \mathbf{e}_z = (\omega/\rho_0) V_{1,z}^0 (i\rho_1^\delta) \mathbf{e}_z$ ,

$$\frac{1}{\omega} \langle (i\mathbf{V}_1^0 \cdot \nabla) \mathbf{v}_1^{d,T} \rangle|_{r=s_0} = \frac{1}{2\rho_0} \text{Re} \left[ V_{1,z}^0 \rho_1^{\delta 0*} \right] \mathbf{e}_z. \quad (53)$$

In terms of the  $\mathbf{A}$ - and  $\mathbf{B}$ -vector notation of Ref. 11, the boundary condition [Eq. (48d)] for the streaming velocity  $\mathbf{v}_2^d$  is given by the purely viscous terms (superscript “vs”) from Ref. 11 and the thermal corrections (superscript “th”) due to  $\mathbf{v}_2^{\delta 0,T}$ , Eqs. (45) and (47), and  $\mathbf{v}_1^{d0,T}$ , Eq. (53),

$$\mathbf{v}_2^{d0} = (\mathbf{A} \cdot \mathbf{e}_x) \mathbf{e}_x + (\mathbf{A} \cdot \mathbf{e}_y) \mathbf{e}_y + (\mathbf{B} \cdot \mathbf{e}_z) \mathbf{e}_z, \quad (54a)$$

with  $\mathbf{A} = \mathbf{A}^{\text{vs}} + \mathbf{A}^{\text{th}}$ ,  $\mathbf{B} = \mathbf{B}^{\text{vs}} + \mathbf{B}^{\text{th}}$ ,

$$\mathbf{A}^{\text{vs}} = -\frac{1}{2\omega} \text{Re} \left[ \mathbf{v}_1^{\delta 0*} \cdot \nabla \left( \frac{1}{2} \mathbf{v}_1^{\delta 0} - i\mathbf{V}_1^0 \right) - i\mathbf{V}_1^{0*} \cdot \nabla \mathbf{v}_1^{d,p} + \left\{ \frac{2-i}{2} \nabla \cdot \mathbf{v}_1^{\delta 0*} + i \left( \nabla \cdot \mathbf{V}_1^0 - \partial_z v_{1z}^{d,p*} \right) \right\} \mathbf{v}_1^{\delta 0} \right], \quad (54b)$$

$$\mathbf{A}^{\text{th}} = \frac{1}{2\rho_0} \frac{\delta_t^2}{\delta_s^2} \text{Re} \left[ \frac{\delta_s}{\delta_s - i\delta_t} \mathbf{v}_1^{\delta 0} \rho_1^{\delta 0*} + \mathbf{v}_1^{d0,p} \rho_1^{\delta 0*} \right] + \frac{1}{2\eta_0} \text{Re} \left[ \frac{\delta_t}{\delta_t - i\delta_s} \eta_1^{\delta 0} \mathbf{v}_1^{\delta 0*} + \eta_1^{d0} \mathbf{v}_1^{\delta 0*} \right], \quad (54c)$$

$$\mathbf{B}^{\text{vs}} = \frac{1}{2\omega} \text{Re} \left[ i\mathbf{v}_1^{d0,p*} \cdot \nabla \mathbf{v}_1^{d,p} \right], \quad (54d)$$

$$\mathbf{B}^{\text{th}} = \frac{1}{2\rho_0} \text{Re} \left[ \left( \mathbf{v}_1^{d0,p} - \mathbf{V}_1^0 \right) \rho_1^{\delta 0*} \right]. \quad (54e)$$

The magnitude of the thermal terms are  $(\gamma - 1)a_q$  times the magnitude of the leading viscous terms. For water,  $(\gamma - 1)|a_\eta| \approx 0.9$  and  $(\gamma - 1)|a_\rho| \approx 0.01$  at room temperature, so here, the  $\eta_1$ -terms are important and must be included in acoustofluidic analyses, whereas  $\rho_1$ -terms are negligible. For gases with  $\gamma - 1 \approx 0.4$ , the density terms may be important.

The results in Eqs. (52) and (54) are our main results for the second-order streaming part of the effective thermoviscous theory, and they form the equations that are implemented in our numerical model.

## VI. NUMERICAL IMPLEMENTATION AND EXAMPLES

We implement the effective thermoviscous model in the commercial finite-element software COMSOL Multiphysics.<sup>19</sup> It is validated by comparisons to full

numerical simulations, and two examples of significant thermal effects in acoustofluidic devices are shown. All simulations are done in COMSOL 5.6<sup>19</sup> on a HP-G4 workstation with a processor Intel Core i9-7960X @ 4.20 GHz and with 128 GB ram.

The effective thermoviscous model solver contains three steps: (1) the zeroth-order thermal field, (2) the acoustic pressure and displacement fields, and (3) the stationary streaming fields. The acoustic temperature field  $T_1$  is included analytically and therefore does not increase the numerical workload compared to the purely viscous model. The effective thermoviscous theory allows us to simulate acoustofluidic systems in three dimensions, which has prohibitive numerical costs for the full model.

Following our previous work,<sup>5,6,11,12,20</sup> the governing equations [Eqs. (16), (19), (22a), and (52)] are implemented in COMSOL using the mathematical PDE Module. The surface fields (superscript “0”) are defined only on the fluid-solid interfaces. The effective boundary conditions [Eq. (34)] for  $p_1$  and  $\mathbf{u}_1$  are implemented as weak contributions, whereas the boundary condition in Eq. (54) for  $\mathbf{v}_2^d$  is implemented as a Dirichlet boundary condition. Further details on the implementation of the numerical model in COMSOL are presented in the supplementary material.<sup>21</sup>

### A. Example I: Two-dimensional (2D) streaming in a square channel

The first example is the square channel, which has been studied both experimentally<sup>22–24</sup> and numerically.<sup>22</sup> In a square channel, a rotating acoustic wave can be set up by two perpendicular, out-of-phase standing waves, as analyzed theoretically by Bach and Bruus.<sup>14</sup> We apply the effective thermoviscous model in the fluid domain of the square channel in the 2D  $yz$  cross section with the velocity  $\mathbf{V}_1^0 = V_0 e^{-i\omega t} \mathbf{e}_y$  at the vertical sides  $y = \pm(1/2)W$  and  $\mathbf{V}_1^0 = iV_0 e^{-i\omega t} \mathbf{e}_z$  at the horizontal sides  $z = \pm(1/2)H$ , a rigid-wall model with side length  $H = W = 230 \mu\text{m}$ . The zeroth-order temperature field is set to be constant,  $T_0 = 20 \text{ }^\circ\text{C}$ . We emphasize three main points of the results, shown in Fig. 2: (1) The effective model reduces the computational time and memory requirements significantly. (2) Given that it is 2D, the full model can be simulated, and it agrees with and thus validates the effective model. (3) The thermal corrections strongly influence the streaming flow pattern.

The meshes plotted on top of the pressure field in Fig. 2(a) are the ones needed to obtain an  $L_2$ -norm-convergence<sup>5</sup> of 0.1% for  $p_1$  and 1% for the streaming  $\mathbf{v}_2$  for the full and for the effective model. With computation times of 15 versus 2 s and 130 042 degrees of freedoms versus 1788, the effective model is in this case seven times faster and requires 130 times less memory than the full mode to achieve the same accuracy. Figures 2(b)–2(f) show the resulting streaming  $\mathbf{v}_2$  obtained using different assumptions. Figures 2(e) and 2(f) illustrate that the effective and full models agree, thus validating the former. Figure 2(b) shows how much  $\mathbf{v}_2$  is changed when disregarding all thermal



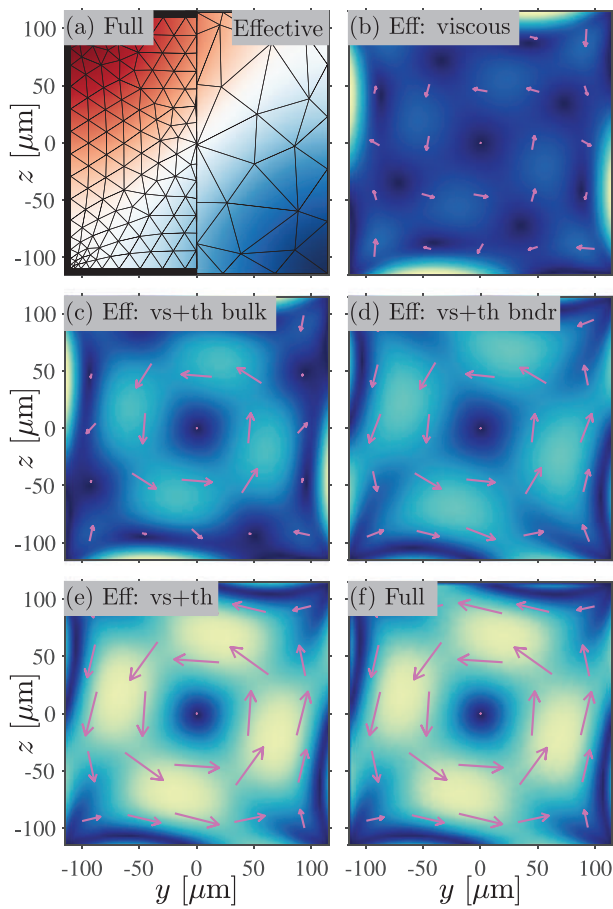


FIG. 2. (Color online) Simulated fields in a square channel with a rotating pressure wave of energy density  $E_{ac} = 19 \text{ J/m}^3$  actuated as described in the text. (a) Color plot of  $p_1$  at time  $t = 0$  from  $-0.4$  (blue) to  $+0.4$  MPa (red), and the mesh used in the full (left) and in the effective (right) thermoviscous model. (b) Vector plot of the streaming velocity  $v_2$  (magenta) and color plot of its magnitude from  $0$  (dark blue) to  $20 \mu\text{m/s}$  (yellow) [same scale in (b)–(f)] for the effective viscous model without thermal terms. (c)  $v_2$  for the effective viscous model with thermal bulk terms. (d)  $v_2$  for the effective viscous model with thermal boundary terms. (e)  $v_2$  for the complete effective thermoviscous model. (f)  $v_2$  for the full thermoviscous model.

effects as in Ref. 11, whereas Figs. 2(c) and 2(d) illustrate the effect of adding only the thermal bulk effects of Eq. (52), and adding only the thermal correction to the boundary condition of Eq. (54). Clearly, all the thermal effects need to be added, and in this example, they stem from the temperature dependence of the viscosity through  $\eta_1$  in the bulk term [Eq. (50)]  $\nabla \cdot \tau_{11}$  and the boundary term [Eq. (54)]  $A^T$ . Physically, the bulk term strengthens the central streaming roll, whereas the boundary term changes the morphology of the boundary streaming and additionally strengthens the central streaming roll.

### B. Example II: 3D streaming due to thermal fields

The second example is the capillary glass tube widely used as a versatile acoustic trap in many experimental studies.<sup>23–26</sup> Inside the tube, in the region above the piezoelectric transducer, a characteristic streaming flow pattern containing four horizontal flow rolls is established.<sup>25</sup> This

pattern cannot be explained in numerical modeling<sup>20,27</sup> in terms of boundary-driven streaming or classical bulk Eckart streaming; however, here we argue, based on our thermoacoustic simulation results, that thermal effects are responsible for this streaming pattern. This result is important as the streaming pattern is used to lead nanoparticles into the central region, where they are trapped by larger seed particles.

The 3D model, see Fig. 3, is similar to device C1 in our previous work:<sup>20</sup> a glass capillary tube of width  $W = 2 \text{ mm}$  and height  $H = 0.2 \text{ mm}$ , actuated from below in its central region by a piezoelectric transducer. The temperature is set to  $T_{\text{air}} = 25 \text{ }^\circ\text{C}$  at  $x = L_{\text{end}}$  and to zero flux on all other outer surfaces except on the transducer. For simplicity, the transducer is represented by a (red) region of width  $W_{\text{PZT}}$ , length  $L_{\text{PZT}} = 1.16 \text{ mm}$  on the glass surface, with a given oscillatory displacement  $\mathbf{u} = \mathbf{u}_{\text{PZT}} e^{-i\omega t}$  and steady temperature<sup>28</sup>  $T = T_{\text{air}} + T_{\text{PZT}}$ , where  $\mathbf{u}_{\text{PZT}} = u_0 \mathbf{e}_z$  with  $u_0 = 0.25 \text{ nm}$  and  $T_{\text{PZT}} = 1.5 \text{ }^\circ\text{C}$ . We exploit the  $xz$  and  $yz$  symmetry planes and simulate only a quarter of the system. To simulate an infinitely long channel, we use a perfectly matched layer (PML) to avoid reflections from the ends.<sup>20,21,29</sup>

The mesh shown in Fig. 3(a) results in an  $L_2$ -norm-convergence<sup>5</sup> of 1% in the pressure  $p_1$  and in the streaming  $v_2$ , and of 3% in the displacement  $u_1$ . The simulation requires 491,959 degrees of freedom and takes 7 min.

For the steady temperature  $T_0$  shown in Fig. 3(b), we find by inspection a resonance at  $f = 3.898 \text{ MHz}$ , for which the resulting acoustic displacement  $\mathbf{u}_1$  and pressure  $p_1$  are

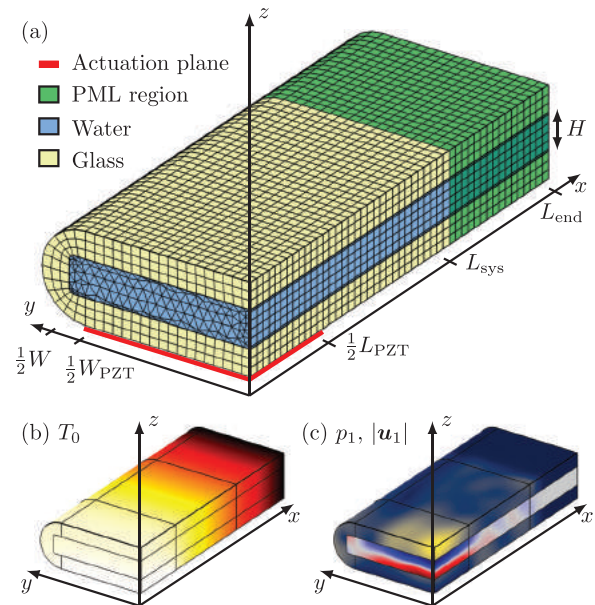


FIG. 3. (Color online) (a) The simulated 3D system (reduced to a quarter by symmetry) consisting of the water (blue), the glass (yellow), and the artificially absorbing PML (green) domains described further in the supplementary material (Ref. 21). Also, shown are the actuation region (red) and the mesh (black). (b) Color plot of the steady temperature  $T_0$  from  $20.0$  (black) to  $21.5 \text{ }^\circ\text{C}$  (yellow). (c) Color plots of the displacement  $|u_1|$  in the glass from  $0$  (blue) to  $9.5 \text{ nm}$  (yellow) and the acoustic pressure  $p_1$  in the water from  $-1.6$  (blue) to  $+1.6 \text{ MPa}$  (red). Note the dampening of  $u_1$  and  $p_1$  in the PML region.

shown in Fig. 3(c).  $T_0$  is inhomogeneous with an almost constant temperature gradient along the tube in the  $x$ -direction, and, in agreement with previous experiments<sup>25</sup> and simulations,<sup>20</sup>  $p_1$  appears as a vertical half-wave resonance localized in the region above the transducer, but stronger in the center than at the sides. Combining the effects of  $p_1$  and the  $T_0$ -dependency of the density  $\rho_0$  and compressibility  $\kappa_{s0}$ , the acoustic body force [Eq. (52c)] driving the streaming  $v_2$  becomes

$$\begin{aligned} f_{ac}^d &\approx -\frac{1}{4} |v_1|^2 \nabla \rho_0 - \frac{1}{4} |p_1|^2 \nabla \kappa_{s0} \\ &= -\frac{1}{4} (a_\rho \rho_0 |v_1|^2 + a_\kappa \kappa_{s0} |p_1|^2) \alpha_{p0} \nabla T_0. \end{aligned} \quad (55)$$

Since by Eq. (5),  $\kappa_s$  has a stronger temperature dependency than  $\rho$ ,  $f_{ac}^d$  is dominated by the  $|p_1|^2$ -term. This results in a body force parallel to  $\nabla T_0$  and strongest in the center, where  $|p_1|$  is maximum.

The numerical simulation result for  $v_2$  is shown in Fig. 4: The characteristic four horizontal flow rolls are clearly seen, the radius of which is determined by the width of the

channel and the width of the actuation as observed by Hammarström *et al.*<sup>25</sup> This phenomenon is explained in terms of the acoustic body force  $f_{ac}^d$ , which pushes the liquid into the center region near the vertical  $xz$ -plane at  $y = 0$ , where it is strongest, accompanied by a back-flow at the edges near  $y = \pm(1/2)W$ , where the body force is weaker. In Fig. 4(a),  $v_2$  is shown in three different horizontal planes. The variation in the flow rolls reflects the  $z$ -dependence of the thermal gradient above the transducer. In Fig. 4(b),  $v_2$  is shown in the full horizontal plane at  $z = 0 \mu\text{m}$ . Note how the four flow roll centers are located near the edge (red lines) of the actuation region. To emphasize the crucial role of the thermal effects, we show in Fig. 4(c) the streaming flow resulting from neglecting all thermal effects: In agreement with previous purely viscous models, but in contrast to experimental observations, the characteristic four-flow-roll pattern does not appear. Another important feature of the thermoviscous streaming is its magnitude. In Fig. 4,  $|v_2| = 50 \mu\text{m/s}$  is obtained with an acoustic energy density of  $E_{ac} = 77 \text{ J/m}^3$ . This is five times larger than the  $10 \mu\text{m/s}$  of the purely viscous streaming, and notably only a factor of 3 lower than the  $150\text{-}\mu\text{m/s}$ -limit of Sec. II E that marks the validity of the applied effective thermoviscous model.

In conclusion, the example highlights two important aspects: (1) The effective thermoviscous model enables 3D thermoviscous simulations in acoustofluidic systems, and (2) even moderate thermal gradients may create high streaming velocities in acoustofluidic systems. Such gradients can of course be created not only by heat generation in the transducer as in this example, but also more controllable by ohmic wires, Peltier elements, and external light sources. Notably, the validity of the perturbation approach breaks down at moderately high, but experimentally obtainable acoustic energy densities above  $\sim 100 \text{ J/m}^3$  in combination with a moderate thermal gradient  $\sim 1 \text{ K/mm}$ , and this calls for an extension beyond perturbation theory of the presented theory.

## VII. CONCLUSION

We have derived an effective thermoviscous theory for a fluid embedded in an elastic solid. The steady zeroth order temperature field is governed by Eq. (16). The acoustic fields are governed by the Helmholtz equations, Eqs. (19) and (23), the decompositions [Eqs. (20) and (24)], and the effective boundary conditions [Eq. (34)]. The time-averaged acoustic streaming is governed by the effective Stokes equation, Eq. (52), and the effective boundary conditions, Eq. (54). The theory includes the thermoviscous boundary layers and the acoustic temperature field  $T_1$  analytically, and impose them as effective boundary conditions and time-averaged body forces on the thermoacoustic bulk fields.

The theory has been implemented in a numerical model,<sup>21</sup> which, because it avoids resolving numerically the boundary layers, allows for simulating both the first-order thermoviscous acoustic fields and second-order steady fields in 3D models of acoustofluidic systems. A conventional

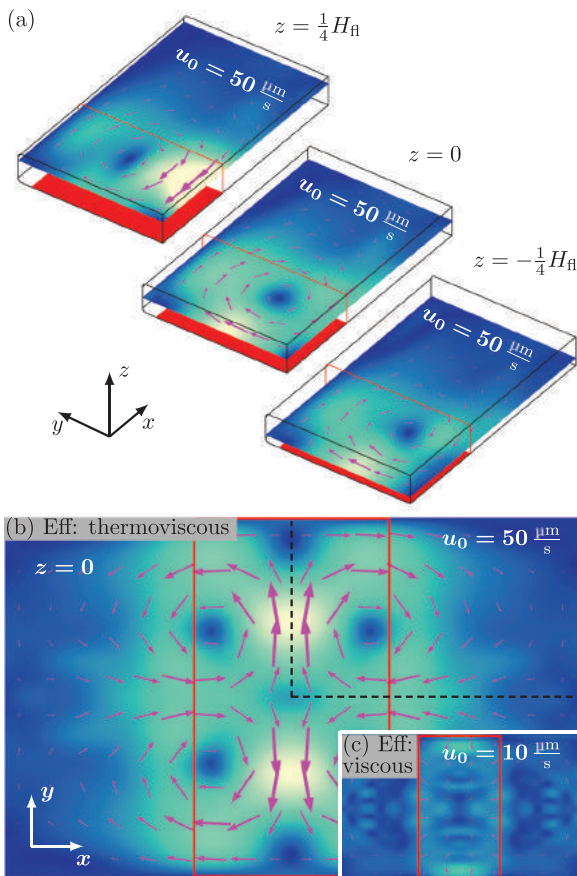


FIG. 4. (Color online) The streaming velocity  $v_2$  (magenta arrows) and its magnitude from 0 (blue) to  $u_0 = 50 \mu\text{m/s}$  (yellow) in a symmetry quarter of the trapping capillary tube. (a)  $v_2$  in three different horizontal planes. (b)  $v_2$  in the full central plane  $z = 0$ . The dashed black lines show the symmetry planes, and the red lines the edge of the actuation region. (c)  $v_2$  in the central plane  $z = 0$  without thermal effects. Note that here  $u_0 = 10 \mu\text{m/s}$ .

brute-force direct numerical simulations is very difficult due to large memory requirements. In 2D, the model was validated by direct numerical simulations, and in 3D, its self-consistency has been checked by mesh-convergence analyses.

We have applied the effective thermoviscous model in two numerical examples to demonstrate the importance of thermoviscous effects in microscale acoustofluidic devices. In particular, we have shown how the acoustic streaming depends strongly on the thermal fields: (1) The oscillating temperature field  $T_1$  impacts the streaming through the temperature dependency of the viscosity, causes corrections to the effective boundary condition, and spawns an additional body force in the bulk. In the 2D model of the square channel in Sec. VIA and Fig. 2, we have shown how the thermoviscous effects are particularly important for the morphology and magnitude of the streaming in a rotating acoustic field. (2) The presence of an inhomogeneous stationary temperature field  $T_0$  affects the streaming through the induced gradients in compressibility and density. In the 3D model of the capillary glass tube in Sec. VIB and Fig. 4, we have shown, how the experimentally-observed characteristic horizontal streaming rolls in the standing acoustic resonance of Fig. 3, are caused by heating from the actuation area. We have also shown, how very high streaming velocities ( $\sim 1$  mm/s) can be caused by small temperature gradients ( $\sim 1$  K/mm) for moderate acoustic energy densities ( $\sim 100$  J/m<sup>3</sup>).

Our theoretical model enables 3D simulations of thermoviscous effects in microscale acoustofluidic devices. The results point to new ways for microscale handling of fluids and particles using a combination of acoustic and thermal fields. Although we have developed the effective thermoviscous theory within the narrow scope of microscale acoustofluidics, it is more general and may find wider use in other branches of thermoacoustics.

## ACKNOWLEDGEMENTS

This work was supported by Independent Research Fund Denmark, Natural Sciences (Grant No. 8021-00310B).

<sup>1</sup>A. A. Doynikov, "Acoustic radiation force on a spherical particle in a viscous heat-conducting fluid. I. General formula," *J. Acoust. Soc. Am.* **101**(2), 713–721 (1997).  
<sup>2</sup>S. D. Danilov and M. A. Mironov, "Mean force on a small sphere in a sound field in a viscous fluid," *J. Acoust. Soc. Am.* **107**(1), 143–153 (2000).  
<sup>3</sup>J. T. Karlsen and H. Bruus, "Forces acting on a small particle in an acoustic field in a thermoviscous fluid," *Phys. Rev. E* **92**, 043010 (2015).  
<sup>4</sup>A. Y. Rednikov and S. S. Sadhal, "Acoustic/steady streaming from a motionless boundary and related phenomena: Generalized treatment of the inner streaming and examples," *J. Fluid. Mech.* **667**, 426–462 (2011).  
<sup>5</sup>P. B. Muller and H. Bruus, "Numerical study of thermoviscous effects in ultrasound-induced acoustic streaming in microchannels," *Phys. Rev. E* **90**(4), 043016 (2014).

<sup>6</sup>J. T. Karlsen, P. Augustsson, and H. Bruus, "Acoustic force density acting on inhomogeneous fluids in acoustic fields," *Phys. Rev. Lett.* **117**, 114504 (2016).  
<sup>7</sup>P. Augustsson, J. T. Karlsen, H.-W. Su, H. Bruus, and J. Voldman, "Iso-acoustic focusing of cells for size-insensitive acousto-mechanical phenotyping," *Nat. Commun.* **7**, 11556 (2016).  
<sup>8</sup>J. T. Karlsen and H. Bruus, "Acoustic tweezing and patterning of concentration fields in microfluidics," *Phys. Rev. Appl.* **7**, 034017 (2017).  
<sup>9</sup>J. T. Karlsen, W. Qiu, P. Augustsson, and H. Bruus, "Acoustic streaming and its suppression in inhomogeneous fluids," *Phys. Rev. Lett.* **120**(5), 054501 (2018).  
<sup>10</sup>W. Qiu, J. T. Karlsen, H. Bruus, and P. Augustsson, "Experimental characterization of acoustic streaming in gradients of density and compressibility," *Phys. Rev. Appl.* **11**(2), 024018 (2019).  
<sup>11</sup>J. S. Bach and H. Bruus, "Theory of pressure acoustics with viscous boundary layers and streaming in curved elastic cavities," *J. Acoust. Soc. Am.* **144**, 766–784 (2018).  
<sup>12</sup>N. R. Skov, J. S. Bach, B. G. Winkelmann, and H. Bruus, "3D modeling of acoustofluidics in a liquid-filled cavity including streaming, viscous boundary layers, surrounding solids, and a piezoelectric transducer," *AIMS Math.* **4**, 99–111 (2019).  
<sup>13</sup>N. R. Skov, P. Sehgal, B. J. Kirby, and H. Bruus, "Three-dimensional numerical modeling of surface-acoustic-wave devices: Acoustophoresis of micro- and nanoparticles including streaming," *Phys. Rev. Appl.* **12**, 044028 (2019).  
<sup>14</sup>J. S. Bach and H. Bruus, "Bulk-driven acoustic streaming at resonance in closed microcavities," *Phys. Rev. E* **100**, 023104 (2019).  
<sup>15</sup>L. D. Landau and E. M. Lifshitz, *Theory of Elasticity. Course of Theoretical Physics*, 3rd ed. (Pergamon Press, Oxford, UK, 1986), Vol. 7.  
<sup>16</sup>L. D. Landau and E. M. Lifshitz, *Fluid Mechanics*, 2nd ed. (Pergamon Press, Oxford, UK, 1993), Vol. 6.  
<sup>17</sup>L. D. Landau and E. M. Lifshitz, *Statistical Physics, Part 1*, 3rd ed. (Butterworth-Heinemann, Oxford, UK, 1980), Vol. 5.  
<sup>18</sup>A. Riaud, M. Baudoin, O. Bou Matar, J.-L. Thomas, and P. Brunet, "On the influence of viscosity and caustics on acoustic streaming in sessile droplets: An experimental and a numerical study with a cost-effective method," *J. Fluid Mech.* **821**, 384–420 (2017).  
<sup>19</sup>COMSOL, "COMSOL Multiphysics 5.6," <http://www.comsol.com> (30 March 2021).  
<sup>20</sup>M. W. H. Ley and H. Bruus, "Three-dimensional numerical modeling of acoustic trapping in glass capillaries," *Phys. Rev. Appl.* **8**, 024020 (2017).  
<sup>21</sup>See supplementary material at <https://www.scitation.org/doi/suppl/10.1121/10.0005005> for details on the material parameters and on the COMSOL implementation of geometry, mesh, PML, and effective and symmetry boundary conditions.  
<sup>22</sup>M. Antfolk, P. B. Muller, P. Augustsson, H. Bruus, and T. Laurell, "Focusing of sub-micrometer particles and bacteria enabled by two-dimensional acoustophoresis," *Lab Chip* **14**, 2791–2799 (2014).  
<sup>23</sup>P. Mishra, M. Hill, and P. Glynn-Jones, "Deformation of red blood cells using acoustic radiation forces," *Biomicrofluidics* **8**(3), 034109 (2014).  
<sup>24</sup>I. Gralinski, S. Raymond, T. Alan, and A. Neild, "Continuous flow ultrasonic particle trapping in a glass capillary," *J. Appl. Phys.* **115**(5), 054505 (2014).  
<sup>25</sup>B. Hammarström, T. Laurell, and J. Nilsson, "Seed particle-enabled acoustic trapping of bacteria and nanoparticles in continuous flow systems," *Lab Chip* **12**, 4296–4304 (2012).  
<sup>26</sup>J. Lei, P. Glynn-Jones, and M. Hill, "Acoustic streaming in the transducer plane in ultrasonic particle manipulation devices," *Lab Chip* **13**(11), 2133–2143 (2013).  
<sup>27</sup>H. Lei, D. Henry, and H. BenHadid, "Acoustic force model for the fluid flow under standing waves," *Appl. Acoust.* **72**(10), 754–759 (2011).  
<sup>28</sup>G. Werr, Z. Khaji, M. Ohlin, M. Andersson, L. Klintberg, S. S. Searle, K. Hjort, and M. Tenje, "Integrated thin film resistive sensors for *in situ* temperature measurements in an acoustic trap," *J. Micromech. Microeng.* **29**(9), 095003 (2019).  
<sup>29</sup>F. Collino and P. B. Monk, "Optimizing the perfectly matched layer," *Comput. Methods. Appl. Mech. Eng.* **164**(1-2), 157–171 (1998).

## 7.2 Paper II in Physical Review Letters

*Fast microscale acoustic streaming driven by a temperature-gradient-induced non-dissipative acoustic body force*

**DOI:** [10.1103/PhysRevLett.127.064501](https://doi.org/10.1103/PhysRevLett.127.064501)

**Authors:** W. Qiu, J. H. Joergensen, E. Corato, H. Bruus, and Per Augustsson.


**Journal:** Phys. Rev. Lett. **127**, 064501 1-6 (2021)

## Fast Microscale Acoustic Streaming Driven by a Temperature-Gradient-Induced Nondissipative Acoustic Body Force

Wei Qiu<sup>1,\*</sup>, Jonas Helboe Joergensen<sup>2,†</sup>, Enrico Corato<sup>1</sup>, Henrik Bruus<sup>2,‡</sup>, and Per Augustsson<sup>1,§</sup>

<sup>1</sup>Department of Biomedical Engineering, Lund University, Ole Römers väg 3, 22363 Lund, Sweden

<sup>2</sup>Department of Physics, Technical University of Denmark, DTU Physics Building 309, DK-2800 Kongens Lyngby, Denmark

 (Received 16 March 2021; accepted 30 June 2021; published 3 August 2021)

We study acoustic streaming in liquids driven by a nondissipative acoustic body force created by light-induced temperature gradients. This thermoacoustic streaming produces a velocity amplitude nearly 100 times higher than the boundary-driven Rayleigh streaming and the Rayleigh-Bénard convection at a temperature gradient of 10 K/mm in the channel. The Rayleigh streaming is altered by the acoustic body force at a temperature gradient of only 0.5 K/mm. The thermoacoustic streaming allows for modular flow control and enhanced heat transfer at the microscale. Our study provides the groundwork for studying microscale acoustic streaming coupled with temperature fields.

DOI: 10.1103/PhysRevLett.127.064501

Acoustic streaming describes the steady time-averaged fluid motion that takes place when acoustic waves propagate in viscous fluids. The streaming flow is driven by a nonzero divergence in the time-averaged acoustic momentum-flux-density tensor [1]. Conventionally, in a homogeneous fluid, this nonzero divergence arises from two dissipation mechanisms of acoustic energy. The first case is the boundary-driven Rayleigh streaming [2], in which acoustic energy is dissipated in viscous boundary layers where the velocity of the oscillating fluid changes to match the surface velocity of the channel walls [3,4] or of the suspended objects [5–8]. The resulting stress drives the flow [9], typically observed in standing wave fields in systems of a size comparable to the wavelength [10]. The second type of streaming, quartz wind or bulk-driven Eckart streaming [11], is driven by gradients induced by high acoustic wave attenuation typically associated with high-frequency traveling waves [11–13]. Both cases have been extensively studied, and the phenomenon of acoustic streaming continues to attract attention due to its importance related to medical ultrasound [14–17], thermoacoustic engines [18,19], acoustic levitation [7,20], manipulation of particles and cells in microscale acoustofluidics [21–28], and control of streaming by the shape of the walls [29,30].

Recently, we discovered that boundary-driven streaming can be significantly suppressed in inhomogeneous media formed by solute molecules [31,32]. This suppression is attributed to the acoustic body force  $f_{ac}$ , which originates from the nonzero divergence in the time-averaged momentum-flux-density tensor induced by gradients in density and compressibility in the fluids [33,34] and competes with the boundary-layer stress. The streaming rolls are confined to narrow regions near the channel walls, before the inhomogeneity is smeared out by diffusion and advection of the solute. This effect enables acoustic manipulation of

submicrometer particles [35], such as bacteria [36], and trapping of hot plasma in gases [37].

In this Letter, we investigate microscale acoustic streaming in a liquid, in which the temperature-dependent compressibility and density have been made inhomogeneous by introducing a steady temperature gradient. We generate this gradient by light irradiation and absorption, and subsequently measure the streaming driven by the temperature-gradient-induced acoustic body force and call it thermoacoustic streaming. Using our newly developed model for thermoviscous acoustofluidics [38], the experimental results are validated and the mechanisms responsible for the thermoacoustic streaming are explained.

Our main findings are (i) the thermoacoustic streaming begins to disturb the boundary-driven Rayleigh streaming for a temperature gradient as small as 0.5 K/mm, resulting in streaming rolls with complex three-dimensional (3D) patterns. (ii) For a temperature gradient of 10 K/mm, the thermoacoustic streaming velocity is nearly 100 times higher than that of the boundary-driven Rayleigh streaming and of the Rayleigh-Bénard convection. (iii) In contrast to other types of acoustic streaming, the mechanism driving the thermoacoustic streaming is nondissipative.

The thermoacoustic streaming is of considerable fundamental relevance to a broad community of researchers working in nonlinear acoustics, thermoacoustics, microscale acoustofluidics, as well as heat transfer. For a microsystem, the advective streaming flow is remarkably high compared to the rate of thermal diffusion, and with a Péclet number  $Pe \approx 1$ , heat transfer is strongly enhanced. Further, our findings pave the way for transient or steady control of the streaming through modulations of the temperature field or the acoustic field.

*Experimental method.*—The experiments were performed using a long straight microchannel of width

$W = 760 \mu\text{m}$  and height  $H = 370 \mu\text{m}$  in a glass-silicon-glass chip with a piezoelectric transducer glued on. The temperature gradient inside the channel was generated by directing the focused light from a 470-nm light-emitting diode (LED) through water containing a dilute dye solution (0.1 wt% Orange G) that has an overlapping absorption peak with the LED, see Fig. 1. We measured that 99% of the LED light was absorbed in the liquid. The transducer was run with an input power of 88 mW at 953 kHz, resulting in a standing half wave across the width with an acoustic energy density  $E_{\text{ac}} = 9.24 \text{ J/m}^3$  measured as in Ref. [32]. The induced streaming was measured using the general defocusing particle tracking technique [39–41] at 5 to 60 fps with  $1.1 \mu\text{m}$ -diameter polystyrene tracer particles (red fluorescence), well below the critical diameter of  $2.9 \mu\text{m}$  that marks the cross-over to where streaming drag becomes the dominant force [35]. Green LED light passes through a band-pass filter (525–550 nm) and excites the tracer particles. It is barely absorbed by the dye and hence does not affect the temperature in the channel. The measurements under each condition were repeated 13 to 27 times and recorded in 7800 to 40 500 frames to improve the statistics. The temperature field around the channel midheight plane was imaged using temperature-sensitive fluorescent dye (Rhodamine B); see the Supplemental Material [42].

**Numerical model.**—The model is the effective pressure acoustics model of Ref. [38], which includes thermoviscous

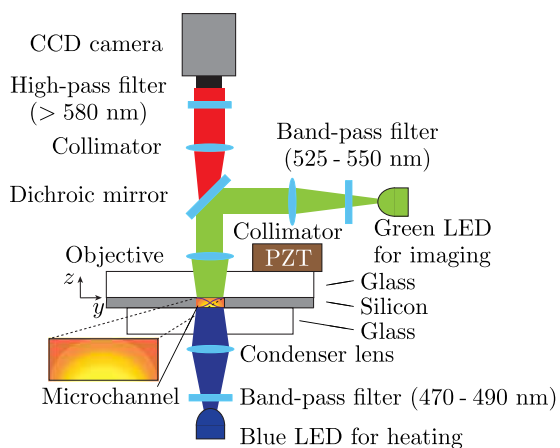


**FIG. 1.** Sketch of the acoustofluidic silicon chip (light gray) sandwiched between two glass layers (white) that allows optical transparency for both heating and particle tracking. The light emitted from a blue LED below the chip is absorbed by the aqueous dye solution and a temperature gradient forms from low (orange) to high (yellow) temperature in the channel. The piezoelectric transducer (PZT, dark brown) excites the resonant half-wave pressure field  $p_1$  (purple) at 953 kHz. A green LED shines light from above to excite red fluorescent light from the tracer particles, which allows for optical recording of the tracer bead motion in a part of length  $L = 1300 \mu\text{m}$  of the channel of width  $W = 760 \mu\text{m}$  and height  $H = 370 \mu\text{m}$ .

boundary layers and enables 3D simulations of thermoviscous acoustofluidic devices. To simulate the long glass-silicon-glass chip, symmetry planes are exploited to only simulate a quarter of the chip. Furthermore, the perfectly matched layer technique [53] is used to avoid simulating the entire length of the chip. The solver consists of three steps: (i) Computing the temperature field  $T_0$  induced by the LED with an amplitude set to match the observed temperature gradients, (ii) computing the acoustic displacement  $u_1$  in the solid and the pressure  $p_1$  in the fluid due to an actuation on the glass, and (iii) computing the resulting acoustic streaming field  $v_2$ . The heating from the LED is modeled with no absorption in the glass and an absorption parameter in the fluid selected to absorb 99% of the light passing through the chip as measured in the experiment. The model is based on perturbation theory, but the highest streaming velocities recorded in the experiments are found to be at the limit of the validity of the model, because there the thermoacoustic streaming begins to alter the temperature field  $T_0$ . For more details on the numerical model see the Supplemental Material [42]. Because the inherent difficulty in measuring the energy density  $E_{\text{ac}}$  at high streaming velocities when temperature gradients are present, the  $E_{\text{ac}}$  used in simulations is obtained by matching the experimental streaming velocity amplitude for each temperature gradient.

**Results and discussion.**—When both acoustics and temperature gradients are present, the streaming flow exhibits a complex 3D pattern. An example is shown in Figs. 2(a)–2(e), corresponding to a temperature difference  $\Delta T_0 = 3.71 \text{ K}$  across the channel of width  $W = 760 \mu\text{m}$ , equivalent to a gradient  $G = 2\Delta T_0/W = 9.76 \text{ K/mm}$ . Here, two counterrotating deformed cylindrical streaming flow rolls appear, whirling with a velocity amplitude  $|v_2| = 1074 \mu\text{m/s}$  around the pair of curved white centerlines shown in Figs. 2(b) and 2(d). This velocity amplitude is about 77 and 87 times higher than that of the boundary-driven Rayleigh streaming and the Rayleigh-Bénard convection, respectively, under the same driving conditions (see Supplemental Material [42]).

The generation of this fast streaming can be explained by the acoustic body force  $f_{\text{ac}}$  spawned by the temperature field induced by the blue LED. In this experiment, the light heats the fluid from beneath, while the silicon layer efficiently transports the heat away, thus cooling the sides of the channel. Temperature gradients are therefore induced in all directions: In the  $x$ - $y$  plane by the Gaussian profile of the light intensity and by the cooling from the silicon sidewalls, and in the  $z$  direction by light absorption following the Beer-Lambert law. The resulting temperature field is highest at the center of the channel bottom, as shown by the measured and simulated temperature fields in the horizontal  $x$ - $y$  plane around channel mid-height  $z = 0 \mu\text{m}$  in Fig. 2(f), and by the simulated temperature field in the vertical  $y$ - $z$  cross section at  $x = 0 \mu\text{m}$  in Fig. 2(g). The acoustic body force  $f_{\text{ac}}$  depends on the gradients in

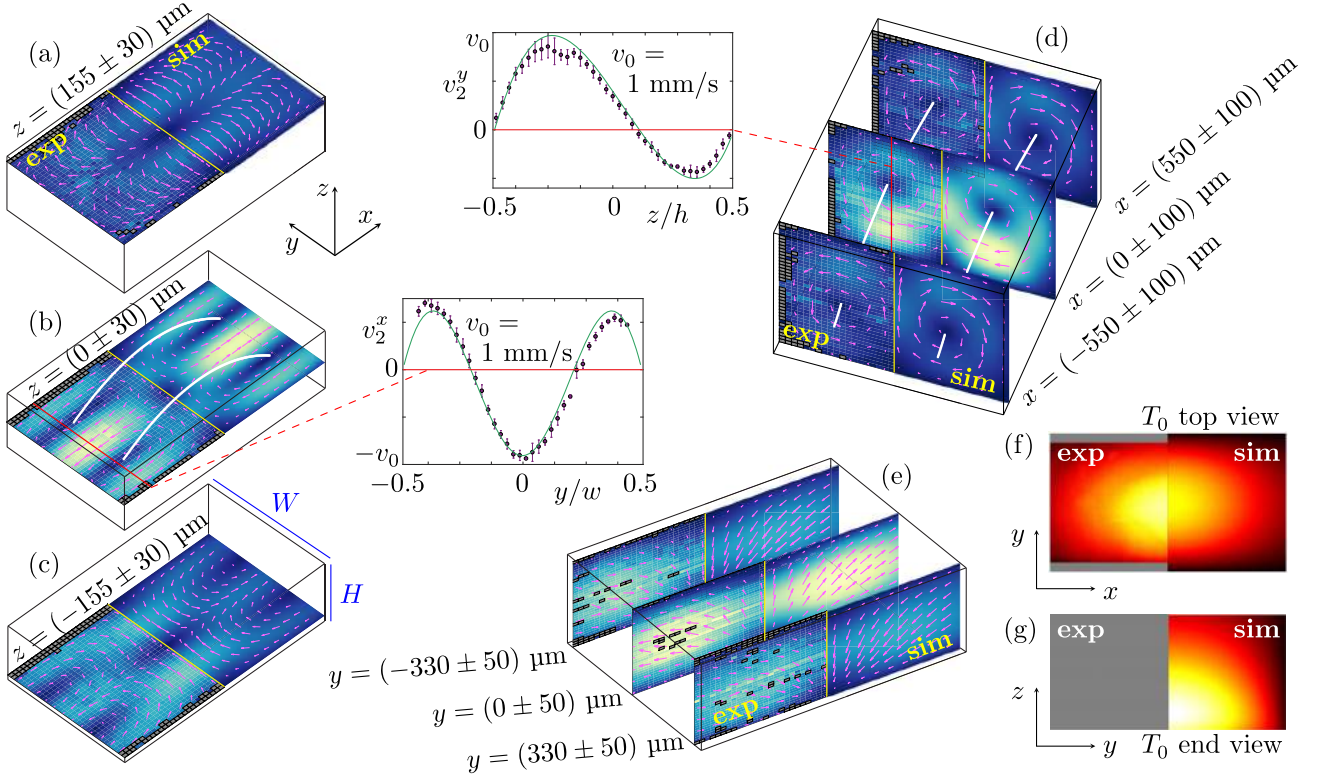


FIG. 2. (a)–(e) The measured (exp, left half) and simulated (sim, right half) streaming flow for  $G = 9.76$  K/mm ( $\Delta T_0 = 3.71$  K across the channel width  $W$ ), averaged in the indicated intervals (midposition  $\pm$  half-width) normal to the triplets of horizontal  $x$ - $y$  planes and vertical  $x$ - $z$  and  $y$ - $z$  planes. The vector plot (magenta) in a given plane is the in-plane velocity and the color plot is its magnitude from 0 (dark blue) to  $1042 \mu\text{m/s}$  (yellow). The simulation is performed at  $E_{\text{ac}} = 23 \text{ J/m}^3$ . Spatial bins with no experimental data are excluded (gray). The pair of curved white lines in (b) and (d) represents the centerlines of the two counterrotating deformed cylindrical streaming flow rolls. The two line-plot insets show the measured (purple) and the simulated (green)  $x$  (or  $y$ ) component  $v_2^x$  (or  $v_2^y$ ) of the velocity along the red lines. (f) Color plot from  $25.0^\circ\text{C}$  (black) to  $30.1^\circ\text{C}$  (white) of the measured and simulated temperature  $T_0$  in the horizontal  $x$ - $y$  plane around  $z = 0$ ; see more details in the Supplemental Material [42]. The regions where the fluorescence intensity is affected by the channel sidewalls are excluded (gray). (g)  $T_0$  as in panel (f) but for the vertical  $y$ - $z$  plane at  $x = 0$ ; here, no experimental data are available.

compressibility and density, the acoustic pressure  $p_1$ , and the acoustic velocity  $\mathbf{v}_1$  [33]. When the inhomogeneities are created by a temperature field,  $\mathbf{f}_{\text{ac}}$  can be expressed as,

$$\begin{aligned} \mathbf{f}_{\text{ac}} &= -\frac{1}{4}|p_1|^2 \nabla \kappa_{s,0} - \frac{1}{4}|\mathbf{v}_1|^2 \nabla \rho_0 \\ &= -\frac{1}{4} \left[ |p_1|^2 \left( \frac{\partial \kappa_s}{\partial T} \right)_{T_0} + |\mathbf{v}_1|^2 \left( \frac{\partial \rho}{\partial T} \right)_{T_0} \right] \nabla T_0. \quad (1) \end{aligned}$$

Three factors determine the action of  $\mathbf{f}_{\text{ac}}$  on the fluid. (i) Both the compressibility and density decrease with temperature, thus  $\mathbf{f}_{\text{ac}}$  points towards the high temperature region, here the center of the channel heated by the LED. (ii) At room temperature,  $\kappa_s |p_1|^2 \approx \rho |\mathbf{v}_1|^2$  and  $1/\kappa_s |\partial_T \kappa_s| \gg 1/\rho |\partial_T \rho|$ , so  $\mathbf{f}_{\text{ac}}$  is dominated by the  $|p_1|^2$  compressibility term and thus is strongest at the pressure antinodes at the sides of the channel. (iii) As shown in

Fig. 2(g), the temperature gradient is larger at the bottom than at the top of the channel, resulting in a stronger  $\mathbf{f}_{\text{ac}}$  at the bottom. Consequently, in the bottom part of the LED spot,  $\mathbf{f}_{\text{ac}}$  pushes the fluid horizontally inward to the vertical  $x$ - $z$  center plane at  $y = 0$  and by mass conservation lets it escape outward along the axial  $x$  direction and upward along the vertical  $z$  direction. The resulting streaming flow contains the two aforementioned deformed cylindrical flow rolls, which when projected onto horizontal and vertical planes appear as the four horizontal streaming rolls in Figs. 2(a)–2(c) strongest in the center plane  $z = 0$ , and as the two vertical streaming rolls in Fig. 2(d).

The thermoacoustic streaming is more than one order of magnitude faster than the boundary-driven Rayleigh streaming. It is mainly due to the nondissipative  $\mathbf{f}_{\text{ac}}$ , a mechanism fundamentally different from the dissipation mechanism of the conventional forms of acoustic streaming. Moreover, the fast thermoacoustic streaming is stationary, because it is driven by the PZT transducer and the

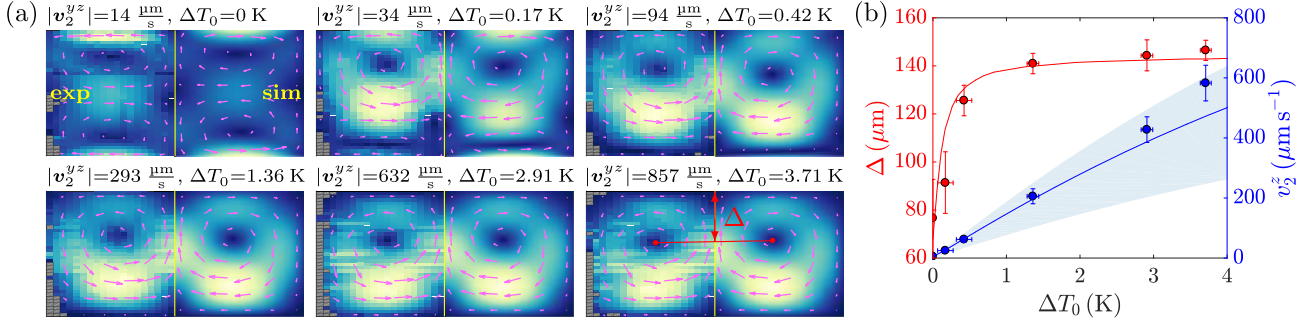


FIG. 3. (a) Measured (exp, left half) and simulated (sim, right half) in-plane streaming velocity  $v_2^{yz}$  (magenta vectors) and its magnitude  $|v_2^{yz}|$  from 0 (dark blue) to its maximum (yellow) in the vertical  $y$ - $z$  plane averaged over the vertical slab  $x = (0 \pm 100) \mu\text{m}$  for six temperature differences across the channel ranging from  $\Delta T_0 = 0$  to 3.71 K. Also shown is the vortex size  $\Delta$  (red). Simulations are performed with the energy density  $E_{ac}$  for which  $|v_2^{yz}|$  matches the experimental one under each  $\Delta T_0$ . Spatial bins with no experimental data points are excluded (gray). (b) Simulated (lines) and measured (points) vortex size  $\Delta$  (red) and the  $z$  component of the streaming velocity  $|v_2^z|$  (blue) versus  $\Delta T_0$ . The light blue region represents the simulated  $|v_2^z|$  for  $E_{ac}$  ranging from 9.24 (lower bound) to 23 J/m<sup>3</sup> (upper bound) with a reference (blue line) obtained at  $E_{ac} = 18 \text{ J/m}^3$ .

LED light kept in steady state. In contrast, as shown in our previous studies [33,54], the streaming driven by an inhomogeneous distribution of solute molecules is unsteady, and it is fast only during the short initial transient advection-dominated relocation of solute molecules. In the subsequent long-lasting phase, where the solute concentration gradients are smeared out by diffusion [31,32], the streaming is strongly suppressed in the bulk in this system is much slower than the fast thermoacoustic streaming.

The transition from boundary-driven Rayleigh streaming to thermoacoustic streaming is studied in the vertical  $y$ - $z$  cross section ( $-100 \mu\text{m} < x < 100 \mu\text{m}$ ) by gradually increasing the output power of the LED. Following Refs. [31,32], we quantify the streaming evolution by the vortex size  $\Delta$ , defined as the average of the distance from the center of each of the two upper flow rolls to the channel ceiling at  $z = \frac{1}{2}H$ . Figure 3 shows that for a zero temperature gradient  $G = 0$ , the streaming is governed by the four conventional boundary-driven Rayleigh streaming rolls, whereas at a high gradient  $G \approx 3.6 \text{ K/mm}$  ( $\Delta T_0 = 1.36 \text{ K}$ ), only two big temperature-gradient-induced streaming rolls are present, driven by the relatively large  $f_{ac}$  and occupying the whole channel cross section. In transitioning from the former to the latter situation, the two top Rayleigh flow rolls appear to expand downwards squeezing the bottom rolls against the channel floor at  $z = -\frac{1}{2}H$ . This phenomenon can be explained by the fact that the two top (bottom) Rayleigh flow rolls have the same (opposite) rotation direction as the two temperature-gradient-induced streaming rolls. Already at  $G = 0.5 \text{ K/mm}$  ( $\Delta T_0 = 0.17 \text{ K}$ ),  $f_{ac}$  is large enough to distort the four-flow-roll Rayleigh streaming pattern. When  $\Delta T_0$  further increases, the two-flow-roll thermoacoustic streaming pattern dominates, and eventually remains unchanged, while

the velocity amplitude increases almost linearly for the investigated range, see Fig. 3(b).

The observation that thermoacoustic streaming occurs already at temperature gradients below 0.5 K/mm calls for caution when combining acoustofluidic devices with optical systems. For an absorbing liquid, the light in a standard microscope is enough to induce strong velocity fields that may interfere with the study object. While we did not record the transient buildup of the streaming field upon activating the light, it can be noted that the development of the temperature field, and thus the streaming field, occurs within a few hundred milliseconds at the studied length scale, which enables rapid spatiotemporal modulation of local streaming fields through fast reconfigurable optical fields. Further, the induced streaming velocity is high enough to match the thermal diffusion time and thereby impact the heat transfer in the structure.

*Conclusion.*—This Letter describes a comprehensive experimental and numerical study of the thermoacoustic streaming in liquids induced by temperature gradients generated by light absorption in a microchannel. We have obtained a good match between measured and simulated velocity fields in three dimensions. As summarized by the main findings (i)–(iii) in the Introduction, the thermoacoustic streaming, driven by the nondissipative acoustic body force, has a markedly different origin than that of the conventional acoustic streaming associated with energy dissipation. Moreover, it reaches much higher velocity amplitudes compared to the boundary-driven Rayleigh streaming and the Rayleigh-Bénard convection under comparable conditions. The acoustic body force relies on the acoustic field and the gradients in compressibility and density, analogous to the driving force of the classical Rayleigh-Bénard convection relying on the gravitational field and the gradient in density.



By including the temperature dependence of both density and compressibility in this work through our theory in Ref. [38], our analysis of thermoacoustic streaming in terms of the acoustic body force is valid for both liquids and gases. Thus, we have extended previous related work on gases, where compressibility effects are unimportant and therefore neglected [19,55–62].

This study is fundamental in scope, but also demonstrates a method with a clear potential for controlling local flows spatiotemporally in microchannels. Further, we highlight important implications of this phenomenon relating to heat transfer and integration of optical fields with micro-scale acoustofluidic devices.

We are grateful to R. Barnkob (Technical University of Munich) and M. Rossi (Technical University of Denmark) for providing the software DefocusTracker, and Masahiko Taniguchi (North Carolina State University) for the valuable information regarding dye properties. W.Q. was supported by the Foreign Postdoctoral Fellowship from Wenner-Gren Foundations and by MSCA EF Seal of Excellence IF-2018 from Vinnova, Sweden’s Innovation Agency (Grant No. 2019-04856). This work has received funding from Independent Research Fund Denmark, Natural Sciences (Grant No. 8021-00310B) and the European Research Council (ERC) under the European Union’s Horizon 2020 research and innovation programme (Grant Agreement No. 852590).

\*wei.qiu@bme.lth.se

†jonashj@fysik.dtu.dk

‡bruus@fysik.dtu.dk

§per.augustsson@bme.lth.se

- [1] J. Lighthill, Acoustic streaming, *J. Sound Vib.* **61**, 391 (1978).
- [2] Lord Rayleigh, On the circulation of air observed in Kundt’s tubes, and on some allied acoustical problems, *Phil. Trans. R. Soc. London* **175**, 1 (1884).
- [3] W.L. Nyborg, Acoustic streaming near a boundary, *J. Acoust. Soc. Am.* **30**, 329 (1958).
- [4] M. Hamilton, Y. Ilinskii, and E. Zabolotskaya, Acoustic streaming generated by standing waves in two-dimensional channels of arbitrary width, *J. Acoust. Soc. Am.* **113**, 153 (2003).
- [5] S. A. Elder, Cavitation microstreaming, *J. Acoust. Soc. Am.* **31**, 54 (1959).
- [6] C. P. Lee and T. G. Wang, Outer acoustic streaming, *J. Acoust. Soc. Am.* **88**, 2367 (1990).
- [7] A. Yarin, G. Brenn, O. Kastner, D. Rensink, and C. Tropea, Evaporation of acoustically levitated droplets, *J. Fluid Mech.* **399**, 151 (1999).
- [8] P. Tho, R. Manasseh, and A. Ooi, Cavitation microstreaming patterns in single and multiple bubble systems, *J. Fluid Mech.* **576**, 191 (2007).
- [9] H. Schlichting, Berechnung ebener periodischer Grenzschichtströmungen, *Phys. Z.* **33**, 327 (1932).
- [10] P. B. Muller, M. Rossi, A. G. Marin, R. Barnkob, P. Augustsson, T. Laurell, C. J. Kähler, and H. Bruus, Ultrasound-induced acoustophoretic motion of microparticles in three dimensions, *Phys. Rev. E* **88**, 023006 (2013).
- [11] C. Eckart, Vortices and streams caused by sound waves, *Phys. Rev.* **73**, 68 (1948).
- [12] W. L. Nyborg, Acoustic streaming due to attenuated plane waves, *J. Acoust. Soc. Am.* **25**, 68 (1953).
- [13] N. Riley, Steady streaming, *Annu. Rev. Fluid Mech.* **33**, 43 (2001).
- [14] P. Marmottant and S. Hilgenfeldt, Controlled vesicle deformation and lysis by single oscillating bubbles, *Nature (London)* **423**, 153 (2003).
- [15] L. van der Sluis, M. Versluis, M. Wu, and P. Wesselink, Passive ultrasonic irrigation of the root canal: A review of the literature, *Int. Endod. J.* **40**, 415 (2007).
- [16] J. Wu and W. L. Nyborg, Ultrasound, cavitation bubbles and their interaction with cells, *Adv. Drug Delivery Rev.* **60**, 1103 (2008).
- [17] A. A. Doinikov and A. Bouakaz, Theoretical investigation of shear stress generated by a contrast microbubble on the cell membrane as a mechanism for sonoporation, *J. Acoust. Soc. Am.* **128**, 11 (2010).
- [18] H. Bailliet, V. Gusev, R. Raspet, and R. A. Hiller, Acoustic streaming in closed thermoacoustic devices, *J. Acoust. Soc. Am.* **110**, 1808 (2001).
- [19] M. Hamilton, Y. Ilinskii, and E. Zabolotskaya, Thermal effects on acoustic streaming in standing waves, *J. Acoust. Soc. Am.* **114**, 3092 (2003).
- [20] E. Trinh and J. Robey, Experimental study of streaming flows associated with ultrasonic levitators, *Phys. Fluids* **6**, 3567 (1994).
- [21] M. Wiklund, R. Green, and M. Ohlin, Acoustofluidics 14: Applications of acoustic streaming in microfluidic devices, *Lab Chip* **12**, 2438 (2012).
- [22] R. Barnkob, P. Augustsson, T. Laurell, and H. Bruus, Acoustic radiation- and streaming-induced microparticle velocities determined by microparticle image velocimetry in an ultrasound symmetry plane, *Phys. Rev. E* **86**, 056307 (2012).
- [23] B. Hammarström, T. Laurell, and J. Nilsson, Seed particle enabled acoustic trapping of bacteria and nanoparticles in continuous flow systems, *Lab Chip* **12**, 4296 (2012).
- [24] M. Antfolk, P. B. Muller, P. Augustsson, H. Bruus, and T. Laurell, Focusing of sub-micrometer particles and bacteria enabled by two-dimensional acoustophoresis, *Lab Chip* **14**, 2791 (2014).
- [25] A. Marin, M. Rossi, B. Rallabandi, C. Wang, S. Hilgenfeldt, and C. J. Kähler, Three-Dimensional Phenomena in Microbubble Acoustic Streaming, *Phys. Rev. Applied* **3**, 041001 (R) (2015).
- [26] P. Hahn, I. Leibacher, T. Baasch, and J. Dual, Numerical simulation of acoustofluidic manipulation by radiation forces and acoustic streaming for complex particles, *Lab Chip* **15**, 4302 (2015).
- [27] F. Guo, Z. Mao, Y. Chen, Z. Xie, J. P. Lata, P. Li, L. Ren, J. Liu, J. Yang, M. Dao, S. Suresh, and T. J. Huang, Three-dimensional manipulation of single cells using surface acoustic waves, *Proc. Natl. Acad. Sci. U.S.A.* **113**, 1522 (2016).

- [28] D. J. Collins, Z. Ma, J. Han, and Y. Ai, Continuous microvortex-based nanoparticle manipulation via focused surface acoustic waves, *Lab Chip* **17**, 91 (2017).
- [29] N. Nama, P.-H. Huang, T. J. Huang, and F. Costanzo, Investigation of acoustic streaming patterns around oscillating sharp edges, *Lab Chip* **14**, 2824 (2014).
- [30] J. S. Bach and H. Bruus, Suppression of Acoustic Streaming in Shape-Optimized Channels, *Phys. Rev. Lett.* **124**, 214501 (2020).
- [31] J. T. Karlsen, W. Qiu, P. Augustsson, and H. Bruus, Acoustic Streaming and Its Suppression in Inhomogeneous Fluids, *Phys. Rev. Lett.* **120**, 054501 (2018).
- [32] W. Qiu, J. T. Karlsen, H. Bruus, and P. Augustsson, Experimental Characterization of Acoustic Streaming in Gradients of Density and Compressibility, *Phys. Rev. Applied* **11**, 024018 (2019).
- [33] J. T. Karlsen, P. Augustsson, and H. Bruus, Acoustic Force Density Acting on Inhomogeneous Fluids in Acoustic Fields, *Phys. Rev. Lett.* **117**, 114504 (2016).
- [34] P. Augustsson, J. T. Karlsen, H.-W. Su, H. Bruus, and J. Voldman, Iso-acoustic focusing of cells for size-insensitive acousto-mechanical phenotyping, *Nat. Commun.* **7**, 11556 (2016).
- [35] W. Qiu, H. Bruus, and P. Augustsson, Particle-size-dependent acoustophoretic motion and depletion of micro- and nano-particles at long timescales, *Phys. Rev. E* **102**, 013108 (2020).
- [36] D. Van Assche, E. Reithuber, W. Qiu, T. Laurell, B. Henriques-Normark, P. Mellroth, P. Ohlsson, and P. Augustsson, Gradient acoustic focusing of sub-micron particles for separation of bacteria from blood lysate, *Sci. Rep.* **10**, 3670 (2020).
- [37] J. P. Koulakis, S. Pree, A. L. F. Thornton, and S. Putterman, Trapping of plasma enabled by pycnoclinic acoustic force, *Phys. Rev. E* **98**, 043103 (2018).
- [38] J. H. Joergensen and H. Bruus, Theory of pressure acoustics with thermoviscous boundary layers and streaming in elastic cavities, *J. Acoust. Soc. Am.* **149**, 3599 (2021).
- [39] R. Barnkob, C. J. Kähler, and M. Rossi, General defocusing particle tracking, *Lab Chip* **15**, 3556 (2015).
- [40] R. Barnkob and M. Rossi, General defocusing particle tracking: Fundamentals and uncertainty assessment, *Exp. Fluids* **61**, 110 (2020).
- [41] M. Rossi and R. Barnkob, A fast and robust algorithm for general defocusing particle tracking, *Meas. Sci. Technol.* **32**, 014001 (2020).
- [42] See Supplemental Material at <http://link.aps.org/supplemental/10.1103/PhysRevLett.127.064501> for details about the temperature measurements, the comparison between measured and simulated temperature fields, the numerical model, and the measured and simulated Rayleigh-Bénard convection, which includes Refs. [43–52].
- [43] R. F. Kubin and A. N. Fletcher, Fluorescence quantum yields of some rhodamine dyes, *J. Lumin.* **27**, 455 (1982).
- [44] D. A. Hinckley, P. G. Seybold, and D. P. Borris, Solvatochromism and thermochromism of rhodamine solutions, *Spectrochim. Acta A Mol. Spectrosc.* **42**, 747 (1986).
- [45] J. Yoo, D. Mitchell, D. F. Davidson, and R. K. Hanson, Near-wall imaging using toluene-based planar laser-induced fluorescence in shock tube flow, *Shock Waves* **21**, 523 (2011).
- [46] B. Zhang, J. Zerubia, and J.-C. Olivo-Marin, Gaussian approximations of fluorescence microscope point-spread function models, *Appl. Opt.* **46**, 1819 (2007).
- [47] N. R. Skov, J. S. Bach, B. G. Winckelmann, and H. Bruus, 3D modeling of acoustofluidics in a liquid-filled cavity including streaming, viscous boundary layers, surrounding solids, and a piezoelectric transducer, *AIMS Math.* **4**, 99 (2019).
- [48] M. W. H. Ley and H. Bruus, Three-Dimensional Numerical Modeling of Acoustic Trapping in Glass Capillaries, *Phys. Rev. Applied* **8**, 024020 (2017).
- [49] J. Arnaud, W. Hubbard, G. Mandeville, B. De la Claviere, E. Franke, and J. Franke, Technique for fast measurement of gaussian laser beam parameters, *Appl. Opt.* **10**, 2775 (1971).
- [50] P. B. Muller, R. Barnkob, M. J. H. Jensen, and H. Bruus, A numerical study of microparticle acoustophoresis driven by acoustic radiation forces and streaming-induced drag forces, *Lab Chip* **12**, 4617 (2012).
- [51] A. Riaud, M. Baudoin, O. Bou Matar, J.-L. Thomas, and P. Brunet, On the influence of viscosity and caustics on acoustic streaming in sessile droplets: an experimental and a numerical study with a cost-effective method, *J. Fluid Mech.* **821**, 384 (2017).
- [52] J. S. Bach and H. Bruus, Theory of pressure acoustics with viscous boundary layers and streaming in curved elastic cavities, *J. Acoust. Soc. Am.* **144**, 766 (2018).
- [53] A. Bermúdez, L. Hervella-Nieto, A. Prieto, and R. Rodríguez, An optimal perfectly matched layer with unbounded absorbing function for time-harmonic acoustic scattering problems, *J. Comput. Phys.* **223**, 469 (2007).
- [54] J. T. Karlsen and H. Bruus, Acoustic Tweezing and Patterning of Concentration Fields in Microfluidics, *Phys. Rev. Applied* **7**, 034017 (2017).
- [55] M. K. Aktas and T. Ozgumus, The effects of acoustic streaming on thermal convection in an enclosure with differentially heated horizontal walls, *Int. J. Heat Mass Transfer* **53**, 5289 (2010).
- [56] G. Chini, Z. Malecha, and T. Dreeben, Large-amplitude acoustic streaming, *J. Fluid Mech.* **744**, 329 (2014).
- [57] M. Červenka and M. Bednařík, Effect of inhomogeneous temperature fields on acoustic streaming structures in resonators, *J. Acoust. Soc. Am.* **141**, 4418 (2017).
- [58] G. Michel and G. P. Chini, Strong wave-mean-flow coupling in baroclinic acoustic streaming, *J. Fluid Mech.* **858**, 536 (2019).
- [59] R. Fand and J. Kaye, Acoustic streaming near a heated cylinder, *J. Acoust. Soc. Am.* **32**, 579 (1960).
- [60] M. W. Thompson and A. A. Atchley, Simultaneous measurement of acoustic and streaming velocities in a standing wave using laser doppler anemometry, *J. Acoust. Soc. Am.* **117**, 1828 (2005).
- [61] M. W. Thompson, A. A. Atchley, and M. J. Maccaroni, Influences of a temperature gradient and fluid inertia on acoustic streaming in a standing wave, *J. Acoust. Soc. Am.* **117**, 1839 (2005).
- [62] M. Nabavi, K. Siddiqui, and J. Dargahi, Effects of transverse temperature gradient on acoustic and streaming velocity fields in a resonant cavity, *Appl. Phys. Lett.* **93**, 051902 (2008).

# Supplemental material for: Fast microscale acoustic streaming driven by a temperature-gradient-induced non-dissipative acoustic body force

Wei Qiu,<sup>1,\*</sup> Jonas Helboe Joergensen,<sup>2,†</sup> Enrico Corato,<sup>1</sup> Henrik Bruus,<sup>2,‡</sup> and Per Augustsson<sup>1,§</sup>

<sup>1</sup>*Department of Biomedical Engineering, Lund University, Ole Römers väg 3, 22363 Lund, Sweden*

<sup>2</sup>*Department of Physics, Technical University of Denmark,  
DTU Physics Building 309, DK-2800 Kongens Lyngby, Denmark*

(Dated: 24 June 2021)

This supplemental material provides details about the temperature measurements, the comparison between measured and simulated temperature fields, the numerical model, as well as the measured and simulated Rayleigh-Bénard convection.

## S1. TEMPERATURE MEASUREMENTS

The temperature gradients inside the microchannel were measured in  $x$ - $y$  plane using an aqueous 1-mM solution of the temperature-sensitive fluorescent dye rhodamine B that has a peak wavelength at 554 nm, which is outside the absorption range of Orange G. Thus fluorescence imaging of rhodamine B molecules did not affect the temperature gradients produced by the light absorption of Orange G molecules. The optical properties of each substance used in the solution are summarized in Table S1.

The temperature dependence of dye fluorescence intensity for each pixel was obtained using the setup shown in Fig. S1. Two 1-mm-thick aluminum plates with two Peltier elements make contact with the two edges of the silicon layer of the microchip. Constant temperature inside the channel was obtained by applying the same temperature to both Peltier elements from 22 °C to 42 °C with an interval of 4 °C using a PID control loop from the resistance thermometer Pt1000. Through a 2D simulation of heat transfer including air cooling in an extreme case with the temperature of the Peltier elements and the air set to 42 °C and 25 °C, respectively, we confirmed that the

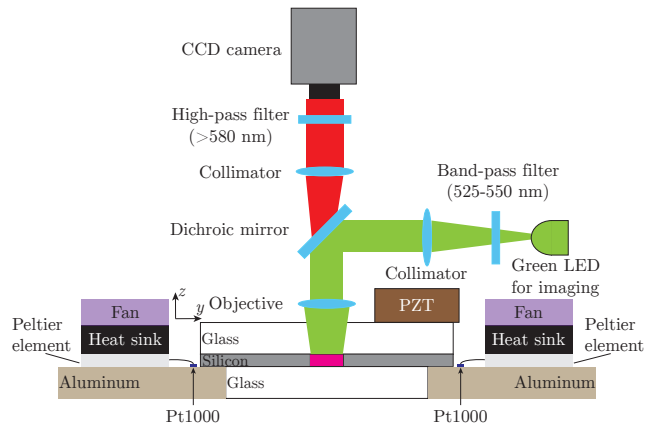


FIG. S1. Sketch of the calibration setup for temperature measurements. Two 1-mm-thick aluminum plates with two Peltier elements sitting on top make contact with the two edges of the silicon layer of the microchip to create uniform temperature field inside the microchannel. The temperature control of the Peltier elements are assisted by heat sinks and fans with a PID control loop from the resistance thermometer Pt1000 (blue). Temperature-sensitive fluorescent dye (rhodamine B, pink) is mixed with the medium, and green light is used to excite its fluorescence which is acquired by the CCD camera. The transducer ( $25 \times 6 \times 2 \text{ mm}^3$ ) is made of PZT Pz26 (Meggit Ferroperm Piezoceramics, Kvistgaard, Denmark).

TABLE S1. The optical properties of the Orange G (Sigma-Aldrich, St. Louis, MO) and rhodamine B (Acros Organics, Fair Lawn, NJ) solutions as well as the 1.1  $\mu\text{m}$ -diameter tracer particles (Thermo Fisher Scientific, Waltham, MA) used in experiments.

| Substance        | Absorption peak | Emission peak |
|------------------|-----------------|---------------|
| Orange G         | 478 nm          | —             |
| Rhodamine B      | 554 nm          | 575 nm        |
| Tracer particles | 542 nm          | 612 nm        |

\* [wei.qiu@bme.lth.se](mailto:wei.qiu@bme.lth.se)  
† [jonashj@fysik.dtu.dk](mailto:jonashj@fysik.dtu.dk)  
‡ [bruus@fysik.dtu.dk](mailto:bruus@fysik.dtu.dk)  
§ [per.augustsson@bme.lth.se](mailto:per.augustsson@bme.lth.se)

maximum temperature difference between the Peltier elements and the microchannel is less than 0.09 °C, and the maximum temperature difference in the microchannel is less than 0.03 °C, see Fig. S2. The dye fluorescence intensity for each temperature was recorded with the camera focal plane placed at the channel mid-height  $z = 0 \mu\text{m}$ . The intensity at each pixel was calculated by averaging in total 27 frames recorded for each temperature, with an exposure time of 11 ms and a frame rate of 20 fps. Noise was reduced by a  $3 \times 3$  mean filter. The intensity at all pixels far from the sidewalls decreases linearly as temperature increases (Fig. S3), which agrees with the literature [1], and pixel-wise calibration curves were used to calculate the temperature value at each pixel to eliminate the effect of aberration-induced spatial variations in

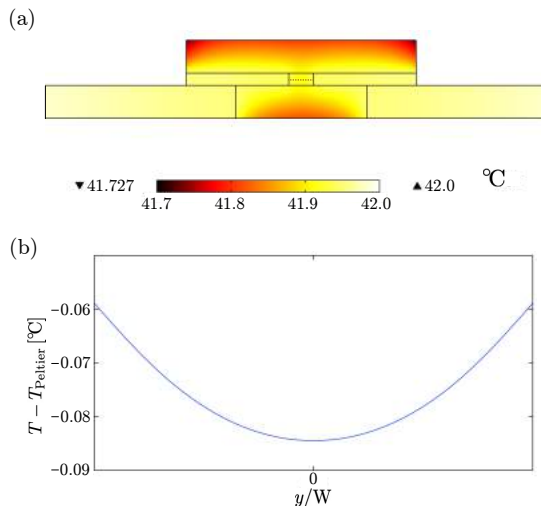


FIG. S2. (a) Color plot from 41.7 °C (black) to 42 °C (white) of the simulated heat transfer including air cooling with the temperature of the Peltier elements and the air set to  $T_{\text{Peltier}} = 42$  °C and  $T_{\text{air}} = 25$  °C, respectively. (b) The difference between the temperature in the microchannel  $T$  and  $T_{\text{Peltier}}$  along the channel width at channel mid-height, indicated by the brown dashed line in panel (a).

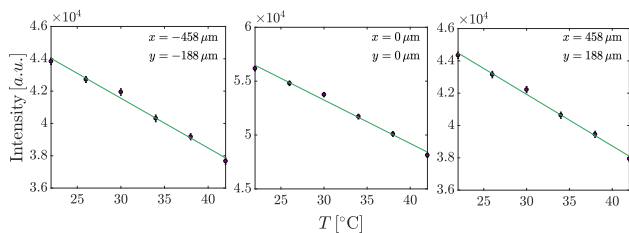


FIG. S3. The measured dye fluorescence intensity as a function of temperature at three arbitrary positions inside the microchannel. The intensity at all pixels far from the sidewalls shows linear decrease as temperature increases.

the optical signal. The absorption of rhodamine B in water varies less than 2% within the temperature range in our measurements [2], thus the fluorescence intensity is not affected by the different absorption levels at different temperatures.

The liquid was heated by shining the blue LED from below, the ultrasound field was activated, and the corresponding dye fluorescence intensity was recorded and converted to temperature using pixel-wise calibration curves, see Fig. S4. It is worth noting that this method is not applicable to measure the temperature close to the walls, in our case within 50  $\mu\text{m}$ , mainly because of the light scattering when walls are present. Hence, the obtained temperature dependence of dye fluorescence intensity close to the walls is error prone. This error can only be minimized by using specific wall materials and optical configurations [3], which is hard to perform in our acoustofluidic devices. We therefore excluded regions

within a distance of 50  $\mu\text{m}$  from the silicon sidewalls, indicated by gray in Fig. S4. The mapped temperature field was then fitted by a 2D Gaussian function to determine the temperature difference  $\Delta T_0$  across the channel and the corresponding temperature gradient  $G = 2\Delta T_0/W$ . The resolution of dye fluorescence intensity variation was not sufficiently high for  $\Delta T_0$  below 1 K, and the two lowest temperature gradients were therefore extrapolated based on the linear dependence of temperature on the LED power. We have not attempted to resolve the temperature variation along the  $z$ -direction due to the intricate influence of the fluorescence intensity on the focal plane from the adjacent planes.

## S2. COMPARISON BETWEEN MEASURED AND SIMULATED TEMPERATURE FIELDS

The images acquired by the compound microscope are convoluted in all three directions, and are therefore difficult to directly compare with the simulated temperature field which provides a super-resolution temperature value at each position. Thus, we first determined the point spread functions (PSFs) in all three directions in our imaging system using Gaussian approximations [4]

$$g(x, y, z) = A \exp\left(-\frac{x^2 + y^2}{2\sigma_{xy}^2} - \frac{z^2}{2\sigma_z^2}\right), \quad (\text{S1a})$$

$$\sigma_{xy} = \frac{\sqrt{2}}{k_{\text{em}} \text{NA}}, \quad (\text{S1b})$$

$$\sigma_z = \frac{2\sqrt{6}n}{k_{\text{em}} \text{NA}^2}, \quad (\text{S1c})$$

where  $k_{\text{em}} = 2\pi/\lambda_{\text{em}}$ ,  $n$ , and NA are the emission wavenumber, the refractive index of the liquid, and the numerical aperture of the objective lens, respectively. The calculated PSFs in the  $x$ - $y$  plane and the  $z$  direction for the imaging system are plotted in Fig. S5. The PSFs in the  $x$ - $y$  plane drop to zero within  $2 \times 2 \mu\text{m}^2$ , which is close to the smooth filter size of  $3 \times 3$  pixels that was used to obtain the pixel intensity (each pixel has a size of  $0.641 \times 0.641 \mu\text{m}^2$ ), and thus the effect of convolution in the  $x$ - $y$  plane can be neglected. Along the  $z$  axis the intensity value was convoluted in a range of 50  $\mu\text{m}$ . Considering that the PSF in  $z$  direction  $g(z)$  is symmetric, the convoluted intensity in experiments  $I_z^{\text{con}}$  can be written in its discrete form as

$$I_z^{\text{con}} = I_z^{\text{sup}} * g(z) = \sum_{i=1}^N I_{z_i}^{\text{sup}} g(z_i), \quad (\text{S2})$$

where  $I_z^{\text{sup}}$  is the super-resolution intensity in the  $z$  direction and  $z_i$  with  $i = 1, \dots, N$  are the discrete grid points in the same direction corresponding to the mesh elements in the simulation. When the temperature is uniform along the  $z$  direction, which is the case for calibration, the linear dependence of dye fluorescence intensity

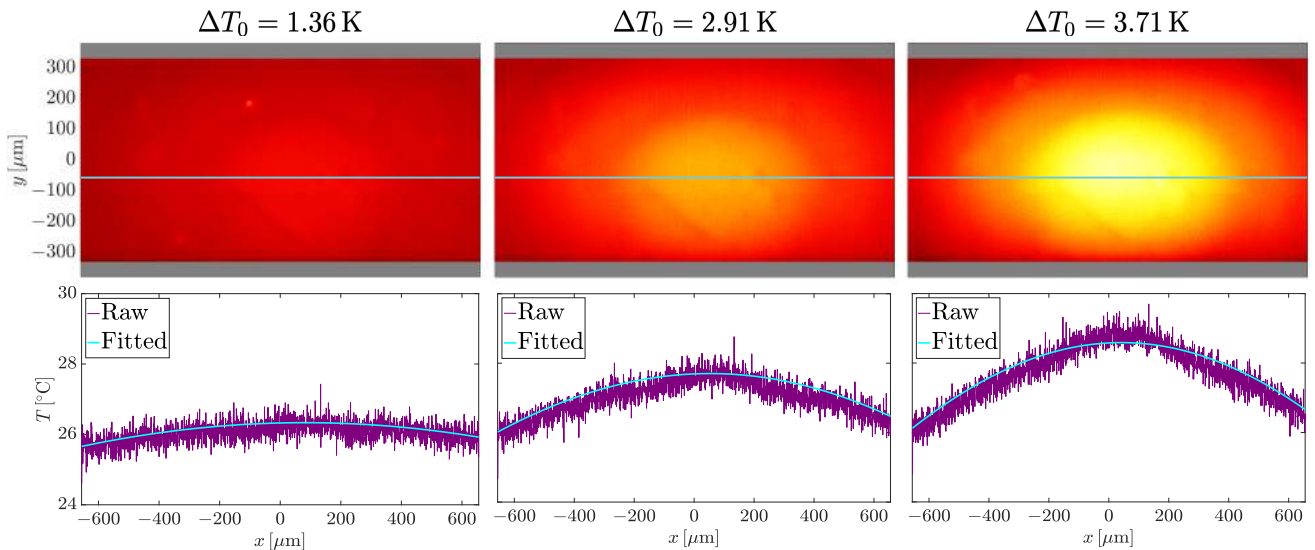


FIG. S4. The upper row: Color plots of the mapped temperature fields in the  $x$ - $y$  plane around  $z = 0$   $\mu\text{m}$  from 23.7 (black) to 30  $^{\circ}\text{C}$  (white) at  $\Delta T_0 = 1.36, 2.91,$  and  $3.71$  K. Regions where the fluorescence intensity is affected by the channel sidewalls are excluded (gray). The lower row: Line plots of the raw (purple) and fitted (cyan, 2D Gaussian fit) temperature along the respective cyan lines in the above color plots.  $\Delta T_0$  is determined by the difference between the maximum and minimum values in the fitted temperature profile.

on temperature can be expressed as

$$I_z^{\text{sup}} = a^{\text{sup}}T + b^{\text{sup}}, \quad (\text{S3a})$$

$$I_z^{\text{con}} = a^{\text{con}}T + b^{\text{con}}, \quad (\text{S3b})$$

where the superscripts “sup” and “con” denote super-resolution and convoluted cases. Combining Eqs. (S2) and (S3), we obtain

$$a^{\text{sup}} \sum_{i=1}^N g(z_i)T + b^{\text{sup}} \sum_{i=1}^N g(z_i) = a^{\text{con}}T + b^{\text{con}}. \quad (\text{S4})$$

Therefore, the relationship between super-resolution and

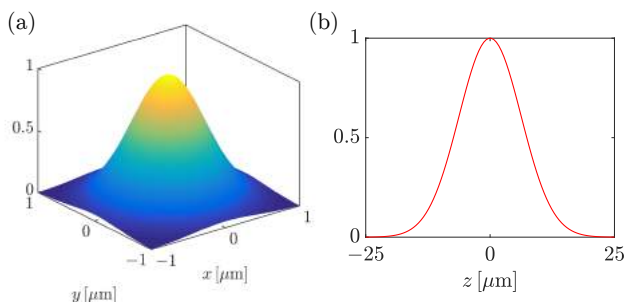


FIG. S5. The calculated point spread functions of the imaging system (a) in the  $x$ - $y$  plane and (b) along the  $z$ -axis based on Gaussian approximations described by Eq. (S1).

convoluted coefficients are found to be

$$a^{\text{con}} = a^{\text{sup}} \sum_{i=1}^N g(z_i), \quad (\text{S5a})$$

$$b^{\text{con}} = b^{\text{sup}} \sum_{i=1}^N g(z_i). \quad (\text{S5b})$$

When the temperature is not uniform along the  $z$  direction (i.e. temperature gradients are present), the relationship between the dye fluorescence intensity and the temperature can be expressed as

$$I_z^{\text{con}} = a^{\text{con}}T^{\text{con}} + b^{\text{con}} = \sum_{i=1}^N I_{z_i}^{\text{sup}} g(z_i), \quad (\text{S6})$$

where  $T^{\text{con}}$  is the experimentally measured temperature with convoluted intensity. After inserting Eq. (S3a), Eq. (S6) becomes

$$a^{\text{con}}T^{\text{con}} + b^{\text{con}} = a^{\text{sup}} \sum_{i=1}^N T(z_i)g(z_i) + b^{\text{sup}} \sum_{i=1}^N g(z_i). \quad (\text{S7})$$

Using the relationship between super-resolution and convoluted coefficients found in Eq. (S5), Eq. (S7) can be reduced to

$$T^{\text{con}} = \frac{\sum_{i=1}^N T(z_i)g(z_i)}{\sum_{i=1}^N g(z_i)}. \quad (\text{S8})$$

Then  $T^{\text{con}}$  can be compared with the simulated temperature values using the above relationship with  $T(z_i)$  known in simulation.

### S3. DETAILS OF THE NUMERICAL MODEL

The numerical model is the effective thermoviscous pressure acoustic model presented by Joergensen and Bruus [5] extended with heating from an external LED. The model is based on perturbation theory and simulates the unperturbed stationary temperature field  $T_0$  in the solid and fluid, the acoustic time-varying pressure  $p_1$  in the fluid and displacement  $\mathbf{u}_1$  in the solid, and the second-order stationary streaming field  $\mathbf{v}_2$  and pressure field  $p_2$  in the fluid resulting from the non-linearity of the Navier-Stokes equation. The model of a glass-silicon-glass chip with a fluid channel of height  $H = 370 \mu\text{m}$  and width  $W = 760 \mu\text{m}$  is shown in Fig. S6. In the model we take advantage of the symmetries in the system and model a quarter of the channel, Fig. S6. In the  $y$ - $z$  symmetry plane at  $x = 0$  all fields are symmetric, and in the  $x$ - $z$  symmetry plane at  $y = 0$  the acoustic fields  $p_1$  and  $\mathbf{u}_1$  are anti-symmetric and the stationary fields  $T_0$ ,  $\mathbf{v}_2$ , and  $p_2$  are symmetric. The model parameters are listed in Table S2.

The actuation is modeled not as a full piezoelectric transducer as in Ref. [6], but merely as a boundary condition with a displacement  $d_0 = 1 \text{ nm}$  and a frequency  $f_0$  on the black actuation plane in Fig. S6 as in Ref. [7]. Note that using the symmetry planes, the model actually has anti-symmetric actuation regions, one on each side of the chip, which is not the case in the experimental setup. This does not change the shape of the pressure field in the fluid because we are at a fluid resonance completely dominated by a pressure component obeying the same anti-symmetry as the actuating regions.

During operation, a piezoelectric transducer generates heat, but this is neglected in the simulations for two reasons: (1) The necessary acoustic energy density is obtained in the system using a relatively low power consumption, and this assures that the heat generation is relatively small. (2) The heat from the transducer is lead through the top glass layer into the silicon layer, where it due to the high heat conductivity of silicon is uniformly

TABLE S2. System parameters characterizing the geometry, the acoustic actuation, and the absorption of the LED spot.

| Parameter                    | Symbol           | Value | Unit             |
|------------------------------|------------------|-------|------------------|
| <b>Geometry parameters:</b>  |                  |       |                  |
| Fluid width                  | $W$              | 760   | $\mu\text{m}$    |
| Fluid height                 | $H$              | 370   | $\mu\text{m}$    |
| Actuation length             | $L_{\text{PZT}}$ | 3.0   | mm               |
| System length                | $L_{\text{sys}}$ | 5.5   | mm               |
| PML length                   | $L_{\text{PML}}$ | 1.75  | mm               |
| Total length                 | $L_{\text{end}}$ | 7.25  | mm               |
| <b>Actuation parameters:</b> |                  |       |                  |
| Actuation amplitude          | $d_0$            | 1.0   | nm               |
| Actuation frequency          | $f_0$            | 0.957 | MHz              |
| <b>LED parameters:</b>       |                  |       |                  |
| Half width of the LED spot   | $d_{\text{LED}}$ | 650   | $\mu\text{m}$    |
| Absorption coefficient       | $\alpha$         | 12.4  | $\text{mm}^{-1}$ |

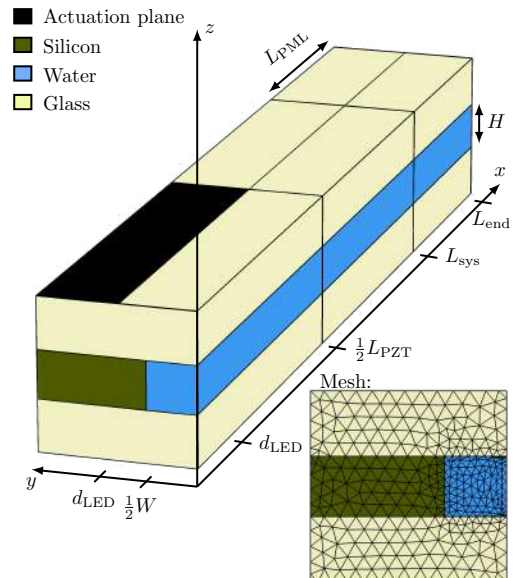


FIG. S6. Sketch of the numerical model of the acoustofluidic chip. Symmetry planes have been used so only a quarter of the channel is simulated. The model consists of a fluid domain with width  $W$  and height  $H$ , a solid domain (glass and silicon), and a special PML (perfectly matched layer) region where the travelling waves are artificially damped to mimic an infinitely long channel. The acoustic actuation is done on the actuation region (black) and the LED has its center at  $x = 0$  and  $y = 0$  and has half of the width  $d_{\text{LED}}$ . The mesh is shown in the  $y$ - $z$  plane, which is swept along the  $x$ -axis so that the mesh node repeats itself with a distance of  $51 \mu\text{m}$ .

distributed throughout the chip, leading to only a minute and nearly uniform temperature rise in the microchannel.

To avoid simulating the entire chip, the perfectly matched layer (PML) method is used to artificially damp travelling waves [8]. Thus, the model consists of an area of length  $L_{\text{PZT}}$  where a piezoelectric transducer actuates the chip at a frequency  $f_0$  with an amplitude  $d_0$ , a part of length  $L_{\text{sys}} - L_{\text{PZT}}$  where there are no actuation, and finally a section of length  $L_{\text{PML}}$  where the acoustic waves are artificially damped using a PML. For the PML to be valid, the distance  $L_{\text{sys}} - L_{\text{PZT}}$  must be long enough for the travelling wave to develop so that the acoustic field does not depend on where the PML starts.

The real device has a long channel with a long piezoelectric transducer. To model the pressure field around the LED spot accurately, the length  $L_{\text{PZT}}$  must be larger than half of the LED spot width  $d_{\text{LED}}$ . The LED spot is modeled as a Gaussian beam with half of the beam width  $d_{\text{LED}} = 650 \mu\text{m}$  (experimentally measured  $d_{\text{LED}} = 750 \pm 150 \mu\text{m}$  using the knife-edge method [9]) and the absorption coefficient is set to  $\alpha = 12.4 \text{ mm}^{-1}$  to match the observed 99% absorption in the channel. The

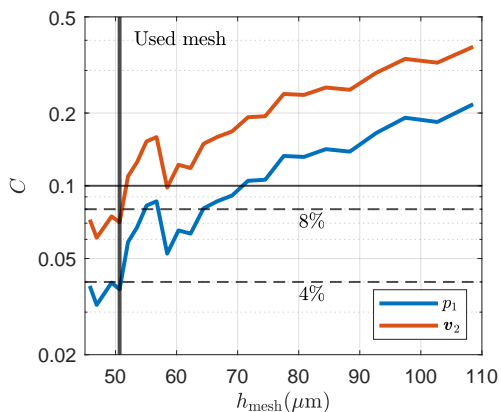


FIG. S7. A semi-logarithmic plot of the mesh convergence error  $C$  of Eq. (S10) versus mesh size  $h_{\text{mesh}}$  using a reference mesh simulated on a HPC-cluster with  $h_{\text{mesh}} = 38 \mu\text{m}$ . The blue and red lines are  $C_{p_1}$  and  $C_{v_2}$  of the acoustic pressure and streaming, respectively. The thick black vertical line marks the mesh  $h_{\text{mesh}} = 51 \mu\text{m}$  used for the simulations in the Letter, and the two dashed horizontal lines indicate the 4% and 8% levels.

Gaussian light intensity through the channel is given as,

$$I(x, y, z) = \frac{2P_{\text{LED}}}{\pi d_{\text{LED}}^2} \exp \left[ -\frac{2(x^2 + y^2)}{d_{\text{LED}}^2} - \alpha \left( z + \frac{1}{2}H \right) \right], \quad (\text{S9})$$

where  $P_{\text{LED}}$  is the total power of the LED and  $-\frac{1}{2}H$  is the bottom of the channel where beam starts to be absorbed. In the solution, the heat absorption is given as  $q(x, y, z) = \alpha I(x, y, z)$  for  $-\frac{1}{2}H < z < \frac{1}{2}H$ , while the absorption in the glass is neglected.

The entire model is implemented in COMSOL Multiphysics 5.6, with the governing equations and effective boundary conditions given by Joergensen and Bruus [5].

All calculations, except the mesh reference simulation, were performed on an HP-Z4 workstation with a processor Intel Core i9-7960X at 4.20 GHz and with 128 GB RAM. The model had  $10^6$  degrees of freedom in both the first- and second-order equations (acoustic and stationary fields). A mesh convergence analysis based on the standard  $L_2$ -norm error  $C_g$  [10],

$$C_g = \sqrt{\frac{\int |g(\mathbf{r}) - g_{\text{ref}}(\mathbf{r})|^2 dV}{\int |g_{\text{ref}}(\mathbf{r})|^2 dV}}, \quad (\text{S10})$$

was performed for the pressure field  $g = p_1$ , and the streaming field  $g = v_2$ , with a reference simulation  $g_{\text{ref}}$  computed on a HPC-cluster with a mesh size  $h_{\text{mesh}} = 38 \mu\text{m}$ , see Fig. S7. The analysis shows that for a mesh with  $h_{\text{mesh}} = 51 \mu\text{m}$ , shown in Fig. S6, the acoustic pressure field and the streaming field are converged to an  $L_2$ -error of 4% and 8%, respectively. The fairly good convergence obtained on the relatively coarse mesh shown in Fig. S6 is due to the use of the effective theory [5], because, (1) in the bulk, the body force driving the streaming contains no small length scales, and (2) as discussed

in Refs. [11, 12], large canceling terms leading to numerical errors in the full model are explicitly removed when using the effective theory.

The numerical model uses cubic test functions for the streaming field and the acoustic pressure field, but quadratic test functions for the acoustic displacement field in the solid and the second-order pressure field.

#### S4. RAYLEIGH-BÉNARD CONVECTION

As a control experiment, the 3D Rayleigh-Bénard convection in the microchannel was investigated for a temperature gradient  $G = 9.76 \text{ K/mm}$  across the channel measured at channel mid-height  $z = 0$  (corresponding to  $G = 13.78 \text{ K/mm}$  along the channel height obtained from simulation) when the sound field was off, and was compared with numerical simulation, see Fig. S8. Under the experimental conditions studied here, the Rayleigh-Bénard convection is in the laminar regime due to the low Rayleigh number  $Ra = \frac{\rho g \beta}{\eta \alpha} H^3 \Delta T_0 = 5.06$ , where  $\rho$ ,  $\beta$ ,  $\eta$ , and  $\alpha$  are the density, thermal expansion coefficient, dynamic viscosity, and thermal diffusivity of water, respectively, and  $H$  is the channel height.

At the bottom center of the channel, the fluid expe-

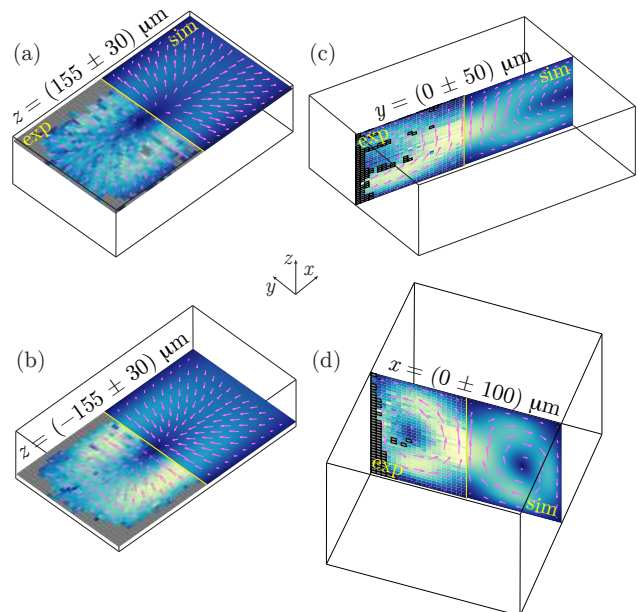


FIG. S8. (a)-(d) The measured (exp, left side) and simulated (sim, right side) pattern of Rayleigh-Bénard convection for  $G = 9.76 \text{ K/mm}$  across the channel measured at  $z = 0$  (corresponding to  $G = 13.78 \text{ K/mm}$  along the channel height obtained from simulation), observed in different planes  $x$ - $y$  horizontally,  $x$ - $z$  vertically, and  $y$ - $z$  vertically. The vector plot (magenta) in a given plane is the in-plane velocity and the color plot is its magnitude from 0 (dark blue) to  $12.3 \mu\text{m s}^{-1}$  (yellow). Spatial bins with no experimental data points are excluded (gray).

riences the highest temperature due to light absorption, hence it expands and becomes less dense, resulting in a convection from the bottom to the top. The fluid is able to flow in both the  $x$ - and  $y$ -directions at the ceiling and circulate back along the bottom, creating two big rolls

which can be viewed in the  $x$ - $z$  and the  $y$ - $z$  planes, see Fig. S8(c)-(d). The measured velocity amplitude of the Rayleigh-Bénard convection is  $v_{\text{con}} = (12.3 \pm 4.0) \mu\text{m s}^{-1}$  ( $9.9 \mu\text{m s}^{-1}$  in the simulation), which is almost two orders of magnitude lower than that of the thermoacoustic streaming.

- 
- [1] R. F. Kubin and A. N. Fletcher, Fluorescence quantum yields of some rhodamine dyes, *J. Lumin.* **27**, 455 (1982).
- [2] D. A. Hinckley, P. G. Seybold, and D. P. Borris, Solvatochromism and thermochromism of rhodamine solutions, *Spectrochim. Acta A Mol. Spectrosc.* **42**, 747 (1986).
- [3] J. Yoo, D. Mitchell, D. F. Davidson, and R. K. Hanson, Near-wall imaging using toluene-based planar laser-induced fluorescence in shock tube flow, *Shock Waves* **21**, 523 (2011).
- [4] B. Zhang, J. Zerubia, and J.-C. Olivo-Marin, Gaussian approximations of fluorescence microscope point-spread function models, *Appl. Opt.* **46**, 1819 (2007).
- [5] J. H. Joergensen and H. Bruus, Theory of pressure acoustics with thermoviscous boundary layers and streaming in elastic cavities, *J. Acoust. Soc. Am.* **149**, 3599 (2021).
- [6] N. R. Skov, J. S. Bach, B. G. Winckelmann, and H. Bruus, 3D modeling of acoustofluidics in a liquid-filled cavity including streaming, viscous boundary layers, surrounding solids, and a piezoelectric transducer, *AIMS Mathematics* **4**, 99 (2019).
- [7] M. W. H. Ley and H. Bruus, Three-dimensional numerical modeling of acoustic trapping in glass capillaries, *Phys. Rev. Appl.* **8**, 024020 (2017).
- [8] A. Bermúdez, L. Hervella-Nieto, A. Prieto, and R. Rodríguez, An optimal perfectly matched layer with unbounded absorbing function for time-harmonic acoustic scattering problems, *J. Comput. Phys.* **223**, 469 (2007).
- [9] J. Arnaud, W. Hubbard, G. Mandeville, B. De la Claviere, E. Franke, and J. Franke, Technique for fast measurement of gaussian laser beam parameters, *Appl. Opt.* **10**, 2775 (1971).
- [10] P. B. Muller, R. Barnkob, M. J. H. Jensen, and H. Bruus, A numerical study of microparticle acoustophoresis driven by acoustic radiation forces and streaming-induced drag forces, *Lab Chip* **12**, 4617 (2012).
- [11] A. Riaud, M. Baudoin, O. Bou Matar, J.-L. Thomas, and P. Brunet, On the influence of viscosity and caustics on acoustic streaming in sessile droplets: an experimental and a numerical study with a cost-effective method, *J. Fluid Mech.* **821**, 384 (2017).
- [12] J. S. Bach and H. Bruus, Theory of pressure acoustics with viscous boundary layers and streaming in curved elastic cavities, *J. Acoust. Soc. Am.* **144**, 766 (2018).



### 7.3 Paper III in Physical Review E (under review)

*Theory and modeling of nonperturbative effects at high acoustic energy densities in thermoviscous acoustofluidics*

**Authors:** J. H. Joergensen, and H. Bruus.

**Journal:** Submitted to Physical Review E

**arXiv:** [arxiv.org/abs/2112.10737](https://arxiv.org/abs/2112.10737)

**Remarks:** There is a sign error in equation 42 and 43, these errors will be corrected in the published paper. The correct equation 42 is given as,

$$\begin{aligned}
 0 &= \nabla \cdot \left[ k_0^{\text{th}} \nabla T_0^{\text{fl},d} \right] - c_p \rho_0 \mathbf{v}_0 \cdot \nabla T_0^{\text{fl},d} + P_{\text{ac}}^d + P, \\
 P_{\text{ac}}^d &= \nabla \cdot \left[ \langle k_1^{\text{th},d} \nabla T_1^d \rangle - \langle p_1 \mathbf{v}_1^{d,p} \rangle + \langle \mathbf{v}_1^{d,p} \cdot \boldsymbol{\tau}_1^d \rangle \right] \\
 &\quad - c_p \langle \rho_1^d \mathbf{v}_1^{d,p} \rangle \cdot \nabla T_0^d,
 \end{aligned}$$

and the correct equation 43 is given as,

$$\begin{aligned}
 0 &= \nabla \cdot \left[ k_0^{\text{th}} \nabla T_0^{\text{sl},d} \right] + P_{\text{ac}}^d + P, \\
 P_{\text{ac}}^d &= \nabla \cdot \langle k_1^{\text{th,sl}} \nabla T_1^{\text{sl},d} \rangle.
 \end{aligned}$$

# Theory and modeling of nonperturbative effects at high acoustic energy densities in thermoviscous acoustofluidics

Jonas Helboe Joergensen\* and Henrik Bruus†

*Department of Physics, Technical University of Denmark,  
DTU Physics Building 309, DK-2800 Kongens Lyngby, Denmark*

(Dated: 20 December 2021)

A theoretical model of thermal boundary layers and acoustic heating in microscale acoustofluidic devices is presented. It includes effective boundary conditions allowing for simulations in three dimensions. The model is extended by an iterative scheme to incorporate nonlinear thermoviscous effects not captured by standard perturbation theory. The model predicts that the dominant non-perturbative effects in these devices are due to the dependency of thermoacoustic streaming on gradients in the steady temperature induced by a combination of internal frictional heating, external heating, and thermal convection. The model enables simulations in a nonperturbative regime relevant for design and fabrication of high-throughput acoustofluidic devices.

## I. INTRODUCTION

Modeling and simulations of acoustofluidic devices is used to optimize and develop designs of microscale acoustofluidic devices. Traditionally, acoustofluidic models have been based on perturbation theory [1–7], but in this paper we present an iterative numerical model that enables simulations of nonlinear acoustofluidics beyond the amplitude limitations set by perturbation theory. The motivation for this theoretical development is that combined theoretical and experimental studies of acoustic streaming has shown that the perturbative treatment is pushed to its limit and beyond [8]. In the latter work, the perturbation model is challenged by the fast acoustic streaming, which creates a significant convection, and, as discussed below, also heating from friction in the viscous boundary layers can be important. Both of these effects are not described by standard perturbation theory.

The validity of perturbation theory is mainly challenged in systems with a high acoustic energy density  $E_{ac}$ , needed in the development of faster acoustofluidic handling of suspended particles and molecular suspensions. In particular, the volumetric throughput is often a limiting factor for clinical use of acoustofluidic devices [9–12], so it is of general interest to develop a model that allows for simulation of such high- $E_{ac}$  devices. Nonlinear effects due to fast acoustic streaming have previously been studied numerically in gases with a model using an ideal analytical pressure field [13]. Those models include the nonlinear effects of changing the temperature field by convection due to the streaming velocity field, but the nonlinear effect of acoustic heating and nonlinearities in the acoustic fields themselves are not included.

Numerical models in acoustofluidics can be categorized as viscous models [1, 5] and thermoviscous models [2, 7], as well as full models [1, 2] and effective

models [5, 7]. The viscous models include the full viscous fluid description, but assume an adiabatic temperature field governed by the pressure field and typically assume temperature-independent material parameters. The thermoviscous models further include thermal boundary layers, temperature-dependent material parameters, and heating created in the viscous boundary layers. Full models require numerical resolution of the thin boundary layers, and they are therefore numerically expensive. In contrast, effective models include analytical expressions for the boundary layers, so a fine boundary-layer mesh is avoided, and they therefore enables three-dimensional (3D) simulations. In this work we build on and expand our previous perturbative thermoviscous effective model [7] by including frictional heating due to the acoustic field, and by going beyond perturbation theory with the introduction of an iterative scheme including quasi-steady and acoustic fields to allow for higher acoustic energy densities and larger thermal convection. The developed nonlinear, effective-boundary-layer, thermoviscous acoustofluidic model is the main result of this work. Experimental validation of the model is presented in a concurrent Letter [14].

In Section II the basic assumptions and governing equations for the nonperturbative approach are presented. In Section III, our perturbative theory [7] of the thermoviscous acoustic fields is briefly summarized. In Section IV, the known theory [7] for the steady mechanical fields is presented, and we develop the theory for the steady temperature fields. In Section V, we present the nonperturbative iterative procedure for computing nonlinear thermoacoustic effects, and we briefly explain how to implement it in the software Comsol Multiphysics [15]. In Section VI, we validate the implementation of our numerical model, and we present two model examples of nonlinear acoustofluidics: a model in two dimensions (2D) involving internal acoustic heating, and a model in three dimensions (3D) involving thermoacoustic streaming induced by absorption of light. Finally, we conclude in Section VII.

\* jonashj@fysik.dtu.dk

† bruus@fysik.dtu.dk

## II. THEORY AND MODEL ASSUMPTIONS

Based on our previous perturbative approach [7], we consider an acoustofluidic device consisting of an elastic solid containing a microchannel filled with a thermoviscous Newtonian fluid and actuated by a piezoelectric transducer at a single frequency in the MHz range. Due to the internal dissipation and hydrodynamic nonlinearities in the fluid, the resulting time-harmonic acoustic field leads to a time-averaged response in the form of acoustic streaming and steady temperature gradients. For simplicity, the piezoelectric transducer is left out of the analysis, and is only represented by an oscillating displacement condition on part of the surface of the elastic solid. We have in other studies included a full model of the transducer in the numerical model [6, 16, 17].

### A. Governing equations

The response of the fluid embedded in the elastic solid to the oscillating-displacement boundary condition is controlled by the hydro-, elasto-, and thermodynamic governing equations of the coupled thermoviscous fluid and elastic solid. The linear elastic solid is described in the Lagrangian picture by the fields of the density  $\rho$ , the displacement  $\mathbf{u}$ , the temperature  $T$ , and by the following material parameters: the longitudinal and transverse sound speeds  $c_{10}$  and  $c_{tr}$ , the thermal conductivity  $k^{th}$ , the specific heat capacity  $c_p$ , the ratio of specific heat capacities  $\gamma = c_p/c_v$ , the thermal expansion coefficient  $\alpha_p$ , and the isentropic and isothermal compressibilities  $\kappa_s$  and  $\kappa_T$ . The velocity field is the time derivative of the displacement field,  $\mathbf{v}^{sl} = \partial_t \mathbf{u}$ , so no advection occur, and the governing equations are the transport equations of the momentum density  $\rho \partial_t \mathbf{u}$  and temperature  $T$  [18, 19],

$$\rho \partial_t^2 \mathbf{u} = \nabla \cdot \boldsymbol{\sigma}, \quad (1a)$$

$$\partial_t T + \frac{(\gamma - 1)}{\alpha_p} \partial_t (\nabla \cdot \mathbf{u}) = \frac{\gamma}{\rho c_p} \nabla \cdot (k^{th} \nabla T) + P, \quad (1b)$$

where  $P$  is the external heat power density, and  $\boldsymbol{\sigma}$  is the stress tensor, which for isotropic solids is,

$$\boldsymbol{\sigma} = -\frac{\alpha_p}{\kappa_T} (T - T_0) \mathbf{I} + \boldsymbol{\tau}, \quad (2a)$$

$$\boldsymbol{\tau} = \rho c_{tr}^2 \left[ \nabla \mathbf{u} + (\nabla \mathbf{u})^\dagger \right] + \rho (c_{10}^2 - 2c_{tr}^2) (\nabla \cdot \mathbf{u}) \mathbf{I}. \quad (2b)$$

The fluid is described in the Eulerian picture by the fields of the density  $\rho$ , the pressure  $p$ , the velocity  $\mathbf{v}$ , the temperature  $T$ , and the energy per mass unit  $\epsilon$ , and by the following material parameters: the dynamic and bulk viscosity  $\eta$  and  $\eta^b$ , the thermal conductivity  $k^{th}$ , the specific heat  $c_p$ , the thermal expansion coefficient  $\alpha_p$ , the ratio of specific heats  $\gamma = c_p/c_v$ , and the isentropic and isothermal compressibilities  $\kappa_s$  and  $\kappa_T = \gamma \kappa_s$ . The

governing equations are the transport equations for the density of mass  $\rho$ , momentum  $\rho \mathbf{v}$ , and internal energy  $\rho \epsilon$ , [2, 19, 20]

$$\partial_t \rho = -\nabla \cdot (\rho \mathbf{v}), \quad (3a)$$

$$\partial_t (\rho \mathbf{v}) = \nabla \cdot (\boldsymbol{\sigma} - \rho \mathbf{v} \mathbf{v}), \quad (3b)$$

$$\partial_t \left( \rho \epsilon + \rho \frac{v^2}{2} \right) = \nabla \cdot \left[ k^{th} \nabla T + \mathbf{v} \cdot \boldsymbol{\sigma} - \rho \mathbf{v} \left( \epsilon + \frac{v^2}{2} \right) \right] + P, \quad (3c)$$

where  $P$  is the external heat power density, and  $\boldsymbol{\sigma}$  is the stress tensor,

$$\boldsymbol{\sigma} = -p \mathbf{I} + \boldsymbol{\tau}, \quad (4a)$$

$$\boldsymbol{\tau} = \eta \left[ \nabla \mathbf{v} + (\nabla \mathbf{v})^\dagger \right] + \left( \eta^b - \frac{2}{3} \eta \right) (\nabla \cdot \mathbf{v}) \mathbf{I}. \quad (4b)$$

Pressure  $p$  and temperature  $T$  are related to the internal energy density  $\epsilon$  by the first law of thermodynamics, and to the density  $\rho$  by the equation of state [2, 19, 21],

$$\rho d\epsilon = (\rho c_p - \alpha_p p) dT + (\kappa_T p - \alpha_p T) dp \quad (5a)$$

$$d\rho = -\rho \alpha_p dT + \rho \kappa_T dp \quad (5b)$$

Like the density, any material parameter  $q$  has a temperature and pressure dependency,

$$\frac{1}{q_0} dq = a_q^T \alpha_p dT + a_q^p \kappa_T dp, \quad (6a)$$

$$a_q^T = \frac{1}{\alpha_p q_0} \left( \frac{\partial q}{\partial T} \right)_p, \quad a_q^p = \frac{1}{\kappa_T q_0} \left( \frac{\partial q}{\partial p} \right)_T. \quad (6b)$$

Note that here the variables are  $(T, p)$  and not  $(T, \rho)$  as in Refs. [2, 7]. For a pressure change  $dp$  accompanied by an adiabatic temperature change  $dT = (\gamma - 1) \frac{\kappa_T}{\alpha_p} dp$ , the adiabatic pressure dependency of a parameter  $q$  is,

$$\frac{1}{q_0} dq = a_q^T \alpha_p dT + a_q^p \kappa_T dp = a_q^{p,ad} \kappa_s p_1, \quad (6c)$$

$$a_q^{p,ad} = \gamma (\gamma - 1) a_q^T + \gamma a_q^p. \quad (6d)$$

For steady temperature gradients and oscillating thermal boundary layers,  $a_q^T$  is relevant and for bulk adiabatic pressure wave  $a_q^{p,ad}$  is the relevant quantity. For water at  $T = 25^\circ \text{C}$ , using Eqs. (5b) and (6), we compute the dimensionless sensitivities  $a_q^T$ ,  $a_q^p$  and  $a_q^{p,ad}$  from the  $T$ - $\rho$  dependencies of the parameters  $q$  listed in Ref. [2],

$$\begin{aligned} a_\rho^T &= -1, & a_{\kappa_s}^T &= -10, \\ a_\rho^p &= 1, & a_\rho^{p,ad} &= 1, \\ a_\eta^T &= -88, & a_\eta^{p,ad} &= -1.3, \\ a_{\eta^b}^T &= -100, & a_{\eta^b}^{p,ad} &= -1.1, \\ a_{k^{th}}^T &= 8.4, & a_{k^{th}}^{p,ad} &= 2.3. \end{aligned} \quad (7)$$

We assume  $\eta^b$  to be dependent on temperature and not pressure. These temperature dependencies imply that

thermal gradients may induce gradients in the listed parameters, including the density and the compressibility. This leads to the appearance of the inhomogeneous acoustic body force  $\mathbf{f}_{\text{ac}}$  previously studied for both solute and thermal induced gradients [7, 8, 22].

### B. Separation of length and time scales

Acoustofluidic devices are typically driven at a frequency  $f$  in the range from 1 to 50 MHz. The corresponding fast acoustic time scale  $t$  is

$$t = \frac{1}{\omega} = \frac{1}{2\pi f} = 3 - 160 \text{ ns.} \quad (8)$$

The time scale  $\tau$  associated with the hydrodynamic and thermal flow is slower. Following the analysis by Karlsen and Bruus [22], we estimate for a typical aqueous suspension in a channel of height  $H = 0.5$  mm with density  $\rho$ , relative density difference  $\hat{\rho} = 0.1$  induced by gradients in either concentration or temperature, and kinematic viscosity  $\nu = \eta/\rho$ , the following characteristic time scales: thermal relaxation  $t_{\text{therm}} = H^2/D^{\text{th}}$ , viscous relaxation  $t_{\text{visc}} = H^2/\nu_0$ , inertial motion  $t_{\text{inert}} \approx \sqrt{H/(g\hat{\rho})}$ , and steady shear motion  $t_{\text{shear}} \approx \nu_0/(Hg\hat{\rho})$  are all in the order of 10 ms. So for the slow hydrodynamic time scale  $\tau$ , we have

$$\tau \approx t_{\text{therm}} \approx t_{\text{visc}} \approx t_{\text{inert}} \approx t_{\text{shear}} \approx 10 \text{ ms.} \quad (9)$$

The slow thermo-hydrodynamic and the fast acoustic time scales are thus separated by 4 to 5 orders of magnitude, and we therefore solve the fast and slow dynamics separately as in Ref. [22]. In this work, we only study the steady limit of the slow time scale and describe any given physical field  $Q_{\text{phys}}$  as a sum of a steady field  $Q_0$  and a time-varying acoustic field  $Q_1 e^{-i\omega t}$  with a steady complex-valued amplitude  $Q_1$ ,

$$Q_{\text{phys}}(t) = Q_0 + \text{Re} [Q_1 e^{-i\omega t}]. \quad (10)$$

The steady (or slowly varying) fields sets the density and compressibility, which governs the acoustic fields. Conversely, the fast acoustic time scale creates an oscillation-time-averaged acoustic body force  $\mathbf{f}_{\text{ac}}$  and acoustic heating-power density  $P_{\text{ac}}$  that enter the equations of motion for the steady fields. A time-average of a product of two acoustic terms is also a steady term, as expressed by the well-known relation  $\langle \text{Re} [A_1 e^{-i\omega t}], \text{Re} [B_1 e^{-i\omega t}] \rangle = \frac{1}{2} \text{Re} [A_1 B_1^*]$ , where the asterisk denote complex conjugation. In contrast to perturbation theory [7], we do not require that  $Q_1$  is much smaller than  $Q_0$ , but we do neglect higher harmonic terms with time-dependence  $e^{\pm i n \omega t}$ ,  $n = 2, 3, \dots$

Acoustofluidic systems exhibit dynamics on two length scales, one set by the wavelength of the acoustic fields, and one set by the viscous and thermal boundary layers. The boundary conditions on the velocity field, stress,

heat flux and thermal field at the fluid-solid interface results in the appearance of thermal boundary layer of width  $\delta_t$  in both the fluid and the solid, and in a viscous boundary layer of width  $\delta_s$  in the fluid. These boundary layers are localized near fluid-solid interfaces, and their dynamically-defined widths, jointly referred as  $\delta$ , are small compared to a typical device size or wavelength  $d$  [19],

$$\delta_s = \sqrt{\frac{2\nu_0}{\omega}}, \quad \delta_t = \sqrt{\frac{2D_0^{\text{th}}}{(1-X)\omega}} \approx \sqrt{\frac{2D_0^{\text{th}}}{\omega}}, \quad (11)$$

where  $X = 0$  for fluids and  $X = (\gamma - 1) \frac{4c_{\text{tr}}^2}{3c_{\text{lo}}^2} \lesssim 0.01$  for solids. Typically,  $\delta_t \lesssim \delta_s \lesssim 500$  nm, which is more than two orders of magnitude smaller than  $d \sim 100$   $\mu\text{m}$ . We introduce the usual complex wave numbers  $k_s$  and  $k_t$  associated with the boundary-layer widths  $\delta_s$  and  $\delta_t$ , respectively,

$$k_s = \frac{1+i}{\delta_s}, \quad k_t = \frac{1+i}{\delta_t}. \quad (12)$$

In the following analysis, the fast acoustics fields are separated into a bulk field (superscript  $d$ ) and boundary layer field (superscript  $\delta$ ) that are connected by the boundary conditions.

### C. Boundary conditions

In the usual Lagrangian picture [7], an element in an elastic solid with equilibrium position  $\mathbf{s}_0$  has at time  $t$  the position  $\mathbf{s}(\mathbf{s}_0, t) = \mathbf{s}_0 + \mathbf{s}_1(\mathbf{s}_0) e^{-i\omega t}$  and velocity  $\mathbf{V}^0 = -\partial_t \mathbf{s} = \mathbf{V}_1^0(\mathbf{s}_0) e^{-i\omega t}$  with  $\mathbf{V}_1^0(\mathbf{s}_0) = -i\omega \mathbf{s}_1(\mathbf{s}_0)$ . On the solid-fluid interface, the no-slip and continuous stress conditions apply as in Ref. [7] Eqs. (10) and (11). The velocity of the solid wall at a given time and position must equal the Eulerian-picture fluid velocity  $\mathbf{v}^{\text{fl}}$ ,

$$\mathbf{v}^{\text{fl}}(\mathbf{s}_0 + \mathbf{s}_1 e^{-i\omega t}, t) = \mathbf{V}_1^0(\mathbf{s}_0) e^{-i\omega t} = -i\omega \mathbf{u}_1^0(\mathbf{s}_0) e^{-i\omega t}. \quad (13)$$

This boundary condition must be obeyed separately for the steady and acoustic fields (subscript 0 and 1, respectively), so a Taylor expansion yields

$$\mathbf{v}_0(\mathbf{s}_0) = -\langle (\mathbf{s}_1 \cdot \nabla) \mathbf{v}_1 \rangle|_{\mathbf{s}_0}, \quad (14a)$$

$$\mathbf{v}_1(\mathbf{s}_0) = \mathbf{V}_1^0(\mathbf{s}_0). \quad (14b)$$

Similarly, at a given position on the fluid-solid interface with surface normal  $\mathbf{n}$ , the stress  $\boldsymbol{\sigma}$  must be continuous,

$$\boldsymbol{\sigma}_0^{\text{sl}}(\mathbf{s}_0) \cdot \mathbf{n} = \boldsymbol{\sigma}_0^{\text{fl}}(\mathbf{s}_0) \cdot \mathbf{n} + \langle (\mathbf{s}_1 \cdot \nabla) \boldsymbol{\sigma}_1^{\text{fl}}(\mathbf{s}_0) \cdot \mathbf{n} \rangle|_{\mathbf{s}_0}, \quad (15a)$$

$$\boldsymbol{\sigma}_1^{\text{sl}}(\mathbf{s}_0) \cdot \mathbf{n} = \boldsymbol{\sigma}_1^{\text{fl}}(\mathbf{s}_0) \cdot \mathbf{n}. \quad (15b)$$

Since the viscosity parameters  $\eta$  and  $\eta^b$  depend on the temperature, the explicit expressions of the two stress boundary conditions contains several terms.

Following Ref. [7], two sets of thermal boundary conditions must be imposed. Similar to the velocity, the temperature must be continuous across the solid-fluid interface. This condition must be obeyed separately in the steady and acoustic fields,

$$T_0^{\text{sl}}(\mathbf{s}_0) = T_0^{\text{fl}}(\mathbf{s}_0) + \langle \mathbf{s}_1 \cdot \nabla T_1^{\text{fl}} \rangle|_{\mathbf{s}_0}, \quad (16a)$$

$$T_1^{\text{sl}}(\mathbf{s}_0) = T_1^{\text{fl}}(\mathbf{s}_0). \quad (16b)$$

Similar to the stress, the normal component  $-k^{\text{th}} \mathbf{n} \cdot \nabla T$  of the heat flux must be continuous across the interface,

$$-k^{\text{th,sl}} \mathbf{n} \cdot \nabla T^{\text{sl}}(\mathbf{s}_0, t) = -k^{\text{th,fl}} \mathbf{n} \cdot \nabla T^{\text{fl}}(\mathbf{s}_0 + \mathbf{s}_1 e^{-i\omega t}, t). \quad (17)$$

Here and in the following, we neglect the tiny gradients in  $\mathbf{n}$  and  $\mathbf{s}_1$ . The steady and acoustic boundary conditions on the heat flux become,

$$\begin{aligned} -k_0^{\text{th,sl}} \mathbf{n} \cdot \nabla T_0^{\text{sl}}(\mathbf{s}_0) - \langle k_1^{\text{th,sl}} \mathbf{n} \cdot \nabla T_1^{\text{sl}}(\mathbf{s}_0) \rangle \\ = -k_0^{\text{th,fl}} \mathbf{n} \cdot \nabla T_0^{\text{fl}}(\mathbf{s}_0) - \langle k_1^{\text{th}} \mathbf{n} \cdot \nabla T_1^{\text{fl}}(\mathbf{s}_0) \rangle \end{aligned} \quad (18a)$$

$$\begin{aligned} - \langle \mathbf{s}_1 \cdot \nabla [k_0^{\text{th}} \nabla T_1^{\text{fl}}(\mathbf{s}_0)] \cdot \mathbf{n} \rangle, \\ -k_0^{\text{th,sl}} \mathbf{n} \cdot \nabla T_1^{\text{sl}}(\mathbf{s}_0) = -k_0^{\text{th,fl}} \mathbf{n} \cdot \nabla T_1^{\text{fl}}(\mathbf{s}_0), \end{aligned} \quad (18b)$$

#### D. Range of validity of the model

We briefly discuss the range of validity imposed by the main assumptions. Firstly, in this analysis we study steady fields and acoustic fields with the actuation frequency  $\omega$ . So our model is only valid when these fields are much larger than the higher harmonic fields at frequencies  $2\omega, 3\omega, \dots$ . The magnitudes  $v_{0a}, v_{1a},$  and  $v_{2a}$  of the steady  $\mathbf{v}_0$ , the acoustic  $\mathbf{v}_1$ , and the  $2\omega$ -harmonic  $\mathbf{v}_2$  velocities are given in Muller and Bruus [23] as,

$$v_{0a} = \frac{Q^2 v_{bc}^2}{c_s}, \quad v_{1a} = Q v_{bc}, \quad v_{2a} = \frac{Q^3 v_{bc}^2}{c_s}, \quad (19)$$

where the physical velocity field corresponding to  $\mathbf{v}_2$  is given as  $\mathbf{v}_2^{\text{phys}} = \text{Re}[\mathbf{v}_2 e^{-i2\omega t}]$ . Our model is valid if  $v_{1a} \gg v_{2a}$ , and this implies a limit on the acoustic energy density  $E_{\text{ac}} \approx \frac{1}{4} \rho_0 v_{1a}^2$ ,

$$E_{\text{ac}} \ll \frac{\rho_0 c_s^2}{4Q^2} \approx 10^3 - 10^5 \text{ J m}^{-3}, \quad (20)$$

where  $Q = 100 - 1000$  is typical for acoustofluidic devices. So in systems with high  $Q$  factors the higher order harmonics will be important at a lower  $E_{\text{ac}}$ .

Secondly, due to low oscillatory advection, we assume  $\nabla \cdot (q_0 \mathbf{v}_1) \approx q_0 \nabla \cdot \mathbf{v}_1$ , where  $q_0$  is a parameter of the fluid.

This requires  $|q_0 \nabla \cdot \mathbf{v}_1| \gg |\nabla q_0 \cdot \mathbf{v}_1|$ . At room temperature the validity of our theory is therefore limited by the most temperature sensitive parameter, the viscosity  $\eta_0$ ,

$$|\nabla T_0| \ll \left| \frac{\eta_0 k_c}{(\partial_T \eta)_{T_0}} \right| \approx 5000 \frac{\text{K}}{\text{mm}}. \quad (21)$$

Conventional acoustofluidic systems are well within this limit  $|\nabla T_0| \lesssim 50 \text{ K/mm} \ll 5000 \text{ K/mm}$ .

Thirdly, the effective boundary-layer theory requires the boundary-layer width to be much smaller than the bulk wavelength,  $k_0 \delta \ll 1$ , see Section II B, which is true for MHz acoustics in water.

### III. FAST-TIME-SCALE ACOUSTIC FIELDS

The acoustic or fast-time-scale part of thermoviscous acoustofluidics is thoroughly studied in Ref. [7] as the first order fields in the perturbative model. The governing equations of these fields are the same for the perturbative and the iterative model, and therefore the theory from Ref. [7] can be directly applied. This is an effective theory, in which the thermal and viscous boundary layers are given analytically and incorporated in effective boundary conditions on the pressure  $p_1$  and displacement field  $\mathbf{u}_1$ . The governing equations for the bulk fields and the effective boundary conditions on the solid-fluid boundary are given in Ref. [7], Eqs. (19), (20), (23), (24), and (34), and they are briefly summarized below.

#### A. Governing equations in the bulk

In the bulk of the fluid, as shown in Ref. [7] Sec. IV A, the acoustic pressure field  $p_1$  and the associated bulk velocity  $\mathbf{v}_1^d$  and adiabatic temperature  $T_1^d$  are governed by the Helmholtz equation, derived from Eqs. (3) and (4),

$$\nabla^2 p_1 = -k_c^2 p_1, \quad k_c = \frac{\omega}{c} (1 + i\Gamma_{0c}^{\text{fl}}), \quad (22a)$$

$$\mathbf{v}_1^{d,p} = -i \frac{1 - i\Gamma_{0c}^{\text{fl}}}{\omega \rho_0} \nabla p_1, \quad (22b)$$

$$T_1^d = (\gamma - 1) \frac{\kappa_{s0}}{\alpha p_0} p_1. \quad (22c)$$

Further, as shown in Ref. [7] Sec. IV B, the displacement  $\mathbf{u}_1$  in the solid is governed by the temperature-dependent Cauchy equation, derived from Eqs. (1) and (2),

$$-\rho_0 \omega^2 \mathbf{u}_1^d = \nabla \cdot \boldsymbol{\sigma}_1^{\text{sl},d}, \quad (23a)$$

$$\boldsymbol{\sigma}_1^{\text{sl},d} = -\frac{\alpha_p}{\kappa_T} T_1^d \mathbf{I} + \boldsymbol{\tau}_1, \quad (23b)$$

$$\begin{aligned} \boldsymbol{\tau}_1^{\text{sl},d} = \rho_0 c_{\text{tr}}^2 \left[ \nabla \mathbf{u}_1 + (\nabla \mathbf{u}_1)^T \right] \\ + \rho_0 (c_{10}^2 - 2c_{\text{tr}}^2) (\nabla \cdot \mathbf{u}_1) \mathbf{I}. \end{aligned} \quad (23c)$$

The boundary layers at the fluid-solid interface are incorporated analytically through two effective boundary conditions. Firstly, see Ref. [7] Eq. (34a), the velocity must be continuous across the interface, here imposed on  $\partial_z p_1$  in the fluid,

$$\begin{aligned} \partial_z p_1 = & i \frac{\omega \rho_0}{1 - i\Gamma_s} (V_{1z}^0 - \frac{i}{k_s} \nabla \cdot \mathbf{V}_1^0) - \frac{i}{k_s} (k_c^2 + \partial_z^2) p_1 \\ & + \frac{i}{k_t} \frac{\alpha_p}{\kappa_T} k_0^2 T_1^{\delta 0, \text{fl}}, \quad \text{for } z = 0, \end{aligned} \quad (24a)$$

where  $T_1^{\delta 0, \text{fl}}$  is the boundary-layer temperature field given in the following subsection. Secondly, see Ref. [7] Eq. (34b), the stress must be continuous across the interface, here imposed on  $\sigma_1^{d, \text{sl}}$  in the solid,

$$\sigma_1^{d, \text{sl}} \cdot \mathbf{e}_z = -p_1 \mathbf{e}_z + i k_s \eta_0 \left[ \mathbf{v}_1^{d0, \text{sl}} + \frac{i}{\omega \rho_0} \nabla p_1 \right]. \quad (24b)$$

The effective boundary conditions (24) enable 3D simulations with a coarse mesh, because the boundary layer does not need to be resolved numerically.

## B. Analytical form of the boundary layers

The analytical solution for the boundary layers was in Ref. [7] used to set effective boundary conditions on the acoustic fields and the steady streaming field. Here, we also need them to derive the effective boundary conditions for the steady temperature field. The analytical solution of the temperature boundary layer in the fluid  $T_1^{\delta, \text{fl}}$  and solid  $T_1^{\delta, \text{sl}}$  is given in Ref. [7] Eq. (29) as,

$$T_1^{\delta, \text{fl}} = -\frac{\tilde{Z}}{1 + \tilde{Z}} [T_1^{\text{sl}, d0}(x, y) - T_1^{\text{fl}, d0}(x, y)] e^{i k_t^{\text{fl}} z}, \quad (25a)$$

$$T_1^{\delta, \text{sl}} = +\frac{1}{1 + \tilde{Z}} [T_1^{\text{sl}, d0}(x, y) - T_1^{\text{fl}, d0}(x, y)] e^{-i k_t^{\text{sl}} z}, \quad (25b)$$

$$\tilde{Z} = \frac{k_0^{\text{th}, \text{sl}} k_t^{\text{sl}}}{k_0^{\text{th}, \text{fl}} k_t^{\text{sl}}} = \sqrt{\frac{k_0^{\text{th}, \text{sl}} c_{p0}^{\text{sl}} \rho_0^{\text{sl}}}{k_0^{\text{th}, \text{fl}} c_{p0}^{\text{fl}} \rho_0^{\text{fl}}}}. \quad (25c)$$

The acoustic velocity  $\mathbf{v}_1$  is split into three fields, see Ref. [7] Eqs. (20a): the bulk velocity  $\mathbf{v}_1^{d, p}$  and the thermal boundary-layer velocity  $\mathbf{v}_1^{d, T}$ , both compressible gradient fields in the Helmholtz decomposition (superscript "d"), and the viscous boundary-layer velocity  $\mathbf{v}_1^\delta$ ,

$$\mathbf{v}_1 = \mathbf{v}_1^{d, p} + \mathbf{v}_1^{d, T} + \mathbf{v}_1^\delta \quad (26)$$

As derived analytically in Ref. [7] Eqs. (30) and (33b),  $\mathbf{v}_1^\delta$  and  $\mathbf{v}_1^{d, T}$  are given by,

$$\mathbf{v}_1^\delta = \mathbf{v}_1^{\delta 0}(x, y) e^{i k_s z}, \quad (27a)$$

$$\mathbf{v}_1^{d, T} = \alpha_{p0} D_0^{\text{th}} \nabla T_1^\delta = \frac{\alpha_{p0} k_0^{\text{th}}}{\rho_0 c_{p0}} \nabla T_1^\delta. \quad (27b)$$

These analytical expressions are used in Section IV C to derive the contribution from the acoustic fields to the boundary condition of the steady thermal field.

In terms of bulk and boundary fields combined with Eqs. (5b) and (6a), the first-order density  $\rho_1$ , viscosity  $\eta_1$ , and thermal conductivity  $k_1^{\text{th}}$  are written as

$$\rho_1 = \rho_1^d + \rho_1^\delta, \quad \rho_1^\delta = -\rho_0 \alpha_p T_1^\delta, \quad (28a)$$

$$\eta_1 = \eta_1^d + \eta_1^\delta, \quad \eta_1^\delta = \eta_0 a_\eta^T \alpha_p T_1^\delta, \quad (28b)$$

$$\begin{aligned} \eta_1^d &= \eta_0 a_\eta^{p, \text{ad}} \kappa_s p_1, \\ k_1^{\text{th}} &= k_1^{\text{th}, d} + k_1^{\text{th}, \delta}, \quad k_1^{\text{th}, \delta} = k_0^{\text{th}} a_k^T \alpha_p T_1^\delta, \\ k_1^{\text{th}, d} &= k_0^{\text{th}} a_k^{p, \text{ad}} \kappa_s p_1. \end{aligned} \quad (28c)$$

## IV. SLOW-TIME-SCALE STEADY FIELDS

The steady or slow-time-scale part of thermoviscous acoustofluidics contains mechanical and temperature fields. The mechanical fields are studied in Ref. [7], so the equations for the displacement  $\mathbf{u}_0$  in the solids and pressure  $p_0$  and velocity  $\mathbf{v}_0$  in the fluids, can be carried over unchanged, and we just summarize the main results below. However, we need to develop the theory for the temperature field  $T_0$ , both its bulk part  $T_0^d$  and its boundary-layer part  $T_0^\delta$ , as it is not treated in Ref. [7].

### A. Mechanical bulk and boundary-layer fields

As  $|\mathbf{u}_0| \ll d$ , the steady displacement field  $\mathbf{u}_0$  is to a good approximation decoupled from both the steady thermal field and the acoustic fields, and consequently

$$\mathbf{u}_0 = \mathbf{0}. \quad (29)$$

The steady pressure  $p_0$  and streaming  $\mathbf{v}_0$  are governed by the the steady part of Eqs. (3a) and (3b),

$$0 = \nabla \cdot \mathbf{v}_0^d, \quad (30a)$$

$$0 = -\nabla [p_0^d - \langle \mathcal{L}_{\text{ac}}^d \rangle] - \nabla \cdot [\rho_0 \mathbf{v}_0 \mathbf{v}_0] + \eta_0 \nabla^2 \mathbf{v}_0^d + \mathbf{f}_{\text{ac}}^d. \quad (30b)$$

Here, the Lagrangian density  $\langle \mathcal{L}_{\text{ac}}^d \rangle$  and the acoustic body force  $\mathbf{f}_{\text{ac}}^d$  contain time averages  $\frac{1}{2} \langle A_1 B_1^* \rangle$  of pairs of acoustic fields  $A_1$  and  $B_1$ , given by Ref. [7] Eq. (52c),

$$\langle \mathcal{L}_{\text{ac}}^d \rangle = \frac{1}{4} \kappa_s |p_1|^2 - \frac{1}{4} \rho_0 |\mathbf{v}_1^{d, p}|^2, \quad (31a)$$

$$\begin{aligned} \mathbf{f}_{\text{ac}}^d &= -\frac{1}{4} |\mathbf{v}_1^{d, p}|^2 \nabla \rho_0 - \frac{1}{4} |p_1|^2 \nabla \kappa_s \\ &+ \left[ 1 - \frac{2a_\eta(\gamma - 1)}{\beta + 1} \right] \frac{\Gamma \omega}{c^2} \langle \mathbf{v}_1^{d, p} p_1 \rangle \\ &+ a_\eta \eta_0 (\gamma - 1) k_c^2 \langle \mathbf{s}_1^d \cdot \nabla \mathbf{v}_1^{d, p} \rangle. \end{aligned} \quad (31b)$$

The acoustic boundary layers, are taken into account analytically, and they only appear implicitly and impose a slip velocity on the bulk streaming field given by Ref. [7] Eq. (54) as,

$$\mathbf{v}_0^{d0} = (\mathbf{A} \cdot \mathbf{e}_x)\mathbf{e}_x + (\mathbf{A} \cdot \mathbf{e}_y)\mathbf{e}_y + (\mathbf{B} \cdot \mathbf{e}_z)\mathbf{e}_z, \quad (32a)$$

$$\begin{aligned} \mathbf{A} = & -\frac{1}{2\omega} \text{Re} \left\{ \mathbf{v}_1^{\delta 0*} \cdot \nabla \left( \frac{1}{2} \mathbf{v}_1^{\delta 0} - i \mathbf{V}_1^0 \right) - i \mathbf{V}_1^{0*} \cdot \nabla \mathbf{v}_1^{d,p} \right. \\ & \left. + \left[ \frac{2-i}{2} \nabla \cdot \mathbf{v}_1^{\delta 0*} + i \left( \nabla \cdot \mathbf{V}_1^{0*} - \partial_z v_{1z}^{d*} \right) \right] \mathbf{v}_1^{\delta 0} \right\} \\ & + \frac{1}{2\eta_0} \text{Re} \left\{ \eta_1^{d0} \mathbf{v}_1^{\delta 0*} + \frac{\delta_t}{\delta_t - i\delta_s} \eta_1^{\delta 0} \mathbf{v}_1^{\delta 0*} \right\}, \quad (32b) \end{aligned}$$

$$\mathbf{B} = \frac{1}{2\omega} \text{Re} \left\{ i \mathbf{v}_1^{d0*} \cdot \nabla \mathbf{v}_1^{d,p} \right\}, \quad (32c)$$

$$\mathbf{v}_1^{\delta 0} = -i\omega \mathbf{u}_1^0 - \mathbf{v}_1^{d0}, \quad (32d)$$

$$\eta_1^{\delta 0} = -\frac{\tilde{Z}}{1 + \tilde{Z}} \eta_0 a_\eta^T \alpha_p [T_1^{\text{sl},d0} - T_1^{\text{fl},d0}], \quad (32e)$$

$$\eta_1^{d0} = \eta_0 a_\eta^{p,\text{ad}} \kappa_s p_1, \quad (32f)$$

where the expressions for  $\mathbf{v}_1^{\delta 0}$ ,  $\eta_1^{\delta 0}$ , and  $\eta_1^{d0}$  in terms of bulk fields are obtained from Eqs. (13), (25a), and (28b).

## B. Steady temperature fields

The steady temperature field  $T_0$  is given as the time averaged terms of Eqs. (1b) and (3c) in the solid and fluid, respectively. The time averaged terms either consist of steady fields  $a_0$  or terms with time-averaged products  $\langle a_1 b_1 \rangle$  of two time-varying fields  $a_1$  and  $b_1$ . All terms of the latter type are collected as an acoustic power  $P_{\text{ac}}$ . In the fluid, neglecting small terms by using  $\mathbf{v}_0 \cdot \boldsymbol{\sigma}_{11} \ll \langle \mathbf{v}_1 \cdot \boldsymbol{\sigma}_1 \rangle$ ,  $\rho_1 \mathbf{v}_0 \ll \rho_0 \mathbf{v}_1$ ,  $\nabla \cdot \langle \rho_0 \mathbf{v}_0 + \rho_1 \mathbf{v}_1 \rangle = 0$ ,  $\epsilon_{11} + \frac{1}{2} |\mathbf{v}_0|^2 + \frac{1}{2} |\mathbf{v}_1|^2 \ll \epsilon_0$ ,  $\epsilon_1^d = c_{p0} T_1^d - \frac{\alpha_{p0} T_0}{\rho_0} p_1^d = 0$ ,  $\epsilon_1^\delta = c_{p0} T_1^\delta$ , and  $|\mathbf{v}_0 \cdot \boldsymbol{\sigma}_0| \ll |k_0^{\text{th}} \nabla T_0|$ , the steady part of Eq. (3c) becomes

$$0 = \nabla \cdot \left[ k_0^{\text{th}} \nabla T_0^{\text{fl}} \right] - c_p \rho_0 \mathbf{v}_0 \cdot \nabla T_0^{\text{fl}} + P_{\text{ac}}^{\text{fl}} + P, \quad (33a)$$

$$\begin{aligned} P_{\text{ac}}^{\text{fl}} = & \nabla \cdot \left[ \langle k_1^{\text{th}} \nabla T_1^{\text{fl}} \rangle - \langle p_1 \mathbf{v}_1 \rangle + \langle \mathbf{v}_1 \cdot \boldsymbol{\tau}_1 \rangle \right. \\ & \left. - \rho_0 c_{p0} \langle T_1^{\text{fl}} \mathbf{v}_1 \rangle \right] - c_p \langle \rho_1 \mathbf{v}_1 \rangle \cdot \nabla T_0^{\text{fl}}, \quad (33b) \end{aligned}$$

In the solid there is no advection, and the  $T_0$  part of Eq. (1b) is controlled by thermal diffusion alone,

$$0 = \nabla \cdot (k_0^{\text{th}} \nabla T_0^{\text{sl}}) + P_{\text{ac}}^{\text{sl}} + P, \quad (34a)$$

$$P_{\text{ac}}^{\text{sl}} = \nabla \cdot \langle k_1^{\text{th}} \nabla T_1^{\text{sl}} \rangle. \quad (34b)$$

In both the solid (sl) and the fluid (fl), the temperature field and the acoustic power are separated into a boundary term ( $\delta$ ) and a bulk term ( $d$ ),

$$T_0^{\text{xl}} = T_0^{\text{xl},d} + T_0^{\text{xl},\delta}, \quad P_{\text{ac}} = P_{\text{ac}}^d + P_{\text{ac}}^\delta. \quad (35)$$

The boundary-layer temperature fields  $T_0^{\text{fl},\delta}$  and  $T_0^{\text{sl},\delta}$  are defined as the response to  $P_{\text{ac}}^\delta$ , and all three fields are required to go to zero far away from the boundary.

The two bulk and two boundary-layer fields are linked by the boundary conditions (16a) and (18a) at the fluid-solid interface, which impose continuity of the temperature and of the heat flux density. The first is

$$T_0^{\text{fl},d0} + T_0^{\text{fl},\delta 0} + \langle \mathbf{s}_1 \cdot \nabla T_1^{\text{fl}} \rangle = T_0^{\text{sl},d0} + T_0^{\text{sl},\delta 0}, \quad (36a)$$

and the second is

$$\begin{aligned} k_0^{\text{th}} \mathbf{n} \cdot \nabla (T_0^{\text{fl},d} + T_0^{\text{fl},\delta}) + \langle k_1^{\text{th}} \mathbf{n} \cdot \nabla T_1^{\text{fl}} \rangle \\ + \langle \mathbf{s}_1 \cdot \nabla (k_0^{\text{th}} \nabla T_1^{\text{fl}}) \cdot \mathbf{n} \rangle \\ = -k_0^{\text{th,sl}} \mathbf{n} \cdot \nabla (T_0^{\text{sl},d} + T_0^{\text{sl},\delta}) - \langle k_1^{\text{th,sl}} \mathbf{n} \cdot \nabla T_1^{\text{sl}} \rangle. \quad (36b) \end{aligned}$$

Thus, the steady bulk solid and fluid fields  $T_0^{\text{sl},d}$  and  $T_0^{\text{fl},d}$  can be matched at the interface by using the analytical form of the boundary-layer fields  $T_0^{\text{sl},\delta}$  and  $T_0^{\text{fl},\delta}$ .

## C. Steady boundary-layer temperature fields

In the fluid, the boundary-layer  $T_1^{\delta,\text{fl}}$  is driven by  $P_{\text{ac}}^\delta$  of Eqs. (33b) and (35). We neglect the convection term  $c_{p0} (\rho_0 \mathbf{v}_0 + \langle \rho_1 \mathbf{v}_1 \rangle) \nabla T$  in the boundary layer, because it contains only one gradient  $\propto \delta^{-1}$ , and thus is a factor  $k\delta$  smaller than the viscous term  $\nabla \cdot \langle \mathbf{v}_1 \cdot \boldsymbol{\tau}_1 \rangle$  containing two gradients  $\propto \delta^{-2}$ . Moreover, in the boundary layer  $\nabla \cdot [k_0^{\text{th}} \nabla T_0^{\text{fl},\delta}] \approx k_0^{\text{th}} \partial_z^2 T_0^\delta$ , so the governing equation for the steady boundary-layer temperature field  $T_0^{\text{fl},\delta}$  therefore reduces to,

$$k_0^{\text{th}} \partial_z^2 T_0^{\text{fl},\delta} = -P_{\text{ac}}^\delta \quad (37a)$$

$$\begin{aligned} P_{\text{ac}}^\delta = & \nabla \cdot \left[ \langle k_1^{\text{th}} \nabla T_1 \rangle^{\text{fl},\delta} + \langle \mathbf{v}_1 \cdot \boldsymbol{\tau}_1 \rangle^{\text{fl},\delta} \right. \\ & \left. - \langle p_1 \mathbf{v}_1 \rangle^{\text{fl},\delta} - \rho_0 c_{p0} \langle T_1 \mathbf{v}_1 \rangle^{\text{fl},\delta} \right]. \quad (37b) \end{aligned}$$

The first-order boundary-layer fields are known analytically, see Section III B, so we can now analyze the four terms in  $P_{\text{ac}}^\delta$  one by one and integrate Eq. (37a) once from  $z = \infty$  to  $z = 0$  to find the normal derivative  $\partial_z T_0^{\text{fl},\delta}$  and twice to find the value  $T_0^{\text{fl},\delta}$ . We describe each field at  $z = 0$  as a surface field (with superscript “0”), which depends only on  $x$  and  $y$ , multiplied by the exponential  $z$  dependence given analytically in Section III B. The reduction and integration of the four terms is straightforward but tedious as shown in Appendix A. The normal gradient  $\partial_z T_0^{\text{fl},\delta}$  at the fluid-solid interface becomes

Eq. (A13),

$$\begin{aligned} \partial_z T_0^{\text{fl},\delta 0} = & \text{Re} \left[ \frac{1+i}{4D_0^{\text{th}}} \left\{ \frac{1-i}{2} \frac{\delta_s \omega}{c_p} \mathbf{v}_1^{\delta 0} \cdot \mathbf{v}_1^{\delta 0*} - \frac{\delta_t \omega \alpha_{p0}}{c_p \rho_0} p_1^0 T_1^{\delta 0*} \right. \right. \\ & - \frac{\delta_s}{\delta_s + i\delta_t} \left[ \delta_t \nabla_{\parallel} T_1^{\delta 0} \cdot \mathbf{v}_{1,\parallel}^{\delta 0*} - (1-i) T_1^{\delta 0} v_{1,z}^{\delta 0*} \right] \\ & - iT_1^{\delta 0} \left[ v_{1,z}^{d,T0*} + (1+i) v_{1,z}^{d,p0*} - \delta_t \omega \kappa_s p_1^{0*} \right] \\ & \left. \left. - \delta_t \nabla_{\parallel} T_1^{\delta 0} \cdot \mathbf{v}_{1,\parallel}^{d,p0*} + \delta_t \omega \frac{k_1^{\text{th},\delta 0} + k_1^{\text{th},d0}}{k_0^{\text{th}}} T_1^{\delta 0*} \right\} \right], \quad (38a) \end{aligned}$$

where all quantities are evaluated in the fluid. The boundary-layer heat flux  $k_0^{\text{th},\delta 0} \partial_z T_0^{\text{fl},\delta 0}$  is dominated by the first term  $\mathbf{v}_1^{\delta 0} \cdot \mathbf{v}_1^{\delta 0*}$  which is a factor of  $\alpha_{p0} T_0 \simeq 10$  larger than the terms including the boundary layer temperature field  $T_1^{\delta 0}$ . The two last terms including  $k_1^{\text{th}}$  are smaller by a factor of  $\gamma - 1$  and are therefore only important for gases and not liquids. The result Eq. (A15) for the boundary-layer interface temperature  $T_0^{\text{fl},\delta 0}$  is,

$$\begin{aligned} T_0^{\text{fl},\delta 0} = & \frac{\delta_t}{4D_0^{\text{th}}} \text{Re} \left\{ - \frac{\delta_s^2 \omega}{2\delta_t c_p} \mathbf{v}_1^{\delta 0} \cdot \mathbf{v}_1^{\delta 0*} + \frac{\delta_t \omega \alpha_{p0}}{c_p \rho_0} p_1^0 T_1^{\delta 0*} \right. \\ & + i \frac{\delta_s^2}{(\delta_s + i\delta_t)^2} \left[ \delta_t \nabla_{\parallel} T_1^{\delta 0} \cdot \mathbf{v}_{1,\parallel}^{\delta 0*} - (1-i) T_1^{\delta 0} v_{1,z}^{\delta 0*} \right] \\ & - T_1^{\delta 0} \left[ \frac{1-i}{2} v_{1,z}^{d,T0*} + (1+i) v_{1,z}^{d,p0*} - \delta_t \omega \kappa_s p_1^{0*} \right] \\ & \left. + i\delta_t \nabla_{\parallel} T_1^{\delta 0} \cdot \mathbf{v}_{1,\parallel}^{d,p0*} - \delta_t \omega \frac{(1+i)k_1^{\text{th},\delta 0} + 2k_1^{\text{th},d0}}{2k_0^{\text{th}}} T_1^{\delta 0*} \right\}. \quad (38b) \end{aligned}$$

Again, the first term  $\mathbf{v}_1^{\delta 0} \cdot \mathbf{v}_1^{\delta 0*}$  originating from the viscous boundary layer is the leading term.

In the solid, the boundary layer field  $T_0^{\text{sl},\delta}$  is governed by  $P_{\text{ac}}^{\delta}$  of Eqs. (34b) and (35) as,

$$0 = -\nabla \cdot \left[ k_0^{\text{th,sl}} \nabla T_0^{\text{sl},\delta} + \langle k_1^{\text{th,sl}} \nabla T_1^{\text{sl}} \rangle^{\delta} \right], \quad (39)$$

which, when using  $\nabla^2 T_0^{\text{sl},\delta} \simeq \partial_z^2 T_0^{\text{sl},\delta}$ , gives the following differential equation for the boundary-layer field  $T_0^{\text{sl},\delta}$ ,

$$k_0^{\text{th}} \partial_z^2 T_0^{\text{sl},\delta} = -\nabla \cdot \langle k_1^{\text{th}} \nabla T_1^{\text{sl}} \rangle^{\delta}. \quad (40)$$

The right-hand side is similar to  $\nabla \cdot \langle k_1^{\text{th}} \nabla T_1^{\text{fl}} \rangle^{\delta}$  in the fluid boundary layer, which contributes with terms of the type  $k_1^{\text{th}} T_1^{\delta 0*}$  in Eqs. (38a) and (38b). These terms in the fluid domain can be directly transferred to the solid domain, which results in the following normal heat flux and temperature in the boundary layer on the solid side of the fluid-solid interface,

$$\partial_z T_0^{\text{sl},\delta} = \frac{1}{2\delta_t} \text{Re} \left[ (1+i) \frac{k_1^{\text{th},\delta 0} + k_1^{\text{th},d0}}{k_0^{\text{th}}} T_1^{\delta 0*} \right], \quad (41a)$$

$$T_0^{\text{sl},\delta} = -\frac{1}{4} \text{Re} \left[ \frac{(1+i)k_1^{\text{th},\delta 0} + 2k_1^{\text{th},d0}}{k_0^{\text{th}}} T_1^{\delta 0*} \right], \quad (41b)$$

where all quantities are evaluated in the solid. For a fluid-solid interface these terms are negligible compared to the leading term in the fluid boundary layer. They can be important for certain gas-solid interfaces.

#### D. Steady bulk temperature fields

The steady bulk temperature field  $T_0^{\text{fl},d}$  in the fluid is governed by the long-range bulk terms of Eq. (33),

$$0 = -\nabla \cdot \left[ k_0^{\text{th}} \nabla T_0^{\text{fl},d} \right] - c_p \rho_0 \mathbf{v}_0 \cdot \nabla T_0^{\text{fl},d} + P_{\text{ac}}^d + P, \quad (42a)$$

$$P_{\text{ac}}^d = -\nabla \cdot \left[ \langle k_1^{\text{th},d} \nabla T_1^d \rangle - \langle p_1 \mathbf{v}_1^{d,p} \rangle + \langle \mathbf{v}_1^{d,p} \cdot \boldsymbol{\tau}_1^d \rangle \right] - c_p \langle \rho_1^d \mathbf{v}_1^{d,p} \rangle \cdot \nabla T_0^d. \quad (42b)$$

Similarly,  $T_0^{\text{sl},d}$  in the solid is governed by the long-range bulk terms of Eq. (34),

$$0 = -\nabla \cdot \left[ k_0^{\text{th}} \nabla T_0^{\text{sl},d} \right] + P_{\text{ac}}^d + P, \quad (43a)$$

$$P_{\text{ac}}^d = -\nabla \cdot \langle k_1^{\text{th,sl}} \nabla T_1^{\text{sl},d} \rangle. \quad (43b)$$

Here,  $P$  is an external heat power source from fields not included in the model, such as heat generated by light absorption or by Joule heating from electric currents. The bulk fields  $T_0^{\text{sl},d}$  and  $T_0^{\text{fl},d}$  are connected at the fluid-solid interface by the Dirichlet and Neumann boundary conditions (36a) and (36b).

We choose to apply the Dirichlet condition (36a) on  $T_0^{\text{fl},d}$  in the fluid and therefore write

$$\begin{aligned} T_0^{\text{fl},d} = & T_0^{\text{sl},d} - T_0^{\text{fl},\delta 0} \\ & - \frac{1}{2} \text{Re} \left[ \mathbf{s}_1 \cdot \nabla T_1^{\text{fl},d*} - k_t^{\text{fl}} (\mathbf{s}_1 \cdot \mathbf{n}) T_1^{\delta 0*,\text{fl}} \right]. \quad (44) \end{aligned}$$

All fields on the right-hand side can be expressed in terms of bulk fields: the acoustic boundary-layer fields  $T_1^{\delta,\text{fl}}$  and  $T_1^{\delta,\text{sl}}$  through  $T_1^{\text{fl},d}$  and  $T_1^{\text{sl},d}$  by Eq. (25), the steady boundary-layer fields  $T_0^{\text{fl},\delta}$  and  $T_0^{\text{sl},\delta}$  through  $T_1^{\delta,\text{fl}}$ ,  $T_1^{\delta,\text{sl}}$ ,  $T_1^{\text{fl},d}$ ,  $T_1^{\text{sl},d}$ , and  $p_1$  by Eqs. (28), (38b), and (41b), and finally  $\mathbf{s}_1$  through  $\mathbf{u}_1$  by the simple identification  $\mathbf{s}_1 = \mathbf{u}_1(\mathbf{s}_0)$ . Consequently,  $T_0^{\text{fl},d}$  is given solely by steady and acoustic bulk fields, a crucial point in the implementation of a numerical simulation involving only bulk fields, which avoids the numerically demanding resolution of the narrow boundary layers. Note how the boundary-layer fields results in a discontinuity in the bulk temperature field, when crossing the fluid-solid interface.

Conversely, the Neumann boundary condition (36b) is enforced on the temperature field  $T_0^{\text{sl},d}$  in the solid. Together with the evaluation of the steady boundary layer terms in Eqs. (38a) and (41), it becomes,

$$\begin{aligned} k_0^{\text{th,sl}} \mathbf{n} \cdot \nabla T_0^{\text{sl},d} = & k_0^{\text{th,fl}} \mathbf{n} \cdot \nabla T_0^{\text{fl},d} + k_0^{\text{th,fl}} \partial_z T_0^{\text{fl},\delta} \\ & + \frac{1}{2} \text{Re} \left[ k_t^{\text{fl}} k_1^{\text{th,fl}} T_1^{\delta*,\text{fl}} - \frac{2i}{\delta_t^2} k_0^{\text{th,fl}} (\mathbf{s}_1 \cdot \mathbf{n}) T_1^{\delta*,\text{fl}} \right]. \quad (45) \end{aligned}$$



Similar to Eq. (44), all fields on the right-hand side of Eq. (45) can be expressed in terms of steady and acoustic bulk fields through  $T_1^{\delta,fl}$ ,  $T_1^{\delta,sl}$ ,  $T_1^{fl,d}$ ,  $T_1^{sl,d}$ , and  $p_1$  by Eqs. (28), (38a), and (41a), and by using  $\mathbf{s}_1 = \mathbf{u}_1(\mathbf{s}_0)$ . Consequently,  $\partial_z T_0^{fl,d}$  is given solely by steady and acoustic bulk fields.

In summary, the bulk temperature fields are governed by equation Eqs. (42) and (43) together with the effective boundary conditions (44) and (45), in which the boundary-layer fields are taken into account analytically and expressed in terms of bulk fields. The boundary conditions on the outer surfaces could either be a Dirichlet boundary condition, such as Peltier elements or heat sinks, a no-flux boundary condition as for an air interface, or a combination such as air cooling and solids made of glass or polymer with a thermal diffusivity similar to water.

## V. AN ITERATIVE PROCEDURE TO ACCOUNT FOR NONLINEAR EFFECTS

The separation of time scales leaves us with one set of equations presented in Section III for the acoustic fields  $p_1$  and  $\mathbf{u}_1$ , and another set presented in Section IV for the steady fields  $\mathbf{v}_0$ ,  $p_0$ ,  $T_0^{sl}$  and  $T_0^{fl}$ . These steady and acoustic fields impact each other through the temperature-dependent material parameters, the acoustic body force  $\mathbf{f}_{ac}^d$ , the acoustic power  $P_{ac}$ , and the effective boundary conditions, in which the boundary-layer fields are taken into account analytically but appear only implicitly through expressions involving only bulk fields. As described in the following, the combined set of equations can be solved by a self-consistent iterative procedure, in which the coupled acoustic and steady fields are solved in an iterative sequence until convergence is obtained.

The steady fields  $\mathbf{v}_0$ ,  $p_0$ ,  $T_0^{sl}$  and  $T_0^{fl}$  are computed from the governing equations in the bulk, (30) (42) and (43) with the effective boundary conditions (32), (44) and (45). The acoustic fields  $p_1$  and  $\mathbf{u}_1$  computed from the governing (22) and (23) with the effective boundary conditions (24a) and (24b).

The equations are implemented in COMSOL Multiphysics [15] using the “Weak Form PDE Module”, and the effective boundary conditions are set using the “Dirichlet boundary condition Module” and the “Weak Contribution Module”. The iterative solver is implemented using the “Segregated Solver” with two steps: “Step 1” computes the steady fields  $\mathbf{v}_0$ ,  $p_0$ ,  $T_0^{sl}$  and  $T_0^{fl}$  based on the current value of the acoustic fields, and “Step 2” computes the acoustic fields  $\mathbf{u}_1$  and  $p_1$  based on the current value of the steady fields. The segregated solver then runs until convergence is obtained.

The benefit of the iterative setup compared to the traditional perturbation setup [1, 5–7] is that nonlinear effects are included. In the steady fields there are two dominating nonlinear effects in typical microscale acoustoflu-

idic devices: (1) Thermal convection proportional to  $\mathbf{v}_0 \cdot \nabla T_0$ , which dominates over thermal diffusion proportional to  $\nabla^2 T_0$ , when  $|\mathbf{v}_0| \gtrsim D_0^{th}/d \approx 0.3 - 1.5$  mm/s for  $d = 100 - 500$   $\mu\text{m}$ . Note that for larger systems convection becomes important at lower velocities, and in recent experimental studies this limit has been reached [8, 24]. (2) Acoustic heating, which is due to the viscous dissipation  $P_{ac}^\delta$  in the viscous boundary layer, and which may lead to temperature gradients in the bulk large enough to result in a significant acoustic body force proportional to  $|p_1|^2 \nabla T_0$  through the temperature-dependent compressibility and density, see Eq. (31b), that drive an acoustic streaming, which at sufficiently high acoustic energy densities dominates over the usual boundary-driven Rayleigh streaming.

## VI. MODEL VALIDATION AND EXAMPLES

In this section, we implement and validate our self-consistent iterative procedure in Comsol. We also study two specific examples of the above-mentioned nonlinear effects, which our model is able to predict.

### A. Example in 2D: Change of the acoustic streaming due to internal acoustic heating

Our basic perturbative thermoviscous acoustofluidics model has been validated both numerically [7] and experimentally [8]. Therefore, we here choose our first example to be a system, where we can validate numerically our model with the effective boundary conditions (44) and (45) with a full model, where the boundary layers are fully resolved. The chosen model system, is a long straight microchannel with a rectangular cross-section, embedded in a silicon base and capped with a glass lid. In the literature, this system running with a horizontal acoustic half-wave resonance has been widely used to separate particles in a flow through device and used in various studies both experimentally [25–28] and numerically [1, 2]. Moreover, in the Letter that we published simultaneously with this work [14], we have provided experimental validation of the numerical model being presented below. The example aims to demonstrate three important points: (1) Validation of the effective model, (2) modeling the internal acoustic heating in an acoustofluidic chip, and (3) demonstrating nonlinear effects at high acoustic energies, effects that are further investigated by modeling and experiments in Ref. [14].

The model is a long straight silicon chip of width  $W_{Si} = 3$  mm and height  $H_{Si} = 0.4$  mm, in the top of which is placed a fluid channel of width  $W = 375$   $\mu\text{m}$  and height  $H = 135$   $\mu\text{m}$  and a capping Pyrex glass lid of height  $H_{Py} = 1$  mm, see Fig. 1(a). On the bottom edge, following Ref. [7], the actuation is set to be  $\mathbf{u}_1^{\text{bot}}(y) = \frac{2d_0}{W} y e_z$ , and the temperature is  $T_0^{\text{bot}} = 25$   $^\circ\text{C}$ .

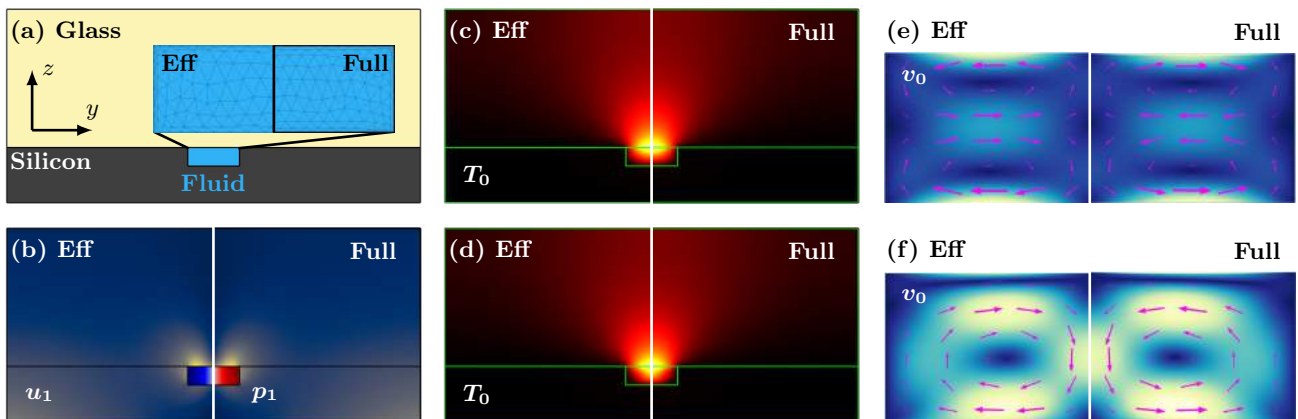


FIG. 1. Comparison between simulation results of the effective model (left, Eff) and the full model (right, Full). (a) Sketch of the 2D model of the chip with silicon, fluid and glass. (b) Color plot at the energy density  $E_{ac} = 28 \text{ J/m}^3$  of the displacement  $|\mathbf{u}_1|$  and pressure  $p_1$  in the fluid. (c) Color plot at  $E_{ac} = 28 \text{ J/m}^3$  of the steady temperature field  $\Delta T_0 = T_0 - T_0^{\text{bot}}$  from black (0) to yellow (8.7 mK). (d) Color plot at  $E_{ac} = 2680 \text{ J/m}^3$  of  $\Delta T_0$  from black (0) to yellow (230 mK). (e) Vector plot at  $E_{ac} = 28 \text{ J/m}^3$  of the streaming  $\mathbf{v}_0$  and color plot of its magnitude  $v_0$  from blue (0) to yellow (34  $\mu\text{m/s}$ ). (f) Same as (e) but at  $E_{ac} = 2680 \text{ J/m}^3$  and with the color scale of  $v_0$  from blue (0) to yellow (4.0 mm/s).

In Fig. 1(a) is shown the coarse mesh of the effective model (422 elements) and the fine mesh (8362 elements) of the boundary-layer-resolving full model that are needed to fulfil a mesh-convergence criterium of an  $L_2$ -norm [1] for the streaming velocity  $\mathbf{v}_0$  below 1% for  $E_{ac} = 28 \text{ J/m}^3$ . The good agreement between the two models is shown in Fig. 1(b)-(f) by the color plots of the resulting steady and acoustic fields computed from the effective (left side) and full (right side) model at both a low and a high acoustic energy density of  $E_{ac} = 28 \text{ J/m}^3$  and  $2680 \text{ J/m}^3$ . Both models show how the well-known four-roll Rayleigh streaming pattern at the low  $E_{ac}$  change into a two-roll pattern at high  $E_{ac}$ , a clear display of the nonlinear effect arising from the boundary layers, but nevertheless included in the effective model of the bulk fields. The relative deviation between the two models in the computed values of the resonance frequency and Q-factor of the 2-MHz half-wave resonance mode is less than 0.1%.

The effective boundary condition for the streaming velocity  $\mathbf{v}_0$  was already validated in Ref. [7], so here we thus just need to validate the effective boundary conditions (42) and (43) on the steady temperature field  $T_0$ . This is done in Fig. 2, showing excellent quantitative agreement between line plots of  $T_0$  for the full and the effective model.

We end the example by discussing the physics of the transition from the linear case with four flow rolls to the nonlinear case with two flow rolls. At the low acoustic energy  $E_{ac} = 28 \text{ J/m}^3$ , the acoustic pressure  $p_1$  and displacement  $\mathbf{u}_1$  field, as well as the steady streaming field  $\mathbf{v}_0$  are shown in Fig. 1(b). The source of the spatial inhomogeneities in the steady temperature field  $T_0$  in the

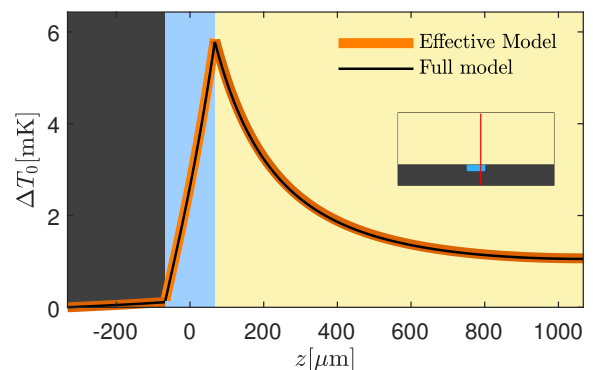


FIG. 2. Line plot at  $E_{ac} = 28 \text{ J/m}^3$  of the simulated steady temperature  $\Delta T_0$  in the effective and full model along the vertical red line  $y = \frac{1}{4}W_{fl}$  shown in the inset. The corresponding color plot of  $\Delta T_0$  is shown in Fig. 1(c).

fluid is the heat generation due to friction in the viscous boundary layer in the fluid at the top and bottom of the channel, and the different heat fluxes resulting from the relatively small values of the heat conductivity of water and glass compared to the large one of silicon. The latter ensures efficient transport of heat away from the bottom edge of the channel. Consequently, heating only occurs at the top of the channel near the glass lid. In Fig. 3(a)-(b), the resulting temperature fields are shown for a low  $E_{ac} = 28 \text{ J/m}^3$  and high  $E_{ac} = 9000 \text{ J/m}^3$  energy density, respectively. In both cases, the temperature is clearly larger at the center of the top edge of the channel. However, for the high- $E_{ac}$  case, the in-

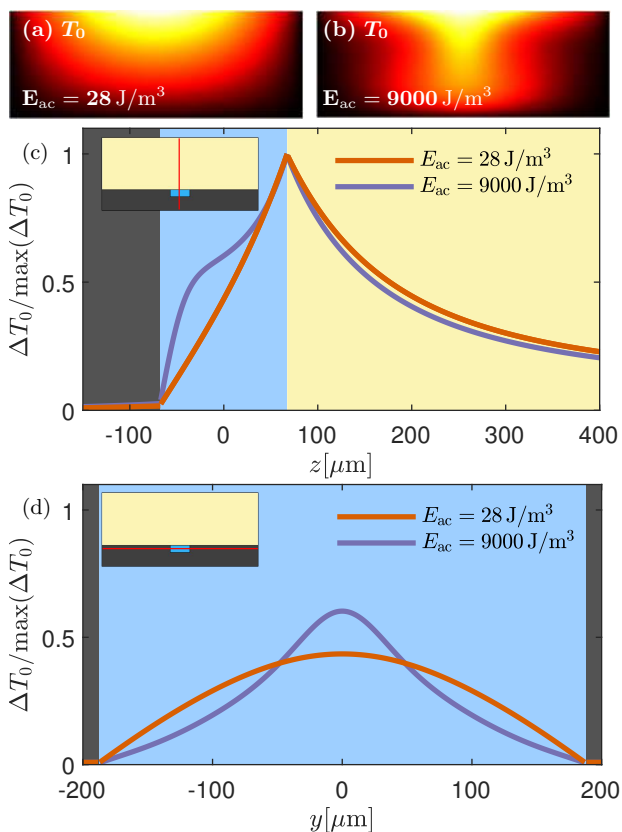


FIG. 3. (a) Color plot from 0 (black) to 8.7 mK (yellow) at  $E_{ac} = 28 \text{ J/m}^3$  of  $\Delta T_0$  from Fig. 1(c) zoomed in on the fluid domain. (b) Same as (a) but for  $E_{ac} = 9000 \text{ J/m}^3$  and a color scale from 0 (black) to 2375 mK (yellow). (c) Line plot of the normalized temperature rise  $\Delta T_0 / \max(\Delta T_0)$  along the vertical line at  $y = 0$  shown in the inset. (d) Same as (c) but along the horizontal line through the center of the microchannel shown in the inset.

created acoustic streaming is distorting the temperature field, as it induces a downward heat convection, which stretches the high-temperature region along a larger portion of the vertical center axis. The temperature boundary condition (44) results in nearly equal bulk and boundary layer temperature fields at the fluid-solid interface,  $T_0^{fl,d0} \approx T_0^{fl,\delta 0}$ , so the gradients in the temperature field are governed by the effective boundary condition on the heat flux (45).

The streaming fields for  $E_{ac} = 28 \text{ J/m}^3$  and  $E_{ac} = 2680 \text{ J/m}^3$  are shown in Fig. 1(e)-(f). First we can see that the full and effective model results in the same streaming field. Secondly, it is clear that at low acoustic energies the streaming is dominated by boundary driven streaming and at high acoustic energy it is dominated by the bulk-driven streaming induced by the acoustic-body-force Eq. (31b). When the gradients in density and compressibility is created due to temperature gradients, and neglecting Eckart streaming, the acoustic body force

is given as

$$\mathbf{f}_{ac}^d = -\frac{1}{4} \left( |p_1|^2 \partial_T \kappa_{s,0} + |\mathbf{v}_1|^2 \partial_T \rho_0 \right) \nabla T_0. \quad (46)$$

The temperature gradient  $\nabla T_0$  and  $|p_1|^2$  both scale with the acoustic energy density  $E_{ac}$ , so the acoustic body force  $\mathbf{f}_{ac}^d$ , and thus the streaming, scales with  $E_{ac}^2$ . In comparison, the boundary-driven Rayleigh streaming scales with  $E_{ac}$ . Consequently, the bulk-driven streaming driven by  $\mathbf{f}_{ac}^d$  will become dominant at sufficiently high  $E_{ac}$ . We study further the nonlinear behavior and transition both numerically and experimentally in the Letter [14] published simultaneously with this work.

Finally, we note that it is important that the device consists of a silicon base with a glass lid and not a pure glass chip, because the asymmetry of the thermal field due to the widely different thermal conductivities in the two materials results in a skew-angled body force which enables a strong thermoacoustic streaming. The modeling of the transition into the nonlinear regime has not been captured by the previous perturbation models in the literature [2, 5, 7], because it requires a nonlinear model such as the one presented here.

### B. Example in 3D: Nonlinear thermoacoustic streaming driven by absorption of light

The effective boundary conditions enables 3D simulations that combined with the iterative solver makes it possible to investigate highly nonlinear effects in a 3D system. As an example, we choose the system, in which we previously studied both experimentally and numerically the thermoacoustic streaming induced by the temperature gradient [8]. In that study, the applied perturbative model was at its limit of validity because of the high streaming velocity. Therefore, we here use the iterative model to examine the nonlinear effects in this system, specifically the impact of advection in the system at high streaming velocities. The example serves to demonstrate the ability to make 3D models with an effective iterative model, and to study the nonlinear thermoviscous effects due to thermal convection in 3D.

The system is a glass-silicon-glass chip with a long rectangular water-filled channel of width  $W_{fl} = 760 \mu\text{m}$  and height  $H_{fl} = 360 \mu\text{m}$ , such that the top and bottom of the fluidic channel is in contact with glass and the sides are in contact with the silicon wafer. The chip is actuated anti-symmetrically around the  $xz$ -plane and symmetrically around the  $yz$ -plane at a frequency  $f_0 = 0.96 \text{ MHz}$  which excites the half-wave resonance in the width of the channel. Dye has been added to the water to absorb the light from a light-emitting diode (LED). The absorbed light heats up the water and induces a temperature gradient and thus the acoustic body force  $\mathbf{f}_{ac}^d$  Eq. (46) in the bulk. As a result, high streaming velocities and thermal convection appears. In contrast to the 2D example of Section VI A, we keep the acoustic energy

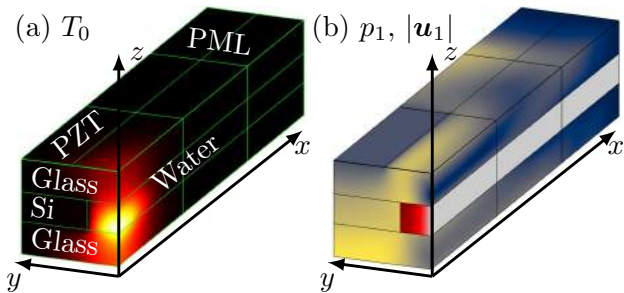


FIG. 4. Simulation of  $T_0$ ,  $p_1$ , and  $|\mathbf{u}_1|$  in a quarter of the glass-Si-glass system. (a) Color plot of  $T_0$  from 20 (black) to 20.8 °C (yellow) due to the absorption of light from an LED with  $P = 5$  mW. (b) Color plot of the corresponding acoustic displacement  $|\mathbf{u}_1|$  from 0 (blue) to 18 nm (yellow) in the solid, and the acoustic pressure  $p_1$  in the water-filled  $0.76 \times 0.36$  mm<sup>2</sup> microchannel from 0 (gray) to 1.2 MPa (red).

density  $E_{ac}$  constant in the 3D example, and only vary the power of the LED. The acoustic body force  $\mathbf{f}_{ac}^d$ , and thus the streaming velocity  $\mathbf{v}_0$ , depends linearly on  $\nabla T_0$ , and therefore depends linearly on the LED power as long as thermal convection is negligible.

For the numerical model we are using symmetry planes and perfectly matched layers (PML) to reduce the size of the 3D model. The LED is placed in the center of the channel, so both the  $yz$ -plane at  $x = 0$  and the  $xz$ -plane at  $y = 0$  are symmetry planes. On the  $yz$ -plane all fields (steady and acoustic fields) are symmetric, whereas on the  $xz$ -plane the steady fields are symmetric, while the acoustic pressure  $p_1$  and  $y$ -component of the displacement field  $\mathbf{u}$  are anti-symmetric, the  $x$ - and  $z$ -component

of the displacement field are symmetric. The two symmetry planes allows to only solve a quarter of the system as shown in Fig. 4. The PML layer is used to dampen waves traveling along the  $x$ -axis away from the center, and it allows us to restrict the computational domain to the region closest to the LED spot. Further details on the implementation of the PML layer and boundary conditions on the symmetry plane can be found in the Supplemental Material [29].

The actuation is implemented as a displacement on the glass-lid, which sets up an acoustic field with an energy density  $E_{ac} = 150$  J/m<sup>3</sup> at  $x = 0$ , and the LED is modeled to be a Gaussian beam centered at  $x = y = 0$  and with a width of 650  $\mu$ m. With a LED power of  $P = 5$  mW the resulting steady temperature field  $T_0$  and acoustic pressure  $p_1$  and displacement field  $\mathbf{u}_1$  are shown in Fig. 4.  $T_0$  is strongest at the bottom of the fluidic channel, because the light is absorbed there and the silicon wafers keeps the sides of the channel cold by transporting the heat to a heat sink.

When the LED is off, the streaming is dominated by the boundary-driven streaming, but when it is on, the streaming is dominated by the acoustic body force  $\mathbf{f}_{ac}^d$ . The transition from boundary- to bulk-driven streaming is thoroughly studied in Ref. [8]. The resulting streaming for three different LED powers are shown in Fig. 5. Here, the solution in quarter channel has been mirrored in the two symmetry planes to obtain the streaming flow in the full channel. In Fig. 5(a) is shown the classical boundary-driven Rayleigh streaming for zero LED power  $P$ . In this case the streaming pattern contains four characteristic 2D streaming rolls in the  $yz$ -plane with almost no flow in the  $x$ -direction. In Fig. 5(b) is shown the streaming for

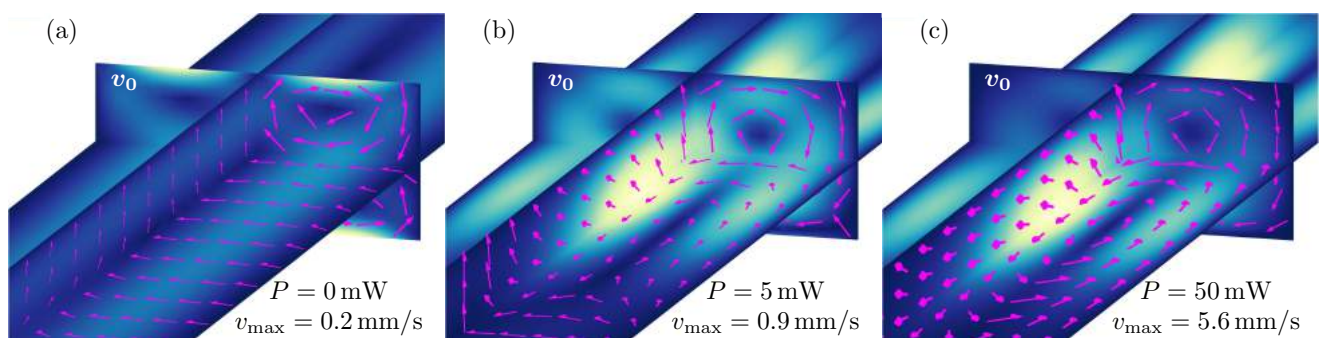


FIG. 5. Simulated streaming  $\mathbf{v}_0$  at acoustic energy density  $E_{ac} = 150$  J/m<sup>3</sup> for the LED power  $P = 0, 5,$  and  $50$  mW, respectively. The color plots from 0 mm/s (blue) to  $v_{max}$  (yellow) are the in-plane velocity of the respective planes, on the  $yz$ -plane it is  $(v_{0,y}^2 + v_{0,z}^2)^{1/2}$ , and likewise for the  $xy$ - and  $xz$ -planes. All arrows are unit vectors showing the direction of  $\mathbf{v}_0$ . (a)  $\mathbf{v}_0$  for  $P = 0$  mW showing the usual four boundary-driven streaming rolls with  $v_{max} = 0.2$  mm/s. (b)  $\mathbf{v}_0$  for  $P = 5$  mW showing a slightly dominant thermoacoustic streaming flow with  $v_{max} = 0.9$  mm/s driven by the acoustic body force  $\mathbf{f}_{ac}^d$  (46) in the bulk. (c)  $\mathbf{v}_0$  for  $P = 50$  mW completely dominated by the fast streaming flow with  $v_{max} = 5.6$  mm/s driven by the acoustic body force  $\mathbf{f}_{ac}^d$  in the bulk.

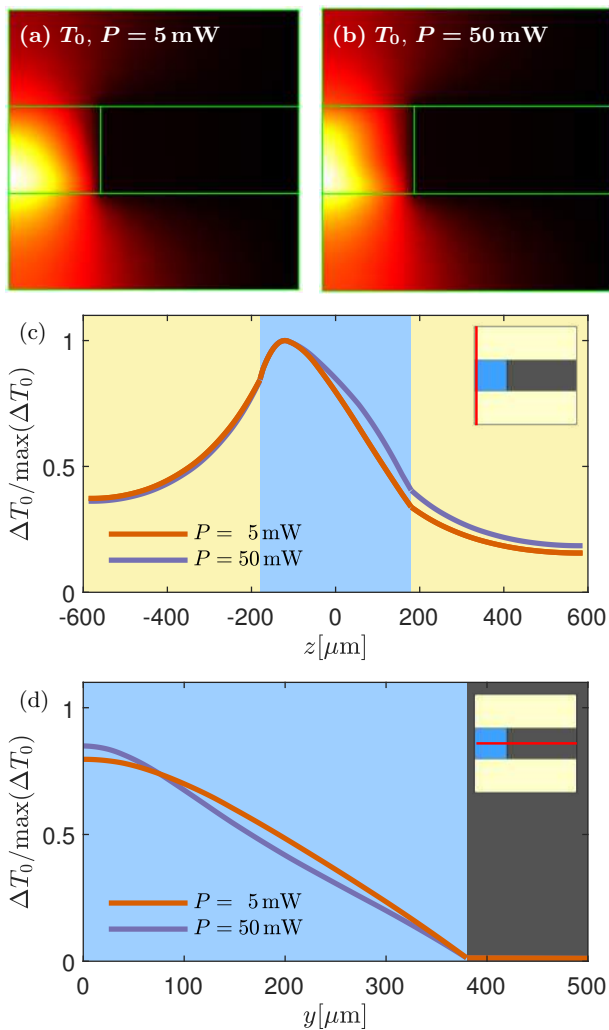


FIG. 6. Convection due to high streaming velocities. (a) shows the temperature field in the  $yz$ -plane at  $x=0$  generated by the light absorption from a LED of power  $P=5$  mW ranging from  $T_0=20.0$  °C (black) to  $T_0=20.8$  °C (yellow). (b) Same as (a) but for  $P=50$  mW and a color-range from  $T_0=20.0$  °C (black) to  $T_0=27.3$  °C (yellow). (c) Shows a line plot of the two normalized temperature fields along a line at  $x=y=0$  shown in the inset. (d) Shows a line plot of the two normalized temperature fields along a line at  $x=z=0$  shown in the inset. The difference in the two temperature fields are due to convection.

moderate LED power  $P=5$  mW with a maximum velocity of 0.9 mm/s, which recovers the 3D flow pattern driven by the bulk acoustic body-force  $\mathbf{f}_{ac}^d$  as observed in Ref. [8]. In Fig. 5(c) is shown the streaming for high LED power  $P=50$  mW with a maximum velocity of 5.6 mm/s. This pattern looks like the one for  $P=5$  mW, but is slightly deformed due to changes in  $\nabla T_0$  and thus in  $\mathbf{f}_{ac}^d$  due to nonlinear thermal convection.

The temperature fields for  $P=5$  and 50 mW are shown in Fig. 6(a,b) in the  $yz$ -plane at  $x=0$ . In the

case of  $P=50$  mW, the streaming-induced convection has stretched the temperature field up along the center axis and thereby altering  $T_0$  and  $\mathbf{f}_{ac}^d$ . This stretching reduces the temperature gradient and  $\mathbf{f}_{ac}$  along  $z$ , and therefore leads to the reduction of  $v_0$  in the vertical  $yz$ -plane relative to the one in the horizontal  $xy$ -plane seen when comparing Fig. 5(b) to (c). The dependence of the  $\Delta T_0$ -profile on the LED power  $P$  is quantified by the line plots of the temperature along the vertical line  $y=x=0$  in Fig. 6(c) and the horizontal line  $x=z=0$  in Fig. 6(d). These line plots show the same tendency as was observed in the 2D-example in Fig. 3.

When simulating convection-diffusion processes, the numerical mesh needs to satisfy the stability condition  $h_{\text{mesh}} < 2D_0^{\text{th}}/v_0$  on the numerical Péclet number, which restricts the size  $h_{\text{mesh}}$  of the mesh elements. In this system, with  $D_0^{\text{th}} \approx 2 \times 10^{-7}$  m<sup>2</sup>/s and  $v_0 = 5.6$  mm/s, we find  $h_{\text{mesh}} < 40$   $\mu\text{m}$ . Consequently, in systems with a high streaming velocity, a fine mesh is required in the bulk, which quickly can make numerical 3D simulation computationally expensive. It is possible to mathematically stabilize the diffusion-advection equations which can enable simulations with a coarser mesh, but this we have not yet implemented in our simulation.

## VII. CONCLUSIONS

We have presented an effective nonlinear model for thermoviscous acoustofluidics, which enables simulations of high acoustic energies in 3D. The model differs from previous acoustofluidic models [2, 5] on two main points: (1) it contains an effective boundary condition for the steady temperature field, which enables 3D simulations of acoustic heating in thermoviscous acoustofluidics, and (2) it relies on an iterative solver, which incorporate nonlinear effects, and thus allows simulations of higher acoustic energies than models based on perturbation theory.

To validate the model and to demonstrate its potential, we firstly presented a 2D example of a widely used rectangular channel was modeled in Section VI A. In Fig. 1, the effective model was validated against a full iterative model, and the internal acoustic heating due to friction was shown in Fig. 1(b)-(c) to be of the order mK. Secondly, the capability of simulating nonlinear effects in 3D systems was demonstrated in Section VI B, an example showing the importance of convective heat transport in a acoustofluidic device with externally controlled temperature gradients. We have presented experimental validation of the nonlinear model as well as further experimental and numerical studies of the transition from perturbative to nonperturbative behavior as a function of  $E_{ac}$  around 500 J/m<sup>3</sup> in the Letter [14] published simultaneously with this work. We note that  $E_{ac} \gtrsim 500$  J/m<sup>3</sup> can easily be obtained in standard acoustofluidic devices, where  $E_{ac} \approx 10 - 50$  J/m<sup>3</sup>  $[U_{pp}/(1 \text{ V})]^2$  has been reported in the literature,  $U_{pp}$  being the applied voltage

on the piezoelectric transducer [25, 26, 28, 30].

In many applications of acoustofluidic devices, as high a throughput as possible is desired. Generally, a higher acoustic energy will allow for such a higher throughput. The presented iterative model allows simulations of higher acoustic energies and will likely contribute to an increased understanding of nonlinear effects in acoustofluidics and to an improved design capability of acoustofluidic devices with a higher throughput.

## ACKNOWLEDGMENTS

This work was supported by Independent Research Fund Denmark, Natural Sciences (Grant No. 8021-00310B).

## Appendix A: Reduction and integration

In this appendix, we present the mathematical steps going from Eq. (37) to Eqs. (38a) and (38b) for the heat flux and the temperature in the fluid at the fluid-solid interface. Beginning with Eq. (37), but suppressing the superscript “fl” for simplicity, we have

$$k_0^{\text{th}} \partial_z^2 T_0^\delta = -\nabla \cdot \left[ \langle k_1^{\text{th}} \nabla T_1 \rangle^\delta + \langle \mathbf{v}_1 \cdot \boldsymbol{\tau}_1 \rangle^\delta - \langle p_1 \mathbf{v}_1 \rangle^\delta - \rho_0 c_{p0} \langle T_1 \mathbf{v}_1 \rangle^\delta \right]. \quad (\text{A1})$$

First, the four terms on the right-hand side are evaluated and reduced one by one. Then, they are integrated with respect to  $z$ , once to find  $-k_0^{\text{th}} \partial_z T_0^\delta$ , and twice to find  $T_0^\delta$ , which both are needed for the boundary conditions in Eqs. (36a) and (36b). Similarly, we repeatedly use in the following that gradient terms are dominated by  $z$  derivatives of boundary-layer fields  $T_1^\delta$ ,  $\mathbf{v}_1^\delta$ , and  $\mathbf{v}_1^{d,T}$ , as each such derivative results in a factor  $(k_c \delta)^{-1} \gg 1$ . We also note that  $\langle (ip_1) p_1 \rangle = \langle (iT_1) T_1 \rangle = 0$ , and another helpful relation is found in Ref. [7] Eq. (33a),

$$\nabla \cdot \mathbf{v}_1 = i(1 - i\Gamma_s) \omega \kappa_{s0} p_1 - i\omega \alpha_{p0} T_1^\delta, \quad (\text{A2})$$

revealing that  $\nabla \cdot \mathbf{v}_1$  depends not only on the bulk pressure  $p_1$  but also on the boundary-layer temperature field  $T_1^\delta$ . Using this insight together with the exponentially decaying boundary-layer fields from Eq. (27), we find for the pressure-generated power,

$$\begin{aligned} \nabla \cdot \left[ \langle p_1 \mathbf{v}_1 \rangle^\delta \right] &= \left[ \langle \nabla p_1 \cdot \mathbf{v}_1^\delta \rangle + \langle p_1 \nabla \cdot \mathbf{v}_1 \rangle \right] \\ &\approx \frac{\omega}{2} \left[ \rho_0 \text{Re} \left\{ i \mathbf{v}_1^{d,p} \cdot \mathbf{v}_1^{\delta*} \right\} + \alpha_{p0} \text{Re} \left\{ i p_1 T_1^{\delta*} \right\} \right]. \end{aligned} \quad (\text{A3})$$

The first term, being of the order  $\omega \rho_0 v_1^2 \approx \omega \kappa_{s0} p_1^2$ , turns out to be the dominant term. Likewise, for the heat-generated power, we find that

$$\begin{aligned} \nabla \cdot \left[ c_{p0} \rho_0 \langle T_1 \mathbf{v}_1 \rangle^\delta \right] &\approx c_{p0} \rho_0 \left[ \langle \nabla T_1^\delta \cdot \mathbf{v}_1 \rangle + \langle T_1^\delta (i\omega \kappa_{s0} p_1) \rangle \right] \\ &\approx \frac{c_{p0} \rho_0}{2} \text{Re} \left\{ k_t T_1^\delta v_{1z}^{\delta*} - i\omega \kappa_s T_1^\delta p_1^* \right\}. \end{aligned} \quad (\text{A4})$$

In the stress-generated power  $\nabla \cdot \langle \mathbf{v}_1 \cdot \boldsymbol{\tau}_1 \rangle^\delta$ , we keep only terms  $\partial_z \mathbf{v}_1^\delta$ , each producing a factor of  $(k_c \delta)^{-1} \gg 1$ . Thus,  $\mathbf{v}_1 \cdot \boldsymbol{\tau}_1 \approx \eta_0 [v_{1z} (\partial_z \mathbf{v}_1^\delta) + (\mathbf{v}_1 \cdot \partial_z \mathbf{v}_1^\delta) \mathbf{e}_z]$  gives,

$$\begin{aligned} \nabla \cdot \langle \mathbf{v}_1 \cdot \boldsymbol{\tau}_1 \rangle^\delta &\approx \eta_0 \nabla \cdot \langle v_{1z} (\partial_z \mathbf{v}_1^\delta) \rangle + \eta_0 \partial_z \langle \mathbf{v}_1 \cdot (\partial_z \mathbf{v}_1^\delta) \rangle \\ &\approx \eta_0 \left[ \langle (\partial_z v_{1z})^2 \rangle + \langle |\partial_z \mathbf{v}_1^\delta|^2 \rangle + \langle \mathbf{v}_1 \cdot \partial_z^2 \mathbf{v}_1^\delta \rangle \right] \\ &= \frac{\eta_0}{2} \text{Re} \left[ |k_s|^2 v_{1z}^\delta v_{1z}^{\delta*} + |k_s|^2 \mathbf{v}_1^\delta \cdot \mathbf{v}_1^{\delta*} - (k_s^*)^2 \mathbf{v}_1 \cdot \mathbf{v}_1^{\delta*} \right] \\ &= \frac{\rho_0 \omega}{2} \text{Re} \left[ v_{1z}^\delta v_{1z}^{\delta*} + \mathbf{v}_1^\delta \cdot \mathbf{v}_1^{\delta*} + i \mathbf{v}_1^{d,p} \cdot \mathbf{v}_1^{\delta*} \right]. \end{aligned} \quad (\text{A5})$$

Here, we have used that  $\text{Re} [i \mathbf{v}_1^\delta \cdot \mathbf{v}_1^{\delta*}] = 0$ , and that  $k_s = (1+i)\delta_s^{-1}$  implies the relations  $(k_s^*)^2 = -i2\delta_s^{-2}$ ,  $|k_s|^2 = 2\delta_s^{-2}$ , and  $2\eta_0 \delta_s^{-2} = \rho_0 \omega$ .

The last term is the power generated by thermal conduction, which only contains the thermal boundary layer characterized by the wave number  $k_t = (1+i)\delta_t^{-1}$ , Eq. (25),

$$\begin{aligned} \nabla \cdot \langle k_1^{\text{th}} \nabla T_1 \rangle^\delta &\approx \langle (\partial_z k_1^{\text{th}}) \partial_z T_1^\delta \rangle + \langle k_1^{\text{th}} \partial_z^2 T_1^\delta \rangle \\ &= \frac{1}{2} \text{Re} \left[ k_t k_t^* k_1^{\text{th},\delta} T_1^{\delta*} - (k_1^{\text{th},d} + k_1^{\text{th},\delta}) (k_t^*)^2 T_1^{\delta*} \right] \\ &= \frac{1}{\delta_t^2} \text{Re} \left[ (1+i) k_1^{\text{th},\delta} T_1^{\delta*} + i k_1^{\text{th},d} T_1^{\delta*} \right] \end{aligned} \quad (\text{A6})$$

For water, this term is a factor  $(\gamma-1) a_k \alpha_{p0} T_0 \approx 10^{-2}$  smaller than  $\omega \kappa_{s0} p_1^2$ , as can be seen by using  $\delta_t^{-2} k_1^{\text{th}} \approx \omega \rho_0 c_p k_1^{\text{th}} / k_0^{\text{th}} \approx \omega \rho_0 c_p a_k \alpha_{p0} T_1 = a_k \omega \alpha_{p0}^2 T_0 p_1$  and  $T_1 \approx (\gamma-1)(\kappa_{s0}/\alpha_{p0}) p_1$ . So the power generated by thermal conduction can be neglected in fluids, but it may be important for gases. Inserting the power contributions (A3)-(A6) into Eq. (A1), we arrive at the expression

$$\begin{aligned} k_0^{\text{th}} \partial_z^2 T_0^\delta &= -\frac{\omega \rho_0}{2} \text{Re} \left\{ \mathbf{v}_1^\delta \cdot \mathbf{v}_1^{\delta*} \right\} + \frac{\omega \alpha_{p0}}{2} \text{Re} \left\{ i p_1 T_1^{\delta*} \right\} \\ &+ \frac{c_p \rho_0}{2} \text{Re} \left\{ \nabla T_1^\delta \cdot (\mathbf{v}_1^{\delta*} + \mathbf{v}_1^{d,T*} + \mathbf{v}_1^{d,p*}) - i\omega \kappa_s T_1^\delta p_1^* \right\} \\ &- \frac{\omega c_p \rho_0}{k_0^{\text{th}}} \text{Re} \left\{ (1+i) k_1^{\text{th},\delta} T_1^{\delta*} + i k_1^{\text{th},d} T_1^{\delta*} \right\}, \end{aligned} \quad (\text{A7})$$

where the first term is the leading term, which originates from the viscous boundary layer. This expression is now integrated from  $z = \infty$  to  $z = 0$  once to obtain the heat flux and twice to obtain the boundary-layer temperature at the interface. The fields in the boundary layer are well approximated by surface fields that does not depend on the normal coordinate  $z$  but only on the in-plane coordinates  $x$  and  $y$ , according to the following separations,

$$\begin{aligned} p_1^d &= p_1^{d0}(x, y), & T_1^{\delta,\text{fl}} &= T_1^{\delta0,\text{fl}}(x, y) r(z), \\ \mathbf{v}_1^{d,p} &= \mathbf{v}_1^{d0,p}(x, y), & T_1^{\delta,\text{sl}} &= T_1^{\delta0,\text{sl}}(x, y) r^*(z), \\ \mathbf{v}_1^\delta &= \mathbf{v}_1^{\delta0}(x, y) q(z), & \mathbf{v}_1^{d,T} &= \alpha_{p0} D_0^{\text{th}} \nabla [T_1^{\delta0,\text{fl}}(x, y) r(z)], \\ q(z) &= e^{i k_s z}, & r(z) &= e^{i k_t z}. \end{aligned} \quad (\text{A8})$$

Inserting this into Eq. (A7), we obtain,

$$\begin{aligned}
k_0^{\text{th}} \partial_z^2 T_0^\delta &= \frac{1}{2} \omega \rho_0 \text{Re} \left\{ -\mathbf{v}_1^{\delta 0} \cdot \mathbf{v}_1^{\delta 0*} q q^* + i \frac{\alpha_{p0}}{\rho_0} p_1^0 T_1^{\delta 0*} r^* \right. \\
&+ \frac{c_p}{\omega} \left[ \nabla_{\parallel} T_1^{\delta 0} \cdot \mathbf{v}_{1,\parallel}^{\delta 0*} q^* + i k_t T_1^{\delta 0} (v_{1,z}^{\delta 0*} q^* + v_{1,z}^{d,T0*} r^*) \right] r \\
&+ \frac{c_p}{\omega} \left[ \nabla_{\parallel} T_1^{\delta 0} \cdot \mathbf{v}_{1,\parallel}^{d,p0*} + i k_t T_1^{\delta 0} v_{1,z}^{d,p0*} - i \omega \kappa_s T_1^{\delta 0} p_1^{0*} \right] r \\
&\left. - \frac{c_p}{k_0^{\text{th}}} \left[ (1+i) k_1^{\text{th},\delta 0} r + i k_1^{\text{th},d0} \right] r^* T_1^{\delta 0*} \right\}. \quad (\text{A9})
\end{aligned}$$

When integrating Eq. (A9) with respect to  $z$ , the  $xy$ -dependent surface fields (superscript 0) move outside the integral. Using the procedure of Ref. [5], we introduce the integrals  $I_{ab}^{(n)}$  of the integrand  $a(z) b(z)^*$ , where  $a(z)$  and  $b(z)$  are any of the functions 1,  $q(z)$ , and  $r(z)$ ,

$$\begin{aligned}
I_{ab}^{(n)} &= \int^z dz_n \int^{z_n} dz_{n-1} \dots \int^{z_2} dz_1 a(z_1) b(z_1)^* \Big|_{z=0}, \\
I_{ab}^{(n)} &\propto \delta^n, \text{ with } \delta = \delta_s, \delta_t \text{ and } n = 1, 2, 3, \dots \quad (\text{A10})
\end{aligned}$$

Integrating Eq. (A9) once with respect to  $z$  thus gives

$$\begin{aligned}
\partial_z T_0^\delta &= \frac{1}{2D_0^{\text{th}}} \text{Re} \left\{ -\frac{\omega}{c_p} \mathbf{v}_1^{\delta 0} \cdot \mathbf{v}_1^{\delta 0*} I_{qq}^{(1)} + i \frac{\omega \alpha_{p0}}{c_p \rho_0} p_1^0 T_1^{\delta 0*} I_{1r}^{(1)} \right. \\
&+ \left[ \nabla_{\parallel} T_1^{\delta 0} \cdot \mathbf{v}_{1,\parallel}^{\delta 0*} + i k_t T_1^{\delta 0} v_{1,z}^{\delta 0*} \right] I_{rq}^{(1)} + i k_t T_1^{\delta 0} v_{1,z}^{d,T0*} I_{rr}^{(1)} \\
&+ \left[ \nabla_{\parallel} T_1^{\delta 0} \cdot \mathbf{v}_{1,\parallel}^{d,p0*} + i k_t T_1^{\delta 0} v_{1,z}^{d,p0*} - i \omega \kappa_s T_1^{\delta 0} p_1^{0*} \right] I_{r1}^{(1)} \\
&\left. - \frac{\omega}{k_0^{\text{th}}} \left[ (1+i) k_1^{\text{th},\delta 0} I_{rr}^{(1)} + i k_1^{\text{th},d0} I_{1r}^{(1)} \right] T_1^{\delta 0*} \right\}. \quad (\text{A11})
\end{aligned}$$

Inserting here the values of  $I_{ab}^{(1)}$  given by

$$\begin{aligned}
I_{r1}^{(1)} &= -\frac{1+i}{2} \delta_t, & I_{rr}^{(1)} &= -\frac{1}{2} \delta_t, & I_{ba}^{(n)} &= \left[ I_{ab}^{(n)} \right]^*, \\
I_{rq}^{(1)} &= -\frac{1+i}{2} \frac{\delta_s \delta_t}{\delta_s + i \delta_t}, & I_{qq}^{(1)} &= -\frac{1}{2} \delta_s, \quad (\text{A12})
\end{aligned}$$

leads to  $\partial_z T_0^{\text{fl},\delta 0}$  at the fluid-solid interface,

$$\begin{aligned}
\partial_z T_0^{\text{fl},\delta 0} &= \text{Re} \left[ \frac{1+i}{4D_0^{\text{th}}} \left\{ \frac{1-i}{2} \frac{\delta_s \omega}{c_p} \mathbf{v}_1^{\delta 0} \cdot \mathbf{v}_1^{\delta 0*} - \frac{\delta_t \omega \alpha_{p0}}{c_p \rho_0} p_1^0 T_1^{\delta 0*} \right. \right. \\
&- \frac{\delta_s}{\delta_s + i \delta_t} \left[ \delta_t \nabla_{\parallel} T_1^{\delta 0} \cdot \mathbf{v}_{1,\parallel}^{\delta 0*} - (1-i) T_1^{\delta 0} v_{1,z}^{\delta 0*} \right] \\
&- i T_1^{\delta 0} \left[ v_{1,z}^{d,T0*} + (1+i) v_{1,z}^{d,p0*} - \delta_t \omega \kappa_s p_1^{0*} \right] \\
&\left. \left. - \delta_t \nabla_{\parallel} T_1^{\delta 0} \cdot \mathbf{v}_{1,\parallel}^{d,p0*} + \delta_t \omega \frac{k_1^{\text{th},\delta 0} + k_1^{\text{th},d0}}{k_0^{\text{th}}} T_1^{\delta 0*} \right\} \right]. \quad (\text{A13})
\end{aligned}$$

To obtain the temperature  $T_0^{\delta 0}$  at the fluid-solid interface, we integrate Eq. (A9) twice with respect to  $z$ . This is easily done by changing  $I_{ab}^{(1)}$  to  $I_{ab}^{(2)}$  in Eq. (A11) followed by insertion of the values

$$\begin{aligned}
I_{r1}^{(2)} &= \frac{i}{2} \delta_t^2, & I_{rr}^{(2)} &= \frac{1}{4} \delta_t^2, \\
I_{rq}^{(2)} &= \frac{i}{2} \frac{\delta_s^2 \delta_t^2}{(\delta_s + i \delta_t)^2}, & I_{qq}^{(2)} &= \frac{1}{4} \delta_s^2. \quad (\text{A14})
\end{aligned}$$

The result for  $T_0^{\text{fl},\delta 0}$  becomes

$$\begin{aligned}
T_0^{\text{fl},\delta 0} &= \frac{\delta_t}{4D_0^{\text{th}}} \text{Re} \left\{ -\frac{\delta_s^2 \omega}{2 \delta_t c_p} \mathbf{v}_1^{\delta 0} \cdot \mathbf{v}_1^{\delta 0*} + \frac{\delta_t \omega \alpha_{p0}}{c_p \rho_0} p_1^0 T_1^{\delta 0*} \right. \\
&+ i \frac{\delta_s^2}{(\delta_s + i \delta_t)^2} \left[ \delta_t \nabla_{\parallel} T_1^{\delta 0} \cdot \mathbf{v}_{1,\parallel}^{\delta 0*} - (1-i) T_1^{\delta 0} v_{1,z}^{\delta 0*} \right] \\
&- T_1^{\delta 0} \left[ \frac{1-i}{2} v_{1,z}^{d,T0*} + (1+i) v_{1,z}^{d,p0*} - \delta_t \omega \kappa_s p_1^{0*} \right] \\
&\left. + i \delta_t \nabla_{\parallel} T_1^{\delta 0} \cdot \mathbf{v}_{1,\parallel}^{d,p0*} - \delta_t \omega \frac{(1+i) k_1^{\text{th},\delta 0} + 2 k_1^{\text{th},d0}}{2 k_0^{\text{th}}} T_1^{\delta 0*} \right\}. \quad (\text{A15})
\end{aligned}$$

Again the first term is the leading term that originates from the viscous boundary layer.

- 
- [1] P. B. Muller, R. Barnkob, M. J. H. Jensen, and H. Bruus, A numerical study of microparticle acoustophoresis driven by acoustic radiation forces and streaming-induced drag forces, *Lab Chip* **12**, 4617 (2012).  
[2] P. B. Muller and H. Bruus, Numerical study of thermo-viscous effects in ultrasound-induced acoustic streaming in microchannels, *Phys. Rev. E* **90**, 043016 (2014).  
[3] P. Hahn and J. Dual, A numerically efficient damping model for acoustic resonances in microfluidic cavities, *Physics of Fluids* **27**, 062005 (2015).  
[4] P. Hahn, I. Leibacher, T. Baasch, and J. Dual, Numer-

- ical simulation of acoustofluidic manipulation by radiation forces and acoustic streaming for complex particles, *Lab Chip* **15**, 4302 (2015).  
[5] J. S. Bach and H. Bruus, Theory of pressure acoustics with viscous boundary layers and streaming in curved elastic cavities, *J. Acoust. Soc. Am.* **144**, 766 (2018).  
[6] N. R. Skov, J. S. Bach, B. G. Winkelmann, and H. Bruus, 3D modeling of acoustofluidics in a liquid-filled cavity including streaming, viscous boundary layers, surrounding solids, and a piezoelectric transducer, *AIMS Mathematics* **4**, 99 (2019).

- [7] J. H. Joergensen and H. Bruus, Theory of pressure acoustics with thermoviscous boundary layers and streaming in elastic cavities, *J. Acoust. Soc. Am.* **149**, 3599 (2021).
- [8] W. Qiu, J. H. Joergensen, E. Corato, H. Bruus, and P. Augustsson, Fast microscale acoustic streaming driven by a temperature-gradient-induced non-dissipative acoustic body force, *Phys. Rev. Lett.* **127**, 064501 1 (2021).
- [9] J. D. Adams, C. L. Ebbesen, R. Barnkob, A. H. J. Yang, H. T. Soh, and H. Bruus, High-throughput, temperature-controlled microchannel acoustophoresis device made with rapid prototyping, *J Micromech Microeng* **22**, 075017 (2012).
- [10] Y. Chen, M. Wu, L. Ren, J. Liu, P. H. Whitley, L. Wang, and T. J. Huang, High-throughput acoustic separation of platelets from whole blood, *Lab Chip* **16**, 3466 (2016).
- [11] M. Antfolk and T. Laurell, Continuous flow microfluidic separation and processing of rare cells and bioparticles found in blood - a review, *Anal. Chim. Acta* **965**, 9 (2017).
- [12] M. Wu, A. Ozcelik, J. Rufo, Z. Wang, R. Fang, and T. J. Huang, Acoustofluidic separation of cells and particles, *Microsys Nanoeng* **5**, 32, 1 (2019).
- [13] G. Michel and G. P. Chini, Strong wave-mean-flow coupling in baroclinic acoustic streaming, *J. Fluid Mech.* **858**, 536 (2019).
- [14] J. H. Jørgensen, W. Qiu, and H. Bruus, A transition from boundary to bulk driven acoustic streaming driven by nonlinear thermoviscous effects at high acoustic energies, *Phys. Rev. Lett.* **submitted**, 5 pages (2022), <https://arxiv.org/abs/2107.xxxxx>.
- [15] COMSOL Multiphysics 5.6 (2020), <http://www.comsol.com>.
- [16] F. Lickert, M. Ohlin, H. Bruus, and P. Ohlsson, Acoustophoresis in polymer-based microfluidic devices: Modeling and experimental validation, *J. Acoust. Soc. Am.* **149**, 4281 (2021).
- [17] W. N. Bodé and H. Bruus, Numerical study of the coupling layer between transducer and chip in acoustofluidic devices, *J. Acoust. Soc. Am.* **149**, 3096 (2021).
- [18] L. D. Landau and E. M. Lifshitz, *Theory of Elasticity. Course of Theoretical Physics*, 3rd ed., Vol. 7 (Pergamon Press, Oxford, 1986).
- [19] J. T. Karlsen and H. Bruus, Forces acting on a small particle in an acoustical field in a thermoviscous fluid, *Phys. Rev. E* **92**, 043010 (2015).
- [20] L. D. Landau and E. M. Lifshitz, *Fluid Mechanics*, 2nd ed., Vol. 6 (Pergamon Press, Oxford, 1993).
- [21] L. D. Landau and E. M. Lifshitz, *Statistical Physics, Part 1*, 3rd ed., Vol. 5 (Butterworth-Heinemann, Oxford, 1980).
- [22] J. T. Karlsen, P. Augustsson, and H. Bruus, Acoustic force density acting on inhomogeneous fluids in acoustic fields, *Phys. Rev. Lett.* **117**, 114504 (2016).
- [23] P. B. Muller and H. Bruus, Theoretical study of time-dependent, ultrasound-induced acoustic streaming in microchannels, *Phys. Rev. E* **92**, 063018 (2015).
- [24] G. Michel and C. Gissinger, Cooling by baroclinic acoustic streaming, *Phys. Rev. Applied* **16**, L051003 (2021).
- [25] R. Barnkob, P. Augustsson, T. Laurell, and H. Bruus, Measuring the local pressure amplitude in microchannel acoustophoresis, *Lab Chip* **10**, 563 (2010).
- [26] P. Augustsson, R. Barnkob, S. T. Wereley, H. Bruus, and T. Laurell, Automated and temperature-controlled micro-PIV measurements enabling long-term-stable microchannel acoustophoresis characterization, *Lab Chip* **11**, 4152 (2011).
- [27] R. Barnkob, P. Augustsson, T. Laurell, and H. Bruus, Acoustic radiation- and streaming-induced microparticle velocities determined by microparticle image velocimetry in an ultrasound symmetry plane, *Phys. Rev. E* **86**, 056307 (2012).
- [28] P. B. Muller, M. Rossi, A. G. Marin, R. Barnkob, P. Augustsson, T. Laurell, C. J. Kähler, and H. Bruus, Ultrasound-induced acoustophoretic motion of microparticles in three dimensions, *Phys. Rev. E* **88**, 023006 (2013).
- [29] See Supplemental Material at [http://bruus-lab.dk/files/Joergensen\\_nonperturb\\_theory\\_Suppl.pdf](http://bruus-lab.dk/files/Joergensen_nonperturb_theory_Suppl.pdf) for details about the implementation of the symmetry planes and PML in the 3D model.
- [30] R. Barnkob, I. Iranmanesh, M. Wiklund, and H. Bruus, Measuring acoustic energy density in microchannel acoustophoresis using a simple and rapid light-intensity method, *Lab Chip* **12**, 2337 (2012).



# Supplemental material for: Theory and modeling of nonperturbative effects at high acoustic energy densities in thermoviscous acoustofluidics

Jonas Helboe Joergensen\* and Henrik Bruus†

Department of Physics, Technical University of Denmark,  
DTU Physics Building 309, DK-2800 Kongens Lyngby, Denmark

(Dated: 20 December 2022)

This supplemental material provides details the numerical model used in the 3D example in section VI-B in the main article.

The numerical model is the iterative and effective thermoviscous pressure acoustic model presented in the main paper with heating from an external LED. The model is an iterative model that solves the steady fields temperature field  $T_0$  in the fluid and solid and the steady velocity  $\mathbf{v}_0$  and pressure  $p_0$  in fluid and the acoustic time-varying pressure  $p_1$  in the fluid and displacement  $\mathbf{u}_1$  in the solid. The model of a glass-silicon-glass chip with a fluid channel of height  $H = 360 \mu\text{m}$  and width  $W = 760 \mu\text{m}$  is shown in Fig. S1. In the model we take advantage of the symmetries in the system and model a quarter of the channel, Fig. S1. In the  $y$ - $z$  symmetry plane at  $x = 0$  all fields are symmetric, and in the  $x$ - $z$  symmetry plane at  $y = 0$  the acoustic fields  $p_1$  and  $\mathbf{u}_1$  are anti-symmetric and the stationary fields  $T_0$ ,  $\mathbf{v}_0$ , and  $p_0$  are symmetric. The model parameters are listed in Table S1.

The actuation is modeled not as a full piezoelectric transducer as in Ref. [1], but merely as a boundary condition with a displacement  $d_0 = 5 \text{ nm}$  and a frequency  $f_0$  on the black actuation plane in Fig. S1 as in Ref. [2]. Note that using the symmetry planes, the model actually has anti-symmetric actuation regions, one on each side of the chip.

TABLE S1. System parameters characterizing the geometry, the acoustic actuation, and the absorption of the LED spot.

| Parameter                    | Symbol           | Value | Unit             |
|------------------------------|------------------|-------|------------------|
| <i>Geometry parameters:</i>  |                  |       |                  |
| Fluid width                  | $W$              | 760   | $\mu\text{m}$    |
| Fluid height                 | $H$              | 360   | $\mu\text{m}$    |
| Actuation length             | $L_{\text{PZT}}$ | 2.0   | mm               |
| System length                | $L_{\text{sys}}$ | 4.0   | mm               |
| PML length                   | $L_{\text{PML}}$ | 1.75  | mm               |
| Total length                 | $L_{\text{end}}$ | 5.75  | mm               |
| <i>Actuation parameters:</i> |                  |       |                  |
| Actuation amplitude          | $d_0$            | 5.0   | nm               |
| Actuation frequency          | $f_0$            | 0.957 | MHz              |
| <i>LED parameters:</i>       |                  |       |                  |
| Half width of the LED spot   | $d_{\text{LED}}$ | 850   | $\mu\text{m}$    |
| Absorption coefficient       | $\alpha$         | 12.3  | $\text{mm}^{-1}$ |

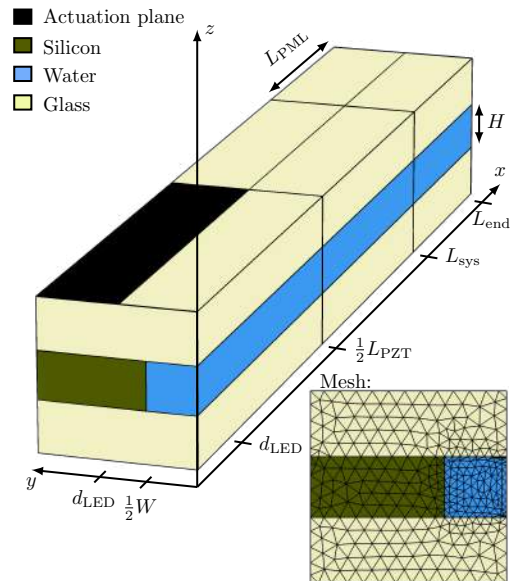


FIG. S1. Sketch of the numerical model of the acoustofluidic chip. Symmetry planes have been used so only a quarter of the channel is simulated. The model consists of a fluid domain with width  $W$  and height  $H$ , a solid domain (glass and silicon), and a special PML (perfectly matched layer) region where the travelling waves are artificially damped to mimic an infinitely long channel. The acoustic actuation is done on the actuation region (black) and the LED has its center at  $x = 0$  and  $y = 0$  and has half of the width  $d_{\text{LED}}$ . The mesh is shown in the  $y$ - $z$  plane, which is swept along the  $x$ -axis so that the mesh node repeats itself with a distance of  $51 \mu\text{m}$ .

During operation, a piezoelectric transducer generates heat, but this is neglected in the simulations for two reasons: (1) The necessary acoustic energy density is obtained in the system using a relatively low power consumption, and this assures that the heat generation is relatively small. (2) The heat from the transducer is lead through the top glass layer into the silicon layer, where it due to the high heat conductivity of silicon is uniformly distributed throughout the chip, leading to only a minute and nearly uniform temperature rise in the microchannel.

To avoid simulating the entire chip, the perfectly matched layer (PML) method is used to artificially damp

\* jonashj@fysik.dtu.dk

† bruus@fysik.dtu.dk

travelling waves [3]. Thus, the model consists of an area of length  $L_{\text{PZT}}$  where a piezoelectric transducer actuates the chip at a frequency  $f_0$  with an amplitude  $d_0$ , a part of length  $L_{\text{sys}} - L_{\text{PZT}}$  where there are no actuation, and finally a section of length  $L_{\text{PML}}$  where the acoustic waves are artificially damped using a PML. For the PML to be valid, the distance  $L_{\text{sys}} - L_{\text{PZT}}$  must be long enough for the travelling wave to develop so that the acoustic field does not depend on where the PML starts.

The real device has a long channel with a long piezoelectric transducer. To model the pressure field around the LED spot accurately, the length  $L_{\text{PZT}}$  must be larger than half of the LED spot width  $d_{\text{LED}}$ . The LED spot is modeled as a Gaussian beam with half of the beam width  $d_{\text{LED}} = 850 \text{ }\mu\text{m}$ ,

$$I(x, y, z) = \frac{2P_{\text{LED}}}{\pi d_{\text{LED}}^2} \exp \left[ -\frac{2(x^2 + y^2)}{d_{\text{LED}}^2} - \alpha \left( z + \frac{1}{2}H \right) \right], \quad (\text{S1})$$

where  $P_{\text{LED}}$  is the total power of the LED and  $-\frac{1}{2}H$  is the bottom of the channel where beam starts to be absorbed. In the solution, the heat absorption is given as  $q(x, y, z) = \alpha I(x, y, z)$  for  $-\frac{1}{2}H < z < \frac{1}{2}H$ , while the absorption in the glass is neglected.

The entire model is implemented in COMSOL Multiphysics 5.6, with the governing equations and effective boundary conditions given in the main article. The numerical model uses cubic test functions for the streaming field and the acoustic pressure field, but quadratic test functions for the acoustic displacement field in the solid and the second-order pressure field.

- 
- [1] N. R. Skov, J. S. Bach, B. G. Winckelmann, and H. Bruus, 3D modeling of acoustofluidics in a liquid-filled cavity including streaming, viscous boundary layers, surrounding solids, and a piezoelectric transducer, *AIMS Mathematics* **4**, 99 (2019).
- [2] M. W. H. Ley and H. Bruus, Three-dimensional numerical

- modeling of acoustic trapping in glass capillaries, *Phys. Rev. Appl.* **8**, 024020 (2017).
- [3] A. Bermúdez, L. Hervella-Nieto, A. Prieto, and R. Rodríguez, An optimal perfectly matched layer with unbounded absorbing function for time-harmonic acoustic scattering problems, *J. Comput. Phys.* **223**, 469 (2007).

## 7.4 Paper IV in Physical Review Letters (under review)

*A transition from boundary- to bulk-driven acoustic streaming due to nonlinear thermoviscous effects at high acoustic energy densities*

**Authors:** J. H. Joergensen, W. Qiu, and H. Bruus.

**Journal:** Submitted to Physical Review Letters

**arXiv:** [arxiv.org/abs/2112.11410](https://arxiv.org/abs/2112.11410)

**Remarks:** There is a sign error in equation 5 and 6, these errors will be corrected in the published paper. The correct equation 5 is given as,

$$\begin{aligned}
 0 &= \nabla \cdot \left[ k_0^{\text{th}} \nabla T_0^{\text{fl},d} \right] - c_p \rho_0 \mathbf{v}_0 \cdot \nabla T_0^{\text{fl},d} + P_{\text{ac}}^d + P, \\
 P_{\text{ac}}^d &= \nabla \cdot \left[ \langle k_1^{\text{th},d} \nabla T_1^d \rangle - \langle p_1 \mathbf{v}_1^{d,p} \rangle + \langle \mathbf{v}_1^{d,p} \cdot \boldsymbol{\tau}_1^d \rangle \right] \\
 &\quad - c_p \langle \rho_1^d \mathbf{v}_1^{d,p} \rangle \cdot \nabla T_0^d,
 \end{aligned}$$

and the correct equation 6 is given as,

$$\begin{aligned}
 0 &= \nabla \cdot \left[ k_0^{\text{th}} \nabla T_0^{\text{sl},d} \right] + P_{\text{ac}}^d + P, \\
 P_{\text{ac}}^d &= \nabla \cdot \langle k_1^{\text{th,sl}} \nabla T_1^{\text{sl},d} \rangle.
 \end{aligned}$$

# A transition from boundary- to bulk-driven acoustic streaming due to nonlinear thermoviscous effects at high acoustic energy densities

Jonas Helboe Joergensen,<sup>1,\*</sup> Wei Qiu,<sup>2,†</sup> and Henrik Bruus<sup>1,‡</sup>

<sup>1</sup>*Department of Physics, Technical University of Denmark,  
DTU Physics Building 309, DK-2800 Kongens Lyngby, Denmark*

<sup>2</sup>*Department of Biomedical Engineering, Lund University, Ole Römers väg 3, 22363, Lund, Sweden*

(Dated: 21 December 2021)

Acoustic streaming is studied in a rectangular microfluidic channel. It is demonstrated theoretically, numerically, and experimentally with good agreement, frictional heating can alter the streaming pattern qualitatively at high acoustic energy densities  $E_{ac}$  above  $500 \text{ J/m}^3$ . The study shows, how as a function of increasing  $E_{ac}$  at fixed frequency, the traditional boundary-driven four streaming rolls created at a half-wave standing-wave resonance, transition into two large streaming rolls. This nonlinear transition occurs because friction heats up the fluid resulting in a temperature gradient, which spawns an acoustic body force in the bulk that drives thermoacoustic streaming.

Microscale acoustofluidic devices are used to manipulate and control microparticles and cells. In such devices, two main forces act on the suspended particles, the acoustic radiation force and the drag force due to acoustic streaming, which is a time-averaged flow caused by the inherent nonlinearities of fluid dynamics. Recent work has clarified many subtle details pertaining to the radiation force on microparticles, including thermoviscous effects [1] and microstreaming [2]. Concurrently, similar progress has been made in the theory of acoustic streaming, especially regarding thermoviscous effects. The fundamental boundary-driven streaming caused by time-averaged forces in the oscillatory boundary-layer flow [3], and the fundamental bulk-driven streaming generated by the time-averaged dissipation of traveling waves [4], have recently been supplemented by bulk-driven baroclinic [5, 6] and thermoacoustic [7, 8] streaming, caused by an interplay between standing acoustic waves and steady temperature gradients. However, as noted in Refs. [7, 8], the validity of the conventional perturbation approach breaks down at moderately high, but experimentally obtainable acoustic energy densities above  $100 \text{ J/m}^3$  in combination with moderate thermal gradients above  $1 \text{ K/mm}$ . This need for an extension of the theory beyond perturbation theory is addressed in this Letter and in the accompanying detailed presentation of the nonperturbative model in Ref. [9].

We introduce a nonperturbative iteration approach to investigate theoretically and numerically, the nonlinear effects appearing in a conventional acoustofluidic channel at high acoustic energy density  $E_{ac}$ , and we validate experimentally the model predictions. We take as our generic acoustofluidic model system, the widely used rectangular channel driven at resonance with a transverse half-wave standing acoustic wave, for which the streaming at low  $E_{ac}$  is dominated by conventional boundary-driven streaming with four streaming rolls [10–13]. We show how nonlinear effects in the form of heating by viscous dissipation from the acoustic field inside the bound-

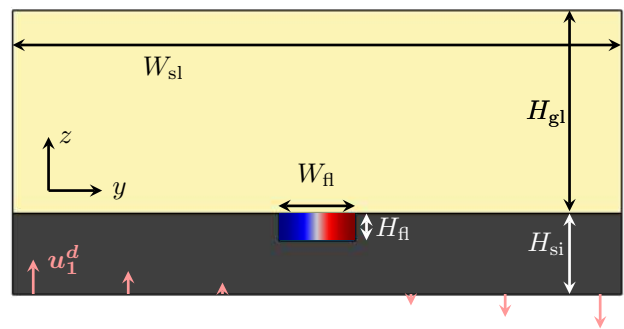


FIG. 1. Cross-section of the modeled rectangular channel of width  $W_{fl} = 375 \mu\text{m}$  and height  $H_{fl} = 135 \mu\text{m}$  embedded in a silicon base of width  $W_{sl} = 3 \text{ mm}$  and height  $H_{si} = 0.4 \text{ mm}$ , and covered by a glass lid of height  $H_{gl} = 1 \text{ mm}$ . The bottom-edge actuation is the displacement  $u_1^d = d_0(y/W_{sl}) e_y$  with an adjustable amplitude  $d_0$  at frequency  $f_0 = 1.911 \text{ MHz}$ .

ary layers, set up a steady temperature gradient. This gradient drives a strong thermoacoustic streaming in the bulk, which changes the streaming flow qualitatively from four to two flow rolls, and which by thermal convection alters the temperature field. Our analysis of this nonlinear phenomenon and its underlying mechanism fills a knowledge gap in nonlinear acoustics, and it provides a guidance for understanding and optimizing acoustofluidic systems running at high  $E_{ac}$  such as high-intensity ultrasound focusing [14–16], acoustic streaming-based micromixers [17–20], particle manipulation devices [21–23], and high-throughput acoustophoresis devices [24–26].

*Physical model.*—We consider a long straight microchannel with a cross-sectional of width  $W_{fl} = 375 \mu\text{m}$  and height  $H_{fl} = 135 \mu\text{m}$  embedded in a silicon base with a glass lid, see Fig. 1 and Refs. [9–13]. To excite the horizontal half-wave resonance mode in the fluid, the system is actuated at frequency  $f_0 = 1.911 \text{ MHz}$  by the bottom-edge displacement sketched in Fig. 1. The response to the acoustic actuation is governed by the conservation

equation for mass, momentum, and energy in the fluid and solid. The independent fields are the pressure  $p$ , the velocity  $\mathbf{v}$ , and the temperature  $T$  in the fluid, and the displacement  $\mathbf{u}$  and  $T$  in the solid.

We study a fluid characterized by the following material parameters: density  $\rho$ , isothermal compressibility  $\kappa_T$ , thermal conductivity  $k^{\text{th}}$ , specific heat  $c_p$ , dynamic and bulk viscosity  $\eta$  and  $\eta^{\text{b}}$ , thermal expansion coefficient  $\alpha_p$ , the ratio of specific heats  $\gamma = c_p/c_v$ , and the isentropic and isothermal compressibility  $\kappa_s$  and  $\kappa_T = \gamma\kappa_s$ . The temperature dependence of the parameters for water are given by the polynomials derived in Ref. [12]. The elastic solid is characterized by density  $\rho$ , longitudinal and transverse sound speed  $c_{\text{lo}}$  and  $c_{\text{tr}}$ , thermal conductivity  $k^{\text{th}}$ , thermal expansion coefficient  $\alpha_{p0}$  and isothermal compressibility  $\kappa_T$  [9].

We use the iterative thermoviscous model presented in our concurrent paper [9], a model that is nonperturbative unlike the perturbative models traditionally used in acoustofluidics [7, 12]. The model exploits that the acoustic fields varies much faster ( $\sim 10^{-7}$  s) than the hydrodynamic and thermal flows ( $\sim 10^{-2}$  s), so that the fast and slow dynamics can be solved separately. Here, we study the stationary limit of the slow time scale and describe any given physical field  $Q_{\text{phys}}$  as a sum of a stationary field  $Q_0$  and a time-varying acoustic field  $\text{Re}\{Q_1 e^{-i\omega t}\}$  with a stationary complex-valued amplitude  $Q_1$ ,

$$Q_{\text{phys}}(t) = Q_0 + \text{Re}\{Q_1 e^{-i\omega t}\}. \quad (1)$$

A product of two acoustic fields will contain a steady part  $\langle a_1 b_1 \rangle = \frac{1}{2} \text{Re}\{a_1 b_1^*\}$  where the asterisk denotes complex conjugation. We neglect higher harmonics with angular frequency  $n\omega$ ,  $n = 2, 3, \dots$ . In Ref. [9], we use this ansatz to separate the governing equations in a set that controls the acoustic fields, and a set that controls the stationary fields.

Acoustofluidic systems also exhibit dynamics on two different length scales, one set by the wavelength of the acoustic fields and one set by the viscous and thermal boundary layers. The boundary conditions on the velocity field, stress, heat flux, and temperature at the fluid-solid interface results in the appearance of thermal boundary layer of width  $\delta_t$  in both the fluid and the solid, and in a viscous boundary layer of width  $\delta_s$  in the fluid. These boundary layers are localized near fluid-solid interfaces, and their dynamically-defined widths (jointly called  $\delta$ ) are small compared to a typical device size or wavelength  $d$  [1],  $\delta_s = \sqrt{2\nu_0/\omega}$  and  $\delta_t \approx \sqrt{2D^{\text{th}}/\omega}$ . Typically,  $\delta_t \lesssim \delta_s \lesssim 500$  nm, which is more than two orders of magnitude smaller than  $d \sim 100$   $\mu\text{m}$ . In our model [9], we use  $\delta \ll d$  to separate the fields into a bulk field ( $d$ ) and boundary layer field ( $\delta$ ), that are connected through the boundary conditions at the fluid-solid interface. The model presented in Ref. [9] uses the separation of time and length scales to setup an iterative model with ef-

fective boundary conditions that enables simulations of nonperturbative acoustofluidic systems without numerically resolving the viscous and thermal boundary layers. All dependent fields are given analytically by the independent fields as shown in Ref. [9].

*Acoustic fields.*—In the thermoviscous model of Ref. [9], the acoustics is fully described by the pressure field  $p_1$  in the fluid and by the displacement field  $\mathbf{u}_1^d$  in the solid through the Helmholtz and Cauchy equations,

$$\nabla^2 p_1 = -k_c^2 p_1, \quad k_c = \frac{\omega}{c_0} (1 + i\Gamma_{0c}^{\text{fl}}), \quad (2a)$$

$$-\rho\omega^2 \mathbf{u}_1^d = \nabla \cdot \boldsymbol{\sigma}_1^{d,\text{sl}}, \quad (2b)$$

$$\boldsymbol{\sigma}_1^{d,\text{sl}} = -\frac{\alpha_p}{\kappa_T} T_1 \mathbf{I} + \rho c_{\text{tr}}^2 \left[ \nabla \mathbf{u}_1 + (\nabla \mathbf{u}_1)^T \right] + \rho (c_{\text{lo}}^2 - 2c_{\text{tr}}^2) (\nabla \cdot \mathbf{u}_1) \mathbf{I}, \quad (2c)$$

where  $\boldsymbol{\sigma}_1$  is the stress tensor.  $p_1$  and  $\mathbf{u}_1^d$  are connected through effective boundary conditions on the fluid-solid interface taking the boundary layers into account analytically: a no-slip condition for the velocity and a continuity condition on the stress, as described in Ref. [9]. The acoustic velocity  $\mathbf{v}_1$  and the temperature field  $T_1$  are given by  $p_1$  and the analytical boundary-layer fields [7].

*Stationary fields.*—The stationary fields are the pressure  $p_0$  and streaming velocity  $\mathbf{v}_0^d$  in the fluid, and the temperature  $T_0^d$  in the solid and fluid. The acoustic timescale affects  $T_0^d$ ,  $p_0$ , and  $\mathbf{v}_0^d$  through bulk terms (heating and the acoustic body force  $\mathbf{f}_{\text{ac}}^d$ ) and corrections due to the boundary layers to the boundary conditions. The governing equations for  $\mathbf{v}_0^d$  and  $p_0$  are [9],

$$0 = \nabla \cdot \mathbf{v}_0^d, \quad (3a)$$

$$0 = -\nabla \left[ p_0^d - \langle \mathcal{L}_{\text{ac}}^d \rangle \right] + \eta_0 \nabla^2 \mathbf{v}_0^d - \nabla \cdot \left[ \rho_0 \mathbf{v}_0 \mathbf{v}_0 \right] + \mathbf{f}_{\text{ac}}^d. \quad (3b)$$

$$\begin{aligned} \mathbf{f}_{\text{ac}}^d = & -\frac{1}{4} |\mathbf{v}_1^{d,p}|^2 \nabla \rho_0 - \frac{1}{4} |p_1|^2 \nabla \kappa_s \\ & + \left( 1 - \frac{2a_\eta(\gamma-1)}{\beta+1} \right) \frac{\Gamma\omega}{c_0^2} \langle \mathbf{v}_1^{d,p} p_1 \rangle \\ & + 2a_\eta \eta_0 (\gamma-1) \frac{\omega}{c_0^2} \langle i \mathbf{v}_1^{d,p} \cdot \nabla \mathbf{v}_1^{d,p} \rangle. \end{aligned} \quad (3c)$$

The boundary layers generate a slip velocity on the solid-fluid interface, and the resulting effective boundary condition on  $\mathbf{v}_0^d$  is [9],

$$\mathbf{v}_0^{d0} = (\mathbf{A} \cdot \mathbf{e}_x) \mathbf{e}_x + (\mathbf{A} \cdot \mathbf{e}_y) \mathbf{e}_y + (\mathbf{B} \cdot \mathbf{e}_z) \mathbf{e}_z, \quad (4a)$$

$$\begin{aligned} \mathbf{A} = & -\frac{1}{2\omega} \text{Re} \left\{ \mathbf{v}_1^{\delta 0*} \cdot \nabla \left( \frac{1}{2} \mathbf{v}_1^{\delta 0} - i \mathbf{V}_1^0 \right) - i \mathbf{V}_1^{0*} \cdot \nabla \mathbf{v}_1^{d,p} \right. \\ & \left. + \left[ \frac{2-i}{2} \nabla \cdot \mathbf{v}_1^{\delta 0*} + i \left( \nabla \cdot \mathbf{V}_1^{0*} - \partial_z v_{1z}^{d*} \right) \right] \mathbf{v}_1^{\delta 0} \right\} \\ & + \frac{1}{2\eta_0} \text{Re} \left\{ \eta_1^{d0} \mathbf{v}_1^{\delta 0*} + \frac{1}{1 - i\delta_s/\delta_t} \eta_1^{\delta 0} \mathbf{v}_1^{\delta 0*} \right\}, \end{aligned} \quad (4b)$$

$$\mathbf{B} = \frac{1}{2\omega} \text{Re} \left\{ i \mathbf{v}_1^{d0*} \cdot \nabla \mathbf{v}_1^{d,p} \right\}. \quad (4c)$$

Here,  $\mathbf{V}_1^0$  is the velocity of the fluid-solid interface,  $\mathbf{e}_z$  is the surface normal vector, and  $\mathbf{e}_x$  and  $\mathbf{e}_y$  are perpendicular to  $\mathbf{e}_z$ . The streaming flow  $\mathbf{v}_0^d$  can be driven either by the acoustic body force  $\mathbf{f}_{ac}^d$ , called bulk-driven streaming, or by the effective boundary condition on  $\mathbf{v}_0^{d0}$ , called boundary-driven streaming.

The stationary temperature  $T_0^{d,fl}$  in the fluid is governed by the heat equation (energy conservation) [9],

$$0 = -\nabla \cdot \left[ k_0^{th} \nabla T_0^{fl,d} \right] - c_p \rho_0 \mathbf{v}_0 \cdot \nabla T_0^{fl,d} + P_{ac}^d, \quad (5a)$$

$$P_{ac}^d = -\nabla \cdot \left[ \langle k_1^{th,d} \nabla T_1^d \rangle - \langle p_1 \mathbf{v}_1^{d,p} \rangle + \langle \mathbf{v}_1^{d,p} \cdot \boldsymbol{\tau}_1^d \rangle \right] - c_p \langle \rho_1 \mathbf{v}_1^{d,p} \rangle \cdot \nabla T_0^d, \quad (5b)$$

and similarly for  $T_0^{d,sl}$  in the solid [9],

$$0 = -\nabla \cdot \left[ k_0^{th} \nabla T_0^{sl,d} \right] + P_{ac}^d \quad (6a)$$

$$P_{ac}^d = -\nabla \cdot \langle k_1^{th,sl} \nabla T_1^{sl,d} \rangle \quad (6b)$$

Here,  $P_{ac}^d$  is the power density delivered by the acoustic wave through frictional dissipation and energy flux.  $T_0^{d,fl}$  and  $T_0^{d,sl}$  are connected at the fluid-solid interface by the two effective boundary conditions taking the boundary layers into account analytically: continuity of temperature and of heat flux, applied respectively as a Dirichlet condition on  $T_0^{d,fl}$  and a flux condition on  $\mathbf{n} \cdot \nabla T_0^{d,sl}$  [9],

$$T_0^{fl,d} = T_0^{sl,d} - T_0^{fl,\delta 0} - \frac{1}{2} \text{Re} \left\{ \mathbf{u}_1 \cdot \nabla T_1^{fl,d*} - k_t^{fl} (\mathbf{u}_1 \cdot \mathbf{n}) T_1^{fl,\delta 0*} \right\}, \quad (7a)$$

$$k_0^{th,sl} \mathbf{n} \cdot \nabla T_0^{sl,d} = k_0^{th,fl} \mathbf{n} \cdot \nabla T_0^{fl,d} + k_0^{th,fl} \partial_z T_0^{fl,\delta} + \frac{1}{2} \text{Re} \left\{ k_t^{fl} k_1^{th,fl} T_1^{fl,\delta*} - \frac{2i}{\delta_t^2} k_0^{th,fl} (\mathbf{u}_1 \cdot \mathbf{n}) T_1^{fl,\delta*} \right\} \quad (7b)$$

In summary, the bulk temperature  $T_0^d$  is governed by the heat equations (5) and (6) together with the effective boundary conditions (7).

*Experimental method.*—The experiments were performed using a long straight microchannel of width  $W = 375 \mu\text{m}$  and height  $H = 135 \mu\text{m}$  in a glass-silicon chip with a piezoelectric transducer glued underneath. The transducer was driven at a frequency of 1.97 MHz at input power  $P_{in} = 6.1, 86.8, \text{ and } 182.5 \text{ mW}$ , resulting in the energy density  $E_{ac} = 27.2 \pm 1.1, 388.7 \pm 15.9, \text{ and } 817.3 \pm 33.5 \text{ J/m}^3$ , respectively, as measured from the focusing of 5.0- $\mu\text{m}$ -diameter particles at 140 fps using confocal micro-particle image velocimetry ( $\mu\text{PIV}$ ) at the low  $P_{in}$  [27]. At higher  $P_{in}$ ,  $E_{ac}$  is estimated using the proportionality  $E_{ac} \propto P_{in}$ . The confocal  $\mu\text{PIV}$  technique only captures the particle motion near the focal plane (channel mid-height), excluding particles near

the top and bottom walls influenced by hydrodynamic and acoustic particle-wall interactions, and as a result,  $E_{ac}$  is measured accurately. The acoustic streaming for each  $E_{ac}$  was measured at 10 to 60 fps by tracking the motion of 0.5- $\mu\text{m}$ -diameter particles using a defocusing-based 3D particle tracking technique [28–30]. To avoid the resonance frequency shift due to the temperature rise of the transducer under moderate (86.8 mW) and high (182.5 mW)  $P_{in}$ , each measurement was run for 2 s and repeated 100 times to improve the statistics, resulting in 7800–12000 recorded frames for each driving condition.

*Results and discussion.*—The simulation and experimental results shown in Fig. 2 reveal the dominant nonlinear behavior of the stationary streaming  $\mathbf{v}_0^d$  and temperature  $T_0$  in a standard acoustofluidic device. In the linear regime at low  $E_{ac} \lesssim 30 \text{ J/m}^3$ ,  $\mathbf{v}_0^d$  is dominated by the boundary-driven streaming entering the model through the slip-velocity condition (4), and the usual four boundary-driven streaming rolls appear, see Fig. 2(a). Due to friction in the viscous boundary layers, heat is generated both at the top and bottom of the channel. At the bottom, this heat is removed efficiently because of the high heat conductivity of silicon. At the top, however, the heat is removed less efficiently by the lower heat conductivity of glass, and a steady temperature gradient  $\nabla T_0$  is established, which explains the temperature  $T_0^d$  seen in Fig. 2(f).

The gradient  $\nabla T_0$  created by the acoustic frictional heating results in gradients in  $\nabla \rho_0$  and  $\nabla \kappa_0$ , thus inducing a thermoacoustic body force (3c)  $\mathbf{f}_{ac}^d$  [7, 8],

$$\begin{aligned} \mathbf{f}_{ac}^d &\approx -\frac{1}{4} |p_1|^2 \nabla \kappa_{s,0} - \frac{1}{4} |\mathbf{v}_1|^2 \nabla \rho_0 \\ &= -\frac{1}{4} |p_1|^2 \left( \frac{\partial \kappa_s}{\partial T} \right)_{T_0} \nabla T_0 - \frac{1}{4} |\mathbf{v}_1|^2 \left( \frac{\partial \rho}{\partial T} \right)_{T_0} \nabla T_0. \end{aligned} \quad (8)$$

Since  $|p_1|^2 \propto |\mathbf{v}_1|^2 \propto E_{ac}$  and  $|\nabla T_0| \propto P_{ac}^d \propto E_{ac}$ , we have  $|\mathbf{f}_{ac}^d| \propto E_{ac}^2$ , and  $\mathbf{f}_{ac}^d$  will become important in the bulk at high  $E_{ac}$  and cause qualitative nonlinear changes of the streaming pattern. According to Eq. (8),  $\mathbf{f}_{ac}^d$  is pointing toward high temperature at the top and is strongest at the pressure antinodes at the sides [7, 8]. Consequently,  $\mathbf{f}_{ac}^d$  pushes liquid from the sides up toward the top center, with a back-flow down along vertical center axis, thus creating a streaming pattern that consists of two streaming rolls in each side of the channel. This pattern is seen at the high  $E_{ac} = 5300 \text{ J/m}^3$  in Fig. 2(d), where the streaming is completely dominated by the thermoacoustic streaming. The transition from boundary-driven streaming at low  $E_{ac}$  to bulk-driven streaming at high  $E_{ac}$  is studied qualitatively in Fig. 2(a)-(d) and quantitatively in Fig. 2(e). During the transition, the two bottom streaming rolls expand and the two top rolls shrink, see Fig. 2(b)-(c) at  $E_{ac} = 380$  and  $800 \text{ J/m}^3$ , respectively. The bottom rolls expand because they rotate the same way as the two thermoacoustic streaming rolls.

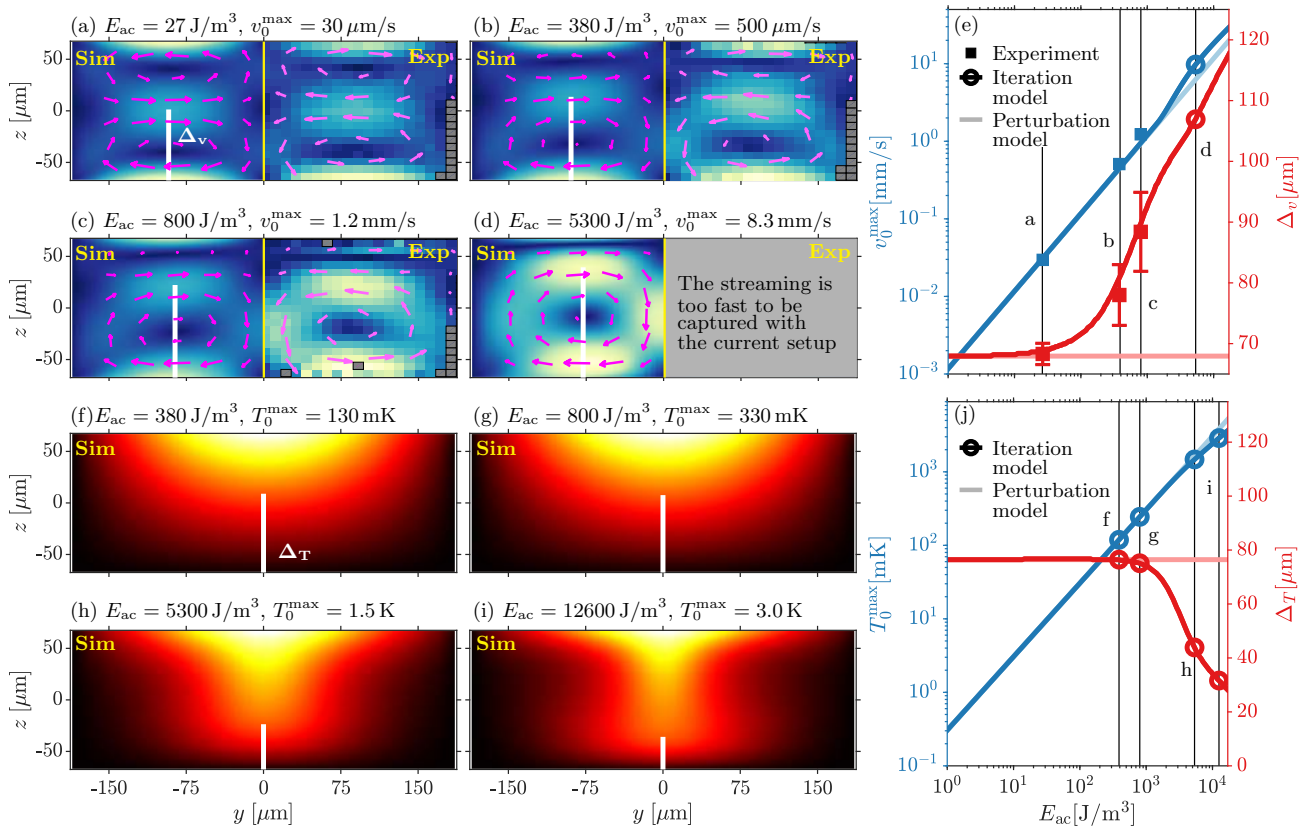


FIG. 2. Simulation and experimental results for  $v_0$  and  $T_0$  in the microchannel. (a)-(d) Vector of  $v_0$  and color plot of  $|v_0|$  from 0 (blue) to  $v_0^{\max}$  (yellow) at four  $E_{ac}$ . For each  $E_{ac}$ , the left half are simulations and the right half are experiments.  $\Delta_v$  (white bar) is the height where  $v_{0y}$  is maximal. (e) Plots of  $v_0^{\max}$  and  $\Delta_v$  vs.  $E_{ac}$  with data from simulations and experiments, showing the transition from boundary- to bulk-driven streaming. The error bars on experimental  $v_0^{\max}$  and  $E_{ac}$  are within the square markers. The round markers represent the simulations shown in panels (d) and (f)-(i). (f)-(i) Color plot of simulated temperature increase  $T_0$  from 0 (black) to  $T_0^{\max}$  at four  $E_{ac}$ .  $\Delta_T$  (white bar) is the height where  $T_0 = \frac{1}{2} T_0^{\max}$ . (j) Plots of simulated  $T_0^{\max}$  and  $\Delta_T$  vs.  $E_{ac}$  showing a transition from diffusion- to convection-dominated heat transport.

This transition is studied quantitatively in Fig. 2(e) by plotting the maximum streaming velocity  $v_0^{\max}$  and the vertical distance  $\Delta_v$  (thick white line) from the bottom of the channel to the position of the maximum horizontal streaming velocity  $\max(v_{0y})$  toward the center occurs. In the log-log plot (dark blue), the perturbative result  $v_0^{\max} \propto E_{ac}$  is valid up to  $E_{ac} \approx 1000 \text{ J/m}^3$ , but at higher values  $v_0^{\max}$  increases faster. A stronger signal is seen in the log-lin plot (dark red), where the perturbative result  $\Delta_v \propto E_{ac}^0$  only holds for  $E_{ac} \lesssim 30 \text{ J/m}^3$ , after which point  $\Delta_v$  increases with increasing  $E_{ac}$ .

As the streaming velocity increases, convection becomes increasingly important for the heat transport (5) and strongly affects the temperature field, see Fig. 2(f-i) for  $E_{ac} = 380, 800, 5300$ , and  $12,600 \text{ J/m}^3$ . Convection becomes important at a Péclet number  $\text{Pe} = |v_0| H_{fl} / D^{\text{th}} \sim 1$  corresponding to  $|v_0| \sim 1 \text{ mm/s}$ , consistent with Fig. 2(f-j). Qualitatively, we see that for

$E_{ac} \gtrsim 800 \text{ J/m}^3$ , the two flow rolls pull the temperature profile down along the vertical center axis. We quantify this effect by the maximum temperature  $T_0^{\max}$  and the vertical distance  $\Delta_T$  along the center axis from the bottom edge to the point where  $T_0 = \frac{1}{2} T_0^{\max}$ . The thermoacoustic streaming increases the heat transport from the fluid-glass interface to the silicon wafer, thus  $T_0^{\max}$  increases less steeply than the perturbative result,  $T_0^{\max} \propto E_{ac}$ , as seen in the log-log plot (blue) of  $T_0^{\max}$  vs.  $E_{ac}$  for  $E_{ac} \gtrsim 5000 \text{ J/m}^3$  in Fig. 2(j). A stronger signal is seen in the log-lin plot (dark red), where the perturbative result  $\Delta_T \propto E_{ac}^0$  only holds for  $E_{ac} \lesssim 500 \text{ J/m}^3$ , after which point  $\Delta_T$  decreases with increasing  $E_{ac}$ .

*Conclusion.*—In this Letter we have shown numerically and experimentally that the acoustic streaming in a standard microscale acoustofluidic device is changed qualitatively for moderately high acoustic energy densities  $E_{ac} \gtrsim 500 \text{ J/m}^3$ . We have explained this effect

by a nonperturbative model [9], in which a transition from boundary- to bulk-driven acoustic streaming occurs, as the acoustic body force  $\mathbf{f}_{ac}$  begins to dominate the streaming at increased  $E_{ac}$  due to the internal heating generated in the viscous boundary layers. We have shown good qualitative and quantitative agreement between our model predictions and experimental data.

$E_{ac} \gtrsim 500 \text{ J/m}^3$  can easily be obtained in standard acoustofluidic devices, where  $E_{ac} \approx 10 - 50 \text{ J/m}^3 \times [U_{pp}/(1 \text{ V})]^2$  has been reported in the literature,  $U_{pp}$  being the applied voltage on the piezoelectric transducer [11, 31–33]. The physical understanding of how such acoustofluidic devices behave at high  $E_{ac}$  is important for the continued development of high throughput devices in particular for biotech applications.

We thank R. Barnkob and M. Rossi for providing the software DefocusTracker, [defocustracking.com/](http://defocustracking.com/). WQ was supported by MSCA EF Seal of Excellence IF-2018 from Vinnova, Sweden’s Innovation Agency (Grant No. 2019-04856). HB and JHJ was supported by Independent Research Fund Denmark, Natural Sciences (Grant No. 8021-00310B).

---

\* [jonashj@fysik.dtu.dk](mailto:jonashj@fysik.dtu.dk)

† [wei.qiu@bme.lth.se](mailto:wei.qiu@bme.lth.se)

‡ [bruus@fysik.dtu.dk](mailto:bruus@fysik.dtu.dk)

- [1] J. T. Karlsen and H. Bruus, Forces acting on a small particle in an acoustical field in a thermoviscous fluid, *Phys. Rev. E* **92**, 043010 (2015).
- [2] T. Baasch, A. Pavlic, and J. Dual, Acoustic radiation force acting on a heavy particle in a standing wave can be dominated by the acoustic microstreaming, *Phys. Rev. E* **100**, 061102 (2019).
- [3] Lord Rayleigh, On the circulation of air observed in Kundt’s tubes, and on some allied acoustical problems, *Philos. Trans. R. Soc. London* **175**, 1 (1884).
- [4] C. Eckart, Vortices and streams caused by sound waves, *Phys. Rev.* **73**, 68 (1948).
- [5] G. Chini, Z. Malecha, and T. Dreeben, Large-amplitude acoustic streaming, *J. Fluid Mech.* **744**, 329 (2014).
- [6] G. Michel and C. Gissinger, Cooling by baroclinic acoustic streaming, *Phys. Rev. Applied* **16**, L051003 (2021).
- [7] J. H. Joergensen and H. Bruus, Theory of pressure acoustics with thermoviscous boundary layers and streaming in elastic cavities, *J. Acoust. Soc. Am.* **149**, 3599 (2021).
- [8] W. Qiu, J. H. Joergensen, E. Corato, H. Bruus, and P. Augustsson, Fast microscale acoustic streaming driven by a temperature-gradient-induced non-dissipative acoustic body force, *Phys. Rev. Lett.* **127**, 064501 1 (2021).
- [9] J. H. Joergensen and H. Bruus, Theory and modeling of nonperturbative effects at high acoustic energy densities in thermoviscous acoustofluidics, *Phys. Rev. E* **submitted**, 15 pages (2021), <https://arxiv.org/abs/2112.10737>.
- [10] R. Barnkob, P. Augustsson, T. Laurell, and H. Bruus, Acoustic radiation- and streaming-induced microparticle velocities determined by microparticle image velocimetry in an ultrasound symmetry plane, *Phys. Rev. E* **86**, 056307 (2012).
- [11] P. B. Muller, M. Rossi, A. G. Marin, R. Barnkob, P. Augustsson, T. Laurell, C. J. Kähler, and H. Bruus, Ultrasound-induced acoustophoretic motion of microparticles in three dimensions, *Phys. Rev. E* **88**, 023006 (2013).
- [12] P. B. Muller and H. Bruus, Numerical study of thermoviscous effects in ultrasound-induced acoustic streaming in microchannels, *Phys. Rev. E* **90**, 043016 (2014).
- [13] J. S. Bach and H. Bruus, Theory of pressure acoustics with viscous boundary layers and streaming in curved elastic cavities, *J. Acoust. Soc. Am.* **144**, 766 (2018).
- [14] M. A. Solovchuk, T. W. Sheu, M. Thiriet, and W.-L. Lin, On a computational study for investigating acoustic streaming and heating during focused ultrasound ablation of liver tumor, *Appl. Therm. Eng.* **56**, 62 (2013).
- [15] M. A. Solovchuk, M. Thiriet, and T. W. Sheu, Computational study of acoustic streaming and heating during acoustic hemostasis, *Appl. Therm. Eng.* **124**, 1112 (2017).
- [16] A. Sedaghatkish, M. Rezaeian, H. Heydari, A. M. Ranjbar, and M. Soltani, Acoustic streaming and thermosensitive liposomes for drug delivery into hepatocellular carcinoma tumor adjacent to major hepatic veins; an acoustics-thermal-fluid-mass transport coupling model, *Int. J. Therm. Sci.* **158**, 106540 (2020).
- [17] A. Ozcelik, D. Ahmed, Y. Xie, N. Nama, Z. Qu, A. A. Nawaz, and T. J. Huang, An acoustofluidic micromixer via bubble inception and cavitation from microchannel sidewalls, *Anal. Chem.* **86**, 5083 (2014).
- [18] M. V. Patel, I. A. Nanayakkara, M. G. Simon, and A. P. Lee, Cavity-induced microstreaming for simultaneous on-chip pumping and size-based separation of cells and particles, *Lab Chip* **14**, 3860 (2014).
- [19] H. Bachman, C. Chen, J. Rufo, S. Zhao, S. Yang, Z. Tian, N. Nama, P.-H. Huang, and T. J. Huang, An acoustofluidic device for efficient mixing over a wide range of flow rates, *Lab Chip* **20**, 1238 (2020).
- [20] C. Zhang, P. Brunet, L. Royon, and X. Guo, Mixing intensification using sound-driven micromixer with sharp edges, *Chem. Eng. J.* **410**, 128252 (2021).
- [21] M. Wiklund, R. Green, and M. Ohlin, Acoustofluidics 14: Applications of acoustic streaming in microfluidic devices, *Lab Chip* **12**, 2438 (2012).
- [22] D. J. Collins, Z. Ma, and Y. Ai, Highly localized acoustic streaming and size-selective submicrometer particle concentration using high frequency microscale focused acoustic fields, *Anal. Chem.* **88**, 5513 (2016).
- [23] D. J. Collins, Z. Ma, J. Han, and Y. Ai, Continuous micro-vortex-based nanoparticle manipulation via focused surface acoustic waves, *Lab Chip* **17**, 91 (2017).
- [24] J. D. Adams, C. L. Ebbesen, R. Barnkob, A. H. J. Yang, H. T. Soh, and H. Bruus, High-throughput, temperature-controlled microchannel acoustophoresis device made with rapid prototyping, *J Micromech Microeng* **22**, 075017 (2012).
- [25] M. Antfolk, C. Magnusson, P. Augustsson, H. Lilja, and T. Laurell, Acoustofluidic, label-free separation and simultaneous concentration of rare tumor cells from white blood cells, *Anal. Chem.* **87**, 9322 (2015).
- [26] A. Urbansky, F. Olm, S. Scheduling, T. Laurell, and A. Lenshof, Label-free separation of leukocyte subpopulations using high throughput multiplex acoustophoresis,



- [Lab Chip](#) **19**, 1406 (2019).
- [27] W. Qiu, J. T. Karlsen, H. Bruus, and P. Augustsson, Experimental characterization of acoustic streaming in gradients of density and compressibility, [Phys. Rev. Appl.](#) **11**, 024018 (2019).
- [28] R. Barnkob, C. J. Kähler, and M. Rossi, General defocusing particle tracking, [Lab Chip](#) **15**, 3556 (2015).
- [29] R. Barnkob and M. Rossi, General defocusing particle tracking: fundamentals and uncertainty assessment, [Exp. Fluids](#) **61**, 110 (2020).
- [30] M. Rossi and R. Barnkob, A fast and robust algorithm for general defocusing particle tracking, [Meas. Sci. Technol.](#) **32**, 014001 (2020).
- [31] R. Barnkob, P. Augustsson, T. Laurell, and H. Bruus, Measuring the local pressure amplitude in microchannel acoustophoresis, [Lab Chip](#) **10**, 563 (2010).
- [32] P. Augustsson, R. Barnkob, S. T. Wereley, H. Bruus, and T. Laurell, Automated and temperature-controlled micro-PIV measurements enabling long-term-stable microchannel acoustophoresis characterization, [Lab Chip](#) **11**, 4152 (2011).
- [33] R. Barnkob, I. Iranmanesh, M. Wiklund, and H. Bruus, Measuring acoustic energy density in microchannel acoustophoresis using a simple and rapid light-intensity method, [Lab Chip](#) **12**, 2337 (2012).



## Chapter 8

# Conclusions and outlook

Here the research of the PhD thesis is summarized and the future perspectives of temperature fields in acoustofluidic devices are discussed. The possible future applications for temperature fields would demand new features of the numerical model and a set of possible extensions to the numerical model are presented.

### 8.1 Conclusions

The main results of the thesis are the theoretical development of a thermoviscous acoustofluidic model [1, 3] and the experimental and numerical studies of streaming due to temperature gradients either induced by light absorption or attenuation of the acoustic wave [2, 4].

The numerical model includes the effects of temperature fields both the acoustic field  $T_1$  and the stationary temperature fields  $T_0$  and  $T_2$ . The temperature fields impact the acoustics and the streaming fields due to the temperature dependency of the water parameters, especially the density  $\rho$ , the compressibility  $\kappa$ , the sound speed  $c$ , and the viscosity  $\eta$ . The gradients in the material parameters are important for the inhomogeneous acoustic body force and the thermoviscous corrections to the bulk-streaming and boundary-driven streaming, while the absolute values of the material parameters are important for the resonance frequency and  $Q$ -factor of the acoustofluidic devices. In addition to include the temperature fields the developed numerical model has two main characteristics that makes it feasible to simulate complex acoustofluidic devices. Firstly, it is an effective model where the thin viscous and thermal boundary layers are solved analytically and expressed through effective boundary conditions on the pressure  $p_1$ , streaming field  $\mathbf{v}_0/\mathbf{v}_2$ , and stationary temperature field  $T_0/T_2$  which enables 3D modeling of centimetre scaled acoustofluidic devices on classical workstations. Secondly, the model can be implemented either as a perturbative or an iterative model enabling modeling of non-perturbative effects at high acoustic energy densities. Thus, the model is able to simulate non-linear effects in complex acoustofluidic devices. A limiting factor for the model is the inherent difficulty of solving the heat equation when convection is important, this requires a fine mesh in the bulk of the fluid. This currently limits 3D simulations with high convective heat flow and an improvement of the model could be made by implementing a stabilization algorithm

for the diffusion and convective heat transport.

The inhomogeneous acoustic body force that motivated the research into thermoviscous acoustofluidics has been thoroughly studied and it has been shown that small temperature differences  $\Delta T_0 \sim 0.1$  K can cause thermoacoustic streaming. The bulk-driven thermoacoustic streaming caused by the temperature induced inhomogeneous acoustic body force has been shown to be important for a range of devices: (i) devices with a temperature gradient due to heating in the piezo-electric transducer, see Section 4.2, (ii) devices with a temperature field controlled independently of the acoustic field by light absorption from an LED or laser, see Sections 4.3 and 4.5, and (iii) devices with non-linear effects due to high acoustic energy density see Section 4.4. The thermoacoustic streaming is understood theoretically and with the numerical model it is possible to include the effects when designing and optimizing acoustofluidic devices. The research have demonstrated the importance of temperature gradients for the acoustic streaming, they are important for understanding previous streaming patterns which could not be explained by a purely mechanical theory and gives an opportunity for an extra parameter when designing acoustofluidic systems, as including absorption from an LED or laser. A light source gives a high spatial and temporal resolution which can be used to control the streaming field in an acoustofluidic channel. The iterative solver was used to model non-perturbative effects at high acoustic energy densities and demonstrated nonlinear effects at acoustic energies of  $\sim 500$  J/m<sup>3</sup> which is achievable in many acoustofluidic systems.

The work on streaming in acoustic tweezers in Chapter 5 developed an axis-symmetrical model of the fluid flow driven by the bulk acoustic body force. The streaming flow can be a limiting factor for the axial trapping strength especially for high frequency acoustic tweezers. The model was validated by the analytical solution at low Reynolds numbers in a free space. The numerical model was then used to investigate the inertial effects at high Reynolds numbers and the effect of nearby boundaries (microscope slide, etc.). It was shown that in a microscope setup the streaming is heavily reduced compared to free space. It could be interesting to determine a maximum frequency where axial trapping can be obtained and investigate the effect of using spherical vortex beams instead of focalized vortex beams as proposed by Zhao et al. in Ref. [70].

The work on spatial localization of acoustic fields in Chapter 6 by either controlling the temperature field  $T_0$  or altering the chip geometry is still in an explorative phase, but does have promising aspects. The ability to control an acoustic trap by an LED gives the opportunity to move a trap around in a microfluidic chip. The dimensions of the acoustic trap is determined by the temperature field and thereby restricted by the chip dimensions, specifically the height of the fluid domain and the width of the light beam. The geometrical cavity does not offer the same flexibility but does enable to move an acoustic trap between different positions by changing the frequency of a single piezo-electric element.

## 8.2 Outlook

The model development and experimental validation of the model has led to a situation where we have a good understanding of the physics of the thermoacoustic streaming, the

next step is to identify suitable applications. It could be argued that it is already used in the trapping glass capillary tube [61, 62] to ensure nano-particles get to the vicinity of the seed particles. The opportunity to have a secondary design parameter (acoustics and temperature field) gives extra opportunities for designing an acoustofluidic system, especially the spatial and temporal control offered by LEDs and lasers should enable interesting applications. Whether it being mixing, controlled use of streaming to separate/manipulate particles, or light absorption by the particles as seen in Refs. [67, 68]. For light absorbing particles it might be necessary to consider other effects, than the bulk acoustic streaming, induced by the temperature field. There might be effects on the the acoustic radiation force when gradients in the material parameters on the length scale of the particle radius are present. A study of including temperature gradients in the acoustic radiation force would require extensive analytical work.

As acoustic tweezers is further developed and investigated so will the streaming fields that they create. The work on streaming in acoustic tweezers is currently only demonstrating some important aspects in regards to inertial effects and the impact of nearby boundaries. There is a good amount of work to be done in investigating at which frequencies the axial trapping force can not counteract the streaming induced drag force.

For further research it would be interesting to work with the temperature induced acoustic trap presented in Chapter 6. Firstly, it would be satisfying to see if it can be observed in an experimental setup. The first indication could be the ability to catch very large and heavy particles to demonstrate the localization of the acoustic wave or alternatively accurate measurements of the acoustic energy density around the LED spot. Secondly, it is natural to study the streaming induced by the temperature gradients. The temperature gradients needs to be large to localize the acoustic wave and will induce streaming as seen in Chapter 4 which will impact the ability to trap smaller particles. There could be a possibility to control the streaming pattern by making an elliptical shape of the light beam, instead of a circular ring, thereby breaking the symmetry and control the direction of the resulting streaming rolls. This could lead to a stronger trap along one axis and a weaker trap along the other axis: This could be used to design a trap with a strong trapping strength in the direction of the flow and weaker trapping strength perpendicular to the flow direction. One difficulty from a modelling perspective is the high streaming velocities together with temperature gradients will require numerical stabilization to solve the convection/diffusion problem.

### 8.3 Extending the numerical model

To explore and investigate the different research paths discussed above the numerical model would need to be extended in a few areas. The following extensions to the model would be interesting and beneficial to further study the interplay between temperature fields and acoustic waves

- **Piezo-electric transducer** – Include the piezo-electric transducer both for a more realistic acoustic actuation and for the modelling of the heat generation. The inclusion of the heat generation in the piezo-electric transducer combined with the

iterative nonlinear model would enable to model the acoustic trapping capillary in Section 4.2 where the heating and acoustic actuation are both coupled to the same electrical potential applied on the piezo-electric transducer. The mechanical actuation of the transducer has been modelled previously [31, 77], but it would be important to also include the heat generation in the transducer.

- **Stabilization algorithm** – A limiting factor for the current model is that a fine mesh is required for high streaming velocities because of the inherent difficulty of solving the diffusion/convection heat transfer. This limits the acoustic energy densities possible to study in a 3D simulation. The problem is well-known and can be solved by stabilizing the governing equations [78]. To enable simulations of higher streaming velocities it would be necessary to implement a stabilization algorithm.
- **Transient model** – When using LEDs and lasers one of the big advantages is that it gives a temporal control over the temperature field. To model the transient behaviours a transient model is necessary. The iterative model presented in Section 7.4 could be made quasi-stationary by not assuming the slow time-scale to be stationary. It can be implemented in a similar manner as presented by Orosco and Friend in Ref. [79].
- **Concentration field of particles** – An interesting experimental setup to model is the experiment presented by Dumy, Hoyos, and Aider in Refs. [67, 68] where particles are caught in an acoustic trap and illuminated by an LED. The observed *optoacoustic* effect causes the particles to leave the trap if they absorb the wavelength of the LED. This is an inherent transient problem so it requires a transient model, but it also requires an implementation of the correlation between the absorption coefficient and the concentration of particles, which could be done by implementing the particle distribution as a concentration profile similar to Ref. [80].

These extensions of the current model would enable the possibility to study new and interesting phenomena in the field of thermoviscous acoustofluidics.

# Bibliography

- [1] J. H. Joergensen and H. Bruus, *Theory of pressure acoustics with thermoviscous boundary layers and streaming in elastic cavities*. J. Acoust. Soc. Am. **149**(5), 3599–3610 (2021).
- [2] W. Qiu, J. H. Joergensen, E. Corato, H. Bruus, and P. Augustsson, *Fast microscale acoustic streaming driven by a temperature-gradient-induced non-dissipative acoustic body force*. Phys. Rev. Lett. **127**, 064501 1–6 (2021).
- [3] J. H. Joergensen and H. Bruus, *Theory and modeling of nonperturbative effects at high acoustic energy densities in thermoviscous acoustofluidics*. Phys. Rev. E **submitted**, 15 pages (2021), <https://arxiv.org/abs/2112.10737>.
- [4] J. H. Joergensen, W. Qiu, and H. Bruus, *A transition from boundary- to bulk-driven acoustic streaming due to nonlinear thermoviscous effects at high acoustic energy densities*. Phys. Rev. Lett. **submitted**, 5 pages (2022), <https://arxiv.org/abs/2112.11410>.
- [5] G. M. Whitesides, *The origins and the future of microfluidics*. Nature **442**, 368–372 (2006).
- [6] E. K. Sackmann, A. L. Fulton, and D. J. Beebe, *The present and future role of microfluidics in biomedical research*. Nature **507**(7491), 181–189 (2014).
- [7] Y. Song, Y.-Y. Huang, X. Zhang, M. Ferrari, and L. Quake, *Point-of-care technologies for molecular diagnostics using a drop of blood*. Trends Biotechnology **32**(5731), 132–9 (2014).
- [8] M. Wu, A. Ozcelik, J. Rufo, Z. Wang, R. Fang, and T. Jun Huang, *Acoustofluidic separation of cells and particles*. Microsystems & Nanoengineering **5**, 32 (2019).
- [9] F. K. Balagaddé, L. You, C. L. Hansen, F. H. Arnold, and S. R. Quake, *Long-term monitoring of bacteria undergoing programmed population control in a microchemostat*. Science **309**(5731), 137–140 (2005).
- [10] P. J. A. Kenis, R. F. Ismagilov, and G. M. Whitesides, *Microfabrication inside capillaries using multiphase laminar flow patterning*. Science **285**(5424), 83–85 (1999).

- [11] Q. Wu, J. Liu, X. Wang, L. Feng, J. Wu, X. Zhu, W. Wen, and X. Gong, *Organ-on-a-chip: recent breakthroughs and future prospects*. BioMedical Engineering OnLine **19**(1) (2020).
- [12] J. D. Caplin, N. G. Granados, M. R. James, R. Montazami, and N. Hashemi, *Microfluidic organ-on-a-chip technology for advancement of drug development and toxicology*. Advanced Healthcare Materials **4**(10), 1426–1450 (2015).
- [13] H. Amini, W. Lee, and D. Di Carlo, *Inertial microfluidic physics*. Lab Chip **14**, 2739–2761 (2014).
- [14] L. Fan, T. Luo, Z. Guan, Y. T. Chow, S. Chen, T. Wei, A. Shakoob, R. H. W. Lam, and D. Sun, *Gravitational sedimentation-based approach for ultra-simple and flexible cell patterning coculture on microfluidic device*. Biofabrication **12**(3), 035005 (2020).
- [15] S. J. Kim, Y.-C. Wang, J. H. Lee, H. Jang, and J. Han, *Concentration polarization and nonlinear electrokinetic flow near a nanofluidic channel*. Phys. Rev. Lett. **99**, 044501 (2007).
- [16] F. Alnaimat, S. Dagher, B. Mathew, A. Hilal-Alnqbi, and S. Khashan, *Microfluidics based magnetophoresis: A review*. The Chemical Record **18**(11), 1596–1612 (2018).
- [17] A. Jaffe and J. Voldman, *Multi-frequency dielectrophoretic characterization of single cells*. Microsystems and Nanoengineering **4** (2018).
- [18] D. Grier, *A revolution in optical manipulation*. Nature **424**, 810–816 (2003).
- [19] T. Laurell and A. Lenshof (eds.), *Microscale Acoustofluidics* (Royal Society of Chemistry, Cambridge) (2015).
- [20] D. Baresch, J.-L. Thomas, and R. Marchiano, *Observation of a single-beam gradient force acoustical trap for elastic particles: Acoustical tweezers*. Phys. Rev. Lett. **116**, 024301 (2016).
- [21] L. P. Gorkov, *On the forces acting on a small particle in an acoustical field in an ideal fluid*. Sov. Phys.–Dokl. **6**(9), 773–775 (1962), [Doklady Akademii Nauk SSSR **140**, 88 (1961)].
- [22] M. Settnes and H. Bruus, *Forces acting on a small particle in an acoustical field in a viscous fluid*. Phys. Rev. E **85**, 016327 (2012).
- [23] Lord Rayleigh, *On the circulation of air observed in Kundt’s tubes, and on some allied acoustical problems*. Philos. Trans. R. Soc. London **175**, 1–21 (1884).
- [24] C. Eckart, *Vortices and streams caused by sound waves*. Phys. Rev. **73**, 68–76 (1948).
- [25] F. Petersson, A. Nilsson, C. Holm, H. Jönsson, and T. Laurell, *Separation of lipids from blood utilizing ultrasonic standing waves in microfluidic channels*. Analyst **129**(10), 938–43 (2004).



- [26] D. Baresch, J.-L. Thomas, and R. Marchiano, *Three-dimensional acoustic radiation force on an arbitrarily located elastic sphere*. *J. Acoust. Soc. Am.* **133**(1), 25–36 (2013).
- [27] M. Baudoin, J.-C. Gerbedoen, A. Riaud, O. B. Matar, N. Smagin, and J.-L. Thomas, *Folding a focalized acoustical vortex on a flat holographic transducer: Miniaturized selective acoustical tweezers*. *Science Advances* **5**(4), eaav1967 (2019).
- [28] M. Baudoin, J.-L. Thomas, R. A. Sahely, J.-C. Gerbedoen, Z. Gong, A. Sivery, O. B. Matar, N. Smagin, P. Favreau, and A. Vlandas, *Spatially selective manipulation of cells with single-beam acoustical tweezers*. *Nature Communications* **11**(4244) (2020).
- [29] P. B. Muller and H. Bruus, *Numerical study of thermoviscous effects in ultrasound-induced acoustic streaming in microchannels*. *Phys. Rev. E* **90**(4), 043016 (2014).
- [30] J. S. Bach and H. Bruus, *Theory of pressure acoustics with viscous boundary layers and streaming in curved elastic cavities*. *J. Acoust. Soc. Am.* **144**, 766–784 (2018).
- [31] N. R. Skov, J. S. Bach, B. G. Winckelmann, and H. Bruus, *3D modeling of acoustofluidics in a liquid-filled cavity including streaming, viscous boundary layers, surrounding solids, and a piezoelectric transducer*. *AIMS Mathematics* **4**, 99–111 (2019).
- [32] J. T. Karlsen, P. Augustsson, and H. Bruus, *Acoustic force density acting on inhomogeneous fluids in acoustic fields*. *Phys. Rev. Lett.* **117**, 114504 (2016).
- [33] G. Chini, Z. Malecha, and T. Dreeben, *Large-amplitude acoustic streaming*. *J. Fluid Mech.* **744**, 329–351 (2014).
- [34] G. Michel and C. Gissinger, *Cooling by baroclinic acoustic streaming*. *Phys. Rev. Applied* **16**, L051003 (2021).
- [35] B. G. Winckelmann and H. Bruus, *Theory and simulation of electroosmotic suppression of acoustic streaming*. *The Journal of the Acoustical Society of America* **149**(6), 3917–3928 (2021).
- [36] J. S. Bach and H. Bruus, *Suppression of acoustic streaming in shape-optimized channels*. *Phys. Rev. Lett.* **124**, 214501 (2020).
- [37] J. T. Karlsen, W. Qiu, P. Augustsson, and H. Bruus, *Acoustic streaming and its suppression in inhomogeneous fluids*. *Phys. Rev. Lett.* **120**(5), 054501 (2018).
- [38] W. Qiu, J. T. Karlsen, H. Bruus, and P. Augustsson, *Experimental characterization of acoustic streaming in gradients of density and compressibility*. *Phys. Rev. Applied* **11**, 024018 (2019).
- [39] P. Augustsson, J. T. Karlsen, H.-W. Su, H. Bruus, and J. Voldman, *Iso-acoustic focusing of cells for size-insensitive acousto-mechanical phenotyping*. *Nat. Commun.* **7**, 11556 (2016).

- [40] J. T. Karlsen and H. Bruus, *Acoustic tweezing and patterning of concentration fields in microfluidics*. Phys. Rev. Applied **7**, 034017 (2017).
- [41] T. D. Dreeben and G. P. Chini, *Two-dimensional streaming flows in high-intensity discharge lamps*. Physics of Fluids **23**(5), 056101 (2011).
- [42] G. Michel and G. P. Chini, *Strong wave-mean-flow coupling in baroclinic acoustic streaming*. Journal of Fluid Mechanics **858**, 536–564 (2019).
- [43] P. B. Muller, R. Barnkob, M. J. H. Jensen, and H. Bruus, *A numerical study of microparticle acoustophoresis driven by acoustic radiation forces and streaming-induced drag forces*. Lab Chip **12**, 4617–4627 (2012).
- [44] M. W. H. Ley and H. Bruus, *Three-dimensional numerical modeling of acoustic trapping in glass capillaries*. Phys. Rev. Applied **8**, 024020 (2017).
- [45] L. D. Landau and E. M. Lifshitz, *Fluid Mechanics*, vol. 6 (Pergamon Press, Oxford), 2nd edn. (1993).
- [46] L. D. Landau and E. M. Lifshitz, *Statistical Physics, Part 1*, vol. 5 (Butterworth-Heinemann, Oxford), 3rd edn. (1980).
- [47] J. T. Karlsen and H. Bruus, *Forces acting on a small particle in an acoustical field in a thermoviscous fluid*. Phys. Rev. E **92**, 043010 (2015).
- [48] L. D. Landau and E. M. Lifshitz, *Theory of Elasticity. Course of Theoretical Physics*, vol. 7 (Pergamon Press, Oxford), 3rd edn. (1986).
- [49] M. Antfolk, P. B. Muller, P. Augustsson, H. Bruus, and T. Laurell, *Focusing of sub-micrometer particles and bacteria enabled by two-dimensional acoustophoresis*. Lab Chip **14**, 2791–2799 (2014).
- [50] A. Riaud, M. Baudoin, O. Bou Matar, J.-L. Thomas, and P. Brunet, *On the influence of viscosity and caustics on acoustic streaming in sessile droplets: an experimental and a numerical study with a cost-effective method*. J. Fluid Mech. **821**, 384–420 (2017).
- [51] J. S. Bach and H. Bruus, *Bulk-driven acoustic streaming at resonance in closed microcavities*. Phys. Rev. E **100**, 023104 (2019).
- [52] A. A. Doinikov, *Acoustic radiation force on a spherical particle in a viscous heat-conducting fluid .1. general formula*. J. Acoust. Soc. Am. **101**(2), 713–721 (1997).
- [53] A. A. Doinikov, *Acoustic radiation force on a spherical particle in a viscous heat-conducting fluid .2. force on a rigid sphere*. J. Acoust. Soc. Am. **101**(2), 722–730 (1997).
- [54] A. A. Doinikov, *Acoustic radiation force on a spherical particle in a viscous heat-conducting fluid. 3. Force on a liquid drop*. J. Acoust. Soc. Am. **101**(2), 731–740 (1997).

- [55] K. Yosioka and Y. Kawasima, *Acoustic radiation pressure on a compressible sphere*. *Acustica* **5**, 167–173 (1955).
- [56] R. Barnkob, I. Iranmanesh, M. Wiklund, and H. Bruus, *Measuring acoustic energy density in microchannel acoustophoresis using a simple and rapid light-intensity method*. *Lab Chip* **12**, 2337–2344 (2012).
- [57] COMSOL Multiphysics 5.6. <http://www.comsol.com> (2020).
- [58] H. Bruus, *Notes for course 01350 numerical studies in physics*. Technical University of Denmark, Department of Physics (2020).
- [59] F. Collino and P. B. Monk, *Optimizing the perfectly matched layer*. *Comput. Methods. Appl. Mech. Eng.* **164**(1-2), 157–171 (1998).
- [60] A. Bermúdez, L. Hervella-Nieto, A. Prieto, and R. Rodríguez, *An optimal perfectly matched layer with unbounded absorbing function for time-harmonic acoustic scattering problems*. *Journal of Computational Physics* **223**(2), 469–488 (2007).
- [61] B. Hammarström, T. Laurell, and J. Nilsson, *Seed particle enabled acoustic trapping of bacteria and nanoparticles in continuous flow systems*. *Lab Chip* **12**, 4296–4304 (2012).
- [62] AcouSort AB. [www.acousort.com](http://www.acousort.com).
- [63] C. L. Ebbesen and H. Bruus, *Analysis of laser-induced heating in optical neuronal guidance*. *Journal of Neuroscience Methods* **209**(1), 168–177 (2012).
- [64] R. Barnkob, P. Augustsson, T. Laurell, and H. Bruus, *Measuring the local pressure amplitude in microchannel acoustophoresis*. *Lab Chip* **10**(5), 563–570 (2010).
- [65] P. Augustsson, R. Barnkob, S. T. Wereley, H. Bruus, and T. Laurell, *Automated and temperature-controlled micro-piv measurements enabling long-term-stable microchannel acoustophoresis characterization*. *Lab Chip* **11**(24), 4152–4164 (2011).
- [66] R. Barnkob, P. Augustsson, T. Laurell, and H. Bruus, *Acoustic radiation- and streaming-induced microparticle velocities determined by microparticle image velocimetry in an ultrasound symmetry plane*. *Phys. Rev. E* **86**, 056307 (2012).
- [67] G. Dumy, M. Hoyos, and J.-L. Aider, *Observation of selective optical manipulation of particles in acoustic levitation*. *The Journal of the Acoustical Society of America* **146**(6), 4557–4568 (2019).
- [68] G. Dumy, M. Hoyos, and J.-L. Aider, *Influence of the temperature on the opto-acoustophoretic effect*. *The Journal of the Acoustical Society of America* **149**(1), 556–568 (2021).
- [69] D. Baresch, J.-L. Thomas, and R. Marchiano, *Spherical vortex beams of high radial degree for enhanced single-beam tweezers*. *Journal of Applied Physics* **113**(18), 184901 (2013).

- [70] D. Zhao, J.-L. Thomas, and R. Marchiano, *Generation of spherical vortex beams to trap large particles for enhanced axial force*. *Ultrasonics* **111**, 106296 (2021).
- [71] J. Happel and H. Brenner, *Low Reynolds number hydrodynamics with special applications to particulate media* (Martinus Nijhoff Publishers, The Hague) (1983).
- [72] M. Wiklund and H. Hertz, *Ultrasonic enhancement of bead-based bioaffinity assays*. *Lab on a Chip* **6**, 1279–1292 (2006).
- [73] B. Hammarström, N. R. Skov, K. Olofsson, H. Bruus, and M. Wiklund, *Acoustic trapping based on surface displacement of resonance modes*. *The Journal of the Acoustical Society of America* **149**(3), 1445–1453 (2021).
- [74] A. Broman, A. Lenshof, M. Evander, L. Happonen, A. Ku, J. Malmström, and T. Laurell, *Multinodal acoustic trapping enables high capacity and high throughput enrichment of extracellular vesicles and microparticles in mirna and ms proteomics studies*. *Analytical Chemistry* **93**(8), 3929–3937 (2021), pMID: 33592145.
- [75] J. N. Coupland and D. J. McClements, *Physical properties of liquid edible oils*. *J. Am. Oil Chem. Soc.* **74**, 1559–1564 (1997).
- [76] R. P. Moiseyenko and H. Bruus, *Whole-system ultrasound resonances as the basis for acoustophoresis in all-polymer microfluidic devices*. *Phys. Rev. Applied* **11**, 014014 (2019).
- [77] W. N. Bodé and H. Bruus, *Numerical study of the coupling layer between transducer and chip in acoustofluidic devices*. *The Journal of the Acoustical Society of America* **149**(5), 3096–3105 (2021).
- [78] A. N. Brooks and T. J. R. Hughes, *Streamline upwind/Petrov-Galerkin formulations for convection dominated flows with particular emphasis on the incompressible Navier-Stokes equations*. *Computer Methods in Applied Mechanics and Engineering* **32**, 199–259 (1982).
- [79] J. Orosco and J. Friend, *Unraveling the complex dynamics of acoustofluidics* (2021).
- [80] M. W. H. Ley and H. Bruus, *Continuum modeling of hydrodynamic particle-particle interactions in microfluidic high-concentration suspensions*. *Lab on a Chip* **16**(7), 1178–1188 (2016).